HELLENIC REPUBLIC

UNIVERSITY OF IOANNINA

SCHOOL OF SCIENCES

DEPARTMENT OF MATERIALS SCIENCE AND ENGINEERING

Computational study, design and applications of nano-composite metallo-dielectric photonic materials

Dimitris V. Bellas

PhD Thesis

IOANNINA 2015

HELLENIC REPUBLIC

UNIVERSITY OF IOANNINA

SCHOOL OF SCIENCES

DEPARTMENT OF MATERIALS SCIENCE AND ENGINEERING

Computational study, design and applications of nano-composite metallo-dielectric photonic materials

Dimitris V. Bellas

PhD Thesis

IOANNINA 2015

Η έγκριση της διδακτορικής διατριβής από το Τμήμα Μηχανικών Επιστήμης Υλικών της Σχολής Θετικών Επιστημών του Πανεπιστημίου Ιωαννίνων δεν υποδηλώνει αποδοχή των γνωμών του συγγραφέα Ν. 5343/32, άρθρο 202, παράγραφος 2.

Ημερομηνία αίτησης του κ. Δημήτρη Μπελλά: 14-01-2011
Ημερομηνία ορισμού Τριμελούς Συμβουλευτικής Επιτροπής: 28-01-2011
Μέλη Τριμελούς Συμβουλευτικής Επιτροπής:
Επιβλέπων
Ελευθέριος Λοιδωρίκης, Αναπληρωτής Καθηγητής του Τ.Μ.Ε.Υ της Σ.Θ.Ε του Π.Ι
Μέλη
Απόστολος Αυγερόπουλος, Καθηγητής του Τ.Μ.Ε.Υ της Σ.Θ.Ε του Π.Ι
Παναγιώτης Πατσαλάς, Αναπληρωτής Καθηγητής του Τμήματος Φυσικής της Σ.Θ.Ε του Α.Π.Θ.
Ημερομηνία ορισμού θέματος: 28-01-2015
Computational study, design and applications of nano-composite metallo-dielectric photonic materials
Ημερομηνία Ανασυγκρότησης Τριμελούς Συμβουλευτικής Επιτροπής : 07-10-2015
Μέλη Τριμελούς Συμβουλευτικής Επιτροπής:
Επιβλέπων
Ελευθέριος Λοιδωρίκης, Αναπληρωτής Καθηγητής του Τ.Μ.Ε.Υ της Σ.Θ.Ε του Π.Ι
Μέλη
Νικόλαος Ζαφειρόπουλος, Αναπληρωτής Καθηγητής του Τ.Μ.Ε.Υ της Σ.Θ.Ε του Π.Ι
Παναγιώτης Πατσαλάς, Αναπληρωτής Καθηγητής του Τμήματος Φυσικής της Σ.Θ.Ε του Α.Π.Θ.
ΔΙΟΡΙΣΜΟΣ ΕΠΤΑΜΕΛΟΥΣ ΕΞΕΤΑΣΤΙΚΗΣ ΕΠΙΤΡΟΠΗΣ : 21-07-2015

Ελευθέριος Λοιδωρίκης, Αναπληρωτής Καθηγητής του Τ.Μ.Ε.Υ της Σ.Θ.Ε του Π.Ι.
Νικόλαος Ζαφειρόπουλος, Αναπληρωτής Καθηγητής του Τ.Μ.Ε.Υ της Σ.Θ.Ε του Π.Ι
Παναγιώτης Πατσαλάς, Αναπληρωτής Καθηγητής του Τμήματος Φυσικής της Σ.Θ.Ε του Α.Π.Θ.
Βασίλειος Καλπακίδης, Καθηγητής του Τ.Μ.Ε.Υ της Σ.Θ.Ε του Π.Ι
Δημήτριος Παπαγεωργίου, Αναπληρωτής Καθηγητής του Τ.Μ.Ε.Υ της Σ.Θ.Ε του Π.Ι
Χριστίνα Λέκκα, Αναπληρώτρια Καθηγήτρια του Τ.Μ.Ε.Υ της Σ.Θ.Ε του Π.Ι
Λεωνίδας Γεργίδης, Επίκουρος Καθηγητής του Τ.Μ.Ε.Υ της Σ.Θ.Ε του Π.Ι

Έγκριση Διδακτορικής Διατριβής με βαθμό «**ΑΡΙΣΤΑ**» στις **29-10-2015**

Ο Πρόεδρος του Τμήματος

Καρακασίδης Μιχαήλ
Καθηγητής

Η Γραμματέας του Τμήματος

Ξανθή Τουτουνζόγλου

TABLE OF CONTENTS

Chapter 1 Introduction

Abstract

In this study we utilize the optical properties of metallic nanoparticles to improve the performance of nano-composite metal-dielectric solar selective coatings for high temperature applications in Concentrated Solar Collectors. Also, we explore the light-induced resonant plasmonic traits of metallic nanoparticles (enhanced fields, scattering etc) on a substrate for enhanced spectroscopy applications. Furthermore, we introduce a modeling process for the design and development of functional plasmonic templates with pre-determined properties. Specifically, we illustrate how metal-dielectric nano-composites consisting of embedded nanoparticles inside a dielectric matrix can be fabricated by using laser annealing to induce reconstructions in an alternating metal-dielectric multilayer film. Also, pre-determined nanoparticle arrangements on a substrate can be fabricated by laser annealing of thin metal film on the substrate, by using specific sequences of laser radiation. For both cases, by tuning the laser annealing and structural parameters once can arrive in surface and subsurface nano-structuring with pre-determined optical response.

1.1 Introduction

The object of this thesis is the computational study and utilization of metallic nanoparticles (MNPs) in solar harvesting and enhanced spectroscopy applications. When MNPs are irradiated by electromagnetic waves, their free electrons oscillate as a response to the external electric field. At the appropriate frequency this oscillation becomes resonant. This optical phenomenon is known as Local Surface Plasmon Resonance (LSPR), with huge polarization fields on the MNPs' surface [1-10]. These fields induce strong scattering of light and promote photo-electric processes (such as fluorescence, Raman scattering and absorption) [11-13]. Also, these fields are very sensitive to the type of metal, shape, size and dielectric environment [14-19], allowing great flexibility in designing applications. MNPs are in the heart of nanotechnology with many applications including biochemical sensing [20-23], surface enhanced spectroscopes [11, 24-26], information and communication technologies [35-38], solar energy harvesting [27-29], optical encoding [30-33], surface decoration [34], lighting [35] and many others.

In this study we use these properties of MNPs firstly, to improve the performance of Concentrated Solar Collectors through the design of nano-composite metal-dielectric solar selective coatings, which maximize the absorption in the solar spectrum and minimize the energy losses from thermal emission. Next, we explore the LSPR traits of MNPs (enhanced fields, scattering etc) on a substrate, relevant to

enhanced spectroscopy applications. Finally, we introduce a way to model and design the development of functional plasmonic templates with pre-determined properties. Specifically, we illustrate how metal-dielectric nano-composites consisting of embedded MNPs in a dielectric matrix can be fabricated by laser annealing (LA) of an alternating metal-dielectric multilayer film [36]. Also, surface MNPs on a substrate can be fabricated by LA of thin metal film on the substrate [30]. For both the above cases, by tuning the LA and structural parameters one can arrive in surface and subsurface nanostructures with pre-determined optical response. These results are presented and compared to accompanying experiments and show good agreement.

The structure of the dissertation is as follows. In Chapter 2 we present the general theoretical background of the thesis: we make a short introduction to electromagnetic theory [37] and the main numerical technique (Finite Differences Time Domain Method [38]) used for modeling the wave propagation in this work. Also, we make a short introduction to the optical properties of LSPR in MNPs. Furthermore, we describe two "tools" used in this work, the first one is the effective medium theory utilized to calculate the effective medium optical response of a nano-composite coating, and the second one is the opto-thermal modeling utilized to simulate the LA process.

In Chapter 3 we present our modeling, design and performance evaluation of nano-composite metal-dielectric absorbers, for high temperature applications to CSC. The CSCs use mirrors or lens to redirect and concentrate the solar flux on a receiver (absorber) and get collected as heat, which is in turn used to power up a turbine or a heat engine to generate electricity [39-43]. Improving the properties of the selective coating on the receiver represents one good opportunity for improving the efficiency of parabolic trough collectors and reducing the cost of solar electricity. Additionally, increasing the operating temperature above the current limits of 400 ^{0}C can improve the power cycle efficiency and reduce the cost of thermal energy storage [44, 45], resulting in reductions in the cost of solar electricity [46].

The objective of this effort is to design a new more-efficient selective coating, with both maximum absorption in the solar spectrum and highest reflection in the infrared spectrum. These optical characteristics, are required for maximum energy collection and lowest thermal emission, resulting into more efficient conversion of solar energy to electricity [47]. Using an in-house software (in which Maxwell's equations are explicitly solved utilizing the FDTD method), we successfully modeled different nano-composite metal-dielectric coatings (MNPs in various dielectric matrixes), composed of materials stable at high temperatures, and calculated the solar absorption and thermal emission coefficients. Afterwards, taking into account these coefficients, the optical parameters of the collectors' structure (sunlight concentration factor and optical losses) and the theoretically predicted Carnot's efficiency, we calculate the total conversion efficiency (η) of the CSC for various coatings in a wide temperature range from 400 ^{0}C up to 1000 ^{0}C, resulting into design rules for getting the maximum efficiency at the optimal operating temperature.

In Chapter 4 we explore the LSPR traits (enhanced electric fields, scattering etc) of MNPs arrays on a substrate relevant to enhanced spectroscopy applications. Surface Enhanced Raman Scattering (SERS) is a fascinating process by which the normally weak Raman signals used for the identification of molecular species can be amplified by many orders of magnitude [11, 24-26]. This impressive enhancement is mainly caused by the enhanced, light-induced electric fields (E-fields) on the surface of a MNP due to LSPR phenomenon [3, 48]. MNP arrays on a substrate can be developed by either top-down (e.g. nanolithography [49]) or bottom-up (e.g. self assembly by thermal [50] or laser annealing [51-54] of a thin metal film) processes, each case resulting into different particle shapes, sizes and arrangements. In this part of the thesis we explore how the LSPR traits (electric field enhancement, scattering etc) are modulated depending on the actual final MNP configuration. To better facilitate our study, we examine two "extreme" shapes: nano-columns as a representative NP shape of top-down methods and spherical nano-domes as a representative NP shape of bottom-up methods.

We produce detailed electric field enchantment maps showing that depending on the MNP shape, the frequency at which the maximum field enhancement occurs varies depending on the location on the MNP's surface. This points towards modulated LSPR oscillations across the MNP. Furthermore, for tuning the LSPR wavelength and in relevance to enhanced spectroscopy applications, we examine the effect of thin dielectric coatings (AlN) on the nanoparticles. The response is again found to dependent on the MNP shape, with results comparing well to recent experiments.

In Chapter 5 we introduce a modeling process for the design and development of functional plasmonic templates with pre-determined properties, relevant to the aforementioned applications and many others. Functional plasmonic templates consisting of MNPs embedded in a dielectric matrix or on a substrate can be fabricated by sub-surface and surface laser nano-structuring respectively. So far, nano-materials and nano-devices have traditional followed two distinct routes, the top-down process that starts from a uniform piece of material and subsequently uses finer and finer tools for creating correspondingly smaller structures (nano-lithography, ion beam nanofabrication), and the bottom-up process, where smaller components of atomic or molecular dimensions self-assemble together, according to a natural physical principle or an externally applied driving force, to give rise to larger and more organized systems (atomic layer deposition, flash thermal annealing etc). In practice, the top-down route offers unparallel control and reproducibility down to a few nanometers in feature size but at high cost for a large area processing, while the bottom-up approach naturally applies to macroscopic scale nano-patterning albeit without the fine feature and reproducibility control.

Laser radiation might be viewed as the means to a third, intermediate route for nanotechnology. Light matter interactions offer precise energy delivery and control over the physico-chemical processes in the nanoworld. Amongst the methodologies followed for creating nanoparticle arrangements and/or nano-composite thin films, LA has been proven to be simple and versatile, providing freedom of design, fast processing, compatibility with large scale manufacturing and allows for the use of inexpensive flexible substrates [30, 32, 36]. For example, LA of a thin metal film results into MNPs arrangements on top of the substrate [36, 51-54], while embedded MNPs in a dielectric matrix can be fabricated by the LA of a stack of alternating layers of metal and dielectric [30].

In this part of the thesis we investigate mainly theoretically, and in comparison with experiments, the photo-thermal processes involved in surface and sub-surface plasmonic nano-structuring. Thus, we present a way to design and develop functional plasmonic nano-structures with pre-determined morphology. Specifically, by tuning the annealing parameters like the laser fluence and wavelength and/or the structure parameters like thickness of the metallic film and the volume ratio of the ceramic metal composite, one can arrive at nano-structures with pre-designed morphology. For the surface plasmonic nano-structuring we utilize the ability to tune the laser's wavelength to either mach the absorption spectral profile of the metal or to be resonant with the plasmon oscillation frequency (LSPR). These different optical absorption mechanisms are size-selective, and a careful design of the irradiation sequence enables the fabrication of pre-determined patterns of metal nanostructures. Thus, we overcome one challenge of Laser Induced Self Assembly, and combine simultaneously large-scale character with atomic scale precision. On the other hand, for subsurface plasmonic nano-structuring, we utilize the temperature gradients that develop spatially across the metal/dielectric nano-composite structure during the laser treatment. In both cases the developed theory and the employed experiments are in good agreement.

1.2 References

[1] S.A. Maier, Plasmonics: fundamentals and applications, Springer, New York, (2007)

[2] U. Kreibig, M. Vollmer, Optical Properties of Metal Clusters, Springer, Berlin, (1995)

[3] K.A. Willets, R.P. Van Duyne, Localized Surface Plasmon Resonance Spectroscopy and Sensing, Annu. Rev. Phys. Chem., 58, 267-297, (2007)

[4] G.V. Hartland, Optical Studies of Dynamics in Noble Metal Nanostructures, Chem. Rev., 111, 3858-3887, (2011)

[5] M.R. Jones, K.D. Osberg, R.J. Macfarlane, M.R. Langille, C.A. Mirkin, Templated techniques for the synthesis and assembly of plasmonic nanostructures. Chem. Rev. 111, 3736-3827, (2011)

[6] X. Lu, M. Rycenga, S.E. Skrabalak, B.J Wiley, Y. Xia, Chemical synthesis of novel plasmonic nanoparticles, Annu. Rev. Phys. Chem., 60, 167-192, (2009)

[7] N.J. Halas, Plasmonics: an emerging field fostered by Nano Letters, Nano Let. 10, 3816-3822, (2010)

[8] M.L. Brongersma, V.M. Shalaev, The case for plasmonics, Science, 328, 440-441, (2010)

[9] J.A. Fan, C Wu, K. Bao, J. Bao, R. Bardhan, N.J. Halas, V.N. Manoharan P. Nordlander, G. Shvets, F. Capasso, Self-assembled plasmonic nanoparticle clusters, Science, 328, 1135-1138, (2010)

[10] E. Ozbay, Plasmonics: merging photonics and electronics at nanoscale dimensions, Science, 311, 189-193, (2006)

[11] E. Lidorikis, Modeling of enhanced absorption and Raman scattering caused by plasmonic nanoparticle near fields, Journal of Quantitative Spectroscopy and Radiative Transfer, 113, 2573–2584, (2012)

[12] C.F. Bohren, D.R. Huffman, Absorption and scattering of light by small particles. Wiley Interscience, New York (1983)

[13] A.J. Haes, C.L. Haynes, A.D. McFarland, G.C. Schatz, R.P. Van Duyne, S.L. Zou, Plasmonic materials for surface-enhanced sensing and spectroscopy, MRS Bull, 30, 368-375, (2005)

[14] K.S. Lee, M.A.J. El-Sayed, Gold and silver nanoparticles in sensing and imaging: sensitivity of plasmon response to size, shape and metal composition, Phys. Chem. B, 110, 19220-19225, (2006)

[15] M.M. Miller, A.A. Lazarides, Sensitivity of metal nanoparticle surface plasmon resonance to the dielectric environment, J. Phys. Chem. B, 109, 21556-21565, (2005)

[16] O. Kvitek, J. Siegel, V. Hnatowicz, V. Svorcik, Noble metal nanostructures: influence of structure and environment on their optical properties, J. Nanomater. 743684, (2013)

[17] N.J. Halas, Playing with plasmons: tuning the optical resonant properties of metallic nanoshells, MRS Bull, 30, 362-367, (2005)

[18] S. Underwood, P. Mulvaney, Effect of solution refractive index on the color of gold colloids, Langmuir, 10, 3427-3430, (1994)
[19] J.J. Mock, M. Barbic, D.R. Smith, D.A. Schultz, S.J. Schultz, Shape effects in plasmon resonance of individual colloidal silver nanoparticles, Chem. Phys., 116, 6755-6759, (2002)
[20] J.N. Anker, W.P. Hall, O. Lyandres, N.C. Shah, J. Zhao, R.P. Van Duyne, Biosensing with plasmonic nanosensors, Nat. Mater.,7, 442-453, (2008)
[21] K. M. Mayer, J. H. Hafner, Localized Surface Plasmon Resonance Sensors, Chem. Rev., 111, 3828-3857, (2011)
[22] Y.Jin, Engineering Plasmonic Gold Nanostructures and Metamaterials for Biosensing and Nanomedicine, Adv. Mater., 24, 5153-5165, (2012)
[23] E. Usukura, S. Shinohara, K. Okamoto, J. Lim, K. Char, K. Tamada, Highly confined enhanced surface fluorescence imaging with two-dimensional silver nanoparticle sheets, Appl Phys Lett,104, 121906 (2014)
[24] Moskovits M., Surface-enhanced spectroscopy, Rev. Mod. Phys, 57, 783-826 (1985)
[25] K. Kneipp, Y. Wang, H. Kneipp, L. T. Perelman, I. Itzkan, R. R. Dasari, M. S. Feld, Single Molecule Detection Using Surface-Enhanced Raman Scattering (SERS), 78(9), 1667(4), 1997
[26] Y. Fang, N.H. Seong, D.D. Dlott, Measurement of the Distribution of Site Enhancements in Surface-Enhanced Raman Scattering, Science, 321, 388-392 (2008)
[27] D. Wan, H. L. Chen, S. C. Tseng, L. A. Wang,Y. P. Chen, One-Shot Deep-UV Pulsed-Laser-Induced Photomodification of Hollow Metal Nanoparticles for High-Density Data Storage on Flexible Substrates, ACS Nano, 4, 165-173, (2010)
[28] P. Zijlstra, J. W. M. Chon, M. Gu, Five-dimensional optical recording mediated by surface plasmons in gold nanorods, Nature, 459, 410-413, (2009)
[29] C. Ryan, C. W. Christenson, B. Valle, A. Saini, J. Lott, J. Johnson, D. Schiraldi, C. Weder, E. Baer, K. D. Singer, J. Shan, Roll-to-Roll Fabrication of Multilayer Films for High Capacity Optical Data Storage, Adv. Mater., 24, 5222-5226, (2012)
[30] A. Siozios, N. Kalfagiannis, D.V. Bellas, C. Bazioti, G.P. Dimitrakopulos, G. Vourlias, W.M. Cranton, E. Lidorikis, D.C. Koutsogeorgis, P. Patsalas, Sub-surface laser nanostructuring in stratified metal/dielectric media: a versatile platform towards flexible, durable and large-scale plasmonic writing, Nanotechnology, (2015) 26 155301 (10pp).
[31] C. Bazioti, G. P. Dimitrakopulos, T. Kehagias, P. Komninou, A. Siozios, E. Lidorikis, D. C. Koutsogeorgis, P. Patsalas, Influence of laser annealing on the structural properties of sputtered AlN:Ag plasmonic nanocomposites, Journal of Materials Science, 49, 3996-4006, (2014)
[32] A. Siozios, D. C. Koutsogeorgis, E. Lidorikis, G. P. Dimitrakopulos, T. Kehagias, H. Zoubos, P. Komninou, W. M. Cranton, C. Kosmidis, P. Patsalas,

Optical Encoding by Plasmon-Based Patterning: Hard and Inorganic Materials Become Photosensitive, Nano Letters, 12, 259-263, (2012)

[33] A. Siozios, H. Zoubos, N. Pliatsikas, D. C. Koutsogeorgis, G. Vourlias, E. Pavlidou, W. Cranton, P. Patsalas, Growth and annealing strategies to control the microstructure of AlN:Ag nanocomposite films for plasmonic applications, Surface and Coatings Technology, 255, 28-36, (2014)

[34] M. Torrell, P. Machado, L. Cunha, N. M. Figueiredo, J. C. Oliveira, C. Louro, F. Vaz, Development of new decorative coatings based on gold nanoparticles dispersed in an amorphous TiO2 dielectric matrix, Surface & Coatings Technology, 204, 1569-1575, (2010)

[35] J. Henson, J. C. Heckel, E. Dimakis, J. Abell, A. Bhattacharyya, G. Chumanov, T. D. Moustakas and R. Paiella, Plasmon enhanced light emission from InGaN quantum wells via coupling to chemically synthesized silver nanoparticles Appl. Phys. Lett., 95, 151109 (3), (2009)

[36] N. Kalfagiannis, A. Siozios, D. V. Bellas, D. Toliopoulos, L. Bowen, N. Pliatsikas, W. M Cranton, C. Kosmidis, D. C. Koutsogeorgis, E. Lidorikis, P. Patsalas, Selective MOdification of Nanoparticle Arrays by Laser-Induced Self Assembly (MONA-LISA): putting control into bottom-up plasmonic nanostructuring, (Submitted).

[37] J.D. Jackson, "Classical Electrodynamics" (John Wiley & Sons, Inc. New York, 1962).

[38] A. Taflove, S. C. Hagness, Computational Electrodynamics: The Finite-Difference Time-Domain Method (3rd Edition), Boston, MA: Artech House (2005).

[39] S.S Mohd, M.K. Khan, M. Pathak, Performance enhancement of solar collectors-A review, Renewable and Sustainable Energy Reviews, 49 (2015) 192-210.

[40] D. Barlev, R. Vidu, P. Stroeve, Innovation in concentrated solar power, Solar Energy Materials and Solar Cells, 95 (2011) 2703-2725.

[41] A. Fernandez-Garcıa, E. Zarza, L. Valenzuela, M. Perez, Parabolic-trough solar collectors and their applications, Renewable and Sustainable Energy Reviews, 14 (2010) 1695-1721.

[42] D. Mills, Advanced in solar thermal electricity technology, Solar Energy, 76 (2004) 19-31.

[43] S. A. Kalogirou, Solar thermal collectors and applications, Progress in Energy and Combustion Science, 30 (2004) 231-295.

[44] C. E. Kennedy, H. Price, Progress in development of high-temperature solar selective coating, Proceedings of International Solar Energy Conference (ISEC 2005).

[45] A. Hall, A. Ambrosini, C. Ho, Solar Selective Coatings for Concentrating, Advanced Materials and Processes, Vol. 170 Is. 1 (2012) 28-32.

[46] C. Steven, M. Arun, Opportunities and challenges for a sustainable energy future, Nature, Vol. 488, Is. 7411 (2012) 294-303.

[47] C. Atkinson, C. L. Sansom, H. J. Almond, C. P. Shaw, Coatings for concentrating solar systems-A review, Renewable and Sustainable Energy Reviews, 45 (2015) 113-122.

[48] E. Hutter, J. H. Fendler, Exploration of Localized Surface Plasmon Resonance. Adv. Mater., 16, 1685-1706, (2004).

[49] J. H. Seo, J. H. Park, S. I. Kim, B. J. Park, Z. Ma, J. Choi, B. K. Ju, Nanopatterning by Laser Interference Lithography: Applications to Optical Devices, Journal of Nanoscience and Nanotechnology, 14, 1521-1532, (2014).

[50] N. T. Panagiotopoulos, N. Kalfagiannis, K. C. Vasilopoulos, N. Pliatsikas, S. Kassavetis, G. Vourlias, M. A. Karakassides, P. Patsalas, Self-assembled plasmonic templates produced by microwave annealing: applications to surface-enhanced Raman scattering, Nanotechnology, 26 205603 (2015)

[51] S. J. Henley, J. D. Carey, S. R. P. Silva, Laser-nanostructured Ag films as substrates for surface-enhanced Raman spectroscopy, Applied Physics Letters, 88, 081904, (2006)

[52] S. J. Henley, S. R. P. Silva, Laser direct write of silver nanoparticles from solution onto glass substrates for surface-enhanced Raman spectroscopy, Applied Physics Letters, 91, 023107 (2007)

[53] K. Christou, I. Knorr, J. Ihlemann, H. Wackerbarth, V. Beushausen, Fabrication and Characterization of Homogeneous Surface-Enhanced Raman Scattering Substrates by Single Pulse UV-Laser Treatment of Gold and Silver Films, Langmuir, 26(23), 18564-18569, (2010)

[54] C. H. Lin, L. Jiang, J. Zhou, H. Xiao, S.J. Chen, H.L Tsai, Laser-treated substrate with nanoparticles for surface-enhanced Raman scattering, 35(7), Opt. Let, (2010)

Chapter 2 Theoretical Background

2.1 Electromagnetic Theory

The propagation of electromagnetic fields in materials depends mainly on the interaction of the electric and magnetic fields of the wave with the charged particles (negative electrons and positive cores) of the material. This interaction appears at different scales depending on the wavelength of the light. For wavelengths large compared to individual distances (radio waves, microwaves, infrared, visible and ultraviolet) the material appears as a continuous medium, and hence the interaction with light can be described with appropriate macroscopic equations. For wavelengths compared to the atomic distances (x-rays) the interaction takes in account the multiple reflections from the periodic crystal. For even lower wavelengths (γ-rays), only in the frame of the quantum theory of light can the interaction be described.

Here, we are only concerned with the first category. We will investigate the interactions and the propagation of light in matter considering that the fields in the material can be taken as an average of the real fields around every atom. Thus, we ignore the deviation of the fields in the atomic scale and we consider that the motion of the electrons under the fields' effect can be described from the macroscopic Maxwell equations [1-4].

2.1.1 Maxwell equations

The macroscopic Maxwell equations in cgs units are:

$$\nabla \cdot \mathbf{E} = 4\pi\rho \tag{1.1}$$

$$\nabla \cdot \mathbf{B} = 0 \tag{1.2}$$

$$\nabla \times \mathbf{E} = -\frac{1}{c}\frac{\partial \mathbf{B}}{\partial t} \tag{1.3}$$

$$\nabla \times \mathbf{B} = \frac{1}{c}\frac{\partial \mathbf{E}}{\partial t} + \frac{4\pi}{c}\mathbf{J} \tag{1.4}$$

where $\mathbf{E}(\mathbf{r},t)$, $\mathbf{B}(\mathbf{r},t)$ are the vectors (as a function of space $\mathbf{r}$ and time t) of the electric field and the magnetic induction respectively, $\rho(\mathbf{r},t)$ is the charge density, $\mathbf{J}(\mathbf{r},t)$ the current density and c is the velocity of light in vacuum. These values are considered to be averages of the corresponding microscopic quantities in a unit cell, which is very small compared to the wavelength but large enough to include many atoms. For example the electric field is:

$$\mathbf{E}(\mathbf{r}) = <\mathbf{e}(\mathbf{r})> = \frac{1}{V_c}\int_{V_c}\mathbf{e}(\mathbf{r}+\xi)d\xi \tag{1.5}$$

where $\mathbf{e}$ is the microscopic local field of the electrons the atomic cores and the electromagnetic wave, V_c the volume in which the average electric field is calculated and ξ is a vector indicating the displacement of the vector $\mathbf{r}$ in the volume V_c.

2.1.2 Polarization charge and current

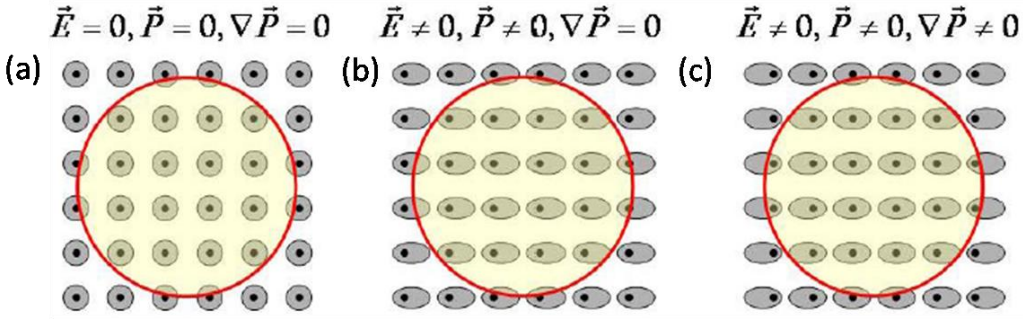

Figure 1. Polarization of atoms in an insulator: a) absence of external electric field, b) uniform external electric field c) non-uniform external electric field.

Here we explore the charge density and current density in a material under the influence of electromagnetic fields. The charge density can be non zero from two contributions. The one is from external charges (e.g. an external source) and the other is from local changes of the charge density due to its polarization from electromagnetic field.

$$\rho = \rho_{pol} + \rho_{ext} \tag{1.6}$$

The most interesting quantity is ρ_{pol}. In order to understand its physical meaning we have to see what happens to a neutral, unpolarized atom or molecule in the presence of an external electric field (fig.1). In the case of no electric field the atoms are unperturbed and are depicted in fig1.a. Integrating in a sphere within the bulk of the material enclosing many atoms we find that the total charge in the sphere is zero. At the presence of a constant electric field the atoms get polarized (fig.1.b), but the total charge in the sphere in the bulk of the material remains zero. This changes when the electric field polarizes the atoms is not uniform. In this case (fig.1.1.c) there is a net charge in the sphere. The actual polarization charge density destrtibution can be calculated from the divergence of a polarization vector.

$$\rho_{pol} = -\nabla\cdot\mathbf{P} \tag{1.7}$$

When the external electric field is changing in time then we have a temporal fluctuation of the polarization charge density, which corresponds to a polarization current.

$$\mathbf{J}_{pol} = \frac{\partial \mathbf{P}}{\partial t} \tag{1.8}$$

The equation of the continuity of charge is satisfied from the combination of equations of 1.7 and 1.8. In the case of a magnetic material, there will be and another contribution to the current, which can be taken in account as the contribution of a macroscopic magnetization **M** defined as the magnetic dipolar moment per unit volume which contributes to the current.

$$\mathbf{J}_{mag} = c\nabla \times \mathbf{M} \tag{1.9}$$

The Maxwell equations 1.1 and 1.4 can be written:

$$\nabla \cdot \mathbf{E} = -4\pi\nabla \cdot \mathbf{P} + 4\pi\rho_{ext} \tag{1.10}$$

$$\nabla \times \mathbf{B} = \frac{1}{c}\frac{\partial \mathbf{E}}{\partial t} + \frac{4\pi}{c}\frac{\partial \mathbf{P}}{\partial t} + 4\pi\nabla \times \mathbf{M} + \frac{4\pi}{c}\mathbf{J}_{ext} \tag{1.11}$$

We define now two new vectors the dielectric displacement (**D**) and the magnetic field (**H**):

$$\mathbf{D} = \mathbf{E} + 4\pi\mathbf{P} \tag{1.12}$$

$$\mathbf{H} = \mathbf{B} - 4\pi\mathbf{M} \tag{1.13}$$

Utilizing the two last equations the Maxwell's equations can be rewritten:

$$\nabla \cdot \mathbf{D} = 4\pi\rho_{ext} \tag{1.14}$$

$$\nabla \cdot \mathbf{B} = 0 \tag{1.15}$$

$$\nabla \times \mathbf{E} = -\frac{1}{c}\frac{\partial \mathbf{B}}{\partial t} \tag{1.16}$$

$$\nabla \times \mathbf{H} = \frac{1}{c}\frac{\partial \mathbf{D}}{\partial t} + \frac{4\pi}{c}\mathbf{J}_{ext} \tag{1.17}$$

2.1.3 Constitutive Relations

We need now a relation which connects the polarization and the magnetization with the electric and the magnetic field respectively. In the general case, the electric polarization and the magnetization can be written as an expansion in the electric field and the magnetic field respectively:

$$P_i = \sum_j \chi_{ij} E_j + \sum_{jk} y_{ijk} E_j E_k + \sum_{jkl} \alpha_{ijkl} E_j E_k + \ldots..$$
$$M_i = \sum_j \chi_{ij} H_j + \sum_{jk} y_{ijk} H_j H_k + \sum_{jkl} \alpha_{ijkl} H_j H_k + \ldots.. \quad (1.18)$$

The first term is the linear term and is dominant for low intensities of radiation. The rest of terms are the non-linear terms which can be contribute only at high intensities of light, for example when a material is irradiated by a high energy laser. In the general case of non-isotropic material the coefficients of the above equation are tensors. Here however, we ignore all these cases and we consider a linear isotropic response:

$$\mathbf{P} = \chi_e \mathbf{E}, \mathbf{M} = \chi_m \mathbf{H} \quad (1.19)$$

where the constants of χ_e and χ_m are the electric and the magnetic susceptibility respectively. The constitutive relations which connect the **D** with the **E** and the **B** with the **H** are the dielectric function ε and the magnetic permeability μ:

$$\mathbf{D} = \varepsilon \mathbf{E}, \mathbf{B} = \mu \mathbf{H} \quad (1.20)$$

Which have been defined as:

$$\varepsilon = 1 + 4\pi\chi_e, \mu = 1 + 4\pi\chi_m \quad (1.21)$$

The dielectric function and the magnetic permeability are functions of frequency. For the visible light all the materials have no magnetic response and their magnetic permeability is one.

The physical meaning of the correlation between **E** and **D** in a material can be understood considering the interaction with an external electric field. This incident field induces additional electric fields, as we discuss before, due to the material polarization $\mathbf{E}_{pol}$. The field entering Maxwell's equations is the total field $\mathbf{E} = \mathbf{E}_{tot} = \mathbf{E}_{ext} + \mathbf{E}_{pol}$. Combining the equations 1.7 and 1.10 with $\mathbf{E}_{pol} = -4\pi\mathbf{P}$, we find:

$$\mathbf{D} = \mathbf{E}_{ext} \quad (1.22)$$

The dielectric displacement is the external electric field (1.14). Usually for dielectric materials the induced polarization is opponent to its cause, so the electric field in the material is lower than the external thus the dielectric function (eq. 1.20) is greater than one. The same relations are applying between $\mathbf{B}$ and $\mathbf{H}$, with the difference that usually at the optical frequencies the materials are non-magnetic and $\mu = 1$. In terms of relating cause and effect, the $\mathbf{B}$ is similarly to $\mathbf{E}$ the total field and $\mathbf{H}$ is similarly to $\mathbf{D}$ the external field.

2.1.4 Plane waves

Here, we consider that there are no external charges or currents so $\rho_{ext} = \mathbf{J}_{ext} = 0$. The physical meaning of equations 1.3 and 1.4 and of equations 1.16 and 1.17 is that the temporal change of one field results into the generation of the other field. For example if an electric field starts to fluctuate in time, this change will generate a magnetic field and vice versa. That sequence between these two fields is self-sustaining, and the fields can be described by a wave equation.

The wave equation is extracted by combining equations 1.16, 1.17 and 1.20 and eliminating one of the two fields. Thus we can write two different, but equivalent wave equations, one for the electric field and one for the magnetic field:

$$\frac{1}{\varepsilon(\mathbf{r})}\nabla\times\left(\nabla\times\mathbf{E}(\mathbf{r},t)\right) = -\frac{1}{c^2}\frac{\partial^2\mathbf{E}(\mathbf{r},t)}{\partial t^2} \tag{1.23}$$

$$\nabla\times\left(\frac{1}{\varepsilon(\mathbf{r})}\nabla\times\mathbf{H}(\mathbf{r},t)\right) = -\frac{1}{c^2}\frac{\partial^2\mathbf{H}(\mathbf{r},t)}{\partial t^2} \tag{1.24}$$

In a homogeneous material the dielectric function doesn't change in space and the above equations can be simplified using the vector identity:

$$\nabla\times\left(\nabla\times\mathbf{E}\right) = \nabla\left(\nabla\cdot\mathbf{E}\right) - \nabla^2\mathbf{E} \tag{1.25}$$

which is valid for every vector field. For an isotropic material $\varepsilon(r) \equiv \varepsilon = const$ and utilizing equation 1.14 we find that $\nabla\mathbf{E} = \varepsilon^{-1}\nabla\mathbf{D} = 0$ resulting to the wave equation for the electric field:

$$\nabla^2\mathbf{E} - \frac{\varepsilon\mu}{c^2}\frac{\partial^2\mathbf{E}}{\partial t^2} = 0 \tag{1.26}$$

The same can be extracted for the magnetic field. Equation 1.26 is applied separately for every Cartesian component of $\mathbf{E}(\mathbf{r},t)$ and $\mathbf{H}(\mathbf{r},t)$. The solution is the known plane waves:

$$\begin{aligned}\mathbf{E} &= \hat{\mathbf{e}}_1 E_0 e^{i(\mathbf{kr}-\omega t)} \\ \mathbf{H} &= \hat{\mathbf{e}}_2 H_0 e^{i(\mathbf{kr}-\omega t)}\end{aligned} \tag{1.27}$$

Where E_0 and H_0 the amplitudes of the oscillation are generally complex numbers, $\hat{\mathbf{e}}_1$ and $\hat{\mathbf{e}}_2$ the unit vectors showing the direction of propagation for electric and magnetic field respectively and ω is the angular frequency which is connected to the circular frequency ν according to the relation:

$$\omega = 2\pi\nu = 2\pi c / \lambda_0 \tag{1.28}$$

$\mathbf{k}$ is the wave vector and it expresses the "spatial frequency", i.e. how the field oscilates in space at fixed time, λ_0 is the wavelength of the wave in vacuum, and c is the light velocity in vacuum. It is common convention that we use complex solutions, but in order to find the real fields we need to extract the real part at the end of the solution. If we insert equation 1.27 in the wave equation 1.26 we find:

$$|\mathbf{k}|^2 \equiv k^2 = \varepsilon\mu\frac{\omega^2}{c^2} = n^2\frac{\omega^2}{c^2} \tag{1.29}$$

which is the well known dispersion relation of light in vacuum and connects the temporal and spatial variations of the wave oscillations, n is the refractive index $n = \sqrt{\mu\varepsilon} \cong \sqrt{\varepsilon}$, where the latter relation is valid for optical frequencies because there all the materials have magnetic permeability one.

The wavelength (λ) in a material is n times smaller than the wavelength in vacuum (λ_0), $\lambda = \lambda_0 / \mathrm{n}$ and the wave vector is connected with the wavelength in the material:

$$k = \frac{2\pi}{\lambda} = \frac{2\pi n}{\lambda_0} \tag{1.30}$$

The velocity $\upsilon = \omega / k$ (fix equation) is the phase velocity of the amplitude (fig 1.2). In our case of a homogenous material with refractive index n, the phace velocity is $\upsilon = c / \mathrm{n}$ which means that the E/M wave is propagating n times slower than in vaccum. The group velocity, is the energy transfer velocity of a wave packet containing many different frequencies is defined as $\upsilon_G = d\omega / dk$. In our case of a monochromatic wave motion the two velocities are the same. They are different when there coexist a continuous distribution of frequencies (wave packet) and the refractive

index depends on the frequency. In that case the group velocity describes the transfer velocity of the center of the wave packet.

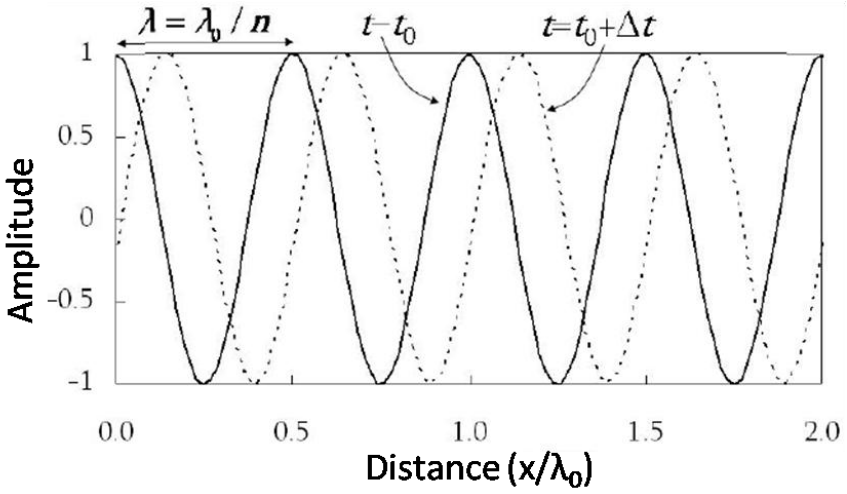

Figure 2. The real part of the first term of the wave motion equation 1.31 for $E_{+}=1$ [$\cos\left(kx-\omega t\right)$] and $n=2$.

We explore now for simplicity the case of propagation in one dimension, specifically the wave is propagating in the x direction and the electric field is polarized along the y direction. In this case the solution is:

$$\mathbf{E}\left(x,t\right)=\mathbf{y}\left[E_{+}e^{i(kx-\omega t)}+E_{-}e^{i(kx+\omega t)}\right] \tag{1.31}$$

The first term corresponds to a plane wave propagating along the positive direction of the x axis, while the second term corresponds to a plane wave propagating along the negative direction of the x axis. We take the case of a wave propagating according to the positive direction of the axis x as it is depicted to figure 2 for a homogeneous material with refractive index $n=2$. The temporal period of the fluctuation is T, i.e. the time period within which an oscillation is repeated, and is defined as:

$$T=2\pi/\omega=\lambda_0/c \tag{1.32}$$

If we go back to the solutions 1.27 and replace them to the equations of 1.14 and 1.15 we find:

$$\begin{aligned}\hat{\mathbf{e}}_1\cdot k&=0\\ \hat{\mathbf{e}}_2\cdot k&=0\end{aligned} \tag{1.33}$$

These equations state that the waves are transverse, i.e. the electric and magnetic field is perpendicular to the direction of the propagation. By replacing to the eq. 1.16

$$\left(\mathbf{k}\times\hat{\mathbf{e}}_1\right)E_0=\frac{\omega}{c}\hat{\mathbf{e}}_2H_0 \tag{1.34}$$

This has a solution:

$$\hat{\mathbf{e}}_2 = \hat{\mathbf{k}} \times \hat{\mathbf{e}}_1 \tag{1.35}$$

and

$$H_0 = nE_0 \tag{1.36}$$

where $\hat{\mathbf{k}} = \mathbf{k} / |\mathbf{k}|$. Equations 1.33 and 1.35-1.36 indicate that the vectors of the electric and magnetic fields and the wavevector (which is alnong the propagation direction) constitute a clockwise ortho-normal system, with the electric and magnetic fields being in phase and with their amplitudes at a fixed ratio.

2.1.5 Energy and momentum

The average energy density of the electromagnetic wave taking into account only the real parts of the fields averaged within one oscilation period is:

$$u = \frac{1}{16\pi}\left(\varepsilon |\mathbf{E}|^2 + \mu |\mathbf{H}|^2\right) = \frac{1}{8\pi}\varepsilon |\mathbf{E}|^2 \tag{1.37}$$

For the last derivation we use the eq.1.36 and the average energy flux is:

$$\mathbf{S} = \frac{c}{8\pi}\left(\mathbf{E} \times \mathbf{H}^*\right) \tag{1.38}$$

The vector $\mathbf{S}$ is the Poynting vector, $\mathbf{H}^*$ is the complex conjugate of the magnetic field. For plane waves in a homogenous medium it is equal to the energy density multiplied by the velocity of the propagation. Dividing equation 1.38 with 1.37 and utilizing equation 1.36, results into $|\mathbf{S}| / u = c / n$ which is the velocity of the propagation in an isotropic medium with refractive index n. The energy conservation equation at its differential form is:

$$\frac{du}{dt} + \nabla \cdot \mathbf{P} = 0 \tag{1.39}$$

which states that the rate of change of energy in a unit volume is equal and opposite to the energy flux out of this volume.

2.1.6 Dielectric Function

The classical theory of absorption and dispersion is due mainly to Lorentz and Drude [2]. The Lorentz model is applicable mainly to insulators; its quantum mechanical analog includes all direct interband transitions, i.e. all transitions of bound electrons for which the final state of an electron lies in a different band. The Drude model is applicable to free electron metals; it's quantum mechanical analog includes intraband transitions, i.e all transitions of free electrons at the conduction band. We shall see that many features of these classical models have quantum mechanical counterparts which are easily understood as generalizations of their classical analogs.

It is known that the bound electrons in an atom are organized in orbitals around the positive nucleus. At the absence of an external electric field this cloud of electrons has a spherical symmetry with the center of nucleus. Under an external electric field the electrons cloud is displaced at the opposite direction of the electric field and the atom seems like a dipole. This dipole is oscilating as a response to the external electric field. This oscilation can be described as the forced oscillation of electrons bound to the nucleus, in much the same way as a small mass be bound to a large mass by a spring. This is the Lorentz model. In order to present the Lorentz model we firsly assume one atom with one electron bound to the nucleus. We start by showing the validity of Hooke's law which is applied to describe the forced oscillation in Lorentz model. Then, putting the different forces to the Newton's law we arrive at the equation of motion, the polarization and the dielectric function.

The Lorentz oscillator model assumes a force ($\mathbf{F}_H$) applied to an orbital by the nucleus according to the Hooke's law, $\mathbf{F}_H = -k\mathbf{r}$ where k is the constant of the spring and $\mathbf{r}$ is the displacement of the orbital. While the forces between charges obey Coulombs low $\mathbf{F}_C \sim 1/\mathbf{r}^2$, we take Hooke's law because it is a valid approximation for small perturbations around the equilibrium where the force is zero (in the non-distorted state). If we want to describe this in terms of potential energy: $\mathbf{F} = -\partial V / \partial \mathbf{r} = -\partial V / \partial x$ at $x = x_0$, which when x_0 is the energy minimum, we get $\mathbf{F} = 0$. We can write the potential energy V as a Taylor expansion around x_0:

$$V = V(x_0) + V'|_{x=x_0}(x-x_0) + \frac{1}{2!}V''|_{x=x_0}(x-x_0)^2 + \frac{1}{3!}V'''|_{x=x_0}(x-x_0)^3 \qquad (1.40)$$

If we are close to the minimum, the force will be:

$$F = -\frac{dV}{dx} \simeq V' + V''(x-x_0) \qquad (1.41)$$

But the first term $V' \simeq 0$ (because it's an extremum), thus $F \simeq V''(x-x_0)$, which is just the Hooke's law where $k \equiv V''$. As a matter of fact, any general system, can be

described well by Hooke's law when it is weakly perturbed around equilibrium. So, the force is linear to the displacement, $F = -kx$ assuming $x_0 = 0$.

We can use this model to describe in a classical way how matter reacts to light. As we mentioned before, given an electric field the electrons in an atom will oscillate as a response to the external field. The restoring force of the forced oscillation according to Hooke's law is defined as $\mathbf{F}_H = -m\omega_0^2\mathbf{r}$, where m is the effective mass of the electron and $\omega_0 = \sqrt{k/m}$ is the eigen frequency of the oscilator. Also there is a friction force ($\mathbf{F}_F$), which in the simpliest approximation is propotional to the velocity ($\boldsymbol{\upsilon}$) and is defined as $\mathbf{F}_F = -m\Gamma\boldsymbol{\upsilon} = -m\Gamma(d\mathbf{r}/dt)$, where Γ is a friction constant, it has units of inverse time ($\sec^{-1}$) and it describes the energy loss rate from the oscilator. The actual loss mechanism is radiation damping for a free atom, but it also arises from various scattering mechanisms in a solid, such as electron-phonon scattering. Finally, there is the external force ($\mathbf{F}_E$) from the applied electric field ($\mathbf{E}$) is defined as $\mathbf{F}_E = -e\mathbf{E}$. Putting all the forces to the Newton's law, we write the equation of motion:

$$m\frac{d^2\mathbf{r}}{dt} + m\Gamma\frac{d\mathbf{r}}{dt} + m\omega_0^2\mathbf{r} = -e\mathbf{E} \tag{1.42}$$

In the context of a classical model, there are two approximations in equation (1.42). The nucleus has been assumed to have infinite mass compared to the electron mass, thus it stays stationary during the motion of electron. We have also neglected the force ($\mathbf{F}_M$) from the magnetic field ($\mathbf{B}$) on the electron which is defined as $\mathbf{F}_M = -e\boldsymbol{\upsilon}\times\mathbf{B}/c$. It is negligible because the collective velocity of the electron under the influence of the external perturbing field is small compared with c.

We consider that the electric field has a temporal harmonic dependence $\mathbf{E} \equiv \mathbf{E}e^{-i\omega t}$, thus the displacement $\mathbf{r}$ of the electron cloud for the specific orbital will be $\mathbf{r} \equiv \mathbf{r}e^{-i\omega t}$. By substituting to equation (1.42) and solving to $\mathbf{r}$ we find:

$$\mathbf{r} = -\frac{e\mathbf{E}}{m}\frac{1}{\omega_0^2 - \omega^2 - i\Gamma\omega} \tag{1.43}$$

The induced dipole moment as the effect of the displacement $\mathbf{r}$ of the electron cloud for the specific orbital is $\mathbf{p} = -e\mathbf{r}$,

$$\mathbf{p} = \frac{e^2\mathbf{E}}{m}\frac{1}{\omega_0^2 - \omega^2 - i\Gamma\omega} \tag{1.44}$$

We suppose that the electric field and the displacement are small, thus ω_0 and Γ are independed from the intensity of the electric field. In this case there is a linear dependence of the dipole moment and the electric field, $\mathbf{p} = \alpha(\omega)\mathbf{E}$ where

$$\alpha(\omega) = \frac{e^2}{m}\frac{1}{\omega_0^2 - \omega^2 - i\Gamma\omega} \tag{1.45}$$

is the atomic polarizability for an atom with one electron. The atomic polarizability is a function of frequency and is a complex number because we inserted the friction term. This means that there is a phase diference between the electric field and the dipole moment.

At the real case of many atoms in a material, all the dipole moments together consist the macroscopic polarization:

$$\mathbf{P} = N\alpha\mathbf{E} = \chi_e\mathbf{E} \tag{1.46}$$

where N is the number of atoms per unit volume, and χ_e is the electric susceptibility. We can now define the dielectric function (ε),

$$\begin{aligned} &\mathbf{D} = \varepsilon\mathbf{E} = \mathbf{E} + 4\pi\mathbf{P} = (1 + 4\pi\chi_e)\mathbf{E} \Rightarrow \\ &\varepsilon(\omega) = 1 + 4\pi\chi_e(\omega) \end{aligned} \tag{1.47}$$

which is a complex function of the frequency.

$$\varepsilon(\omega) = 1 + \frac{4\pi Ne^2}{m}\frac{1}{\omega_0^2 - \omega^2 - i\Gamma\omega} \tag{1.48}$$

This is the Lorentz model and gives the response of a material. If we consider classical atoms with more than one electron per atom, we can extend the previous results for m types of electrons with its corresponding orbitals. Let N_j be the density of electrons bound with resonant frequency ω_{0_j}, then :

$$\varepsilon(\omega) = 1 + \frac{4\pi e^2}{m}\sum_{j=1}^{m}\frac{N_j}{\omega_{0_j}^2 - \omega^2 - i\Gamma_j\omega} \tag{1.49}$$

$$\sum_{j=1}^{m} N_j = N \tag{1.50}$$

Now, we introduce the partial contribution of each type of electron f_j, called the oscillator strength, defined as $N_j = Nf_j$, which is a measure of the relative probability of a quantum mechanical transition and for free atoms it satisfies a sum rule $\sum_{j=1}^{m} f_j = 1$. The quantum mechanical equation can be written:

$$\varepsilon(\omega) = 1 + \frac{4\pi e^2}{m}\sum_{j=1}^{m}\frac{Nf_j}{\omega_{0_j}^2 - \omega^2 - i\Gamma_j\omega} \tag{1.51}$$

There is a formal similarity between eq. 1.49 and 1.51, but the meanings of corresponding terms are quite different. In eq. 1.49, ω_{0_j} is the resonance frequency of

a bound electron, whereas in eq.1.51, it is the transition frequency of an electron between two atomic states separated in energy by $\hbar\omega_j$.

For free-elactron metals the conduction electrons are not bound. In this case we don't have a restoring force and we should let $\omega_0 = 0$ in eq. 1.51. Also, N is not anymore the number of bound electrons, it is the number of free electrons. The result is just the Drude model for metals.

Combining now, the contribution of free-electrons (intraband transitions which is described by Drude-model) and the contribution of bound-electrons (interband transitions which is described by Lorentz-model) we result to the Drude-Lorentz model for the dielectric function:

$$\varepsilon(\omega) = 1 - \frac{4\pi e^2 N_{free}}{m}\frac{1}{\omega^2 + i\gamma\omega} + \frac{4\pi e^2 N_{bound}}{m}\sum_{j=1}^{m}\frac{f_j}{\omega_{0_j}^2 - \omega^2 - i\Gamma_j\omega} \qquad (1.52)$$

where γ corresponds to the friction (relaxation) of free electrons due to the scattering with phonons and inpurities. The different transition energies are described by the third term of $\varepsilon(\omega)$, i.e. the contribution of the bound electrons. In reality there are too many different orbitals and transitions, but we don't have to take explicity into account all of them. We can do a fit and consider a small group of characteristic Lorentzians. A common form of the dielectric function is thus:

$$\varepsilon(\omega) = \varepsilon_\infty - \frac{\omega_p^2}{\omega^2 + i\omega/\tau} + \sum_{j=1}^{N}\frac{\Delta\varepsilon_j\Omega_j^2}{\Omega_j^2 - \omega^2 - i\omega\Gamma_j} \qquad (1.53)$$

Where ε_∞ the infinite dielectric function, the plasma frequency $\omega_p = \sqrt{4\pi e^2 N_{free}/m}$, the free electrons relaxation time $\tau = 1/\gamma$, the oscillation strength and the transition frequency $\Delta\varepsilon_j\Omega_j^2 = 4\pi e^2 N_{bound} f_j / m$ and Γ_j the decay rate of the Lorentz term. All these parameters are treated as fitted parameters to experimental refractive index (n) obtained from ellipsometry measurements. For non magnetic materials the dielectric function is $\varepsilon = n^2$ thus, $\varepsilon = \varepsilon_1 + i\varepsilon_2 = (\eta + i\kappa)^2 = (\eta^2 - \kappa^2) + i2\eta\kappa$ where ε_1 and ε_2 are the real and imaginary part of the refractive index, η and κ are the real and imaginary part of the dielectric function. The procedure of calculations will be presented in the next section.

2.1.7 Finite Difference Time Domain Method

Finite Difference Time Domain (FDTD) is a numerical analysis technique used for modeling computational electrodynamics (finding approximate solutions to the associated system of differential equations). Since it is a time domain method, FDTD solutions can cover a wide frequency range with a single simulation run.

The FDTD method belongs in the general class of grid-based differential numerical modeling methods (finite difference methods). The time-dependent Maxwell's equations (in partial differential form) are discretized using central-difference approximations to the space and time partial derivatives [5]. The resulting finite-difference equations are solved in software, in a leapfrog manner: the electric field vector components in a volume of space are solved at a given instant in time; then the magnetic field vector components in the same spatial volume are solved at the next instant in time; and the process is repeated over and over again until the desired transient or steady-state electromagnetic field behavior is fully evolved.

In 1966, Kane Yee originated a set of finite-difference equations for the time-dependent Maxwell's curl equation system [6]. The Yee algorithm solves for both electric and magnetic fields in time and space using the coupled Maxwell's curl-equations for each computational grid. Firstly, we explain how the optical response of the materials are putted in the Maxwell equations and then how they are explicitly solved utilizing the FDTD method.

Maxwell's equations are:

$$\nabla \times \mathbf{E} = -\mu \partial_t \mathbf{H} \tag{1.54}$$

$$\nabla \times \mathbf{H} = \varepsilon_0 \varepsilon_\infty \partial_t \mathbf{E} + \partial_t \mathbf{P}_0 + \sum_{j_N=1}^{N} \partial_t \mathbf{P}_{j_N} \tag{1.55}$$

where the polarization of the material is taken into account trough the polarization of free electrons $\mathbf{P}_0$ according to Drude-model and the sum of the N polarizations $\mathbf{P}_{j_N}$ of the bound electrons according to Lorentz model, both follow their own differential equation:

$$\partial_t^2 \mathbf{P}_0 + \gamma \partial_t \mathbf{P}_0 = \omega_p^2 \varepsilon_0 \mathbf{E} \tag{1.56}$$

$$\partial_t^2 \mathbf{P}_{j_N} + \Gamma_{j_N} \partial_t \mathbf{P}_{j_N} + \Omega_{j_N}^2 \mathbf{P}_{j_N} = \Delta\varepsilon_{j_N} \Omega_{j_N}^2 \varepsilon_0 \mathbf{E} \tag{1.57}$$

Equations 1.56 and 1.57 imply a Drude-Lorentz model as it is discussed in the previous section for the dielectric function:

$$\varepsilon(\omega) = \varepsilon_{\infty} - \frac{\omega_p^2}{\omega^2 + i\omega\gamma} + \sum_{j_N=1}^{N} \frac{\Delta\varepsilon_{j_N}\Omega_{j_N}^2}{\Omega_{j_N}^2 - \omega^2 - i\omega\Gamma_{j_N}} \tag{1.58}$$

where the first term is the Drude free-electron contribution (intraband transitions) and the second contains Lorentz oscillators corresponding to interband transitions, ω_p and $1/\tau$ are the free electron plasma frequency and relaxation time, Ω_{j_N} , $\Delta\varepsilon_{j_N}$, and Γ_{j_N} are transition frequency, oscillator strength, and decay rate for the Lorentz terms respectively. To accurately reproduce the experimental dielectric functions we treat these as fit parameters. We use different measurements from the literature to obtain the bulk optical properties ($n = \sqrt{\varepsilon} = n + \kappa i$) for the used materials at the wavelength range of interest. Then, we apply a Drude-Lorentz fit to the bulk dielectric function and we obtain the fit parameters. Thus, we have the polarization of free (eq. 1.56) and bound (eq. 1.57) electrons, applying the polarization to equation 1.55 we calculate the magnetic field **H** and through this the electric field **E** from equation 1.54, utilizing the FDTD method.

For the display of the Yee process we first present the one dimensional case which is much simpler. The equations are more accurate when they are central differences, thus at each grid point we put the electric field and between the grid points we put the magnetic field. So we put the electric field at the points i, i+1, i+2,…. and the magnetic field at the points of i-1/2, i+1/2, i+3/2…. as it is depicted to the figure 3.

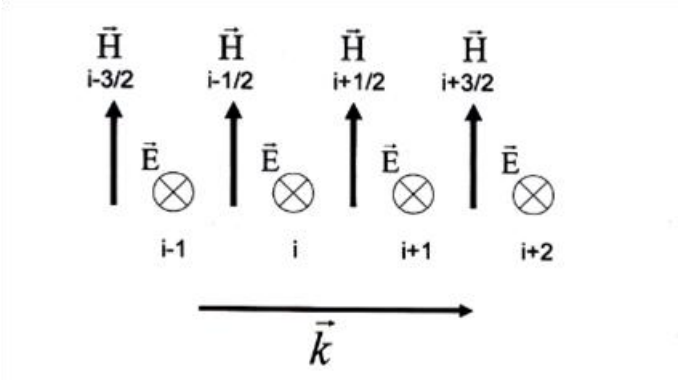

Figure 3. The distribution of fields in space in one dimension, are positioned to solve the equations as central differences.

The same is applied for the time discretization as well, setting the electric field at time steps n, n+1, n+2,… while the magnetic at time steps n+1/2, n+3/2… as it is depicted to the figure 4.

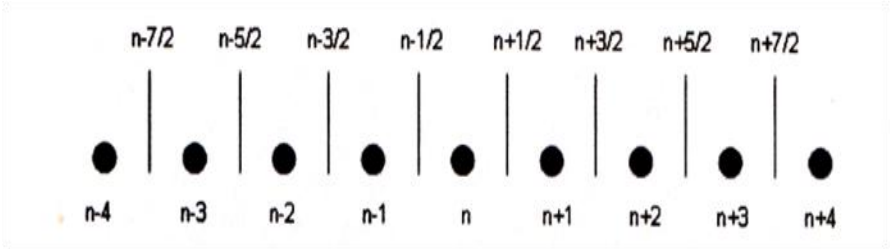

Figure 4. The distribution of fields in time in one dimension.

We consider that the electric field is oscillating at z direction, and the magnetic at y direction. The Maxwell equations for one dimension then become:

$$\varepsilon_0\varepsilon_\infty \frac{\partial E_z}{\partial t} + \sum_{j_N=0}^{N} \frac{\partial P_{j_N}}{\partial t} = (\nabla \times H)_z \Rightarrow \varepsilon_0\varepsilon_\infty \frac{\partial E_z}{\partial t} + \sum_{j_N=0}^{N} \frac{\partial P_{j_N}}{\partial t} = \frac{\partial H_y}{\partial x} \tag{1.59}$$

$$-\mu \frac{\partial H_y}{\partial t} = (\nabla \times E)_y \Rightarrow -\mu \frac{\partial H_y}{\partial t} = \frac{\partial E_z}{\partial x} \tag{1.60}$$

Knowing the electric field everywhere in space (i) at the time n, the magnetic field everywhere in space at time n-1/2 and the polarization moments everywhere in space at times n and n-1, we arrive at the following difference equations:

Firstly, we find the polarization at the time n+1 from eq. 1.56:

$$\begin{gathered} \frac{P_i^{n+1} - 2P_i^n + P_i^{n-1}}{\Delta t^2} + \gamma \frac{P_i^{n+1} - P_i^{n-1}}{2\Delta t} + \omega_0^2 P_i^n = \omega_p^2 \varepsilon_0 E_i{}^n \\ P_i^{n+1} = \frac{4P_i^n + 2P_i^{n-1} + \Delta t \gamma_0 P_i^{n-1} + 2\Delta t^2 (\varepsilon_0 \omega_p^2 E_i^n - \omega_0^2 \vec{P}_i^n))}{2 + \gamma_0 \Delta t} \end{gathered} \tag{1.61}$$

The same is applied for all the other N polarizations (eq. 1.57) taken from the Lorentz term of the dielectric function (eq. 1.58). Then we find the electric field at the time n+1:

$$E_i^{n+1} = E_i^n - \frac{1}{\varepsilon_0\varepsilon_\infty} \sum_{j_N=0}^{N} \left(P_{ij_N}^{n+1} - P_{ij_N}^n \right) - \frac{\Delta t}{\Delta x} \varepsilon_0\varepsilon_\infty \left(H_{i+1/2}^{n+1/2} - H_{i-1/2}^{n+1/2} \right) \tag{1.62}$$

At the same way we find the magnetic field at the time n+3/2:

$$H_{i+1/2}^{n+3/2} = H_{i+1/2}^{n+1/2} - \frac{\Delta t}{\mu \Delta x} (E_{i+1}^{n+1} - E_i^{n+1}) \tag{1.63}$$

The numerical algorithms for Maxwell's curl equations defined by the finite-difference systems require that the time increment Δt have a specific bound relative to the lattice space increments Δx , Δy , Δz . This bound is necessary to avoid numerical instability, an undesirable possibility with explicit differential equation solvers that can cause the computed results to spuriously increase without limit as time-marching continues. In our case of the three-dimensional Yee algorithm which will be presented below, this problem of numerical instability is avoided by setting the upper bound on Δt follows the equation [5]:

$$\Delta t \leq \frac{1}{\sqrt{\frac{1}{(\Delta x)^2}+\frac{1}{(\Delta y)^2}+\frac{1}{(\Delta z)^2}}} \tag{1.64}$$

Denormalizing to a nonunity value of light velocity c , it can be shown that equation 1.64 is slightly modified:

$$\Delta t \leq \frac{1}{c\sqrt{\frac{1}{(\Delta x)^2}+\frac{1}{(\Delta y)^2}+\frac{1}{(\Delta z)^2}}} \tag{1.65}$$

For a cubic lattice case $\Delta x = \Delta y = \Delta z = \Delta$, we can see that the upper bound reduces to:

$$\Delta t \leq \frac{1}{c\sqrt{\frac{1}{\Delta^2}+\frac{1}{\Delta^2}+\frac{1}{\Delta^2}}} = \frac{1}{c\sqrt{\frac{3}{\Delta^2}}} = \frac{\Delta}{c\sqrt{3}} \tag{1.66}$$

The spatial and temporal resolution must be taken with case so that the algorithm is stable and reproduces correctly all physical phenomena. The latter condition is more stringent for the case of plasmonics, where rapid variations of strong fields occur close to metallic nanoparticles, in which case we typically choose a fine spatial grid of 1 nm.

In the three-dimensional case the space is discretized in unit cells and the field placement is illustrated at figure 5. In addition to the electric and magnetic fields being displaced from each other, in the Yee scheme each component of a field is also displaced from the others. Specifically, the electric field components are placed on the edges of the cell, while the magnetic field components are placed along the normal to the faces of the cube.

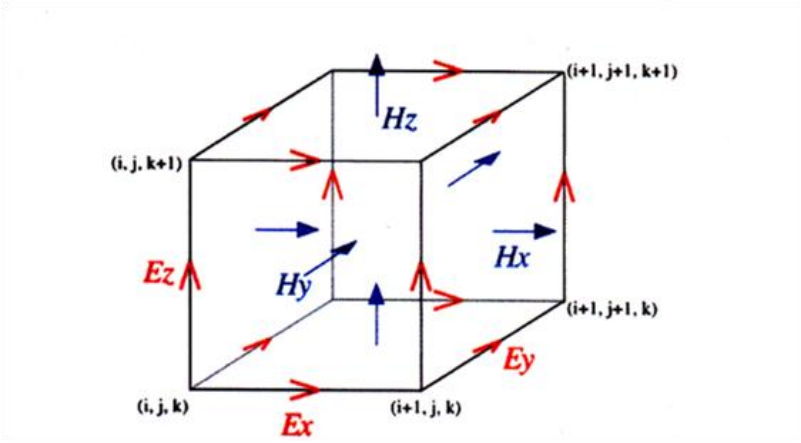

Figure 5. Illustration of a standard Cartesian Yee cell used for FDTD, about which electric and magnetic field vector components are distributed.

Similarly to the 1D case, the fields are alternating in time and space. The update equations for the polarization are written:

$$P_{x,y,z}\Big|_{i,j,k}^{n+1} = \frac{4P_{x,y,z}\Big|_{i,j,k}^{n} + 2P_{x,y,z}\Big|_{i,j,k}^{n-1} + \Delta t\gamma_0 P_{x,y,z}\Big|_{i,j,k}^{n-1} + 2\Delta t^2(\varepsilon_0\omega_p^2 E_{x,y,z}\Big|_{i}^{n} - \omega_0^2 P_{x,y,z}\Big|_{i,j,k}^{n})}{2+\gamma_0\Delta t}$$

(1.67)

The electric fields for each direction:

$$E_x\Big|_{i,j,k}^{n} = E_x\Big|_{i,j,k}^{n} - \frac{1}{\varepsilon_\infty\varepsilon_{i,j,k}}\sum_{j_N=0}^{N}\left(P_{xj_N}\Big|_{i,j,k}^{n+1} - P_{xj_N}\Big|_{i,j,k}^{n-1}\right) - \frac{\Delta t}{\varepsilon_\infty\varepsilon_{i,j,k}}\left(\frac{H_z\Big|_{i,j+1/2,k}^{n+1/2} - H_z\Big|_{i,j-1/2,k}^{n+1/2}}{\Delta y} - \frac{H_y\Big|_{i,j,k+1/2}^{n+1/2} - H_y\Big|_{i,j,k-1/2}^{n+1/2}}{\Delta z}\right)$$

$$E_y\Big|_{i,j,k}^{n+1} = E_y\Big|_{i,j,k}^{n} - \frac{1}{\varepsilon_\infty\varepsilon_{i,j,k}}\sum_{j_N=0}^{N}\left(P_{yj_N}\Big|_{i,j,k}^{n+1} - P_{yj_N}\Big|_{i,j,k}^{n-1}\right) - \frac{\Delta t}{\varepsilon_\infty\varepsilon_{i,j,k}}\left(\frac{H_x\Big|_{i,j,k+1/2}^{n+1/2} - H_x\Big|_{i,j,k-1/2}^{n+1/2}}{\Delta z} - \frac{H_z\Big|_{i+1/2,j,k}^{n+1/2} - H_y\Big|_{i-1/2,j,k}^{n+1/2}}{\Delta x}\right)$$

$$E_z\Big|_{i,j,k}^{n+1} = E_z\Big|_{i,j,k}^{n} - \frac{1}{\varepsilon_\infty\varepsilon_{i,j,k}}\sum_{j_N=0}^{N}\left(P_{zj_N}\Big|_{i,j,k}^{n+1} - P_{zj_N}\Big|_{i,j,k}^{n-1}\right) - \frac{\Delta t}{\varepsilon_\infty\varepsilon_{i,j,k}}\left(\frac{H_y\Big|_{i+1/2,j,k}^{n+1/2} - H_y\Big|_{i-1/2,j,k}^{n+1/2}}{\Delta x} - \frac{H_z\Big|_{i,j+1/2,k}^{n+1/2} - H_y\Big|_{i,j-1/2,k}^{n+1/2}}{\Delta y}\right)$$

(1.68)

And finally, the magnetic fields at each direction:

$$H_x\Big|_{i,j,k}^{n+3/2} = H_x\Big|_{i,j,k}^{n+1/2} - \frac{\Delta t}{\mu_{i,j,k}}\left(\frac{E_y\Big|_{i,j,k+1/2}^{n+1} - E_y\Big|_{i,j,k-1/2}^{n+1}}{\Delta z} - \frac{E_z\Big|_{i,j+1/2,k}^{n+1} - E_z\Big|_{i,j-1/2,k}^{n+1}}{\Delta y}\right)$$

$$H_y\Big|_{i,j,k}^{n+3/2} = H_y\Big|_{i,j,k}^{n+1/2} - \frac{\Delta t}{\mu_{i,j,k}}\left(\frac{E_z\Big|_{i+1/2,j,k}^{n+1} - E_z\Big|_{i-1/2,j,k}^{n+1}}{\Delta x} - \frac{E_x\Big|_{i,j,k+1/2}^{n+1} - E_x\Big|_{i,j,k-1/2}^{n+1}}{\Delta z}\right)$$

$$H_z\Big|_{i,j,k}^{n+3/2} = H_z\Big|_{i,j,k}^{n+1/2} - \frac{\Delta t}{\mu_{i,j,k}}\left(\frac{E_x\Big|_{i,j+1/2,k}^{n+1} - E_x\Big|_{i,j-1/2,k}^{n+1}}{\Delta y} - \frac{E_y\Big|_{i+1/2,j,k}^{n+1} - E_y\Big|_{i-1/2,j,k}^{n+1}}{\Delta x}\right)$$

(1.69)

We solve the wave propagation in time domain and then by applying Furier transforms we extract the fields and the polarizations in frequency domain at each grid point in the computational volume.

$$\begin{aligned}\mathbf{H}(\omega) &= \int_{-\infty}^{+\infty} e^{-i\omega t}\mathbf{H}(t)d \\ \mathbf{E}(\omega) &= \int_{-\infty}^{+\infty} e^{-i\omega t}\mathbf{E}(t)d \\ \mathbf{J}(\omega) &= \int_{-\infty}^{+\infty} e^{-i\omega t}\sum_{j_N=0}^{N}\frac{\Delta\mathbf{P}(t)}{\Delta t}dt\end{aligned} \tag{1.70}$$

And the energy flux F integrating the Poynting vector on a chosen flux plane with area A:

$$F = \int \mathbf{S}dA = \int \frac{c}{8\pi}\left(\mathbf{E}(\omega)\times\mathbf{H}^{*}(\omega)\right)dA \tag{1.71}$$

a typical simulation example will be presented in detail in a next section.

2.2 Plasmons

2.2.1 Introduction in Surface and Localized Plasmons

The physical phenomenon of plasmons has helped to enhance methods of chemical analysis in recent decades, even to the point where it is possible to detect a single molecule. Though many of these methods have not yet found their way into traditional chemistry classes and labs, it is likely that many of today's chemistry and biochemistry majors will encounter plasmon-based techniques in their future. Some techniques, such as surface plasmon resonance, staining for microscopy, and colorimetry have already been commercialized. Other applications for plasmons are still being explored, for example, plasmon-based alternatives to traditional electronic circuits.

Strictly speaking, plasmons are quantized waves in a collection of mobile electrons that are produced when large numbers of these electrons are disturbed from their equilibrium positions [8, 9]. Electrons present in classic gaseous plasmas can support plasmons, hence the name of these waves. The collection of mobile electrons in metals is referred to as quantum plasma [9]. This is composed of delocalized electrons that bathe the metal nuclei and their localized core electrons, as described by the free-electron theory of metals [8]. This description of metallic bonding has been used to explain many metallic properties.

Metals that best exhibit this mobile-electron or free-electron plasma behavior include the alkali metals, Mg, Al, and noble metals such as Cu, Ag, and Au [8]. Plasmons can exist within the bulk of metals, and their existence was used to explain energy losses associated with electrons beamed into bulk metals [10]. For a bulk metal of infinite size, the frequency of oscillation ω_p can be described by the following equation:

$$\omega_p = \sqrt{\frac{Ne^2}{\varepsilon_0 m_e}} \tag{1.72}$$

where N is the number density of mobile electrons, ε_0 is the dielectric constant of a vacuum, e is the charge of an electron and m_e is the effective mass of an electron.

Surface plasmons (SPs) are a type of plasmon associated with the surfaces of metals. They are significantly lower in frequency (and energy) than bulk plasmons and can interact, under certain conditions, with visible light in a phenomenon called Surface Plasmon Resonance (SPR). SPs have been the most useful to chemists. For example, the electric fields of SPs amplify optical phenomena such as Raman scattering [8, 11], which will be discussed in next chapter. There are at least two types of SPs: a) Propagating SPs, which occur on extended metal surfaces and b) Localized SPs, which occur in small volumes such as metal particles.

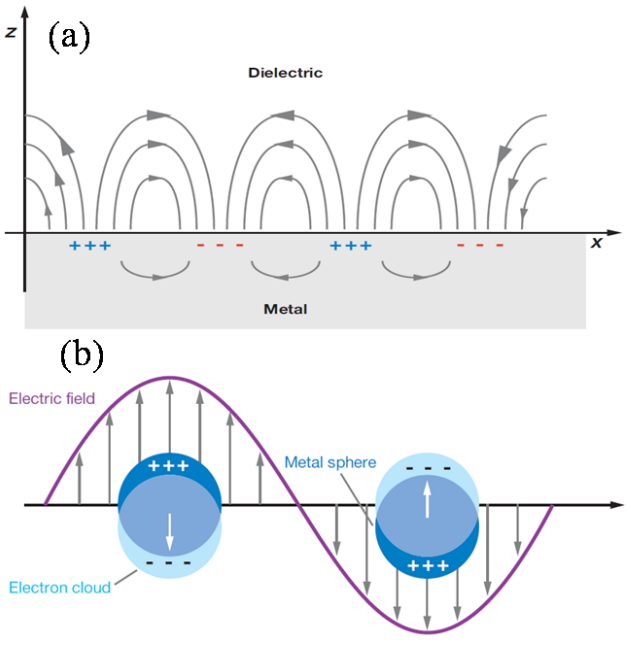

Figure 6. Schematic diagram illustrating the difference between: a) a Surface Plasmon Polariton (or Propagating Plasmon) b) a Localize Surface Plasmon.

Figure 6 illustrates the difference between propagating and localized surface plasmons. In the case of Surface Plasmon Polaritons (Fig 6.a) , plasmons propagate in the x- and y- directions along the metal-dielectric interface, for distances on the order of tens to hundreds of microns, and decay evanescently in the z - direction with 1/e decay lengths on the order of 200 nm. The interaction between the metal surface-confined EM wave and a molecular surface layer of interest leads to shifts in the plasmon resonance condition, which can be observed in three modes: a) angle resolved, b) wavelength shift, and c) imaging. In the first two modes, one measures the reflectivity of light from the metal surface as a function of either angle of incidence (at constant wavelength) or wavelength (at constant angle of incidence). The third method uses light of both constant wavelength and incident angle to interrogate a two-dimensional region of the sample, mapping the reflectivity of the surface as a function of position.

Localized Surface Plasmons (LSPs), are the collective electron oscillations in small volumes, Figure 6b. LSPs also have lower frequencies and energies than bulk plasmons, metal particles in contact with a vacuum have LSPs with a theoretical frequency of $\omega_p / \sqrt{3}$, this will be derived in the next section. LSP resonances are produced in a somewhat different fashion from SPPs. An example of this interaction between light and the electrons of a metal particle is illustrated in figure 1b [8]. For this phenomenon to occur, the particle must be much smaller than the wavelength of incident light. The electric field of the incident light can induce an electric dipole in the metal particle by displacing many of the delocalized electrons in one direction away from the rest of the metal particle and thus producing a net negative charge on one side. Since the rest of the metal particle is effectively a cationic lattice of nuclei and localized core electrons, the side opposite the negative charge has a net positive charge. LSPs have also been referred to as dipole plasmons, but the oscillating field of the incident light can induce quadrupole as well as dipole resonances, especially for particles greater than 30 nm in diameter [12, 13]. If a particle with a dipole can be considered to have a positively charged pole and a negatively charged pole, then a particle with a quadrupole can be considered to have two positively charged poles and two negatively charged poles.

The energy of light required to produce LSP resonance depends on a number of factors, including the kind of metal, the size of the particles, as well as the composition of the surrounding dielectric media. The interactions of light with spherical metal particles can be described by Mie theory, which is based upon an exact solution to Maxwell's equations [4]. This theory also predicts what fraction of light impinging upon colloidal metal particles will be absorbed and what fraction will be scattered. The sum of absorption and scattering is the extinction of light due to the particles. This is actually what is measured when one places a colloidal metal suspension into a UV-vis spectrometer. In the following section we explore the

physics of Localized Surface Plasmons by considering the interaction of metal nanoparticles with the electromagnetic wave in order to arrive at the resonance condition.

2.2.2 Optical Properties of LSPR of MNPs

The interaction of a particle of size d with the electromagnetic field can be analyzed using the simple quasi-static approximation provided that $d \ll \lambda$ i.e. the particle is much smaller than the wavelength of light in the surrounding medium. In this case, the phase of the harmonically oscillating electromagnetic field is practically constant over the particle volume, so that one can calculate the spatial field distribution by assuming the simplified problem of a particle in an electrostatic field. The harmonic time dependence can then be added to the solution once the field distributions are known. As we will show below, this lowest-order approximation of the full scattering problem describes the optical properties of nanoparticles of dimensions below 100 nm adequately for many purposes.

We start with the most convenient geometry for an analytical treatment: a homogeneous, isotropic sphere of radius a located at the origin in a uniform, static electric field $\mathbf{E} = E_0 \hat{z}$ (Fig.7). The surrounding medium is isotropic and non-absorbing with dielectric constant ε_m and the field lines are parallel to the z-direction at sufficient distance from the sphere. The dielectric response of the sphere is further described by the dielectric function $\varepsilon(\omega)$, which we take for the moment as a simple complex number ε.

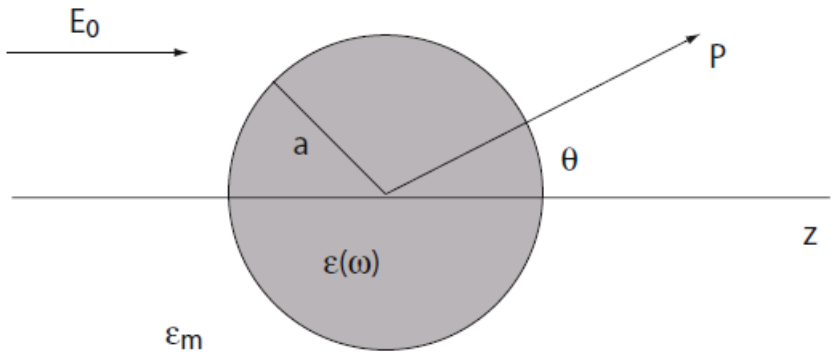

Figure 7. Illustration of a homogeneous placed into an electrostatic field.

In the electrostatic approach, we are interested in a solution of the Laplace equation for the potential, $\nabla^2 \Phi = 0$, from which we will be able to calculate the electric field $\mathbf{E} = -\nabla\Phi$. Due to the azimuthal symmetry of the problem the general solution is [1]:

$$\Phi(r,\theta)=\sum_{l=0}^{\infty}\left[A_l r^l + B_l r^{-(l+1)}\right]P_l(\cos\theta) \tag{1.73}$$

where, $P_l(\cos\theta)$ are the Legendre Polynomials of order l, and θ the angle between the position vector $\mathbf{r}$ at point P and the z axis (Fig. 7). Due to the requirement that the potential remains finite at the origin and applying the equality of the tangerial compoments of the electric field and the normal components of the displacement field, the solution for the potentials Φ_{in} inside and Φ_{out} outside the sphere can be written as [1]:

$$\Phi_{in}=-\frac{3\varepsilon_m}{\varepsilon+2\varepsilon_m}E_0 r\cos\theta \tag{1.74}$$

$$\Phi_{out}=-E_0\cos\theta+\frac{\varepsilon-\varepsilon_m}{\varepsilon+2\varepsilon_m}a^3\frac{\cos\theta}{r^2} \tag{1.75}$$

The physically interpretation of eq. 1.75 is interesting. The Φ_{out} describes the superposition of the applied field and that of a dipole located at the particle center. We can rewrite Φ_{out} by introducing the dipole moment $\mathbf{p}$ as:

$$\Phi_{out}=-E_0 r\cos\theta+\frac{\mathbf{p}\cdot\mathbf{r}}{4\pi\varepsilon_0\varepsilon_m r^3} \tag{1.76}$$

$$\mathbf{p}=4\pi\varepsilon_0\varepsilon_m a^3\frac{\varepsilon-\varepsilon_m}{\varepsilon+2\varepsilon_m}\mathbf{E_0} \tag{1.77}$$

We therefore see that the applied field induces a dipole moment inside the sphere of magnitude proportional to $|\mathbf{E_0}|$.

If we introduce the polarizability α , defined via $\mathbf{p}=\varepsilon_0\varepsilon_m\alpha\mathbf{E_0}$, we arrive at:

$$\alpha=4\pi a^3\frac{\varepsilon-\varepsilon_m}{\varepsilon+2\varepsilon_m} \tag{1.78}$$

The last equation is the central result of this section, the complex polarizability of a small sphere of sub-wavelength diameter in the electrostatic approximation.

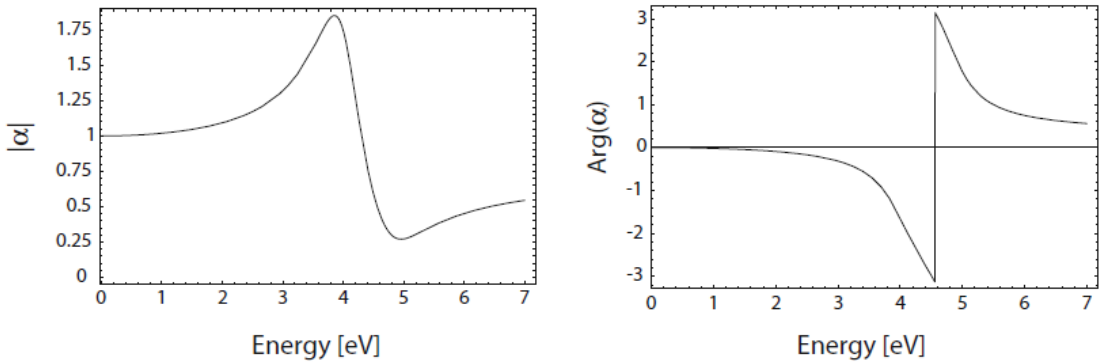

Figure 8. Absolute value and phase of the polarizability a of a sub-wavelength metal nanoparticle with respect to the frequency of the driving field (expressed in eV units). Here, $\varepsilon(\omega)$ is taken as a Drude fit to the dielectric function of silver [14].

Figure 8 shows the absolute value and phase of a with respect to frequency ω (in eV) for a dielectric constant varying as ε(ω) of the Drude form (two first terms of 1.52), in this case fitted to the dielectric response of silver [14]. It is apparent that the polarizability experiences a resonant enhancement under the condition that $|\varepsilon + 2\varepsilon_m|$ is a minimum, which for the case of small or slowly-varying Im[ε] around the resonance simplifies to:

$$\mathrm{Re}\left[\varepsilon(\omega)\right] = -2\varepsilon_m \tag{1.79}$$

This relationship is called the Fröhlich condition and the associated mode (in an oscillating field) the dipole surface plasmon of the metal nanoparticle. For a sphere consisting of a Drude metal with a dielectric function (two first terms of eq.1.58) located in air, the Fröhlich criterion is met at the frequency $\omega_0 = \omega_p / \sqrt{3}$ (1.79) further expresses the strong dependence of the resonance frequency on the dielectric environment: The resonance red-shifts as ε_m is increased. Metal nanoparticles are thus ideal platforms for optical sensing of changes in refractive index.

The distribution of the electric field $\mathbf{E} = -\nabla\Phi$ can be evaluated from the potentials (1.74, 1.75) to:

$$\mathbf{E_{in}} = \frac{3\varepsilon_m}{\varepsilon + 2\varepsilon_m}\mathbf{E_0} \tag{1.80}$$

$$\mathbf{E_{out}} = \mathbf{E_0} + \frac{3\mathbf{n}(\mathbf{n}\cdot\mathbf{p}) - \mathbf{p}}{4\pi\varepsilon_0\varepsilon_m}\frac{1}{r^3} \tag{1.81}$$

Where **n** is the unit vector in the direction of the point P of interest. As expected, the resonance in α also implies a resonant enhancement of both the internal and dipolar fields. It is this field-enhancement at the plasmon resonance on which

many of the prominent applications of metal nanoparticles in optical devices and sensors rely.

Up to this point, we have been on the firm ground of electrostatics, which we will now leave when turning our attention to the electromagnetic fields radiated by a small particle excited at its plasmon resonance. For a small sphere with $\alpha << \lambda$, its representation as an ideal dipole is valid in the quasi-static regime, i.e. allowing for time-varying fields but neglecting spatial retardation effects over the particle volume. Under plane-wave illumination with $\mathbf{E}(\mathbf{r},t) = \mathbf{E}_0 e^{-i\omega t}$ the fields induce an oscillating dipole moment $\mathbf{p}(t) = \varepsilon_0 \varepsilon_m \alpha \mathbf{E}_0 e^{-i\omega t}$ with α given by the electrostatic result (1.78). The radiation of this dipole leads to scattering of the plane wave by the sphere, which can be represented as radiation by a point dipole.

It is useful to briefly review the basics of the electromagnetic fields associated with an oscillating electric dipole. The total fields $\mathbf{H}(t) = \mathbf{H} e^{-i\omega t}$ and $\mathbf{E}(\mathbf{r},t) = \mathbf{E}_0 e^{-i\omega t}$ in the near, intermediate and radiation zones of a dipole can be written as [1]:

$$\mathbf{H} = \frac{ck^2}{4\pi}(\mathbf{n}\times\mathbf{p})\frac{e^{ikr}}{r}\left(1-\frac{1}{ikr}\right) \tag{1.82}$$

$$\mathbf{E} = \frac{1}{4\pi\varepsilon_0\varepsilon_m}\left\{k^2(\mathbf{n}\times\mathbf{p})\times\mathbf{n}\frac{e^{ikr}}{r}+\left[3\mathbf{n}(\mathbf{n}\cdot\mathbf{p})-\mathbf{p}\right]\left(\frac{1}{r^3}-\frac{ik}{r^2}\right)e^{ikr}\right\} \tag{1.83}$$

Where $k = 2\pi/\lambda$ and $\mathbf{n}$ the unit vector in the direction of the point P of interest. The near fields ($kr << 1$) that are responsible for spectroscopy application, the electrostatic result is recovered:

$$\mathbf{E} = \mathbf{E_0} + \frac{3\mathbf{n}(\mathbf{n}\cdot\mathbf{p})-\mathbf{p}}{4\pi\varepsilon_0\varepsilon_m}\frac{1}{r^3} \tag{1.84}$$

And the accompanying magnetic field present for oscillating field amount to

$$\mathbf{H} = \frac{i\omega}{4\pi}(\mathbf{n}\times\mathbf{p})\frac{1}{r^2} \tag{1.85}$$

In the opposite limit the radiated far fields are:

$$\begin{aligned}\mathbf{E} &= \sqrt{\frac{\mu_0}{\varepsilon_0\varepsilon_m}}\mathbf{H}\times\mathbf{n}\\ \mathbf{H} &= \frac{ck^2}{4\pi}(\mathbf{n}\times\mathbf{p})\frac{e^{ikr}}{r}\end{aligned} \tag{1.86}$$

From the viewpoint of optics, it is much more interesting to note that another consequence of the resonantly enhanced polarization α is a concomitant enhancement in the efficiency with which a metal nanoparticle scatters and absorbs light. The corresponding cross sections for scattering and absorption C_{sca} and C_{abs} can be calculated the Poynting-vector determined [14]:

$$C_{sca} = \frac{k^4}{6\pi}|\alpha|^2 = \frac{8\pi}{3}k^4 a^6 \left|\frac{\varepsilon - \varepsilon_m}{\varepsilon + 2\varepsilon_m}\right| \tag{1.87}$$

$$C_{abs} = k\,\mathrm{Im}[\alpha] = 4\pi k a^3\,\mathrm{Im}\left[\frac{\varepsilon - \varepsilon_m}{\varepsilon + 2\varepsilon_m}\right] \tag{1.88}$$

For small particles with $\alpha << \lambda$ the efficiency of absorption, scaling with α^3 dominates over the scattering efficiency, which scales with a^6. We point out that no explicit assumptions were made in our derivations so far that the sphere is indeed metallic. The expressions for the cross sections (1.87 and 1.88) are thus valid also for dielectric scatterers, and demonstrate a very important problem for practical purposes. Due to the rapid scaling of $C_{sca} \propto a^6$, it is very difficult to pick out small objects from a background of larger scatterers. Imaging of nanoparticles with dimensions below 40 nm immersed in a background of larger scatterers can thus usually only be achieved using photothermal techniques relying on the slower scaling of the absorption cross section with size [16]. Equations (1.87 and 1.88) also shows that indeed for metal nanoparticles both absorption and scattering (and thus extinction) are resonantly enhanced at the dipole particle Plasmon resonance, i.e. when the Frölich condition (1.79) is met [17]. For a sphere of volume *V* and dielectric function $\varepsilon = \varepsilon_1 + i\varepsilon_2$ in the quasi-static limit, the explicit expression for the extinction cross section $C_{ext} = C_{abs} + C_{sca}$ is:

$$C_{ext} = 9\frac{\omega}{c}\varepsilon_m^{3/2} V \frac{\varepsilon_2}{[\varepsilon_1 + 2\varepsilon_m]^2 + \varepsilon_2^2} \tag{1.89}$$

2.3 Effective Medium Theories (EMTs)

In this section we present the analytical (Maxwell-Garnet and Bruggeman) and the arithmetical (FDTD) Effective Medium Theories (EMTs) which is used to calculate the optical response of the nano-composite solar selective coating of Concentrated Solar Collectors.

2.3.1 Analytical EMTs

The particles in the composites are orders of magnitude smaller than the wavelengths of the radiation, which implies that their optical properties can be treated in terms of an effective medium whose dielectric function can be obtained by a suitable averaging over the dielectric functions of the two constituents. For generality, we regard two materials "A" and "B" with dielectric functions ε_A and ε_B and filling factors f_A and $f_B = 1 - f_A$. Firstly, we present a framework for obtaining effective medium dielectric function of $\tilde{\varepsilon}$ of ε_A and ε_B. Rest on classical scattering theory applied to Random Unit Cells (RUCs) defined so as to properly represent the basic micro-geometry. Then in the limit of small particles we apply this general formalism of RUCs [18, 20] and obtain the well known constitutive equations of Maxwell Garnet (MG) [20] and Bruggeman (Br) [21] depending on the choice of the RUCs.

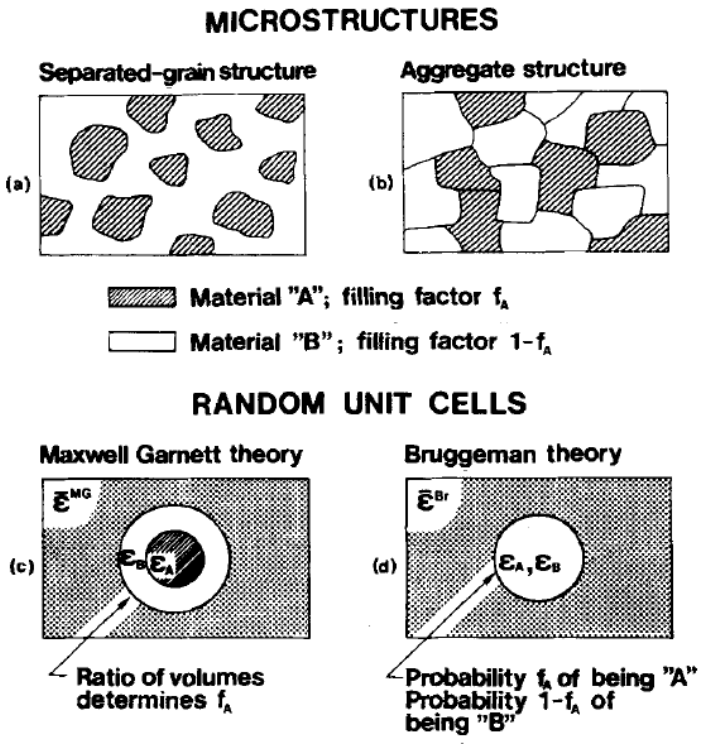

Figure 9. Parts (a) and (b) depict two microstructures of two-phase composite materials. Parts (c) and (d) show the corresponding RUCs used to derive the Maxwell Garnett and Bruggeman EMTs. The RUCs are embedded in the effective media [19]

We consider a two-phase inhomogeneous system whose components are sufficiently large that each point in the material can be associated with a certain macroscopic dielectric function. We start by representing the microstructure with models which are simple enough to permit a theoretical treatment and yet do not leave out the essential physics. Figures 9.a and 9.b show two cases which are regarded as typical: a separated grain structure, with particles of “A” embedded in a continuous host of “B”, and an aggregate structure in which “A” and “B” enter on an equal footing to form a space-filling random mixture.

The RUC is taken to be embedded in an effective medium, whose properties are as yet undefined. For the separated grain structure, the RUC is a core of “A” surrounded by a concentric shell of “B”, as depicted in Fig. 9.c. The ratio of the core volume to the shell volume is equal to f_A. For the aggregate structure, the inherent structural equivalence of the components is ensured by letting the RUC have a probability f_A of being “A” and a probability f_B of being “B” as shown in Fig. 9.d. The RUC is spherical or non-spherical depending on the shape of a "typical" particle.

The basic definition of an effective medium is that the RUC, when embedded in the effective medium, should not be detectable in an experiment using electromagnetic radiation confined to a specific wavelength range. In other words, the extinction of the RUC should be the same as if it were replaced with a material characterized by $\tilde{\varepsilon}$. This criterion makes it fruitful to use the "optical theorem" for absorbing media [22] it relates the extinction of the spherical cell compared to that of the surrounding medium C_{ext} with the scattering amplitude in the direction of the impinging beam $S(0)$ by:

$$C_{ext} = 4\pi \,\mathrm{Re}\left[S(0)/k^2 \right] \tag{1.90}$$

where

$$k = 2\pi\tilde{\varepsilon}^{1/2} / \lambda \tag{1.91}$$

denotes the wave vector amplitude in the effective medium. From the definition of an effective medium it now follows that $C_{ext} = 0 \Rightarrow S(0) = 0$, which express the fundamental property of an effective medium. This indicates that a plane wave entering the inhomogeneous material will propagate with an undeformed plane wave front. Fresnel equations then apply at the boundaries of the effective medium, which is clearly an important point for any EMT to be practically useful.

We move now on the derivation of the effective medium dielectric function for the spherical random unit cells. The scattering properties of uniform and coated spheres [i.e. , of the RUCs of figure 9.c and 9.d] are well known. The Lorentz-Mie [15, 23, 23] gives $S(0)$ as a series expansion according to:

$$S(0)=\frac{1}{2}\sum_{n=1}^{\infty}(2n+1)(\alpha_n+\beta_n) \tag{1.92}$$

where α_n and β_n are complicated expressions containing Bessel functions and derivatives of them. Equation (1.92) can be rewritten as a series in (kb), where b is the sphere radius.

In order to derive the Maxwell Garnett theory we use the series appropriate to a coated sphere (cs) and obtain:

$$S^{cs}(0)=i(kb)^3\frac{(\varepsilon_B-\tilde{\varepsilon})(\varepsilon_A+2\varepsilon_B)+f_A(2\varepsilon_B+\tilde{\varepsilon})(\varepsilon_A-\varepsilon_B)}{(\varepsilon_B+2\tilde{\varepsilon})(\varepsilon_A+2\varepsilon_B)+f_A(2\varepsilon_B-2\tilde{\varepsilon})(\varepsilon_A-\varepsilon_B)}+0\left[(kb)^5\right] \tag{1.93}$$

The filling factor is :

$$f_A=\frac{a^3}{b^3} \tag{1.94}$$

where a ,b is the radius of the inner and outer sphere (fig. 9.c) respectively. In the small sphere limit, the effective medium condition can be satisfied by setting the leading term in eq. (1.93). This yields (with $\tilde{\varepsilon}=\tilde{\varepsilon}^{MG}$):

$$\frac{\tilde{\varepsilon}^{MG}-\varepsilon_B}{\tilde{\varepsilon}^{MG}+2\varepsilon_B}=f_A\frac{\varepsilon_A-\varepsilon_B}{\varepsilon_A+2\varepsilon_B} \tag{1.95}$$

or, rewritten:

$$\tilde{\varepsilon}^{MG}=\varepsilon_B\frac{\varepsilon_A+2\varepsilon_B+2f_A(\varepsilon_A-\varepsilon_B)}{\varepsilon_A+2\varepsilon_B-f_A(\varepsilon_A-\varepsilon_B)} \tag{1.96}$$

The last equation is the constitutive formula for the Maxwell Garnett EMT. By making the replacements $A\to B$ and $B\to A$ one obtains analogous relations for the inverted structure. Our derivation does not require that f_A is small. However, it is clear that for a sufficiently large filling factor one reaches a point where the detailed particle-particle interactions (or multiple scattering) must be considered explicitly. Obviously, such structural multipole features cannot be encompassed by the EMT approach, but supplementary information on inter-particle separations, etc., is demanded.

The Bruggeman theory is derived from the series expansion for a sphere (s) according to:

$$S^{s}(0)=i(kb)^3\frac{\varepsilon-\tilde{\varepsilon}}{\varepsilon+2\tilde{\varepsilon}}+0\left[(kb)^5\right] \tag{1.97}$$

where b is the radius of the RUC in Fig. 9.d and ε denotes ε_A or ε_B. Considering again the small sphere limit, it is found that (with $\varepsilon = \tilde{\varepsilon}^{Br}$):

$$f_A \frac{\varepsilon_A - \tilde{\varepsilon}^{Br}}{\varepsilon_A + 2\tilde{\varepsilon}^{Br}} + (1 - f_A) \frac{\varepsilon_B - \tilde{\varepsilon}^{Br}}{\varepsilon_B + 2\tilde{\varepsilon}^{Br}} = 0 \tag{1.98}$$

where we have invoked the probability f_A for the RUC of having $\varepsilon = \varepsilon_A$ and the probability f_B of having $\varepsilon = \varepsilon_B$. Equation 1.98 is the constitutive formula for the Bruggeman theory.

The two analytical EMT's discussed here are conceptually quite different, and the validity regimes of the two theories are still subject to discussion and investigations. In general terms, the Maxwell-Garnett EMT is expected to be valid at low volume fractions f since it is assumed that the conductive domains are spatially separated. In contrast, the Bruggeman EMT makes no assumptions about the volume fraction. Many factors, such as the size and shape of the conductive domains, influence the predictions of both models. The Bruggeman EMT predicts percolation behavior when the volume fraction of the conductive domains is large enough to form a continuous conducting path throughout the sample [25].

2.3.2 Arithmetical FDTD EMT

In this section we present the arithmetical Finite Differences Time Domain Method EMT [26] which is used to extract the effective medium optical constants of the nano-composite solar selective coating. In order to illustrate the method we present a typical case of extracting the effective medium response of cubic arrays of silver NPs with a diameter of about 10 nm. Furthermore we explore their behavior in the full range of filling fractions and find excellent agreement with the analytical Maxwell Garnett EMT presented above. In this size, quantum confinement effects are infinitesimal and the particle dielectric function is sufficiently well approximated by the bulk metallic dielectric function. Also, this is the size and shape for which the MG effective medium theory is the most accurate, thus we will have a good vehicle for comparison.

We use the FDTD method to study electromagnetic wave propagation in highly dispersive metallic nanoparticle arrays. Material dispersion is naturally incorporated in the FDTD scheme by conveniently introducing electronic polarization terms. By performing a Drude-Lorentz fit to the experimentally bulk dielectric function of Ag [27] at the frequency range of interest we obtain the polarization of the metal. The polarization differential equations are solved in the same Yee lattice and are time marched in lockstep with the electric field using the same leap frog algorithm as we present at the section of the FDTD method.

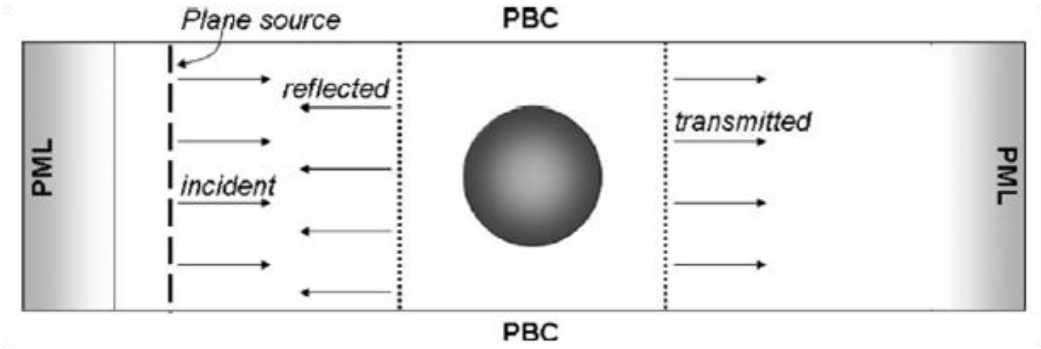

Figure 10. The simulation cell. Periodic boundary conditions are applied on the direction perpendicular to the wave front and perfectly matched layer conditions along it. The effective-slab boundaries are the two dotted lines, on which the complex reflection and transmitted amplitudes are calculated [26].

We calculate the reflection and transmission spectra of plane waves under normal incidence onto square arrays of the metallic nanoparticles. A two dimensional 2D projection of the three dimensional 3D simulation cell is shown in Fig. 10. Perfectly matched layer (PML) [28] and absorbing boundary conditions are applied along the propagation direction, while periodic boundary conditions PBC are applied in the directions normal to propagation. A typical simulation cell has a width along the periodic direction of $a = 20nm$ and a length along the propagating direction of 200 nm, while the metallic sphere diameter is 9.5 nm. The system is discretized to 0.5 nm/grid. The input field has a narrow Gaussian temporal profile. To get the complex reflection and transmission amplitudes in frequency domain, one typically needs to Fourier transform the fields on suitably chosen planes of monitor points and take the appropriate ratios with and without the particle array. However, since we are below the diffraction limit for the frequencies of interest, we can avoid the use of planes and simply use two monitor points, before and after the particle. In our scheme we place these monitor points just before the PML regions, centered in the cell. At the end we multiply by the appropriate phases to get the amplitudes at the effective-slab boundaries, the dotted lines in Figure 10. By repeating with different settings we verified that our results are invariant to the cell size, the position of the monitor points, and the use of full plane or single monitor points.

To illustrate the method we assume an idealized metallic dielectric constant with only the free electron contribution:

$$\varepsilon(\omega) = 1 - \frac{\omega_p^2}{\omega^2 + i\omega/\tau} \tag{1.99}$$

where $\omega_p = 1.37 \times 10^{16} s^{-1}$ and $\tau = 4 \times 10^{-14} s$ are the Drude plasma frequency and relaxation time for Ag, respectively. We omit the interband absorption and the surface scattering [29] contributions in order to simplify the system and amplify all resonant effects. From Mie theory, such a system is expected to exhibit surface plasmon resonances when $\varepsilon(\omega) = -\varepsilon_m (l+1)/l$, where ε_m is the host dielectric matrix and l is

a positive integer. Solving for $\omega = \sqrt{\omega_p^2 / \left[1+\varepsilon_m\left(l+1\right)/l\right] - 1/\tau^2}$ we find the first three resonances at $\lambda = 238$, 217 and $210nm$.

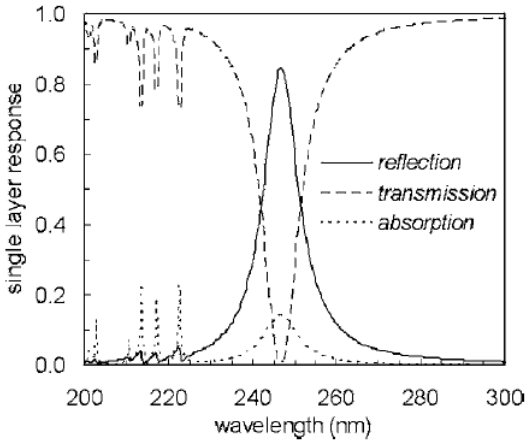

Figure 11. Optical response of a single square array layer of the idealized metallic nanoparticles. The particle diameter is 9.5 nm, and the lattice constant is 20 nm [26].

In Figure 11 we plot the reflection, transmission, and absorption coefficients for a single array layer. The LSPRs manifest themselves as strong modulations in the transmission and reflection spectra. Far from resonance the transmission is practically unity, indicating the small absorption cross section that these nanoparticles have. We also note the higher order resonances at smaller wavelengths. The reasons for the small discrepancies between these frequencies and the Mie results are interparticle interactions due to the relatively high filling ratio in our system ($\sim 5.6\%$) and FDTD discretization errors.

Having the complex spectral transmission and reflection amplitudes $t\left(\omega\right)$ and $r\left(\omega\right)$ from the FDTD simulation, it is easy to calculate the effective response of the nanoparticle array, i.e., the effective refractive index $\tilde{n}$ and impedance $\tilde{z}$, or equivalently the effective dielectric constant $\tilde{\varepsilon}$ and magnetic permeability $\tilde{\mu}$. From a single array layer which is assumed equivalent to an effective material of thickness d equal to the lattice spacing $d = \alpha = 20nm$ (Figure 11). We first calculate the transfer matrix $M \equiv M\left(\omega\right)$:

$$M = \begin{pmatrix} t - r \cdot r / t & r/t \\ -r/t & 1/t \end{pmatrix} \tag{1.100}$$

From here we calculate the transfer matrix M^{∞} of a hypothetical semi-infinite system $M^{\infty} = \lim_{n\to\infty} M^n$ (an efficient way is to perform successive doublings e.g. for $n = 1024 = 2^{10}$ we only need ten operators). If there is no intrinsic absorption (in our case there is), we need to add an infinitesimal amount in order to suppress the Fabry-

Perot oscillations of the infinite system and obtain a converged solution for M^{∞} , i.e., we set:

$$M \to M \begin{pmatrix} e^{-\delta} & 0 \\ 0 & e^{\delta} \end{pmatrix}, 0 < \delta < 1 \tag{1.101}$$

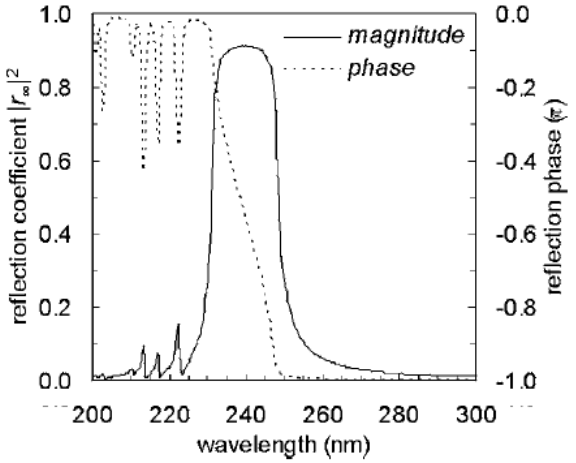

Figure 12. Semi-infinite reflection coefficient and reflection phase. The reflection coefficient becomes resonant close to the Mie frequency, while the reflection phase changes between 0 and $-\pi$ marking the transition between an effective "magnetic wall" behavior to an effective "electric wall" behavior, respectively [26].

In practice we take n large enough so that the transmission coefficient $T = 1/\left|M_{22}^{n}\right|^{2}$ becomes infinitesimally small (typical order $n \sim 10^{4}$). The semi infinite reflection amplitude is then $r_{\infty} = M_{12}^{n} / M_{22}^{n}$. The semi infinite reflection coefficient along with the semi infinite reflection phase, is plotted in Figure 12. Note that the reflection phase is changing at the resonance point from 0 to $-\pi$. One can argue that this semi infinite system transitions from an effective "magnetic wall" behavior at 0 to an "electric behavior wall" at $-\pi$. At resonance the reflection is maximized, while away from the resonance all incident light is absorbed.

Now, r_{∞} is in turn defined through the impedance mismatch between the ambient and the effective medium, thus providing an unambiguous solution for the effective impedance.

$$r_{\infty} = \frac{\tilde{z} - z_m}{\tilde{z} + z_m} \Rightarrow \tilde{z} = z_m \frac{r_{\infty} + 1}{1 - r_{\infty}} \tag{1.102}$$

where $\tilde{z} \equiv \tilde{z}(\omega) = \sqrt{\tilde{\mu}(\omega) / \tilde{\varepsilon}(\omega)}$ is the complex effective material impedance, $z_m = 1/\sqrt{\varepsilon_m}$ is the host impedance, and $\tilde{\varepsilon}$ and $\tilde{\mu}$ are the effective dielectric constant and the magnetic permeability respectively. In order to individually determine $\tilde{\varepsilon}$ and

$\tilde{\mu}$ we need the complex effective refractive index $\tilde{n}(\omega)=\sqrt{\tilde{\varepsilon}(\omega)\tilde{\mu}(\omega)}$, which we gate from the trace of the transfer matrix,

$$Tr[M]=2\cos(\tilde{n}\omega\alpha/c) \tag{1.103}$$

We can now unambiguously determine $\tilde{\varepsilon}(\omega)=\tilde{n}(\omega)/\tilde{z}(\omega)$ and $\tilde{\mu}(\omega)=\tilde{n}(\omega)\tilde{z}(\omega)$. All effective response functions are plotted in Figures 13.a-13.d. We note that besides the expected resonant of $\tilde{\varepsilon}(\omega)$, we also find a resonant form for the effective magnetic permeability $\tilde{\mu}(\omega)$, which is inaccessible to standard effective medium theories.

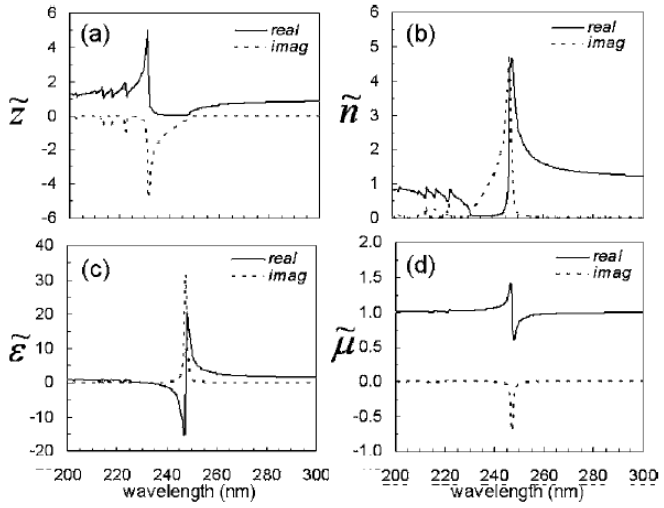

Figure 13. Effective medium constants: a) impedance, b) refractive index, c) dielectric constant, and d) magnetic permeability [26].

To verify our process, we break the periodicity in one direction and use $\tilde{n}$ and $\tilde{z}$ to calculate the reflection coefficient from a system with four layers of spheres separated by distance d , and compare them in Fig. 14 with the result obtained from explicit FDTD. The agreement is exact within numerical precision, same for all amplitudes and phases. We get the same agreement even in cases where the four layers are laterally misaligned with respect to each other this should be expected, however, because we are way below the diffraction limit and we are not really breaking any periodicity by misaligning the layers. Same agreement was also found in every other case studied. The extracted $\tilde{z}(\omega)$, $\tilde{n}(\omega)$ and $\tilde{\mu}(\omega)$ represent an accurate effective description of the metallic sphere lattice, which can thus be accurately described as an effective bulk medium at least for such simple one dimensional 1D arrangements.

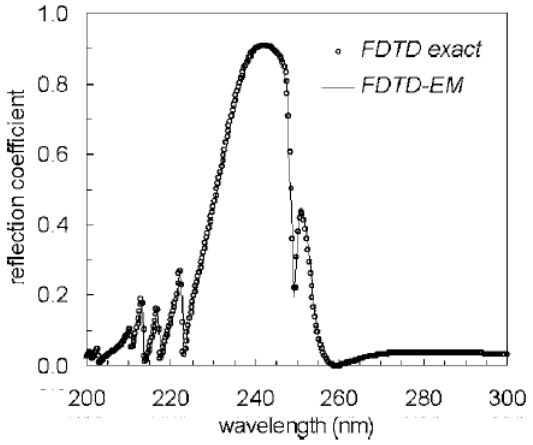

Figure 14. Comparison between the reflection coefficient of a four-layer system obtained by using the effective medium constants obtained from a single layer FDTD calculation and a full four-layer FDTD calculation. The agreement is exact within numerical precision, validating our effective medium scheme [26].

The effective dielectric constant at the fundamental LSPR (Figure 13.c) exhibits the characteristic resonant Lorentzian shape expected at an interband transition frequency, or for a polar material at the transverse phonon-polariton excitation frequency. We can understand this by looking at the metallic nanoparticle array system as it is described by the Maxwell-Garnett effective medium theory:

$$\frac{\tilde{\varepsilon}-\varepsilon_m}{\tilde{\varepsilon}+2\varepsilon_m}=f\frac{\varepsilon-\varepsilon_m}{\varepsilon+\varepsilon_m} \tag{1.104}$$

where ε and ε_m are the metallic sphere and the host dielectric constant, respectively, and f is the sphere filling ratio. Solving equation 1.104 for $\tilde{\varepsilon}$, with equation 1.99 for the metallic dielectric constant and the particularly of $\varepsilon_m=1$ we find:

$$\tilde{\varepsilon}=1+\frac{f\omega_p^2}{\omega_p^2\left[(1-f)/3\right]-\omega^2-i\omega/\tau} \tag{1.105}$$

Which is a Lorentzian response with an effective resonance frequency $\tilde{\omega}_0=\omega_p\sqrt{(1-f)/3}$, an effective coupling strength $\tilde{\sigma}=\omega_p\sqrt{f}$, and an effective linewidth $\tilde{\gamma}=1/\tau$. In Figure 15 we contrast this MG resonant wavelength $\tilde{\lambda}_0=2\pi c/\omega_0$ with one obtained by numerical FDTD computations for different filling ratios f at fixed particle size. We find an excellent agreement. Effective oscillation strength and linewidth are also in good agreement. This verifies that we are working within the validity space of the MG theory. The upside of the FDTD approach, however, is that it will still be valid in any space, i.e for any size, shape and configuration.

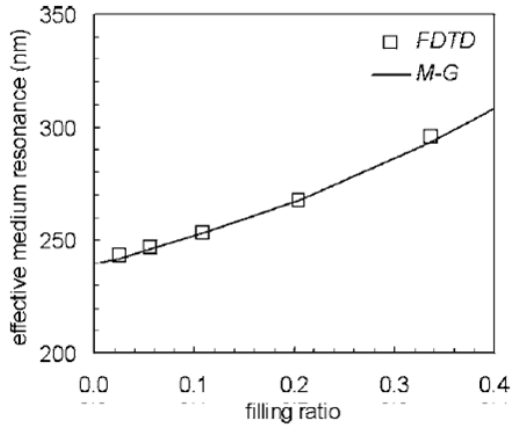

Figure 15. Comparison between the FDTD and Maxwell-Garnett effective medium resonance frequencies. Excellent agreement is also found for all other effective response parameters [26].

We now continue by illustrating the method with the actual optical properties of silver, gold, and copper. We obtain the experimentally determined values for Ag, Au and Cu [27] and perform Drude-Lorentz fits (eq. 1.58) to the bulk dielectric function using the optimization package MERLIN [30] for each metal. In order to have the appropriate dielectric constant for the nano-particle we make a correction, including the surface scattering contribution to the free electrons relaxation time [29]. The reduced relaxation time τ^* is defined as:

$$\frac{1}{\tau^*} = \frac{1}{\tau} + \frac{\upsilon_F}{r} \tag{1.106}$$

where r is the particle radius (4.75 nm) and υ_F is the Fermi velocity. The bulk metallic refractive index $n = n_r + in_i$ along with the corresponding fitted one is shown in Figure 16 for the three selected metals. For the particle refractive index we use $n^* = n_r^* + in_i^*$, which includes the surface scattering contribution.

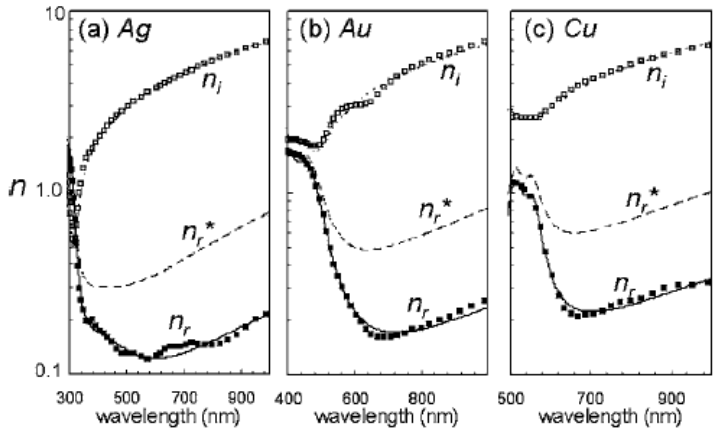

Figure 16. The bulk metallic refractive index (symbols) along with the corresponding one from the fitted model of Eq. 1.44 (lines) for a) Ag b) Au and c) Cu. Surface scattering results into a strong modification of n_r but into an insignificant change for n_i, thus we only plot n_r for clarity of presentation.

We assume that the particle array is embedded inside a transparent dielectric with index of refraction 2. Such a value is appropriate for a variety of dielectrics such as ZnO, ZrO_2, SnO_2, HfO_2, Si_3N_4, and diamond-like carbon DLC. We repeat the same procedure described above for the host dielectric matrix $\varepsilon_m = 4$ and calculate the effective dielectric constants and magnetic permeability for a wide range of filling ratios. We calculate the SPR frequency as a function of filling ratio and plot it in Fig. 17. The characteristic redshift with increasing filling ratio is well reproduced. For increasing filing ratio we also find the expected broadening (due to the interband coupling) and increase in resonance strength (due to increased cross section). In Fig.17 we also plot the LSPR frequency as calculated by the MG theory (Eq. 1.87) with the materials obtained from the Drude-Lorentz fit. The agreement is excellent showing once again that we are working in the validity space of the MG theory.

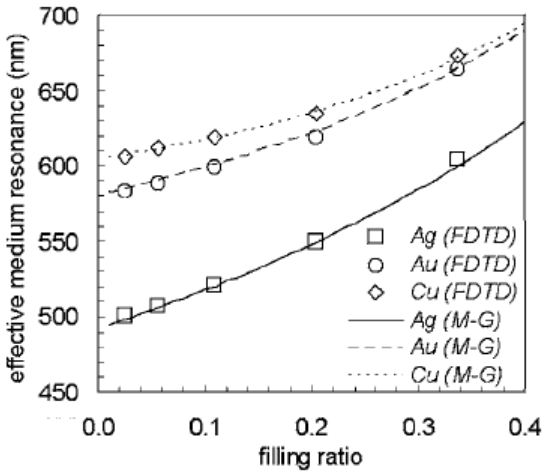

Figure 17. The SPR frequency as a function of filling ratio for fixed particle size. We find excellent agreement between the FDTD and the MG effective medium results.

2.4 Opto-thermal modeling

Laser annealing of a thin metal film on a substrate, or of a stratified ceramic/metal composite on a substrate can result into the formation of nanoparticles on the substrate surface or of nanoparticles embedded inside the dielectric matrix, respectively. This is a promising procedure for large scale fabrication of plasmonic templates with many applications in plasmonics. We have made an extensive theoretical and experimental exploration on surface and sub-surface plasmonic nano-structuring which will be extensively discussed in chapter 5. From the point of view of theory and modeling, in order to get an insight into the heating dynamics involved in these processes, we developed an opto-thermal modeling technique which is used to calculate the full transient temperatures at every point on the nano-structured template and of the substrate during laser annealing. In our model, the laser light is absorbed by the metallic film or the stratified multilayer structure and the substrate. This absorption profile is calculated by the optical modeling described in previous sections. This absorbed energy we assume is instantaneously converted in local heating, which is then diffused by thermal conduction.

The thermal transport effects induced by laser can be then described by the usual heat equation [31] with a source term to include light absorption [32, 33]. If the pulse profile is uniform at the cross plane [33] and the laser spot is extended (~ millimeters) compared to the heating depth (~microns), 1D suffices for the thermal calculations:

$$A(z)c(z)\rho(z)\frac{\partial T(z,t)}{\partial t}=\frac{\partial}{\partial z}\left[A(z)k(z)\frac{\partial T(z,t)}{\partial z}\right]+A(z)Q(z,t) \quad (1.107)$$

Where $A(z)$ is a variable area which is assumed as a function of z in order to take into account the actual shape of the nanoparticles in the case of surface laser nano-structuring. In contrast in the case of stratified multilayer annealing the variable area remains constant across z. The material parameters heat capacity $c(z)$, mass density $\rho(z)$ and thermal conductivity $k(z)$, all three having a spatial dependence due to the interchange of different materials, with their values are obtained from literature [33].

An extended laser heating source term $Q(z,t)=\alpha(z)\varphi(t)$ is used, defined by the product of the absorption spatial profile $\alpha(z)$ (obtained from FDTD calculations) and the experimental laser pulse temporal profile $\phi(t)$, where the total laser fluence Φ is taken by time integrating the temporal profile $\Phi=\int_{-\infty}^{\infty}\varphi(t)dt$. Thus we have the

exact absorbed energy at each point in the structure and its time dependence. The heat diffusion equation is time-integrated numerically utilizing the 4th-order Runge-Kutta scheme. Thus, we obtain the explicit temperature transient profile at every point in the structure. In doing so, we assume that (i) electronic and lattice temperatures are in equilibrium (valid for slow heating times in the ns regime [32]), (ii) material properties (absorption, heat capacity, mass density and thermal conductivity) remain constant during heating, (iii) radiation and convection losses are insignificant (we'll qualify this afterwards presenting the laser structuring). Thus, we obtain the transient temperature at each point in the multilayer volume normalized to the total laser fluence f, i.e. in degrees per mJ/cm^2.

We continue now by presenting the 4th Order Runge-Kutta Method which is a numerical method used to solve ordinary differential equations. The thermal transfer equation can be rewritten in terms of the calculated spatial and time depended temperature:

$$\frac{\partial T(z,t)}{\partial t} = \frac{1}{A(z)c(z)\rho(z)}\left[\frac{\partial\left(A(z)k(z)\right)}{\partial z}\frac{\partial T(z,t)}{\partial z} + A(z)k(z)\frac{\partial^2 T(z,t)}{\partial^2 z} + A(z)Q(z,t)\right] \quad (1.108)$$

To solve numerically this equation we discretize the computational space, in space and time domains. The structure is described by the different materials with their individual thicknesses and materials parameters ($A(z), c(z), k(z)$). Also, the spatial and time depended thermal load $Q(z,t)$ is known as we mentioned above. By time integrating the thermal transfer equation we calculate the time depended temperature at each point in the structure. Specifically, we suppose a starting point at time t_i (practically, $t = 0$) with no external thermal load, so the temperature at each point z in the structure is zero, $T_i = 0$. At the next time step t_{i+1} we apply the thermal load, so the temperature at each point z in the structure has the value T_{i+1}. All the spatial derivatives at the right part of equation 1.08 are known thus, T_{i+1} can be calculated at each point in the structure treating equation as central differences. Then, we move to the next time step t_{i+2} and calculate the next temperature T_{i+2} at each point z in the structure e.t.c.

We utilize the 4th order Runke-Kutta method to calculate the time depended temperature at each point in the structure. In order to clearly present the method we rewrite the equation 1.91 as a function of the unknown time depended temperature.

$$\frac{dT}{dt} = f(\mathrm{t},\mathrm{T}) \quad (1.109)$$

The Runge-Kutta 4th order method is based on the following:

$$T_{i+1} = T_i + \left(a_1 k_1 + a_2 k_2 + a_3 k_3 + a_4 k_4\right) h \tag{1.110}$$

where knowing the value of T_i at t_i we can find the value of T_{i+1} at t_{i+1} and $h = t_{i+1} - t_i$

Equation 1.110 is equated to the first five terms of Taylor series:

$$\begin{aligned} T_{i+1} = T_i + \frac{dT}{dt}\Big|_{t_i,\mathrm{T}_i}\left(t_{i+1} - t_i\right) + \frac{1}{2!}\frac{d^2T}{dt^2}\Big|_{t_i,\mathrm{T}_i}\left(t_{i+1} - t_i\right)^2 + \frac{1}{3!}\frac{d^3T}{dt^3}\Big|_{t_i,\mathrm{T}_i}\left(t_{i+1} - t_i\right)^3 \\ + \frac{1}{4!}\frac{d^4T}{dt^4}\Big|_{t_i,\mathrm{T}_i}\left(t_{i+1} - t_i\right)^4 \end{aligned} \tag{1.111}$$

Knowing that $\frac{dT}{dt} = f(t,T)$ and $t_{i+1} - t_i = h$ equation 1.94 is rewritten:

$$T_{i+1} = T_i + f\left(t_i, \mathrm{T}_i\right)h + \frac{1}{2!} f^{'}\left(t_i, \mathrm{T}_i\right)h^2 + \frac{1}{3!} f^{''}\left(t_i, \mathrm{T}_i\right)h^3 + \frac{1}{4!} f^{'''}\left(t_i, \mathrm{T}_i\right)h^4 \tag{1.112}$$

Based on equations 1.111 and equation 1.110, the solutions is:

$$T_{i+1} = T_i + \frac{1}{6}\left(k_1 + 2k_2 + 2k_3 + k_4\right)h \tag{1.113}$$

with

$$k_1 = f\left(t_i, T_i\right) \tag{1.114}$$

$$k_2 = f\left(t_i + \frac{1}{2}h, T_i + \frac{1}{2}k_1 h\right) \tag{1.115}$$

$$k_3 = f\left(t_i + \frac{1}{2}h, T_i + \frac{1}{2}k_2 h\right) \tag{1.116}$$

$$k_4 = f\left(t_i + h, T_i + k_3 h\right) \tag{1.117}$$

2.5 References

[1] J.D. Jackson, “Classical Electrodynamics” (John Wiley & Sons, Inc. New York, 1962).

[2] F. Wooten, “Optical Properties of Solids” (Academic Press, New York, 1972)

[3] M. Fox , “Optical Properties of Solids” (Oxford University Press 2001)

[4] Stefan A. Maier, “Plasmonics: Fundamentals and Applications”, (Springer, New York, 2007).

[5] A. Taflove, S. C. Hagness, Computational Electrodynamics: The Finite-Difference Time-Domain Method (3rd Edition), Boston, MA: Artech House (2005).

[6] Kane Yee "Numerical solution of initial boundary value problems involving Maxwell's equations in isotropic media". IEEE Transactions on Antennas and Propagation, 14 (3) (1966) 302–307.

[7] D. L. Jeanmarie, R. P. Van Duyne, Surface Raman spectroelectrochemistry part 1: heterocyclic, aromatic, and aliphatic amines adsorbed on the anodized silver electrode. *J. Electroanal. Chem*. (1977) 84:1–20.

[8] Xia, Y.; Halas, N. *MRS Bull.* **2005,** *30*, 338-343.

[9] Ferrell, T. L. Plasmon. In *Concise Encyclopedia of Physics* McGraw–Hill: New York, 2005.

[10] Pitarke, J. M.; Silkin, V. M.; Chulkov, E. V.; Echenique, P M. *J. Opt. A: Pure Appl. Opt.* **2005,** *7*, S73–S84.

[11] Campion, A.; Kambhampati, P. Chem. Soc. Rev. 1998, 27, 241.

[12] Kelly, K. L.; Coronado, E.; Zhao, L. L.; Schatz, G. C. *J. Phys Chem. B* **2003,** *107*, 668-677.

[13] Hutter, E.; Fendler, J. H. Adv. Mater. 2004, 16, 1685–1706.

[14] Johnson, P. B. and Christy, R. W. (1972). Optical constants of the noble metals. *Phys. Rev. B* 6(12):4370–4379.

[15] Bohren, Craig F. and Huffman, Donald R. (1983). *Absorption and scattering of light by small particles*. John Wiley & Sons, Inc., New York, NY, first edition.

[16] Boyer D., Tamarat, P., Maali, A., Lounis, B., and Orrit, M. Photothermal imaging of nanometer-sized metal particles among scatterers. *Science*, (2002) 297 1160-1163.

[17] Kreibig, U. and Vollmer, M. Optical properties of metal clusters. Springer, Berlin (1995).

[18] G. A. Niklasson, C. G. Granqvist, and O. Hunderi, Effective medium models for the optical properties of inhomogeneous materials ,Vol. 20, No. 1 (1981) , Applied Optics,

[19] G. A. Niklasson and C. G. Granqvist, Optical properties and solar selectivity of co-evaporated Co-Al2O3 composite films, Journal of Applied Physics, (1984) 55 3382.

[20] J. C. Maxwell-Garnett, Philos. Trans. R. Soc. London **203**, 385 (1904).

[21] D. A. G. Bruggeman, Ann. Phys. Leipzig 24, 636 (1935).

[22] C. F. Bohren and D. P. Gilra, Extinction by a Spherical Particle in an Absorbing Medium, J. Colloid Interface Sci. 72, 215 (1979).
[23] H. van de Hulst, *Light Scattering by Small Particles* (Dover, New York 1981).
[24] M. Kerker, The scattering of light and other Electromagnetic Radiation (Academic, New York, 1969).
[25] P. U. Jepsen, B. M. Fischer, A. Thoman. H. Helm, J.Y Suh, R. F. Haglud Metal-insulator phase transition in a VO_2 thin film observed with terahertz spectroscopy, (2006) Phys. Rev. B 74 (20) 205103.
[26] E. Lidorikis, S. Egusa and J. D. Joannopoulos, Effective medium properties and photonic crystal superstructures of metallic nanoparticle arrays, Journal Of Applied Physics (2007) 101 054304.
[27] E. D. Palik, Handbook of Optical Constants of Solids, Academic, San Diego, (1998).
[28] J. C. Chen and K. Li, Microwave Opt. Technol. Lett. 10, 319 (1995)
[29] U. Kreibig and C. V. Fragstein, The Limitation of Electron Mean Free Path in Small Silver Particles, Z. Physik 224, 307-323 (1969).
[30] D. G. Papageorgiou, I. N. Demetropoulos , I. E. Lagaris, The Merlin Control Language for strategic optimization, Computer Physics Communications, (1998) 109 250-275.
[31] D.R. Pitts, L. E. Sissom, Schaum's Outline of Theory and Problems of Heat Transfer, (2nd edition) McGraw Hill Professional, (1998).
[32] S. Nolte, C. Momma, H. Jacobs et al. Ablation of metals by ultrashort laser pulses, J. Opt. Soc. Am. B , 1410 (1997).
[33] D. R. Lide, *CRC Handbook of Chemistry and Physics, 85th Edition*. Taylor & Francis, 2004.

Chapter 3 Design of high-temperature solar-selective coatings for application in solar collectors

Abstract

In this work we present a way to design and evaluate the performance of nano-composite metal-dielectric absorbers and selective filters for high temperature applications in high concentration solar energy harvesting, e.g. in parabolic trough collectors. Improving the properties of the receiver's selective coating and optimizing operating temperature above the current limits of 400 ^{0}C represent a good opportunities for improving the efficiency of parabolic trough collectors and thus reducing the cost of solar electricity. The objective of our effort is to study the design rules for a new more-efficient selective coating, with both maximum absorption in the solar spectrum and highest reflection (minimum emissivity) in the infrared spectrum. These optical characteristics are required for maximum energy collection and minimum thermal emission and result to more efficiently conversion of the solar energy to electricity. Using finite-difference time-domain (FDTD) simulations we modeled different nano-composite metal-dielectric coatings composed of materials that are stable at high temperatures as well as selective filters, and calculate the solar absorption and thermal emission coefficients. Afterwards, and taking into account the optical parameters of the collectors' structure (sunlight concentration factor and optical losses) and the theoretical predicted Carnot's efficiency, we calculate the total conversion efficiency (η) of a solar collector for the different coatings. By evaluating the performance of each designed coating for a wide temperature range from 400 ^{o}C up to 1000 ^{o}C, we obtain the maximum efficiency at the optimal operating temperature. We find for one of the best candidate for solar selective coating (Cu nanoparticles in a low index dielectric matrix, e.g. SiO_2), increasing the operating temperature from 400 ^{0}C to 850 ^{0}C we take an increase of the efficiency from 0.405 to 0.52 respectively, which means 28.4 % better performance.

3.1 Introduction

As the world's supply of fossil fuels shrinks, there is a great need for clean and affordable renewable energy sources in order to meet growing energy demands. Achieving sufficient supplies of clean energy for the future is a great societal challenge. Sunlight, the largest available carbon-neutral energy source, provides the Earth with more energy in 1 hour than what is consumed on the planet within an entire year. Despite this, solar electricity currently provides only a percent of the word's power consumption. A great deal of research is put into the harvest and storage of solar energy for power generation. There are two mainstream categories of devices utilized for this purpose, photovoltaics (PV) and Concentrated Solar Power (CSP). The first involves the use of solar cells to generate electricity directly via the photoelectric effect. The latter employs different methods of capturing solar thermal energy. The CSP systems use mirrors or lenses to redirect and concentrate the solar flux on a receiver to be collected as heat, which can in turn be used to power up a turbine or a heat engine to generate electricity.

A lot of research works have been reported in the literature on solar thermal systems. A few important review articles [1-5] highlight these research works. In these articles solar collectors are broadly classified as non-tracking and tracking collectors. The non-tracking, low or non-concentrating collectors, are kept at rest and are also known as fixed or stationary collectors. In these, the same area is used for interception and absorption of the incident radiation. Sun-tracking concentrating collectors, on the other hand, utilize optical elements to focus large amounts of radiation onto a small receiving area and follow the sun throughout its daily course to maintain the maximum solar flux at their focus. Non-tracking collectors are categorized as flat plate, evacuated tube and compound parabolic collectors. On the other hand the tracking collectors are further classified by their focus geometry as either line focus concentrators which need one axis tracking movement to concentrate the solar flux onto the receiver, or point focus concentrators which need two axes tracking movement to concentrate the solar flux onto the receiver. The single axis tracking systems consist of parabolic trough collectors, cylindrical trough collectors and linear Fresnel reflectors. Whereas, the two axis tracking systems consist of central tower receiver, parabolic dish reflector and circular Fresnel lens.

In CSP systems the receiver is located at the focal line or focal point of the reflectors, and consists of an absorbing medium which is designed to absorb and convert the sun's rays to heat. Specifically, parabolic trough collectors focus direct solar radiation on to a focal line on the collector axis. Concentrated sunlight falls at normal incidence on the tube receiver, gets absorbed and turns into heat. A special heat transfer fluid which is pumped through the absorber tube gets heated to about 400 ^{0}C [2, 3]. The hot heat transfer fluid is then used to do work such as generate steam which is used to generate electricity. The receiver tube is sealed inside a bigger glass tube which is in vacuum so to minimize thermal loses. The absorbing receiver is

coated with solar selective coatings which are designed to have high values for solar absorbance (ideally > 0.95 between wavelengths of 300 nm and 2.5 μm) and low values of thermal emissivity in the infra-red (ideally < 0.2, the wavelength range depending on the operating temperature). Clearly the absorber and its coatings must be chemically and structurally stable over the entire operating temperature range of the concentrating solar system.

An efficient way to maximize the harnessing of solar radiation is to optimize the functionality of solar selective coatings [1]. The design of solar selective coatings is complicated because absorbance and emittance are temperature and wavelength depended and strongly affected by the micro-structure [6, 7]. The energy emitted from a body is proportional to the fourth power of its temperature (Stefan-Boltzman law). Also, the photonic energy of radiation is inversely proportional to its wavelength (Planck law). This means a body at higher temperature will emit thermal radiation at shorter wavelengths and vice-versa. Given that the sun's surface temperature is of the order of 6000 ^{o}C, the incoming solar radiation is in shorter wavelengths while the thermal radiation emitted by the absorber surface will obviously be at longer wavelengths. The solar selective coatings allow the incoming solar radiation to pass through it while blocking the emittance of the longer wavelength thermal radiation. Thus, they help in better capturing and keeping the radiative energy, achieving high temperatures. There are many types of solar selective coatings based on different absorption mechanisms, which have been fabricated and categorized into a number of different types [8-10] including: i) intrinsic [11], ii) semiconductor-metal [12, 13], iii) multi-layer [14,15] vi) cermets or metallic composite materials [16-22], and finally v) textured surfaces [6, 23-26]. However, because all the categories of materials are based on chemical compounds and elements and their surfaces will all have textures, there is rarely a clear and absolute distinction between the categories.

Here, we focus on the computational design and optical optimization of a nono-composite metal-dielectric coating for high temperature application in parabolic trough collectors. These composites consist of metallic nano-particles (NPs) or nano-wires (NWs) in a dielectric matrix. We explore different dielectric matrixes and metals, various metal to dielectric volume ratios' and different kinds of nano-textured surface roughness, in order to maximize the total efficiency in parabolic trough collectors. The investigated nano-composites, it's a combination of the two last categories (vi, v). The metal-dielectric composites known as cermets are of special theoretical [27-31] and experimental [32] interest among the solar selective materials because of their high stability, which makes them particularly suitable for high-temperature applications in photo-thermal solar energy conversion. Increasing the operating temperature above the current limits of 400 ^{0}C for parabolic trough collectors [33] and 600 ^{0}C for central tower receiver [34] can improve power cycle efficiency and reduce the cost of solar electricity [35].

In previous theoretical works many materials had been studied and optimized as candidates for spectral selective coatings. Chester et al. [27] reported a thermal efficiency of 84.3% for a four layer silica-tungsten cermet (W NPs in a SiO2 matrix) at 400K with unconcentrated sunlight, and an efficiency of 75.59% for 1000K at 100 suns concentrator. Similar thermal efficiencies have been reported from Sakurai et al. [28] for a three layer silica-tungsten cermet, 82.7% (400 K), 85.91% (700 K), 76.63% (1000 K) for solar concentrators 1, 50, 100 suns respectively. Tungsten had also been studied from Zhang et al. [29] but in a different aluminum oxinitride (AlON) matrix, they report a maximum 85% thermal-conversion efficiency at 350 ^{0}C under a concentration of 30 suns (different antireflection coatings and IR reflector metal substrates had been examinated). Nejati et al. [30] had investigated the novel case of two-layer composite structure, with a metallic of Au, Cu, SS, and a ceramic component of either Al_2O_3 or SiO_2. The calculated results are with the range of 0.91-0.97 for solar absorbance and 0.02-0.07 for thermal emittance at room temperature. Finally, Farooq and Hutchins [31] had studied the performance of various materials such Ni, W, V, Co, Cr inclusions in a SiO_2 and Al_2O_3 matrix. Solar absorbance of 0.98 and 0.96 was achieved by simulation and experimental findings with less than 0.07 thermal emittance at 300 K for a four-layer system of V:Al_2O_3. Other designs showed lower optical performance for all the materials combinations. Common evidence from all the above theoretical works is that gradually changing the concentration of the metal particles from a low metal particle density at the air/cermet interface to high metal particle density at the cermet/substrate interface improves the spectral selectivity of the coatings.

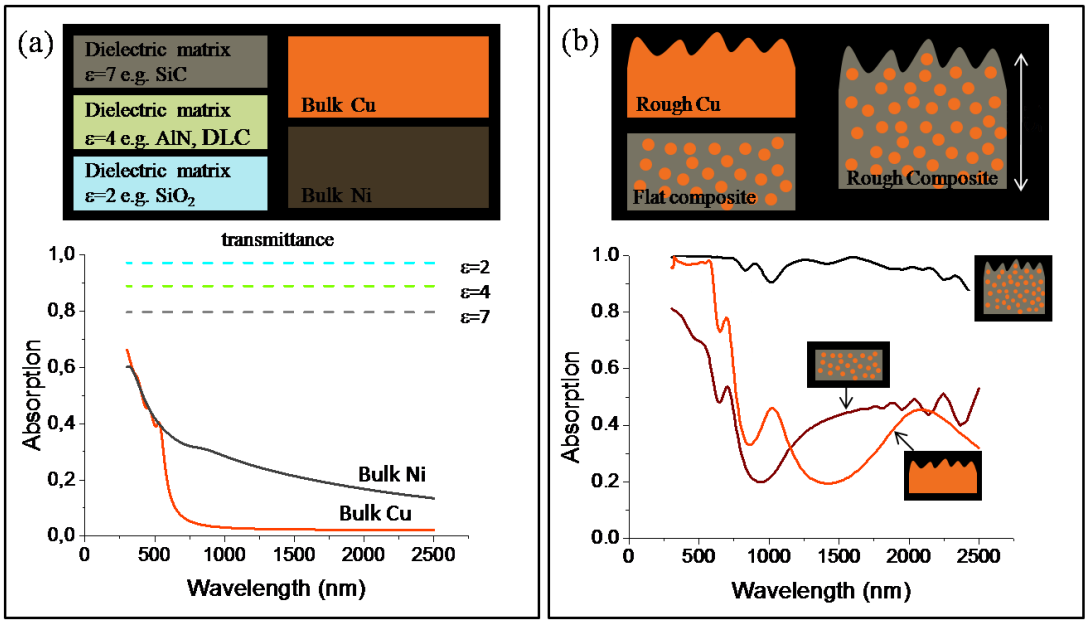

Figure 1. a) Transmittance of various representative matrices with a dielectric function ε=7 (e.g. SiC), ε=4 (e.g. AlN) and ε=2 (e.g. SiO_2). Also plotted is the absorption of flat-surface bulk Cu and Ni metals which will be used as inclusions in this study. b) Absorption of nano-textured rough Cu, alongside with the absorption of flat and rough nano-composites of Cu NPs inside a SiC dielectric matrix.

In this manuscript we consider the design of the best possible nano-composite solar selective coating for the tube receiver of parabolic trough collectors. Thus we examine different transparent matrices, starting from a high dielectric constant of ~7, e.g. SiC, down to low dielectric constant of ~2, e.g. SiO_2. And, for the inclusions we consider many different metals like Cu, Ag, Cr, W, V and Ni. We choose two metals which have high melting point, a characteristic transition metal like Ni (1455 ^{0}C), which is known for high absorption, and a characteristic noble metal like Cu (1085 ^{0}C) which is known for high reflectance (fig 1.a) when it is in the form of a flat film (in Fig. 1.b the dramatic change of the absorption properties of the composite material nanostructure is shown compared to the pristine unstructured materials). Specifically, we evaluate how each component of the nano-composite coating affects its spectral selective performance. That is, we explore various nano-composites for different: a) metal to dielectric volume ratios, b) nano – inclusions, i.e. nanoparticles (NPs) or nanowires (NWs) c) kinds of surface roughness (shape and height) d) thicknesses of un-roughed film e) kind of substrate (flat or rough). This evaluation has been made not only in terms of photo-thermal efficiency as previous theoretical works [27-29] had done, but also in terms of heat to work efficiency which is predicted from the Carnot efficiency [36] resulting into the final energy conversion efficiency. We examine a wide range of operating temperatures (400 ^{0}C - 1000 ^{0}C) and concentration ratios (80-500 suns). In doing so, we find the maximum efficiency at the optimum operating temperature. Furthermore, we work on the external glass envelope and we study how special coatings on the glass like transparent conductive oxides (e.g ITO) can improve the overall efficiency.

The rest of this manuscript is structured as follows. We first, start from the experimental optical constants of the metallic inclusions and introduce their temperature dependence. Then, we calculate the effective medium optical properties of the nano-composites. And finally, we build our model for evaluating the performance of the spectrally selective nano-composites. It is then followed by results and discussion, where the computational and the optimization process and results are presented.

3.2 Methodology

3.2.1 Optical Properties

Utilizing the Finite Difference Time Domain (FDTD) method, Maxwell's equations are time-integrated on a computational grid and solved for the light propagation [37-39]:

$$\nabla \times \mathbf{E} = -\mu \partial_t \mathbf{H} \tag{2.1}$$

$$\nabla \times \mathbf{H} = \varepsilon_0 \varepsilon_\infty \partial_t \mathbf{E} + \partial_t \mathbf{P}_0 + \sum_{j=1}^{N} \partial_t \mathbf{P}_j \tag{2.2}$$

where materials polarization is taken into account through polarizabilities P:

$$\partial_t^2 \mathbf{P}_0 + \Gamma_0 \partial_t \mathbf{P}_0 = \omega_p^2 \varepsilon_0 \mathbf{E} \tag{2.3}$$

$$\partial_t^2 \mathbf{P}_j + \Gamma_j \partial_t \mathbf{P}_j + \Omega_j^2 \mathbf{P}_j = \Delta\varepsilon_j \Omega_j^2 \varepsilon_0 \mathbf{E} \tag{2.4}$$

This yields a Drude-Lorentz model for the dielectric function [5]:

$$\varepsilon(\omega) = \varepsilon_\infty - \frac{\omega_p^2}{\omega^2 + i\omega\Gamma_0} + \sum_{j=1}^{N} \frac{\Delta\varepsilon_j \Omega_j^2}{\Omega_j^2 - \omega^2 - i\omega\Gamma_j} \tag{2.5}$$

where the first term is the Drude free-electron contribution (intraband transitions) and the second contains Lorentz oscillators corresponding to interband transitions. ω_p and $1/\Gamma_0$ are the free electron plasma frequency and relaxation time, Ω_j, $\Delta\varepsilon_j$, and Γ_j are transition frequency, oscillator strength, and decay rate for the Lorentz terms. To accurately reproduce the experimental dielectric functions we treat these as fit parameters. We use different measurements from the literature to obtain the bulk metallic optical properties ($n = \sqrt{\varepsilon} = n + \kappa i$) for the wavelength ranges of interest between 300 nm to 40000 nm, which is needed to calculate the solar absorption and thermal emission at high temperatures. The optical properties for Cu have been extracted from Ref [40-42] and for Ni from Ref [40, 43]. For Cu we use $N = 4$, and $\varepsilon_\infty = 1.02$ eV, $\hbar\omega_p = 7.934$ eV, $\hbar\Gamma_0 = 0.066$ eV, $\Delta\varepsilon_j = (0.947,\ 1.357,\ 0.726,\ 1.308)$ $\hbar\Omega_j = (2.618,\ 3.764,\ 4.383,\ 4.383)$ eV, $\hbar\Gamma_j = (0.719,\ 1.703,\ 0.123,\ 20)$ eV. Finally for Ni we use $N = 4$, and $\varepsilon_\infty = 2.297$ eV, $\hbar\omega_p = 4.92$ eV, $\hbar\Gamma_0 = 0.042$ eV, $\Delta\varepsilon_j =$ (18.767, 1.501, 0.538, 2.54), $\hbar\Omega_j = (0.444,\ 1.551,\ 4.212,\ 7.534)$ eV, $\hbar\Gamma_j =$ (1.834, 0.89, 0.813, 20) eV. In Fig.2 we plot the Drude-Lorentz fit (solid lines) on/and the experimental data (open shapes) showing an excellent agreement.

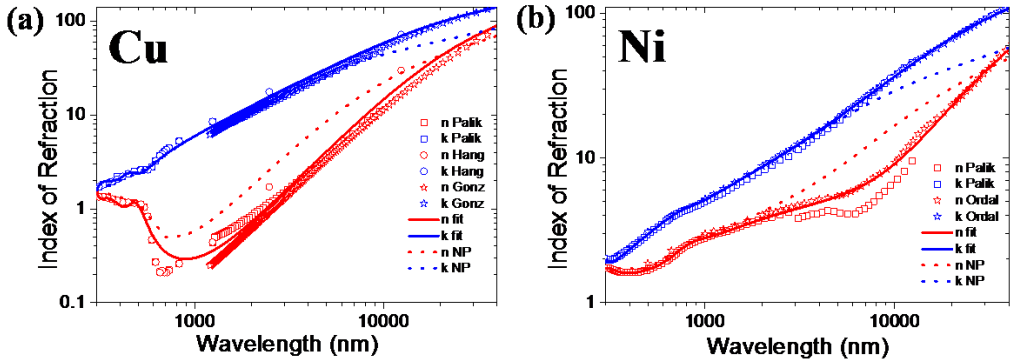

Figure 2. The refractive indices used in the calculations for a) Cu and b) Ni. Open shapes indicate the corresponding bulk metallic refractive index extracted from experimental data [40-43]. Solid lines indicate the Drude-Lorentz fit from Eq. (5). Dashed lines indicate the NP size correction to the fitted bulk dielectric function Eq (5 and 6).

We now continue with the actual optical constants of copper and nickel. As pointed out earlier, the bulk dielectric constant of a metal is approximated by the free electrons' contribution plus four interband transmissions [Eq. 5]. In order to have the appropriate dielectric constant for the NP, we need to include the surface scattering contribution to the free electron relaxation time τ, ($\tau = 1/\Gamma_0$). The reduced relaxation time τ^* is defined [38] as:

$$\frac{1}{\tau^*} = \frac{1}{\tau} + \frac{\upsilon_f}{r} \tag{2.6}$$

where r is the particle radius (10 nm in our study) and υ_F is the Fermi velocity, which is 1.57×10^6 and 1.40×10^6 m/s for Cu and Ni respectively. In Fig. 2 we plot the particle's surface corrected refractive index (dashed lines).The correction affects mostly the real part of the refractive index, which generally makes the particle more absorptive: the difference between real and imaginary parts becomes smaller, and thus the real part of the dielectric function less negative, which means more light can penetrate into the nanoparticle and get absorbed.

It is also an important goal to accurately model the optical properties of metal over a wide range of temperatures. The free electron collision frequency Γ_0 is also dependent on the temperature through the temperature dependence of the phonon population. The phonon population increases with increasing temperature, and as a result the electron-phonon collision frequency is increased [44]. We use a semi-empirical model for modifying the Drude-Lorentz model [45] over a range of temperatures which also had been used in previous theoretical works [27, 28]:

$$\Gamma(T) = \Gamma_0(T_0)\left(\frac{T}{T_0}\right)^{\alpha'} \tag{2.7}$$

where $T_0 = 300K$, T is the operating temperature and α' had been treated as fitting parameter to predict the experimental spectral emissivity for tungsten [27, 28] at specific temperatures and wavelengths. Due to the lack of measured data at high temperatures for Ni and Cu, we follow a different approach in order to obtain an exact value for α' at a wide range of temperatures. Firstly, eq. (2.7) can be rewritten in terms of free electrons relaxation time at the optical AC conductivity, in the first order approximation:

$$\frac{1}{\tau_{AC}(T)} = \frac{1}{\tau_{0AC}(T_0)}\left(1 + a'\frac{T - T_0}{T_0}\right) \tag{2.8}$$

where $\tau_{0AC}(T_0)$ is same as τ which have been obtained from the above Drude-Lorentz fit to the bulk dielectric function. Then, we obtain the experimental electrical resistivity as a function of temperature ($\rho(T)$) [46], from which we can extract the temperature evolution of the free electrons' relaxation time at DC conductivity ($\tau_{DC}(T)$) [47]:

$$\tau_{DC}(T) = \frac{m}{\rho(T)en} \tag{2.9}$$

where m, e, n is the mass, charge and the density of the free electrons respectively. It is known that the electrical resistivity of most materials changes with temperature. If the temperature T does not vary too much, a linear approximation is typically used:

$$\rho(T) = \rho_0[1 + a(T - T_0)] \tag{2.10}$$

where a is called the temperature coefficient of resistivity, T_0 is a fixed reference temperature (usually the room temperature), and ρ_0 is the resistivity at temperature T_0. The parameter a is an empirical parameter fitted from literature data. We found 0.004 and 0.0058 for Cu and Ni respectively. Combining now equations (2.9) and (2.10) we find the temperature dependence of the free electrons relaxation time at DC conductivity:

$$\frac{1}{\tau_{DC}(T)} = \frac{1}{\tau_{0DC}(T_0)}\left(1 + a\left(T - T_0\right)\right) \tag{2.11}$$

Furthermore, we suppose that the temperature evolution of the free electrons' relaxation time at DC conductivity is the same as at AC conductivity and combining equations (2.8) and (2.11) we conclude at the determination of the coefficient a'.

$$a' = aT_0 \tag{2.12}$$

In figure 3 we test our procedure comparing copper's experimental free electrons' relaxation time with its temperature dependence according to equation (2.7) taking into account a' from equation (2.12) for $\Gamma_{0DC}(T_0)$, i.e. with Eq. 13. It shows

an excellent agreement for temperatures less than 1000K and a good agreement above it:

$$\Gamma_{DC}(T) = \Gamma_{0DC}(T_0)\left(\frac{T}{T_0}\right)^{\alpha'} \tag{2.13}$$

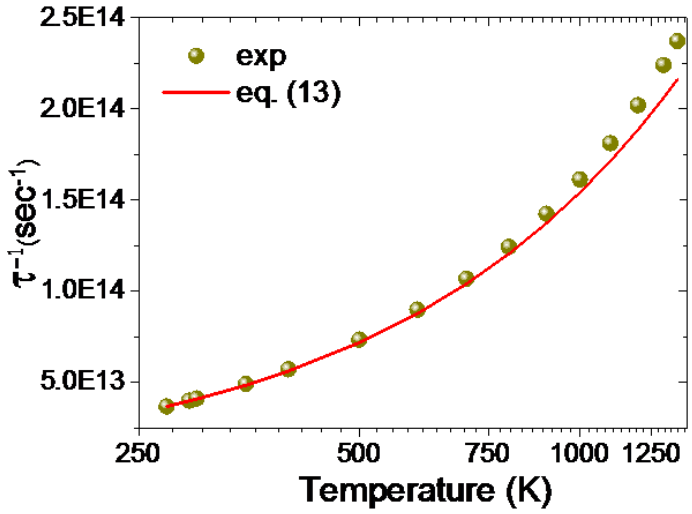

Figure 3. The temperature dependence of Cu's experimental free electrons relaxation time obtained from ref. [47] and its temperature dependence according to eq. (13).

From the Drude-Lorentz fit to the bulk dielectric-function we have obtained the value of $\Gamma_0(T_0 = 300K)$ for the AC conductivity. Assuming that the temperature evolution of the free electrons collision frequency at AC it's the same as that for DC and utilizing the calculated a' from eq. 2.12, we produce from eq. 2.7 the free electron collision frequency as a function of temperature. The total correction to the dielectric function (eq. 2.5) is written now as the sum of electron – phonon collision frequency (eq. 2.7) and surface scattering correction (eq. 2.6):

$$\Gamma_0(T) = \Gamma_0(T_0)\left(\frac{T}{T_0}\right)^{a} + \frac{\upsilon_F}{r} \tag{2.14}$$

The effect of temperature on the Fermi velocity is small, because the thermal energy $k_B T$ (where k_B is the Boltzmann constant) is small compared to the Fermi energy for most metals even at their melting point [44].

Finally, by utilizing the modeled dielectric functions, we are able to extract from the FDTD solutions of Maxwell's equations the electromagnetic fields, fluxes and material absorptions at every point in the structure in time domain, and by applying Fourier transform we get the corresponding quantities in frequency domain [48].

3.2.2 Effective medium optical properties

Multiple length scales appear in this problem because of the various sizes of metal NPs (20 nm diameter) or metal NWs (16 nm diameter), surface roughness (100-1200 nm height) and the total thickness (> 4 μm). We employ a multi-scale approach to solve this, utilizing the Finite Difference Time Domain Effective Medium Theory (FDTD-EMT) [38]. In order to calculate the optical response of the NC coating, we isolate one or more NPs, or a cross connection of three NWs, in a transparent matrix at a specified metal volume ratio, and we extract the optical response (Reflection, Absorption, Transmission) of this system. Then we calculate the effective medium optical constants of fictitious uniform material that produces the same optical response as that of the composite material. Utilizing the effective medium optical constants we are then able to efficiently calculate and design the optical response of the whole nanocomposite (NC) coating.

To choose the appropriate effective medium approach, we compare the FDTD-EMT which is an exact computational method with the Bruggeman (BR) EMT and Maxwell-Garnet (MG) EMT which are analytical approximate methods that have been used in the previous theoretical works [27-31]. The effective dielectric functions ε_{eff} for the two analytical EMT's are [49, 50]:

$$\varepsilon_{eff}^{BR} = \frac{1}{4}\left\{\varepsilon_i(2-3f)+\varepsilon_m(3f-1)\pm\sqrt{\left[\varepsilon_i(2-3f)+\varepsilon_m(3f-1)\right]^2+8\varepsilon_i\varepsilon_m}\right\} \quad (2.15)$$

$$\varepsilon_{eff}^{MG} = \varepsilon_i\frac{\varepsilon_m(1+2f)-\varepsilon_i(2f-2)}{\varepsilon_i(2+f)+\varepsilon_m(1-f)} \quad (2.16)$$

where ε_i and ε_m are the dielectric functions of the insulating and metallic regions respectively and f is the volume fraction of conductive regions. The MG-EMT is expected to be valid at low volume fractions where it is assumed that the conductive domains are spatially separated, and so we use that expression for spherical metallic nanoparticles. The BR-EMT is expected to be valid at high volume fractions where it is assumed that the conductive domains are large enough to form a continue conducting path throughout the dielectric matrix, and so we use that expression for nano-wires metallic inclusions. On the other hand the computational FDTD-EMT is valid for any shape and morphology of metallic inclusions.

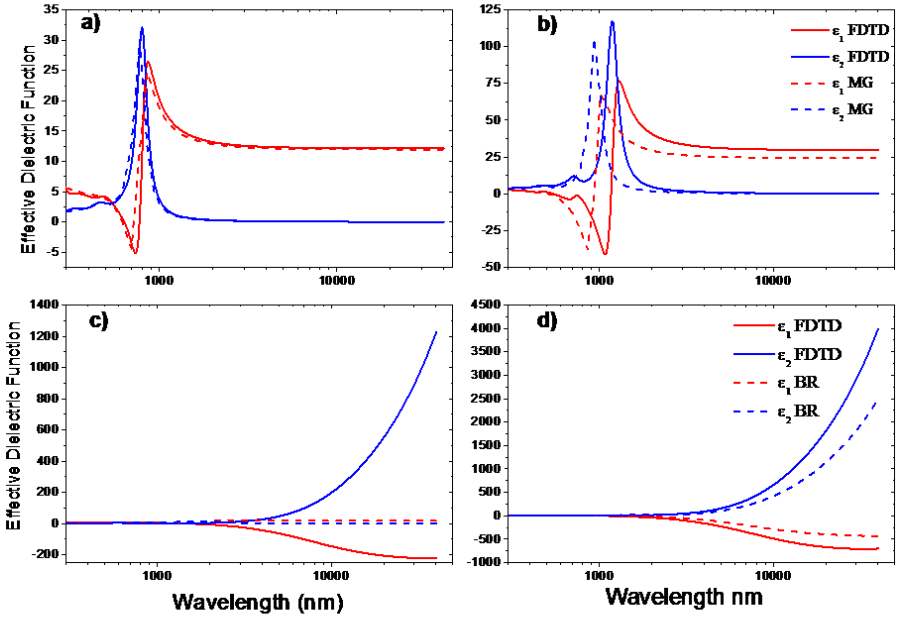

Figure 4. Comparison of the NC's effective medium dielectric function obtained by the exact computational FDTD method and by approximate analytical effective medium theories (Maxwell-Garnett and Bruggeman) for four different systems: a) Cu NPs in a SiC matrix at volume ratio ~20%, b) Cu NPs in a SiC matrix at volume ratio ~45%, c) Cu NWs in a SiC matrix at volume ratio ~20%, d) Cu NWs in a SiC matrix at volume ratio ~45%.

We find that the FDTD-EMT and MG-EMT indeed have a good agreement at low volume ratio (~20%) Cu NPs in a SiC matrix (Fig.4.a), but at high volume ratio (~45%) the MG-EMT cannot accurately produce the effective dielectric function (Fig.4.b). Comparing the FDTD-EMT and the BR-EMT for Cu NWs in a SiC matrix, on the other hand, we find that the BR-EMT is not able to produce the effective dielectric function at low volume ratio (~20%) (Fig.4.c) but at high volume ratio (~45%) FDTD and BR EMT's have a better agreement (Fig.4.d).

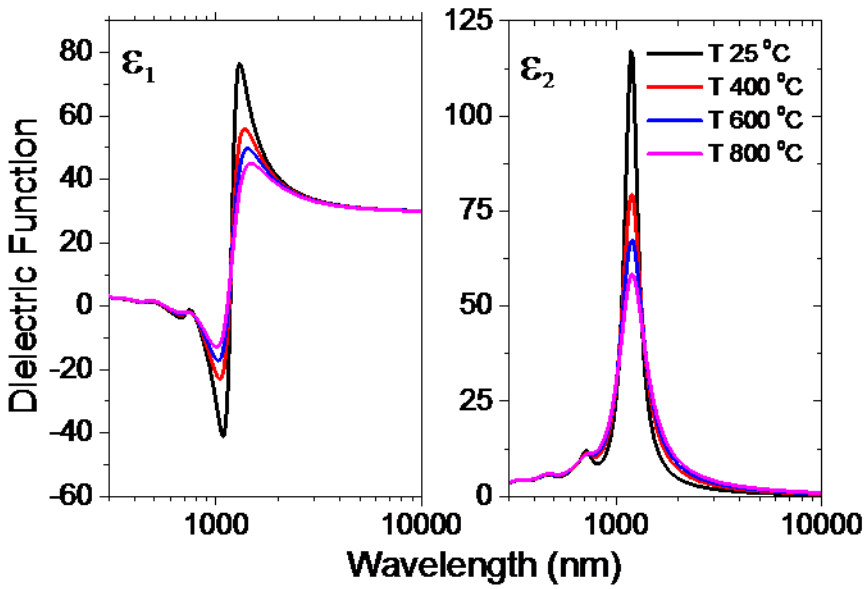

Figure 5. The temperature dependence of the effective medium dielectric function extracted from FDTD-EMT for Cu NPs at volume ratio 45% inside a SiC matrix, the real (ε_1) and the imaginary part (ε_2) .

In our calculations thus we use only the exact arithmetical FDTD-EMT to extract the effective medium optical constants. By modifying the temperature dependence of the metals' dielectric function at each temperature (eq. 2.14) we calculate the effective medium dielectric function for each temperature (400^0C-1000^0C) at the wavelength range of 300nm - 40000nm (fig. 5). Then we perform a Drude-Lorentz fit to the effective medium dielectric function, and then we are able to calculate the optical response of the nano-composite coating at each temperature.

3.2.3 Characterization of Selective Surfaces

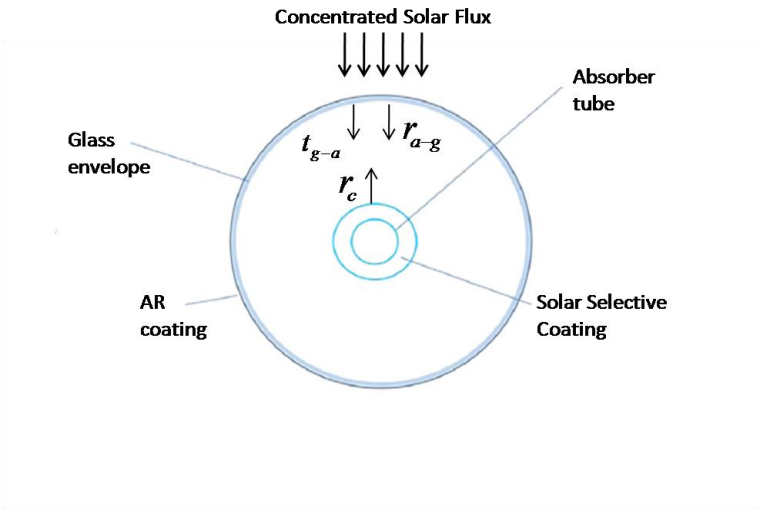

Figure 6. Cross section of an absorber tube with the glass protection tube showing how light is reflected and transmitted from the different interfaces.

Parabolic trough collectors concentrate the solar flux on the receiver tube (Fig.6). We assume a perfect antireflection coating (AR), i.e. all the concentrated solar flux is getting inside the glass without losses from the external air-glass interface. Here, we consider the internal glass-air interface and air-coating interface to calculate the solar absorbance and thermal emittance of the solar selective coating. The concentrated flux is transmitted through the glass-air interface (t_{g-a}) and falls on the internal absorber tube. A portion of the transmitted flux is reflected (r_c) and the rest is absorbed by the solar selective coating. The temperature of the coating is increased and it starts to emit according to its temperature, a portion of the emitted flux is reflected from the air-glass interface (r_{a-g}) and reabsorbed by the coating.

The performance of a candidate solar selective coating can be characterized by its solar absorbance a and thermal emittance ε [8]. Using Kirchoff's law, spectral absorbance can be expressed in terms of the coating's reflectance r_c, and the thermal emittance is equal to the absorbance for each temperature.

$$a(\lambda,T,\theta) = 1 - r_c(\lambda,T,\theta) \tag{2.17}$$

$$\varepsilon(\lambda,T,\theta) = a(\lambda,T,\theta) \tag{2.18}$$

where λ is the wavelength, θ is the incident angle of light, T is the operating temperature. As we mentioned before at parabolic trough collectors sunlight falls at normal incidence on the receiver, so the solar absorption calculations were performed at normal incidence $\theta = 0$. Also for the thermal emittance we find that normal incidence is a good approximation of incidence at different angles.

Taking into account the energy transmitted through the glass-air interface (t_{g-a}) and the energy lost in the environment due to the unreflected thermal flux ($1-r_{a-g}$), we calculate the solar absorption efficiency $n_a(T)$ and the thermal emission efficiency $n_\varepsilon(T)$ respectively:

$$n_a(T) = \frac{\int t_{g-a}(\lambda) a(\lambda,T) S(\lambda) d\lambda}{\int S(\lambda) d\lambda} \tag{2.19}$$

$$n_\varepsilon(T) = \frac{\int (1-r_{a-g}(\lambda)) \varepsilon(\lambda,T) B(\lambda,T) d\lambda}{\int B(\lambda,T) d\lambda} \tag{2.20}$$

where $S(\lambda)$ is the Direct Solar Spectrum AM1.5, as defined for solar concentrator work [3], and it includes the direct beam from the sun plus the circumsolar component in a disk 2.5 degrees around the sun. And $B(\lambda,T)$ is the spectral irradiance of the black body curve from:

$$B(\lambda,T) = \frac{c_1}{\lambda^5 \left[e^{\left(\frac{c_2}{\lambda T}\right)} - 1 \right]} \tag{2.21}$$

where c_1, c_2 are the Planck's first and second radiation constants respectively. The wavelength range of the black body spectrum is depended on the temperature, as the temperature increases the wavelength of maximum emission shifts to smaller wavelengths (fig.7). The key of high efficiency at high operating temperatures is the fine optical design of the solar selective coating. The coating must have maximum possible absorption in the solar spectrum (0.3-2.5 μm) and highest reflection in the infrared spectrum (2.5-50 μm), in order to maximize the solar energy collection and minimize the thermal loses.

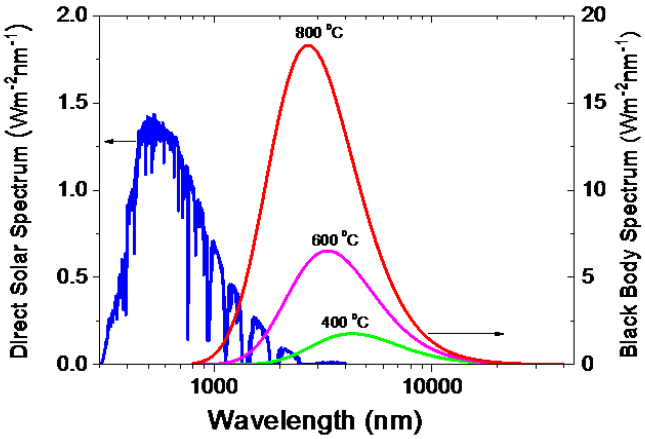

Figure 7. The Direct Solar Spectrum and the Blackbody Spectrum at different temperatures.

For thermodynamic solar systems the maximum solar to work (electricity) efficiency η can be deduced by considering both thermal radiation properties and Carnot's principle [36]. For parabolic trough collectors the solar irradiation must first be converted into heat via a solar receiver with efficiency η_{rec} , and then this heat is converted into work via the Carnot efficiency η_{Car}. Hence a solar receiver providing a heat source at temperature T and a heat sink at temperature $T_0 = 300K$:

$$\eta = \eta_{\mathrm{Rec}} \eta_{Car}$$

$$\eta_{Car} = 1 - \frac{T_0}{T} \tag{2.22}$$

$$\eta = \frac{Q_{absorbed} - Q_{lost}}{Q_{solar}}$$

where $Q_{solar} = I_{global} CA$, $Q_{absorbed} = B_{mirr} n_a(T) I_{direct} CA$, $Q_{lost} = A n_\varepsilon(T) \sigma (T^4 - T_0^4)$ are the incoming solar flux and the fluxes absorbed and lost by the solar receiver respectively. For the direct solar flux $I_{direct} = 900 W/m^2$, is concentrated C times on a solar receiver, with a collecting area A, and with a solar absorption efficiency $n_a(T)$ from eq. 2.19. The parameter B_{mirr} is related to the reflection of the mirrors, typically 0.94 for markets' products. The thermal losses are specified applying the Stefan-Boltzmann law, where A is the reradiating area which is the same with the collecting area, $n_\varepsilon(T)$ is the thermal emission efficiency from eq. 2.20 and $\sigma = 5.67 \times 10^{-8} W m^{-2} K^{-4}$ is the Stefan-Boltzmann constant.

The following thermal to work energy conversion efficiency is used as the figure of merit:

$$\eta(T) = \eta_{\mathrm{Rec}} \eta_{Car} = \left(\frac{B_{mirr} n_a(T) I_{direct}}{I_{global}} - \frac{n_\varepsilon(T) \sigma (T^4 - T_0^4)}{I_{global} C} \right) \left(1 - \frac{T_0}{T} \right) \tag{2.23}$$

From the above equation it is cleare that the absorber's total energy efficiency depends on the optical properties of the solar selective coating, the geometrical concentration ratio and the operating temperature. The optical response of the nano-composite coating is affected from: a) kind of metallic inclusions, b) metal to dielectric volume ratios, c) nano-inclusion type (NPs or NWs), d) kind of surface roughness (shape and height), e) thicknesses of un-roughed film and f) texturing of the substrate (flat or rough). In the next section we will extensively study all these parameters for a wide range of operating temperatures (400^0C-1000^0C) and concentration ratios (80-500 suns) and find a recipe to optimize the overall energy efficiency.

3.3 Results and Discussion

3.3.1 Computational setting

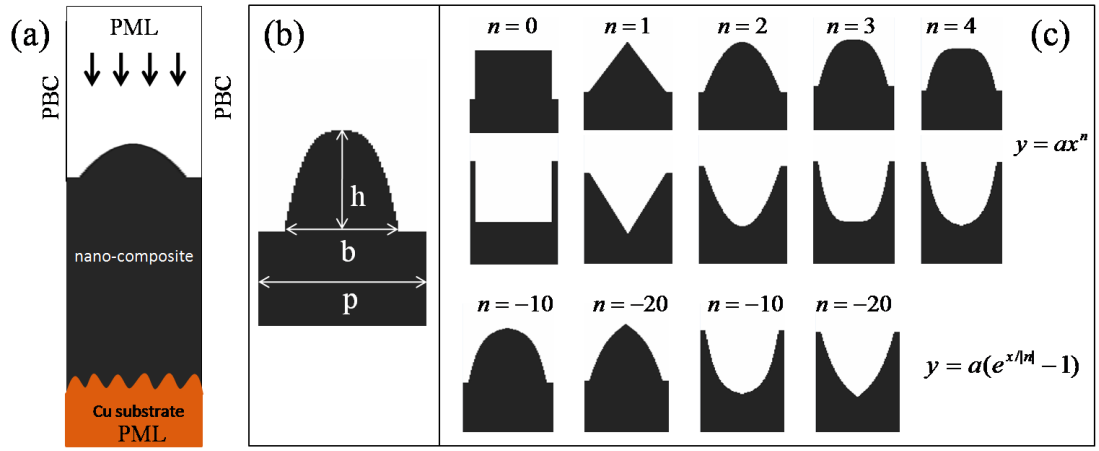

Figure 8. a) The simulation cell. Periodic boundary conditions are applied on the direction perpendicular to the wave front and perfectly matched layer conditions along it. b) The characteristic parameters of our simulated roughness c) The different shapes that have been explored for roughness design (up and reverse shapes).

We simulate rough or flat nano-composite (NC) absorbers on a rough or flat bulk Cu substrate. The reflection spectra of plane waves have been calculated under normal incidence. A 2D projection of the 3D computational cell is shown in Fig.8a. Perfectly matched layer (PML) absorbing boundary conditions are applied along the propagation direction, while periodic boundary conditions are applied in the direction normal to propagation. A typical simulation cell has a width along the periodic direction of a=320nm and the length along the propagation direction is depended from the nano-composite's thickness and the height of the roughness. The system is discretized to 4nm/grid. The input field has a narrow Gaussian temporal profile. In order to calculate the absorption of the NC coating we get the energy losses from the reflection. To get that in frequency space, one needs to Fourier transform the fields on suitably chosen planes and take the appropriate ratios with and without the nano-composite coating and the substrate.

The computational experiments to study the effect of film roughness were performed by normalizing the height and the width of square-based pyramids, assuming both upwards and downwards shapes. The height was normalized as the ratio of the height to the base (h/b) (or aspect ratio) and the width was normalized as the ratio of the base to the period (b/p), as it is shown at figure 8b. We have explored many different shapes of roughness for upwards and downwards pyramids in order to minimize the energy losses from reflection, as shown in figure 8c, which were produced from two functionals for different coefficients (n). The three first shapes for upwards and downwards pyramids of figure 8c are the most representative which we are going to present here.

As we mentioned before, the tested materials are Cu and Ni nano-inclusions in different non-absorbing dielectric matrixes, in particular, a low index dielectric matrix ($\varepsilon = 2$, e.g. SiO_2), a middle index dielectric matrix ($\varepsilon = 4$, e.g. AlN) and a high index dielectric matrix ($\varepsilon = 7$, e.g. SiC). We test two volume ratios of metallic inclusions, a low volume ratio ($f = 20\%$) and a high volume ratio ($f = 45\%$) at each dielectric matrix. We find that both "limits" of the designed nano-composites are representative in terms of optical response, thus we present only the low index and low volume ratio NCs ($\varepsilon = 2$, $f = 20\%$) and the high index and high volume ratio NCs ($\varepsilon = 7$, $f = 45\%$) for Cu and Ni nano-inclusions. We also test and present for comparison the pure metals nano-textured Cu (black-Cu) and nano-textured Ni (black-Ni).

3.3.2 Surface texturing

Here, we start by evaluating the first three representative kinds of surface roughness depicted in figure 8.c, which we parameterize as a function of the base to period ratio. The evaluation is made with the criterion to maximize the solar absorption efficiency (eq. 2.19) assuming no glass envelope and ambient temperature (T_0). We test the different shapes of roughness under the same aspect ratio (1 or 2) and NC's thickness (1.5 μm). To do so, we calculate the absorption of each NC coating under normal incidence, then convolute the absorbance with the solar spectrum, and divide with the integrated solar flux, which yields the solar absorption efficiency of eq. 2.19.

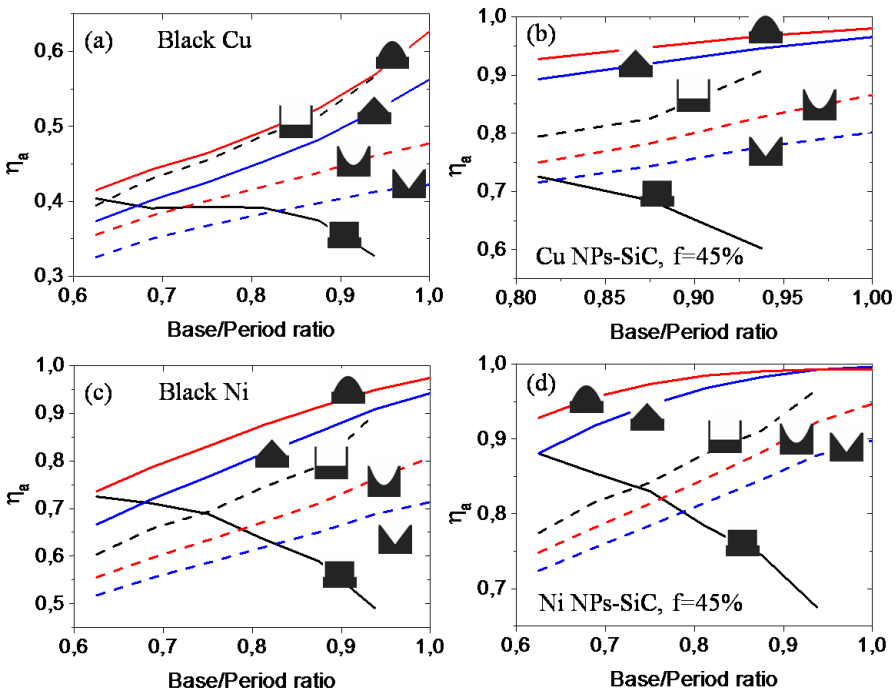

Figure 9. Solar absorption efficiency as a function of base-to-period ratio for NC coatings of aspect ratio 2 and bulk thickness (total thickness-texturing thickness) 1.5 μm: a) Black Cu (textured Cu) b) high index NC with Cu NPs c) Black Ni (textured Ni) d) high index NC with Cu NPs.

The solar absorption efficiency is increased as a function of the base-to-period ratio for all the types of roughness, except of the up-blocks (because the interface becomes flatter when increasing the base to period ratio) as it is depicted from the figure 9. That trend is same for the different materials, which is because the light scattering on the surface is maximized when the bases of the pyramids are coming closer. The best performance is observed with the "upward" quadratic pyramid ($n = 2$) with base-to-period ratio equal to one, when the pyramid bases are touching each other. For the reverse shapes the best performance appears for the block, which comes from the grid that is created on the surface, within which the light is "smoothly" trapped and absorbed. The same trend is observed at low index NCs, but at smaller variations compared to the high index NCs. This will be presented in the next graph comparing different aspect ratios.

Specifically, the maximum achieved solar absorbance efficiencies for each system are: a) 99.3% and 98% for high index Ni and Cu NC respectively, b) 97% and 93% for low index Ni and Cu NC respectively c) 97% and 63% for black-Ni and black-Cu respectively. The high index has better solar performance compared to the low index NC. Generally, Ni as an absorbent metal shows higher yields compared to Cu, which is generally characterized by high reflectance. However, the Cu NC produce high absorption compared to pure metal because of the localized surface plasmon resonance (LSPR), wherein the generated plasmons are eventually absorbed by the metal.

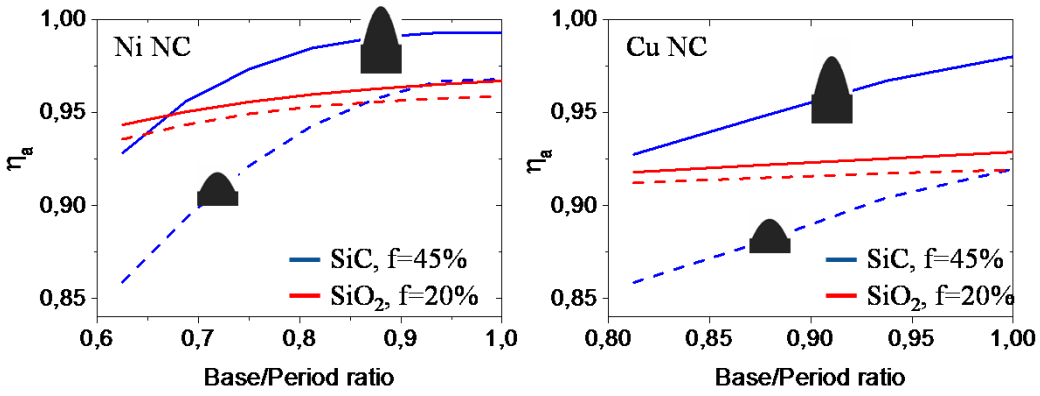

Figure 10. The effect of the aspect ratio on solar absorption efficiency for high and low index with Ni and Cu NCs, presented for "upward" quadratic pyramid, which is the optimal for high solar absorption efficiency. The big pyramids are for aspect ratio 2 and the small for aspect ratio 1.

Furthermore, we investigate the influence of the roughness height on to the solar absorption efficiency of low and high index NCs, for the best case scenario of "upward" quadratic pyramid (fig. 10). We observe that the aspect ratio is more critical for the higher index than for the low index NC coatings. That's because the high index materials are generally more reflective, and the surface texturing becomes critical in order to avoid energy losses from reflectance and thus maximize the solar absorption efficiency. On the other hand, for the low index NC the surface texturing is not critical for maximizing the solar absorption (less reflective), but the thickness of

the NC is, where because of the small absorption coefficient, we need an increased film thickness to maximize solar absorption.

3.3.3 Energy conversion efficiency

We focus now on the evaluation of the energy conversion efficiency ($\eta(T)$) for the different NC coatings assuming the realistic case of the external glass envelop. The optical properties of the SiO_2 glass envelope will be shown in the next section. As it is shown in Eq. 2.23, to optimize the performance of a candidate solar selective coating, one have to consider many parameters such as the optical response of the NC, the operating temperature and the geometrical concentration ratio of the collecting mirror. As the optical response is a temperature depended parameter, so will be the solar absorption efficiency ($n_a(T)$). Thermal emission losses are also temperature dependent, increased according to the fourth power of the operating temperature. Furhtermore, the optical response depends on the microstructure, the roughness, and the thickness of the NC coating. Overall, the maximum efficiency will be achieved at a specific optimum operating temperature which will be strongly depended on the concentration ratio [36].

Our goal is to explore all of the above parameters to get a physical understanding and therefore optimizate the NC coating performance. Up to now we maximized the solar absorption efficiency which is critical for solar collector applications. We use this result for the next set of calculations, i.e. we utilize the optimum "upward" quadratic pyramid at base-to-period ratio of one. We first explore the conversion efficiency as a function of NC's roughness (aspect ratio) and thickness, at a specific concentration ratio and temperature. We then present the evolution of the maximum efficiency as a function of the optimum temperature and concentration ratio. Finally, utilizing the maximum performance we present comparative graphs for both "families" (Cu and Ni) of the NC coating.

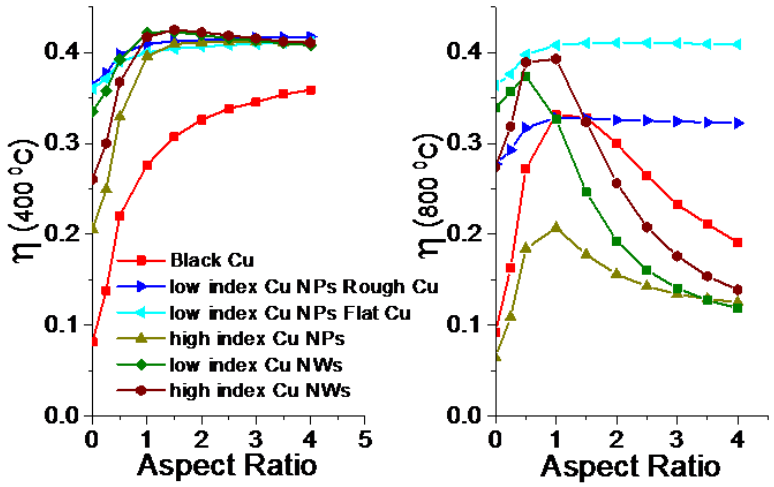

Figure 11. Energy conversion efficiency at 400 ^{0}C and 800 ^{0}C as a function of the NC's roughness aspect ratio, for Cu nano-inclusions (NPs and NWs) and Black Cu at fixed concentration ratio (C=100) and NC's thickness (1500nm).

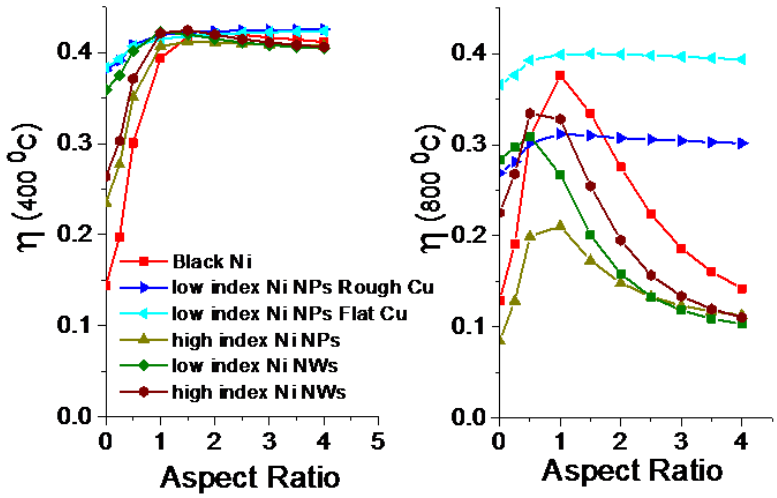

Figure 12. Energy conversion efficiency at 400 ^{0}C and 800 ^{0}C as a function of the NC's roughness aspect ratio for Ni nano-inclusions (NPs and NWs) and Black Ni at fixed concentration ratio (C=100) and NC's thickness (1500nm).

In figures 11 and 12 we present comparative graphs for both "families" of NCs based on Cu and Ni, on flat or rough Cu substrate, as well as of their nano-textured metals. We first explore the effect of aspect ratio on the total energy conversion efficiency for a specific concentration ratio ($C=100$) and for two temperatures, a low temperature of 400 ^{0}C which is the current operating temperature of parabolic trough collectors and a high temperature of 800 ^{0}C which is a "target" temperature. The efficiency evolution is almost identical for both "families" of metals. At low temperature the efficiency increases for small increments of aspect ratio, which is because the solar absorption efficiency increases as we move from a flat (0 aspect ratio) to a rough surface. A further increment to the aspect ratio does not have

significant effects on the efficiency, which stabilizes for aspect ratios 2-4. This trend is almost identical for all the materials except black Cu. That's because Cu as a reflective metal has small solar absorption efficiency and thus surface texturing is highly critical in order to increase the efficiency.

At high temperatures and small increments of aspect ratio the trend is the same for most of the materials, except the low index NC with metallic NPs on rough and flat Cu substrate, for which maximum efficiency is achieved with on a flat Cu substrate. Specifically, for high index NCs (NPs and NWs), low index NCs with NWs and textured metals, the efficiency initially increases for small increments of roughness, because of the absorption increase, but it maximizes at an aspect ratio 0.5-1 and then it drops due to the energy loses by thermal emission, which becomes dominant at high temperatures. We also notice that the Cu substrate roughness does not affect the performance of high index NCs (NPs and NWs) or the low index NCs with NWs. This is due to the high absorbance of NCs, as the light gets absorbed before it reaches the substrate. In contrast, the effect of substrate roughness is critical to the low index NCs with NPs, where higher efficiency is achieved from the flat Cu substrate. This is because the high reflectance of the flat Cu to the thermal IR radiation also causes a reduction in thermal lose.

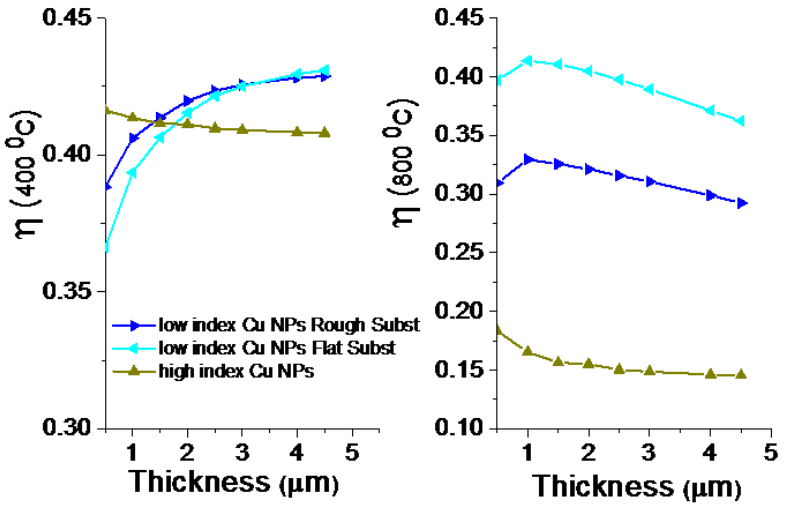

Figure 13. Total energy efficiency at 400 ^{0}C and 800 ^{0}C as a function of thickness for a Cu NC, at fixed concentration ratio (C=100) and roughness aspect ratio 2 (640nm height, 320nm width).

We explore now the effect of bulk film thickness (i.e. the film thickness excluding the rough surface) on the overall efficiency at two temperatures (400 ^{0}C and 800 ^{0}C) for fixed concentration ratio ($C=100$) and NC's aspect ratio (2) for Cu NCs with NPs at low and high index. At low temperature the efficiency increases for low index NCs on both flat and rough Cu substrates because the solar absorption efficiency increases while the thermal emission remains low for these low absorbing materials. In contrast, for high-index NCs for which the thermal emission is high, increasing the NCs thickness causes a monotonic decrease on the efficiency. We

observe a crossing point at a thickness of 1.5 μm, at which the spectral response contributions changes, i.e. for smaller thicknesses solar absorbance dominates and the high index NC yields a larger efficiency, while above that crossing point the thermal emittance becomes dominant and the low index NCs now yield the larger efficiency. The effect of thermal emission is even more dramatic at high temperatures, where the efficiency is generally decreasing for increasing the film thickness. We finally observe that the global trend is that the low index NC on an infrared reflective flat Cu substrate yields the best efficiencies.

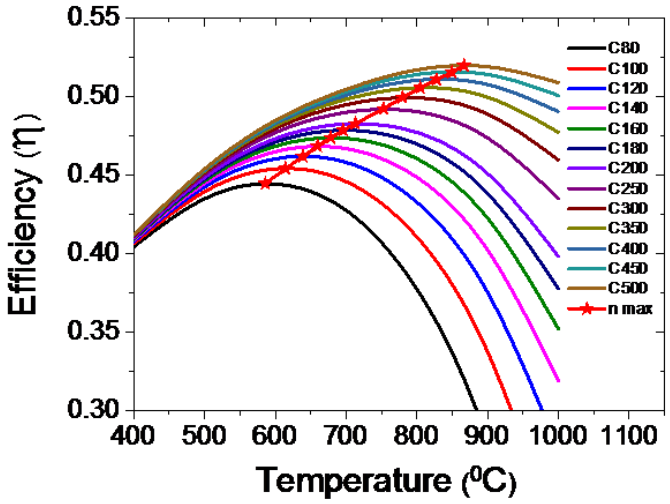

Figure 14. Total energy efficiency as a function of temperature for different concentration ratios, for low index Cu NC with NPs, thickness 1.5 μm and aspect ratio 2, on a flat Cu substrate. The maximum efficiency for each concentration ratio is marked by the red line.

Exploring the potential for high efficiencies in solar collectors we examine a wide range of operating temperatures (400 ^{0}C - 1000 ^{0}C) and concentration ratios (80-500). We note here that there is a theoretical limit for maximum concentration at 213 suns for 2D concentrators [51], however this limit could be overcame by (a) setting the absorbing tube within a dielectric medium for more efficiently focusing the solar flux on the absorber by a factor equal to the medium refractive index, and (b) better optical designing of the reflectors moving from a strictly 2D to 3D designs (for the fully 3D concentrator focusing onto a point the theoretical limit is 45.000 suns). Here, we relax that limit to 500 concentration suns to examine with energy and efficiency terms the necessity for a better optic design.

Based on the previous discussions we choose the optimum microstructure, i.e. low index NCs with NPs on a flat Cu substrate, to present the evolution of the energy conversion efficiency as a function of temperature and concentration ratio (fig.14). The thickness of the NC is chosen to be 1.5 μm and the aspect ratio is chosen to be 2 (640 nm height and 320nm width). Specifically, in figure 14 we plot the temperature dependence of energy conversion efficiency for different concentration ratios. For a specific concentration ratio, increasing the temperature will cause the overall

efficiency to increase, which mainly comes from the Carnot efficiency increase [36]. By further increasing the temperature, the efficiency maximizes at some optimal temperature, and then decreases because of mounting energy lose from thermal emission. At this point, however, one can increase the concentration ratio and enhance the maximum efficiency ($\eta \max$), as the energy losses scale with the absorber area and are thus divided by the concentration ratio (eq. 2.23).

It is obvious that, maximum efficiencies are achieved at higher concentration ratios and at higher operating temperatures, which are defined at specific optimal values. The current parabolic trough collectors are typically working between 300 ^{0}C to 400 ^{0}C operating temperatures and the concentration ratios are 20-80 suns [3]. For the case of 400 ^{0}C operating temperature and 80 suns concentration we find an energy conversion efficiency in our materials example of 0.405. Moving now to higher concentration ratio 200 we have an optimal operating temperature 713 ^{0}C and a maximum efficiency 0.483, which results into a 19.3% increase in performance compared to the current values. Furthermore, moving to an even higher concentration ratio of 500 we find an optimal operating temperature at 866 ^{0}C and a maximum efficiency of 0.52 which results into a 28.4% performance increase. We note however, that only a 7.7% performance increase is obtained as we go from a 200 sun to a 500 concentration ratio.

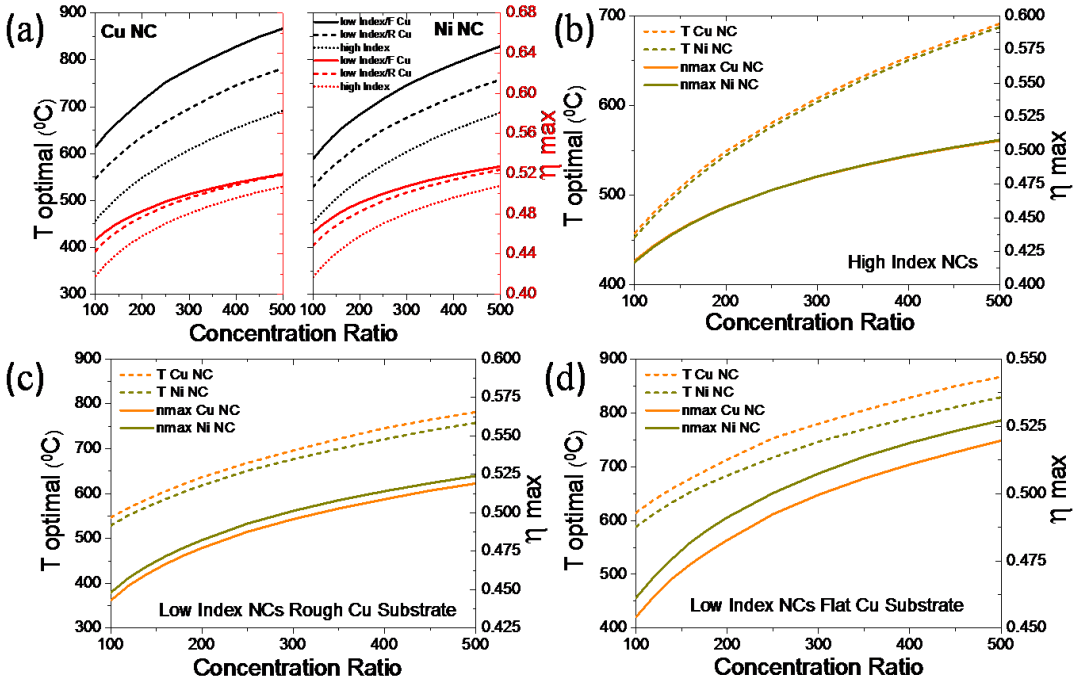

Figure 15. Comparative graphs of the maximum conversion efficiency and the optimal operating temperature as a function of concentration ratio: a) both "families" of Cu and Ni NCs with NPs b) high index Ni and Cu NCs c) low index Ni and Cu NCs on a rough Cu substrate d) high index Ni and Cu NCs on a flat Cu substrate. The thickness of the NC is 1.5 μm and the aspect ratio is 2 (640nm height, 320nm width).

In figure 15 we present comparative graphs of both "families" of NC coatings with Cu and Ni NPs as a function of optimal temperature and concentration ratio. These graphs could be the guiding maps for the design of parabolic trough collectors because one can easily extract the maximum efficiency at a specific operating temperature and concentration ratio, and vice versa. Comparing the different NCs for the same metal we observe that the low index NCs have higher efficiencies compared to the high index NCs, especially on flat Cu substrate, with the trend being the same for both metals Cu and Ni (fig 15.a). Specifically, the low index Cu NC on flat Cu substrate has 3-9% better performance than the high index Cu NC depending on the concentration ratio. Also, the low index Ni NC on flat Cu substrate has 4-11% better performance than the high index Ni NC depending on the concentration ratio. Furthermore, comparing the two metals with respect to their microstructure and Cu substrate we don't find any significant differences. Specifically, for high index NCs we have exactly the same efficiencies (fig. 15.b), for low index NCs on rough Cu substrate Ni NCs are 1% more efficient compared to Cu NCs (fig. 15.c) and finally for low index NCs on flat Cu substrate Ni NCs are 2% more efficient compared to Cu NCs. The slightly better performance of low index Ni NCs is mainly observed at lower temperatures.

3.3.4 Glass envelope optimization

In this section we focus on the optimization of a spectrally selective external glass envelop. The optical properties of the glass envelope are described by the refractive index of SiO_2 obtained from combined experimental data [52, 53] within the wavelength range of 0.3-4 μm (fig.16.a). As we mentioned in the previous section (fig.6), at the external air-glass interface we assume that we have a perfect antireflection coating, so that all the concentrated flux is getting into the glass with no losses. Here, we focus on the internal glass-air interface and try to engineer it so to minimize the thermal loses to the environment. In doing so, we modify the interface by introducing an indium tin oxide layer (glass-ITO-air), a low electron density transparent conductor which is generally characterized by high transparency in the solar spectrum and high reflectance in the infra-red spectrum. ITO is a representative material of the family of Transparent Conductor Oxides (TCOs), which are widely used in solar energy applications as transparent contacts [54], and their optical properties can be controlled by the concentration of charge carrier [55]. We develop a Drude model to explore the optical properties of ITO, i.e. its spectral selectivity, as a function of doping level and thickness.

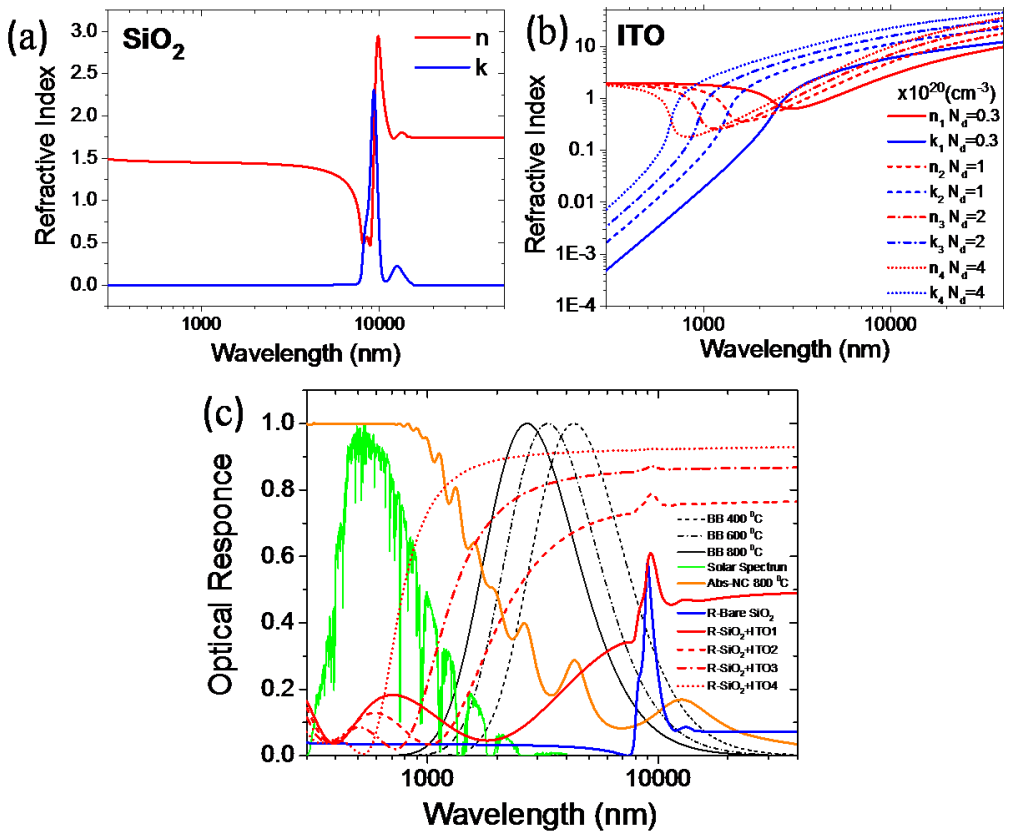

Figure 16. a) Refractive index of SiO_2 obtained from experiments [52, 53] b) Refractive index of ITO for different doping levels obtained from the developed Drude model c) Optical response of ITO layer (100 nm) on a semi-infinite SiO_2 substrate, for the different doping levels in (b). Target is the coating to be transparent in the solar spectrum for maximum solar absorption and reflective in the Black Body (BB) spectrum for minimum thermal radiation loss and thus maximum efficiency of the NC coating.

Specifically, the dielectric function of ITO can be characterized by the free electron gas model:

$$\varepsilon_{ITO}(\omega) = \varepsilon_{\infty} - \frac{\omega_p^2}{\omega^2 + i\omega\gamma} \tag{2.24}$$

where, the plasma frequency $\omega_p = \sqrt{N_d e^2 / \varepsilon_0 m^*}$, the damping frequency $\gamma = e / m^* \mu$ and the mobility $\mu = 22(cm^2 / V\,\text{sec})$, N_d is the doping concentration, e is the free electron charge, ε_0 is the dielectric constant of vacuum, m^* the effective mass $m^* = 0.4m$ where m is the free electrons mass. We fit the only free parameter to experimental results from [56]: $\varepsilon_{\infty} = 4$. From these we observe that the plasma frequency is strongly depended on the doping level. The damping frequency on the other hand is fixed at $131.55meV$. Thus, we end up with the refractive index of ITO for different doping concentration (N_d).

In figure 16.b we plot the refractive index of ITO for various doping concentrations $0.3-4\times10^{20}cm^{-3}$, where we observe that indeed the optical properties are strongly depended on the doping level. Increasing the doping concentration the plasma frequency increases making ITO more reflective at lower wavelengths. The idea is, by tuning the dielectric function and the thickness of ITO, to create spectral windows of transparency and reflectance and achieve the desirable spectral selectivity, i.e. high transparency in the optical and strong reflectance in the infrared. This effort becomes clear in figure 16.c in which we plot the reflectance of a 100nm ITO film on semi-infinite SiO_2 for the doping levels denoted in figure 16.b, along with the reflection from the bare SiO_2. For better physical understanding of the desirable spectral selectivity we also plot the normalized solar spectrum and the normalized black body spectrum at different temperatures. Also, we plot the absorption spectrum of a low index NC on flat Cu substrate with Cu NPs at 800 ^{0}C, which is characterized by 0.92 solar absorption efficiency and 0.26 solar emission efficiency.

Specifically, in figure 16.c we show how to minimize the thermal radiation losses of the NC coating by adjusting the ITO thickness and doping. We observe that by increasing the doping level, the surface becomes more reflective in the IR but at the same time the transparency in the solar spectrum is decreased. The high IR reflectance has a positive contribution to the efficiency; in contrast the lowered solar transmittance has a negative contribution to the efficiency (eq. 2.23). Except of the optical constants the thickness plays a significant role to the optical response of the glass/ITO system. We solve this problem by developing an optimization prosses in which we investigate all the possible optical properties and thickness of ITO in order to maximize the energy conversion efficiency at each concentration ratio.

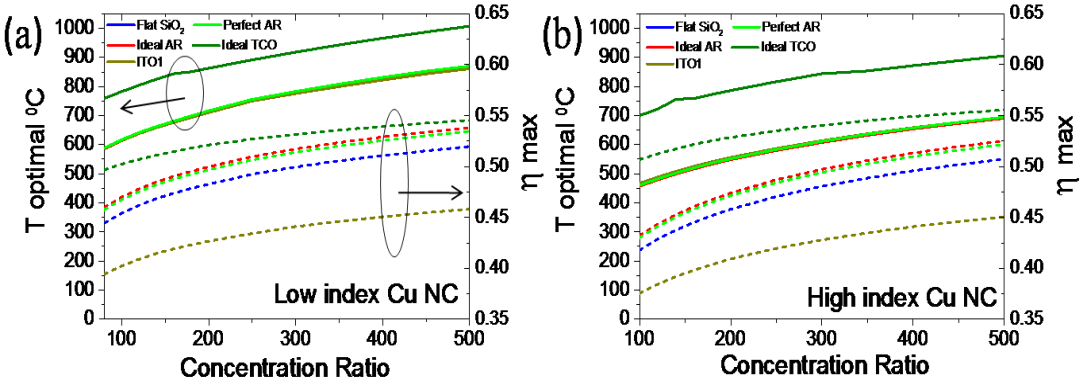

Figure 17. The maximum energy conversion efficiency and the optimal temperature as a function to the concentration ratio for: a) a low index NC with NPs on flat Cu substrate and b) a high index NC with NPs. The thickness of the NC is 1.5 μm and the aspect ratio is 2. For different assumptions of the internal glass envelop interface: 1) a flat SiO_2 interface, 2) an ideal AR coating, practically assuming no glass envelop 3) putting a film of 100nm ITO with doping concentration $0.3\times10^{20}cm^{-3}$ 4) a perfect AR coating putting a non-absorbing dielectric film of 122 nm and $\varepsilon=1.5$ 5) an ideal low absorptive TCO film with optimized dielectric function.

In figure 17 we illustrate our optimization process for a low and high index NC with Cu NPs, the same findings is derived for Ni NPs which for economy are not presented here. We plot the maximum efficiency (dashed lines) and the optimal temperature (solid lines) as a function of concentration ratio for the different cases of the internal glass-air interface treating. We set as reference cases the efficiency of a flat SiO_2 interface as well as the theoretical efficiency of an ideal AR coating, which is obtained by assuming there are no reflections at the glass-air interface. We also plot the typical case of 100nm ITO on SiO_2 with a doping concentration of $0.3\times10^{20}cm^{-3}$ which showes lower efficiency compared to the two first. That's because with the addition of the ITO we decreased the transparency in the solar spectrum, and thus of the overall efficiency.

Trying to explore the spectral selectivity of ITO we start with an optimization for different doping levels ($N_d = 0-10\times10^{20}cm^{-3}$) and thicknesses (0-1.5 μm) keeping constant the typical properties of the dielectric constant at infinity and the damping frequency ($\varepsilon_\infty = 4$ and $\gamma = 131.55meV$). In doing so, we maximize equation 2.23 for each concentration ratio from 80-500 suns at the temperature range of 400-1000 ^{0}C, for each combination of the ITO's refractive index and thickness we calculate its optical response via a transfer matrix method, and get the resulting total maximum efficiency and the optimum temperature. Among all these combinations we find that the maximum efficiency is actually achieved at the absence of ITO, i.e. at the flat SiO_2 interface. As a result, we conclude that ITO cannot provide the desirable spectral selectivity even when we consider a wide range of doping levels and thicknesses.

Not to give up on the idea of the selective IR mirror, we relax the assumption of the dielectric constant at infinity putting in the calculations a wide range ($\varepsilon_\infty = 1-4$), and keeping the same range of doping levels and thicknesses as before. We now find that a new optimum efficiency can now be found for a 122 nm layer with $\varepsilon_\infty = 1.5$ and zero doping concentration. Practically, this is a non-absorbing dielectric layer, which is used as perfect antireflection for light to pass with no losses from glass to air. Actually, this maximum efficiency is identical to the ideal AR and is 3% more efficient compared to the flat SiO_2, for both high index and low index NCs (fig.17). Note also that in all these cases the optimum temperature remains practically the same.

Now, we continue our optimization process relaxing also the absorption of the Drude model by assuming a ten times lower damping frequency ($\gamma = 13.155meV$) and keeping the other parameters at the same range ($\varepsilon_\infty = 1-4$, $N_d = 0-10\times10^{20}cm^{-3}$ and the thickness 0-1500 μm). This could be a generic dielectric function model to a hypothetical low absorptive TCO material. In this case we do manage to achieve a spectral selectivity of the glass/TCO interface and obtain higher efficiencies for both low and high index NCs (fig.17). The doping concentration which provides this

spectral selectivity is independent from the concentration ratio and the optimum temperature and is found to be $N_d = 0.2 \times 10^{20} cm^{-3}$. The other parameters are strongly depended from the concentration ratio and the optimum temperature, the optimal ε_∞ varies between 1.7 and 1.9 while the thickness of the film varriers between 770 nm and 960 nm. Comparing the spectral selective interface efficiencies with the flat SiO_2 interface efficiency we see that we can achieve a gain between 5-11% for low index NCs (fig. 17.a) and 9.5-21% for high index NCs (fig. 17.b) depending on the concentration ratio.

The gain due to the spectral selectivity is greater in low concentration ratios when comparing with the flat SiO_2 interface. That's because the emissivity term in the energy conversion efficiency (eq. 2.23) is divided by the concentration ratio, and so descreasing the thermal emission efficiency is more critical at low concentration ratios. Also, this effect is more dramatic for high index NCs (fig.17b), which are characterized by high thermal emission. Comparing now, the low index NC with high, we observe that at homogeneously transparent interfaces the low index has higher efficiencies (2-6%) due the lower thermal emission. In contrast, at the spectral selective interface of the optimized TCO layer, the high index has slightly higher efficiencies (1-2%).

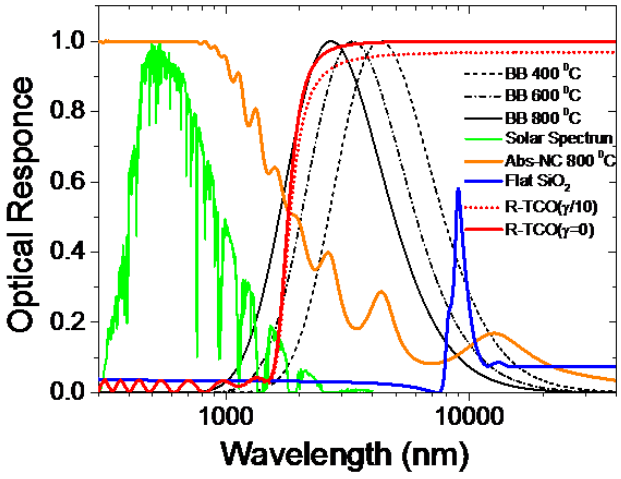

Figure 18. The spectral selectivity of the generic dielectric functions for a low damping frequency and a zero damping frequency.

In figure 18 we plot the reflection of a 866 nm thick dielectric optimized TCO material showing an excellent spectral selectivity. We also plot the unrealistic case of zero damping frequency showing greater reflection yields at IR spectrum. These materials could work to enhance the solar spectrum transparency achieving higher transparency than flat glass, and very high reflections in the IR spectrum. And this spectral selectivity could be adjusted according to the working temperature.

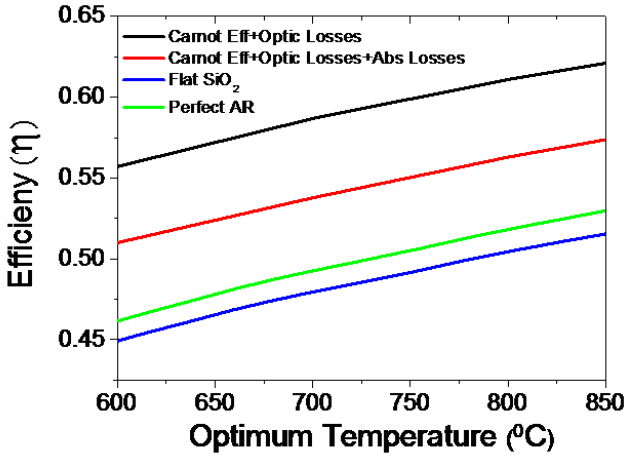

Figure 19. Maximum efficiency as a function of optimum temperature for the different interfaces for a low index Cu NC presented above. The maximum achieved efficiency is compared with the upper theoretical limit of the Carnot efficiency assuming no thermal radiation losses. The Carnot efficiency is presented for two cases; at the first case we assume only the inevitable losses from the mirrors and 100% solar absorption efficiency (black line). At the second case we assume the mirror losses and the actual solar absorption efficiency (red line).

Finally, we make a comparison of the maximum energy conversion efficiency we have achieved to the theoretical upper limit of the Carnot efficiency, assuming only the optical losses while ignoring the thermal emission loses (eq. 2.23). The optical losses are the losses from parabolic trough mirrors ($B_{mirr} = 0.94$) and the solar absorption efficiency loses. In the case of low index NC with NPs (fig.19) the solar absorption loses are ranging from 9% to 7% depending on the temperature. In contrast, in the case of high index NC the solar absorption losses are very small and ranging between 1% to 2%. Comparing this efficiency to our worst case scenario of a perfect antireflection coating, we find that our coating is only 10% less efficient from the maximum possible physically achievable (fig.19) at the specific optimum temperature.

3.4 Conclusions

In this work we designed and evaluated the optical performance of various NC metal-dielectric absorbers, as candidates for solar selective coatings in high temperature applications of parabolic trough collectors. Improving the optical properties of solar selective coatings and increasing the operating temperature above the current limits of 400 ^{0}C can improve the power cycle efficiency, resulting in reductions in the cost of solar electricity.

We explored different transparent dielectric matrixes (low index such as SiO_2 and high index such as SiC) with metallic inclusions (noble metal such as Cu or transition metal such Ni). By successfully modeling the temperature dependence of the optical properties of the metallic inclusions we calculated the effective medium optical properties of the NC coating utilizing an accurate FDTD-based effective medium theory. We extensively studied the optical performance of a low index ceramic matrix with low metallic volume ratio NC, and of a high index ceramic matrix with high metallic volume ratio NC, which are the two "limits" in terms of optical response. We evaluated how each component of the NC (shape of inclusions, surface roughness and thickness) affects its optical response. In doing so, we developed a model to characterize the spectral selectivity of the NC coating and extracted the maximum energy conversion efficiency and the optimum operating temperature. Thus, we examined a wide range of operating temperatures (400 ^{0}C - 1000 ^{0}C) and concentration ratios (80-500 suns).

Firstly, we started by trying to maximize the solar absorption efficiency. Thus, we simulated various kinds of surface texturings for upwards and reverse pyramids. We found that the solar absorption efficiency is maximized with the "upward" quadratic pyramid at a base-to-period ratio equal to one. This was a universal trend for the entire tested NCs and the textured metals (black Ni and black Cu), achieving the highest value of 99.3% for the high index NC. Then, we calculated the energy conversion efficiency, at two operating temperatures (400 ^{0}C and 800 ^{0}C) for a specific concentration ratio ($C = 100$ suns), as a function of NCs' aspect ratio and thickness. At low temperature the efficiency increases for small increments of the aspect ratio, however, further increments to the aspect ratio do not have any significant effects on the efficiency, a trend that is pretty much the same for all the materials. At high temperatures we found that the efficiency of the low index NCs with NPs is almost independent from the aspect ratio, which is in contrast to all the other tested NCs and textured metals, whose efficiency is found to be strongly depended on the aspect ratio. The highest efficiency at high temperatures is achieved by the low index NC with NPs on flat Cu substrate.

Furthermore, we extracted the maximum energy conversion efficiency at the optimum temperature from a wide range of operating temperatures (400 ^{0}C - 1000 ^{0}C) and concentration ratios (80-500 suns). Comparing the maximum efficiency for both "families" of NCs with Cu and Ni NPs, we found that the low index NCs presents higher efficiencies compared to the high index NCs, especially when the film is on a flat Cu substrate. Further comparisons between the two "families" of NCs with respect to the microstructure and Cu substrate don't show significant differences. We found that for our best candidate for a solar selective coating (low index Cu NPs), increasing the operating conditions from the recent limits of 400 ^{0}C and 80 suns concentration to 870 ^{0}C and 500 suns concentration we get an increase in efficiency from 0.405 to 0.52, which means an ~30 % better performance.

Finally, we developed an optimization process to investigate and design the spectral selectivity of the external glass envelop. This optimization was facilitated by exploring the general case of a TCO layer at the internal glass-air interface, whose desired function is to minimize the thermal radiation losses while maximizing the solar absorption efficiency. We found that the maximum efficiency could be increased by utilizing an optimized low-absorbing TCO layer which produces an excellent spectral selectivity of transparency in the solar spectrum and reflectance in the IR. Specifically, in this our work we achieved a gain between 5-11% for low index NCs and 9.5-21% for high index NCs, depending on the concentration ratio.

3.5 References

[1] S.S Mohd, M.K. Khan, M. Pathak, Performance enhancement of solar collectors-A review, Renewable and Sustainable Energy Reviews, 49 (2015) 192-210.

[2] D. Barlev, R. Vidu, P. Stroeve, Innovation in concentrated solar power, Solar Energy Materials and Solar Cells, 95 (2011) 2703-2725.

[3] A. Fernandez-Garcıa, E. Zarza, L. Valenzuela, M. Perez, Parabolic-trough solar collectors and their applications, Renewable and Sustainable Energy Reviews, 14 (2010) 1695-1721.

[4] D. Mills, Advanced in solar thermal electricity technology, Solar Energy, 76 (2004) 19-31.

[5] S. A. Kalogirou, Solar thermal collectors and applications, Progress in Energy and Combustion Science, 30 (2004) 231-295.

[6] C. M. Lampert, Coatings for enhanced photothermal energy collection, I. Selective absorbers, Solar Energy Materials1, (1979) 319-341.

[7] N. Selvakumar, H. C. Barshilia, Review of physical vapor deposited (PVD) spectrally selective coatings for mid- and high- temperature solar thermal applications. Solar Energy Materials and Solar Cells, 98 (2012) 1-23.

[8] C.E. Kennedy, Review of mid to high temperature solar selective absorber materials , NREL report July 2002, NREL / TP-520-31267

[9] C. G. Granqvist, Solar Energy Materials, Advanced Materials, 15 21 (2003) 1789-1803.

[10] C. Atkinson, C. L. Sansom, H. J. Almond, C. P. Shaw, Coatings for concentrating solar systems-A review, Renewable and Sustainable Energy Reviews, 45 (2015) 113-122.

[11] Z. C. Orel, M. K. Gunde, Spectrally selective paint coatings: Preparation and characterization, Solar Energy Materials and Solar Cells, 68 (2001), 337-353.

[12] B. Seraphin, Chemical vapor deposition of thin semiconductor films for solar energy conversion, Thin Solid Films, 39 (1976) 87-94.

[13] J. Moon, D. Lu, B. VanSaders, T. K. Kim, S. D. Kong, S. Jin, R. Chen, Z. Liou, High performance multi-scaled nanostructured spectrally selective coating for concentrating solar power, Nano Energy, 8 (2014) 238-246.

[14] J. H. Schon, G. Binder, E. Bucher, Performance and stability of some new high temperature selective absorber systems based on metal/dielectric multilayer, Solar Energy Materials and Solar Cells, 33 (1994), 403-416.

[15] J. A. Thornton, J. I. Lamb, Thermal stability studies of sputter deposited multi - layer selective absorber coatings, Thin Solid Films, 9 (1982) 175-183.

[16] A. Andersson, O. Hunderi, C. G. Granqvist, Nickel pigmented anodic aluminum oxide for selective absorption of solar energy, J. Appl. Phys, 51 (1980) 754-764.

[17] V. Teixeira, E. Sousa, M. F. Costa, C. Nunes, L. Rosa, M. J. Carvalho, M. Collares-Pereira, E. Roman, J. Gago, Spectrally selective composite coatings of Cr-Cr_2O_3 and Mo-Al_2O_3 for solar energy applications, Thin Solid Films, 392 (2001) 320-326.

[18] E. Sani, L. Mercatelli, P. Sansini, L. Silvestroni, D. Sciti, Spectrally selective ultra-high temperature ceramic absorbers for high-temperature solar plants, J. Renewable Sustainable Energy, 4 (2012) 033104 (14).

[19] Q. C. Zhang, Recent progress in high-temperature solar selective coatings, Solar Energy Materials and Solar Cells, 62 (2000) 63-74.

[20] L. Zhenga, F. Gao, S. Zhao, F. Zhou, J. Pierre Nshimiyimana, X. Diao, Optical design and co-sputtering preparation of high performance Mo-SiO_2 cermet solar selective absorbing coating, Appl. Surf. Sci., 280(2013)240–246.

[21] H. Zoubos, L. E. Koutsokeras, D. F. Anagnostopoulos, E. Lidorikis, S. A. Kalogirou, A. R. Wildes, P. C. Kelires, P. Patsalas, Broadband optical absorption of amorphous carbon/Ag nanocomposite films and its potential for solar harvesting applications, Solar Energy Materials and Solar Cells,117 (2013) 350-356.

[22] F. Cao , D. Kraemer , T. Sun , Y. Lan , G. Chen, Z. Ren, Enchanced thermal stability of W-Ni-Al_2O_3 cermet-based spectrally selective solar absorbers with tungsten infrared reflectors, Adv. Energy Mater. (2014) 1401042 (1-7).

[23] L. C. Botten, I. T. Ritche, Improvements in the design of solar selective thin film absorbers, Optics Communications, 22-3 (1977) 421-426.

[24] G. L Harding, M. R. Lake, Sputter etched metal solar selective absorbing surfaces for high temperature thermal collectors, Solar Energy Materials, 5 (1981) 445-464.

[25] G. Pellegrini, Experimental methods for the preparation of selectively absorbing textured surfaces for photothermal solar conversion, Solar Energy Materials, 3 (1980) 391-404.

[26] P. Konttinen, P. D. Lund, R. J. Kilpi, Mechanically manufactured selective solar absorber surfaces, Solar Energy Materials and Solar Cells, 79 (2003) 273-283.

[27] D. Chester, P. Bermel, J. D. Joannopoulos, M. Soljacic, I. Celonovic, Design and global optimization of high-efficiency solar thermal systems with tungsten cermets, Optics Express, Vol.19, No.S3, (2011), A245-A257.

[28] A. Sakurai, H. Tanikawa, M. Yamada, Computational design for a wide-angle cermet-based solar selective absorber for high temperature applications, Journal of Quantitative Spectroscopy and Radiative Transfer, 132 (2014) 80-89.

[29] Q. C. Zhang, Optimizing analysis of W-AlN cermet solar absorbing coatings, J. Phys. D: Appl. Phys, 34 (2001) 3113-3120.

[30] M. R. Nejati, V. Fathollahi, M. Khalaji Asadi, Computer simulation of the optical properties of high-temperature cermet solar selective coatings, Solar Energy, 78 (2005) 235-241.

[31] M. Farooq, M. G. Hutchins, A novel design in composities of various materials for solar selective coatings, Solar Energy Materials and Solar Cells, 71 (2002) 523-535.

[32] F. Cao, K. McEnaney, G. Chen, Z. Ren, A review of cermet-based spectrally selective solar absorber, Energy Environ. Sci., (2014) 7, 1615-1627.

[33] C. E. Kennedy, H. Price, Progress in development of high-temperature solar selective coating, Proceedings of International Solar Energy Conference (ISEC 2005).

[34] A. Hall, A. Ambrosini, C. Ho, Solar Selective Coatings for Concentrating, Advanced Materials and Processes, Vol. 170 Is. 1 (2012) 28-32.

[35] C. Steven, M. Arun, Opportunities and challenges for a sustainable energy future, Nature, Vol. 488, Is. 7411 (2012) 294-303.

[36] E. A. Fletcher, Solarthermal processing: A review, 2001 Journal of Solar Energy Engineering ASME, Vol. 123, Issue 2,(2011), 63-74.

[37] J. D. Jackson, Classical Electrodynamics, New York: Wiley, (1999)

[38] E. Lidorikis, S. Egusa, J. D Joannopoulos, Effective medium properties and photonic crysal superstructures of metallic nanoparticle arrays, Journal of Applied Physics, (2007) 101, 054304 (1-7).

[39] A. Taflove, S. C. Hagness, Computational Electrodynamics: The Finite-Difference Time-Domain Method (3rd Edition), Boston, MA: Artech House (2005).

[40] E. D. Palik, Handbook of Optical Constants of Solids (Academic, San Diego, 1998).

[41] H. J Hagemann, W.Gudat, C.Kunz, Optical constants from the far infrared to the x-ray region: Mg, Al, Cu, Ag, Au and Al_2O_3, Journal of the Optical Society of America, Vol. 65 No. 6 (1975) 742-744.

[42] F. J Gonzales, J. Alba, J.Simon, J.Ginn, G. Boreman, The effect of metal dispersion on the resonance of antennas at infrared frequencies, Infrared Physics and Technology 52, (2009), 48-51.

[43] M. A. Ordal, R. J. Bell, R.W. Alexander, Jr.L.L. Long, M.R. Querry, Optical Properties of fourteen metals in the infrared: Al, Co, Cu, Au, Fe, Pb, Mo, Ni, Pd, Pt, Ag, Ti, V and W, Applied Optics, Vol 24, No 24 (1985), 4493 -4499.

[44] K. Ujihara, Reflectivity of metals at High Temperatures, Journal of Applied Physics, 43, (1972), 2376 – 2383.

[45] I. Celanovic, D. Perreault, J. Kassakian, Resonant-cavity enhanced thermal emission, Physical Review B, 72, (2007), 075127-1 - 075127-6.

[46] C. Y. Ho, M. W. Ackerman, K. Y. Wu, T.N. Havill, R.H. Bogaard, R. A. Matula, S.G. Oh, H. M. James, Electrical Resistivity of Ten Binary Alloy Systems, J. Phys. Chem. Ref. Data, Vol.12, No.2, (1983), 183-322.

[47] N.W. Ashcroft, N.D. Mermin, Solid State Physics, Holt, Rinehart and Winston, New York, 1976, p.8.

[48] F. Schedin, E. Lidorikis, A. Lombardo, V.G. Kravets, A. K. Geim, A.N. Grigorenko, K.S. Novoselof, A.C. Ferrari, Surface-Enhanced Raman Spectroscopy of Graphene, ACS Nano, Vol.4 No.10, (2010), 5617-5626.

[49] G. A. Niklasson, C. G. Granqvist, and O. Hunderi, Effective medium models of inhomogeneous materials, Applied Optics, Vol. 20, No.1, (1981), 26-30.

[50] P. U. Jepsen, Metal-insulator phase transition in a VO_2 thin film observed with terahertz spectroscopy, Phys. Rev. B, 74, (2006), 205103-1 – 205103-9.

[51] A. Rabl, Comparison of solar concentrators. Solar Energ, (1975) Vol. 18, pp. 93-111.

[52] I. H. Malitson. Interspecimen Comparison of the Refractive Index of Fused Silica, J. Opt. Soc. Am., (1965) 55, 1205-1208.

[53] J. Kischkat, S. Peters, B. Gruska, M. Semtsiv, M. Chashnikova, M. Klinkmüller, O. Fedosenko, S. Machulik, A. Aleksandrova, G. Monastyrskyi, Y. Flores, W. T. Masselink. Mid-infrared optical properties of thin films of aluminum oxide, titanium dioxide, silicon dioxide, aluminum nitride, and silicon nitride, Appl. Opt. (2012) 51, 6789-6798.

[54] C. G. Granqvist, Transparent conductors as solar energy materials: A panoramic review, Solar Energy Materials Solar Cells, 91 (2007) 1529-1598.

[55] A. Gondorf, M. Geller, J. Weißbon, A. Lorke, Mobility and carrier density in nanoporous indium tin oxide films, Physical Review B, (2011) 83 212201.

[56] J. Ederth, P. Johnsson, G. A. Niklasson, A. Hoel, A. Hultaker, P. Heszler, C. G. Graqvist, A. R. van Doorn, M. J. Jongerius, D.Burgard, Electrical and optical properties of thin films consisting of tin-doped indium oxide nanoparticles, Phys. Rev. B, (2003) 68, 155410.

Chapter 4 Shape effects of Ag plasmonic nanoparticles on a substrate in relation to enhanced spectroscopy applications

Abstract

Metallic nanoparticles are of great interest for a number of technological and biomedical applications. They exhibit strong absorption and field enhancement at their Localized Surface Plasmon Resonance (LSPR) frequency, leading to important applications in enhanced spectroscopy, enhanced fluorescence, chemical and biological sensing and catalysis. Nanoparticle arrays on a substrate can be developed by either top-down (e.g. nanolithography) or bottom-up (e.g. self assembly by thermal or laser annealing of a thin metal film) processes, each case resulting into different particle shapes, sizes and arrangements. Here we examine theoretically how the LSPR traits (enhanced fields, scattering, etc) are modulated depending on the different final shape configurations. We present detailed spectral field enhancement analysis showing that depending on its shape, the frequency at which maximum field enhancement occurs varies depending on which location on the nanoparticle's surface we are probing, pointing towards modulated SPR oscillations across the nanoparticle volume. This effect stems from the different nanoparticle-substrate and nanoparticle-environment interactions. Furthermore, and in relevance to enhanced spectroscopy applications, we examine the effect of thin dielectric coatings (AlN) on the nanoparticles. The response is again found to be dependent on the nanoparticle shape, with the theoretical results comparing well to recent experiments.

4.1 Introduction

The mirror-like quality of smooth noble metal films changes markedly when the metal is separated into particles that are much smaller than the wavelength of the light [1, 2]. Light incident on the nanoparticles (NPs) induces their conduction electrons to oscillate collectively, with the oscillation maximized at a specific resonant frequency; this optical phenomenon is known as Localized Surface Plasmon Resonance (LSPR). This strong light/electron coupling forces the confinement of light into small volumes, resulting into extreme local fields, light scattering and absorption [3, 4], with the LSPR frequency strongly depended from the NPs' size, shape, composition and the refractive index of the employed dielectric environment [5-10]. Specifically, the NPs absorb and scatter light so intensely that single NP are easily observed by eye using dark-field (optical scattering) microscopy as a result of LSPR modes [3,4,11]. For example, a single 80 nm silver NP scatters 445 nm blue light with

a scattering cross section of $3\times10^{-2}\,\mu m^2$, a million-fold greater than the fluorescence cross section of a fluorescein molecule, and a thousand-fold greater than the cross section of a similarly sized nanosphere filled with fluorescein [11]. This phenomenon enables noble metal NPs to serve as extremely intense labels for immunoassays [11-13], biological sensors [2, 14 -19] and surface enhanced spectroscopies [20-26].

In the Raman effect, incident light is inelastically scattered from a molecular sample, with the scattered radiation shifted in frequency by an amount equal to the energy of the characteristic molecular vibrations. Since its discovery in 1927, the effect has attracted attention from a basic research point of view as well as a powerful spectroscopic technique with many practical applications. Specifically, Raman scattering is a spectroscopic technique of great utility for identifying molecular species because the signature of re-emitted Raman photons is unique to each molecular species and corresponds to the particular set of its vibrational modes. Unfortunately, only about one in every 10^{12} photons incident on a molecule undergoes Raman scattering, making this technique, while powerful as a diagnosis technique, applicable only in situations where large numbers of molecules are present. Forty years ago it was discovered that Raman signals could be enhanced enormously by placing molecules close to a textured metal surface, raising the prospect of immediate broad applications. This phenomenon is known as Surface Enhanced Raman Scattering (SERS) [27].

SERS is a fascinating process by which the typically weak Raman signal can be amplified by many orders of magnitude [20-25]. This impressive enhancement is mainly caused by the enhanced, light-induced electric fields (E-fields) on the surface of a metallic NP due to LSPR phenomenon [2, 28]. The LSPR is responsible for the strong scattering and absorption of light from a metallic NP, it is also responsible for generating enhanced local E-fields on the surface of a NP, at sites known as "hot spots". Molecules within these hot spots experience an enormous enhancement in the local photon density of states, and thus a corresponding enhancement in terms of their Raman scattering cross section. This enhancement can be so strong, so that single molecule detection is possible [23, 25]. This superb sensitivity has been a catalyst for the resurgence of SERS studies in recent years. These studies have focused on understanding the mechanisms of SERS and, equally, how to implement this technique as a reliable method for trace detection [29, 30]. Both thrusts have resulted in evolution of SERS experiments to studies characterized by a high level of scrutiny and control at the nanometer level [31-33]. In this way, controlling LSPR properties is a key to optimizing SERS, as plasmon resonances are responsible of generating the strong local E-fields necessary for SERS, and in terms of controlling the LSPR, shape engineering of NPs has provident an efficient handle [34].

Plasmonic templates for SERS applications composed of metallic NPs arrays on a substrate can be developed by either top-down (e.g. nanolithography [35]) or bottom-up (e.g. self-assembly by laser [36-39] or thermal [40] annealing of a thin metal film) processes, each case resulting into different particle shapes, sizes and

arrangements. In this work we explore theoretically how the LSPR traits (electric field enhancement, scattering etc) are modulated depending on the different final configuration. Thus, we examine two "extreme" shapes: nano-columns, as a representative NPs' shape of top-down methods and nano-hemispheres, as a representative NPs' shape of bottom-up methods on a Si substrate.

We produce detailed electrics field enchantment maps showing that, depending on their shape, the frequency at which maximum field enhancement occurs varies at different locations on the NP's surface, pointing towards differently modulated LSPR oscillations across the NP's volume. Furthermore, and in relevance to enhanced spectroscopy applications, we examine the effect of thin dielectric coatings (AlN) on the nanoparticles. The response is again found to be dependent on the NP's shape, with our results comparing well to recent experiments.

4.2 Theoretical Approach

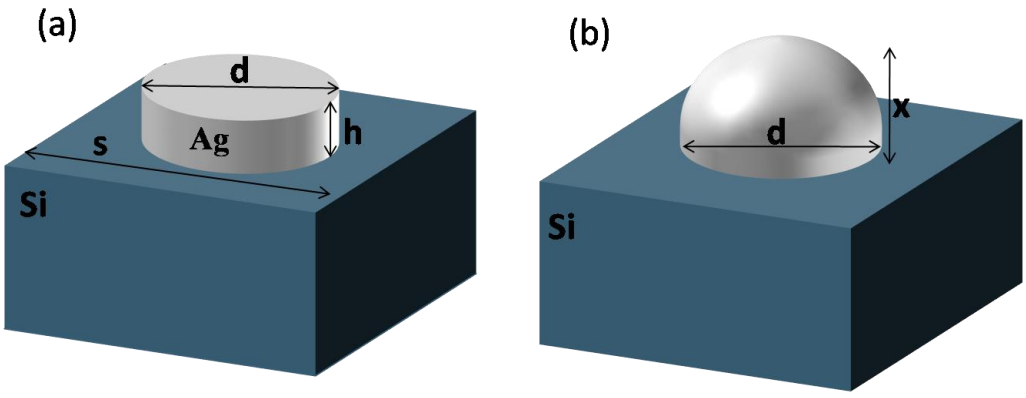

Figure 1. Schematic illustration of the two studied representative NPs: a) nano-columns and b) spherical nano-domes. The two shapes are evaluated under same volume and cross section conditions.

We explore theoretically how the LSPR traits (enhanced E-fields and scattering) of Ag NPs on a Si substrate are modulated depending on their shape. It has been proven that micro-wave thermal annealing of a thin Ag film on a Si substrate results into hemispherical Ag NPs on the substrate, with application on SERS [40]. On the other hand, well defined nano-columns are only expected to be formed within a lithographic process. However, it is expected that different types of bottom-up methods, e.g. like different types of thermal annealing such as the slow thermal produced by a hot plate, could produce intermediate shapes. Thus, and as we mentioned above, we will examine here two shape "extremes", nano-spherical domes (portions of a sphere cut-off by a plane) as a representative shape of bottom-up methods and nano-columns, as a representative shape of top-down methods (fig.1). Assuming no metal loses during thermal annealing, we evaluate the periodic

arrangement (square lattice symmetry) of two different shapes with the same particle volume:

$$V_{col} = V_{hem} = ts^2 \tag{3.1}$$

where V_{col} and V_{hem} is the volume of columns and hemi-spheres respectively, t is the initial nominal thickness of the Ag thin film (which is initially covering the whole area and is afterwards reshaped into the nanoparticle) and s is the periodicity, as shown in fig. 1.

The LSPR traits is very sensitive to the size, shape and surface coverage [6, 10]. In order to extract only the shape effects and avoid other complications coming from different proximities or different volumes between nanoparticles etc, we evaluate the two kinds of NPs under the same volume and the same cross section for the same surface coverage. The surface coverage (f) is the ratio of NPs cross section to the periodic cell area:

$$f = \frac{\pi d^2}{4s^2} \tag{3.2}$$

where d is the diameter of the NPs, which we assume to be the same for the two shapes (fig. 1). Regarding their arrangement, we assume that after threatment the two kinds of NPs could be either arranged at a large periodicity, i.e. far from each other, with a small surface coverage of $f_1 = 44\%$, or close each other, with a big surface coverage of $f_2 = 67\%$. From the surface coverage in eq. 3.2 and the nominal thickness in Eq. 3.1 we can extract the height h of the nano-column $h = t / f$. Regarding the spherical domes, we need to calculate the radius (r) the hypothetical sphere and the specific position x (starting from the top), at which if we cut the sphere we get a spherical dome with the same cross section and volume as the nano-column (fig.1). Applying simple geometry we find that the radius of the position depended "cut-sphere" in order to have the same cross section with the nano-column will be:

$$r(x) = \frac{d^2 + 4x^2}{8x} \tag{3.3}$$

Integrating the x depended cross sections of the "cut-sphere" in order to have the same volume of the nano-column we result at the second equation:

$$r(x) = \frac{3d^2h + 4x^3}{12x^2} \tag{3.4}$$

Solving the two above equations we can find the radius r and the position x of the "cut-sphere": the equation for the cut x is $x^3 + 3d^2x - 6d^2h = 0$, with solution

$x = \sqrt[3]{3d^2h + \sqrt{9d^4h^2 + d^6}} + \sqrt[3]{3d^2h - \sqrt{9d^4h^2 + d^6}}$. When substituted in eq. 3.3 we also get the sphere radius.

We examine three different volumes for both shapes at the two aforementioned surfaces' coverage. Specifically, we suppose three volumes for the nano-columns: a large one ($d_1 = 48nm$, $h_1 = 16nm$), a middle one ($d_2 = 24nm$, $h_2 = 8nm$) and a small one ($d_3 = 12nm$, $h_3 = 4nm$). Each case corresponds also to nano-domes with dimensions: ($d_1 = 48nm$, $x_1 = 24nm$) for the large one, ($d_2 = 24nm$, $x_2 = 12nm$) for the middle one and ($d_3 = 12nm$, $x_3 = 6nm$) for the small one.

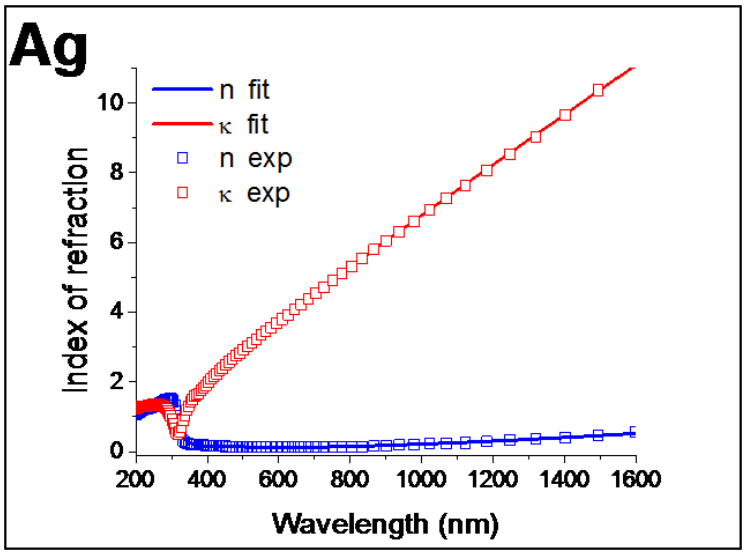

Figure 2. The experimental bulk refractive index of silver taken from ref. 41 (open squares) and the performed Drude-Lorentz fit (solid lines).

In order to have the actual optical properties of the Ag NPs we use the experimental bulk metallic optical properties of Ag [41], and then we apply a Drude-Lorentz fit to the bulk dielectric function. In figure 2 we plot experimental and fitted values showing an excellent agreement. In order to have the appropriate dielectric constant for the NP we make the correction involving the surface scattering contribution to the free electron relaxation time, as it was discussed in section 3.2.1. Here, we apply the same correction for both shapes, assuming the effective radius of a sphere having the same volume as the two NPs. For the Si substrate we start for simplicity by assuming no absorption, utilizing the real part of the dielectric function of Si in the infrared spectrum ($n = 3.4$), which we assume as constant for the whole calculated spectrum (300-1300nm). We assume this simplified non-absorbing Si in order to clearly elucidate the resonant LSPR traits of the two different NPs shapes without any extra complications arising from the substrate's dispersion (i.e. different optical constant at different frequencies).

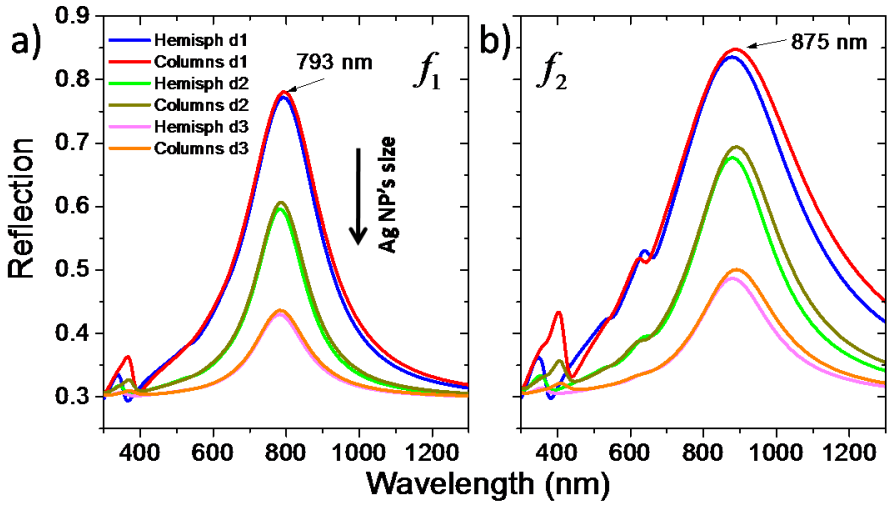

Figure 3. The reflection spectrum for the two studied shapes (nano-domes and nano-columns) for three sizes (d_1 , d_2 , d_3) of Ag NPs at two surface coverages: a) $f_1 = 44\%$ and b) $f_2 = 67\%$.

In figure 3 we plot the reflection spectrum of the nano-domes and nano-columns on the Si substrate, at the aforementioned sizes and surface coverages. We observe that the two different shapes have similar optical response for the same size and surface coverage. The main intense LSPR wavelength is noticed at 793 nm at low surface coverage (fig.3.a), and is red shifted when the NPs come closer at the high volume ratio, specifically to 875 nm (fig.3.b), due to the stronger hybridization between the plasmons. Furthermore, we notice that the spectral position of the LSPR wavelength is not significantly affected when we decrease the NP's size, but the intensity of the reflection is decreased due to lower metal's volume ratio. This trend is similar for both surface coverages. The higher-order resonances, most visible for high volume ratio, at the wavelengths ~630 nm and 340-400 nm (fig.3.b), will be in detail presented and identified below.

We move now to electric field (E) enhancement calculations for these NPs. In these calculations we choose to present the big NPs (d_1, t_1) because the light-induced E-enhancement at the resonant LSPR wavelengths is more intense compared to the smaller sizes. However, similar results and conclusions were extracted for the other sizes. Understanding the E-enhancement spatial distribution around the NP's volume is of high importance because it plays the dominant role at SERS applications as we mentioned before.

In the frame of a classical SERS approach we assume that the presence of nanoparticles affects only the local photon density of states, and through this the absorption and emission rates of nearby molecules, as inferred by Fermi's golden rule. Thus, the absorption (A) of a chemical molecule which is adsorbed on the NP's surface is proportional to the square of the modulus of electric field $A \sim |E|^2$ [3, 42].

We calculate the enhanced absorption ($\varepsilon_A^{0d}(\mathbf{r},\omega)$) at each point ($\mathbf{r}$) around the NP's volume at each frequency ω :

$$\varepsilon_A^{0d}(\mathbf{r},\omega)=\frac{|E(\mathbf{r},\omega)|^2}{|E_0|^2} \tag{3.5}$$

where $E(\mathbf{r},\omega)$ is the electric in that point and E_0 is the electric field associated with the incident plane wave. The enhanced Raman scattering ($\varepsilon_R^{0d}(\mathbf{r},\omega)$) is proportional to the product of the absorption rate and of the emission rate at a Stokes-shifted lower frequency ($\omega-\Delta\omega$), due to the energy losses incurred by the excitation of a vibrational mode (Stokes scattering) [3, 43]. Thus, the enhancement to the Raman scattering signal is proportional to the fourth power of the modulus of the electric field $\mathrm{R}\sim|E|^4$:

$$\varepsilon_R^{0d}(\mathbf{r},\omega)=\frac{|E(\mathbf{r},\omega)|^2\,|E(\mathbf{r},\omega-\Delta\omega)|^2}{|E_0|^4} \tag{3.6}$$

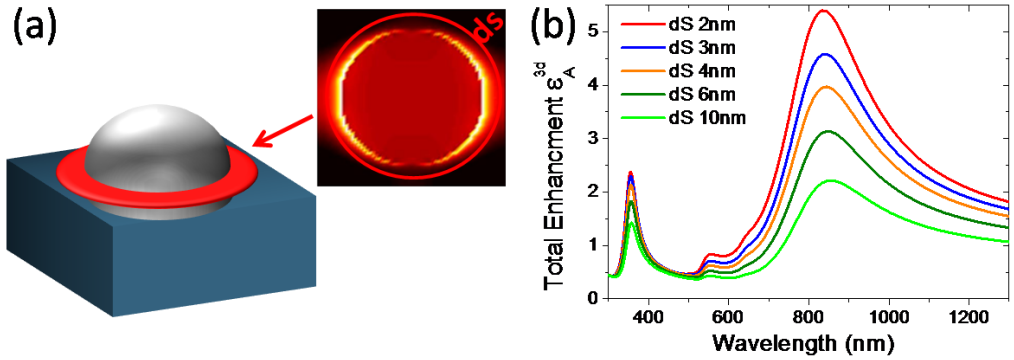

Figure 4. a) Schematic illustration of the electric field enhancement calculations on a specified ring of finite width around the NP's volume. The inset shows the electric field enhancement spatial distribution at the resonance wavelength. b) The total enhancement is calculated integrating all the ring enhancements from the bottom of the NP up to the top, for different ring widths (2-10nm), resulting into the volume enhancement in a shell surounding the NP.

In a practical case, adsorbed molecules can form thin coatings around the NP. To get the cumulative effect of all molecules, we first calculate the E-enhancement on the absorption in a specific ring area (S') around the NP, integrating all the point E-enhancements in this area (fig. 4.a):

$$\varepsilon_A^{2d}(z,\omega)=\int_{S'}\varepsilon_A^{0d}(\mathbf{r},\omega)dS \tag{3.7}$$

Furthermore, the total enhancement in a shell volume around the NP is calculated integrating all the ring enhancements from the bottom of the NP up to the top:

$$\varepsilon_A^{3d}(\omega) = \int \varepsilon_A^{2d}(z,\omega)dz \tag{3.8}$$

In the same way we calculate the enhancement of the Raman scattering, by substituting equation 3.6 instead of 3.5 into the two last equations. In figure 4.b we plot the total enhancement for different integrating widths (2-10 nm) around the nano-dome NP. We observe that increasing the integrating width the total enhancement is decreased, because the local fields are strong only close to the NP's surface and they diminish away as r^{-3} from the surface. This is depicted well in the inset of figure 4.a, where we plot the E-enhancement spatial distribution at the LSPR wavelength, showing the enhanced E-fields close to the NPs surface. From now on, we choose an integration width of 2 nm as the appropriate thickness of a typical molecular layer adsorbed on the nanoparticle surface, to perform our analysis for SERS applications.

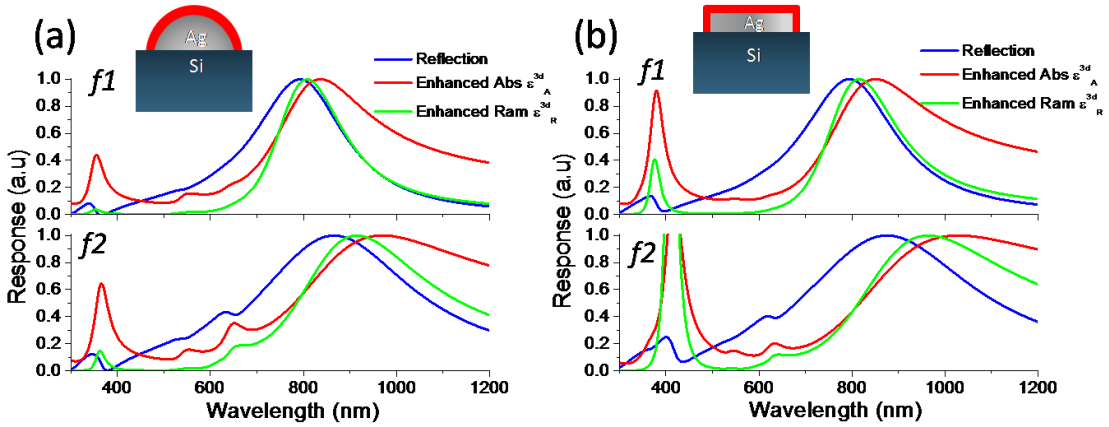

Figure 5. The normalized Reflection, Absorption and Raman response for the two studied shapes on a Si substrate: a) nano-domes and b) nano-columns, for two surface coverages f_1=44% and f_2=67%. The total absorption and Raman enhancements are calculated integrating within a 2 nm shell around the NPs as it is depicted with the red colored cross sectional area in the two insets.

In figure 5 we present combined graphs of the reflection and of the normalized total enhancements of the absorption and Raman scattering, for the two shapes and surface coverage. We observe that the spectral position of the peak Raman scattering is shifted from the peak of enhanced absorption, due to the Raman emission occurring at a different frequency. Also the enhanced absorption peak is shifted compared to the reflection peak: this is because the E-fields maximize at a different frequency (red-shifted) than where the NP's absorption maximizes, is the latter having a similar spectral response as the reflectance. The same trend is observed for both shapes and is more intense at the higher surface coverage due to the higher hybridization of the Plasmon modes. The higher-order resonances also appeare, for the high surface

coverage are very intense, are spectral positioned at the wavelengths ~630 nm and 340-410 nm, and will be in detail presented and identified in the next graph.

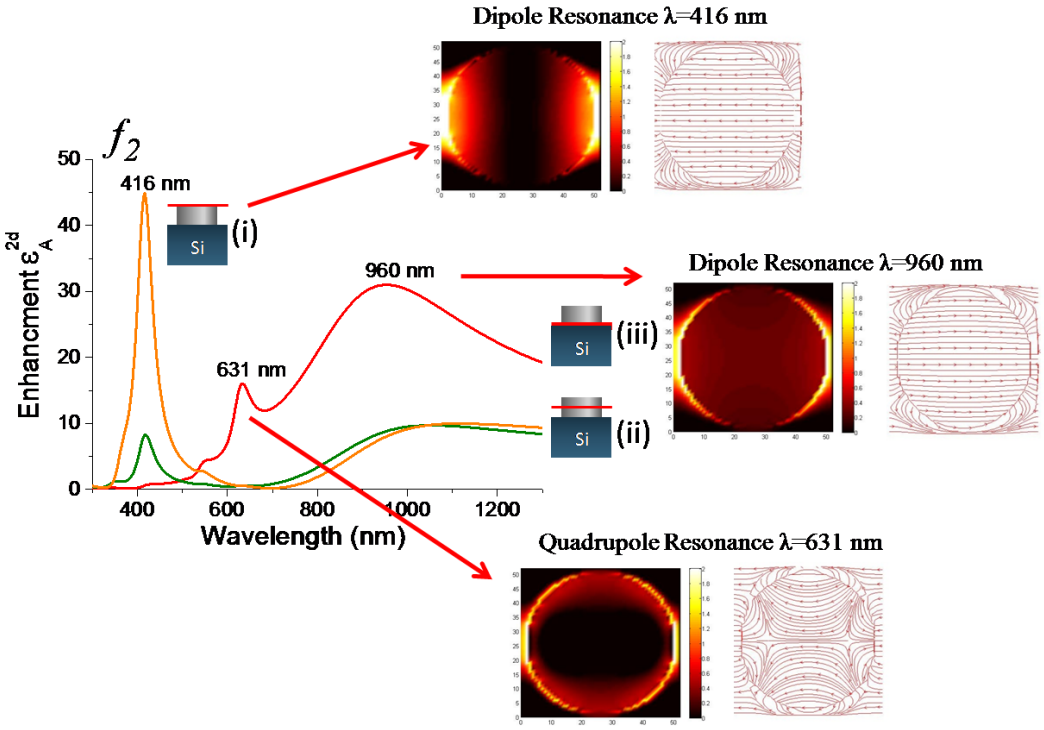

Figure 6. The planar spectral absorption enhancement integrated within a 2 nm distance from the NP's surface at different positions on the nano-column, as depicted in the insets: (i) at the top of the NP (orange line), (ii) at the middle of the NP (green line) and (iii) at the bottom of the NP (red line). The red arrows show the E-field enhancement and field line spatial distribution, plotted at the specified resonant wavelengths at the top and the bottom of the NP.

To get a better view of these resonances, we plot the planar absorption spectral enhancement ($\varepsilon_A^{2d}(z,\omega)$) at different positions (z) on the NP (figure 6), at the top (i), at the middle (ii) and at the bottom (iii) of the nano-column. For the top plane (orange line) we observe an intense resonance at 416 nm: it has the same spectral position moving down to the middle of the NP (green line) but at much lower intensity and it disappeares at the bottom of the NP (red line). This is a dipole resonance, as it is depicted to the E-field's enhancement and electric field lines spatial distribution, and it is related to the NP's free electrons oscillations in the dielectric environment of air. For the bottom plane (red line) we observe two resonances, one at 960 nm and the other at 631 nm. The first one at 960 nm is a dipole resonance, as it is depicted by the E-field's enhancement and field lines spatial distribution, it becomes less intense moving to the top of the NP, and is related to the NP's free electron oscillations screened mostly by the substrate. The final resonance at 631 nm is a quadrupole resonance as depicted by the E-field's enhancement and especially by the field line spatial distribution, it is intense close to the substrate, is related to the NP's free electron oscillations screened mostly by the substrate and it appears only at the bigger surface coverage ($f_2 = 67\%$) where the Plasmon hybridization is stronger.

From the above discussion it is clear that we have two main LSPRs across the NP, one that is related to the NP's interaction with air (air-LSPR) and one that is related to the NP's interaction with the Si substrate (Si-LSPR). In terms of SERS applications, we are interested in the maximum enhancement spatial distribution across the NP's surface. In doing so, we extract the maximum enhancement (ε_A^{0d}) from a ring area with 2 nm thickness around the NP, and plot it from the bottom up to the top of the nanoparticle (figure 7.a). To get insight, we present these calculations starting from the maximum E-field enhancement of free standing NPs in air (fig. 7), and elucidate the different physical enhancement mechanisms at each NP. Then we continue with the enhancement calculations of our NPs (nono-columns and nano-domes) on Si substrate (fig. 8). In the latter case we extract the maximum E-field's enhancement spatial distribution separately for the two different LSPRs, mapping the different spatial evolution of the two resonances from the top of the NP down to the bottom. The enhancement calculations are presented for the lower surface coverage ($f_1 = 44\%$) in order to avoid the complexity of the higher order resonances.

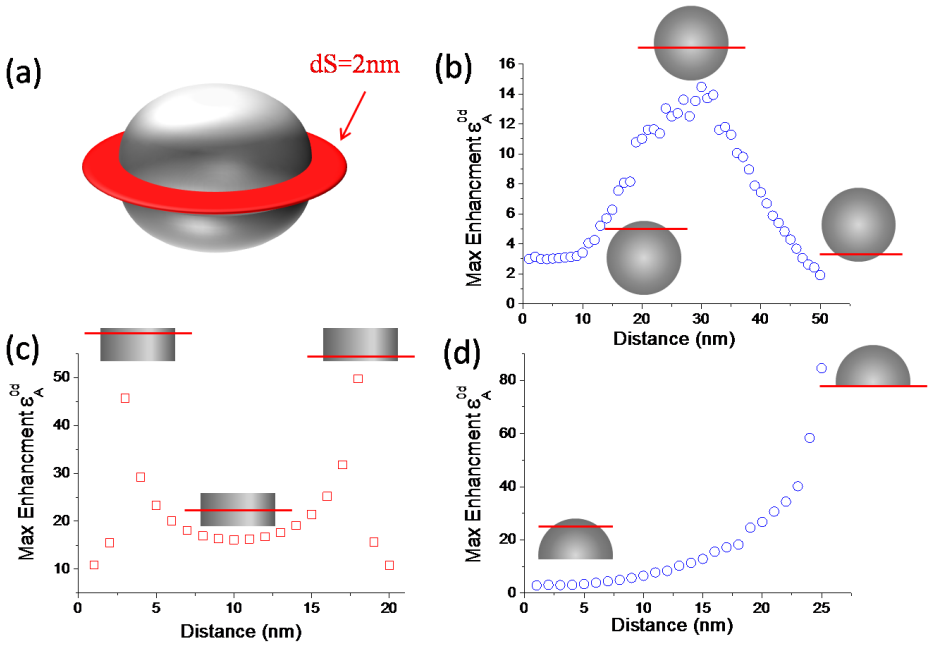

Figure 7. a) A schematic illustrating the calculation for the maximum absorption enhancement in a 2 nm wide ring area around the NP. The NPs are illuminated from the top. At each point between the top and the bottom of free standing NPs in air, the maximum absorption enhancement is plotted for: b) spheres, c) nano-columns and d) nano-domes. The insets depict the various spatial positions at each case. The NPs are evaluated under the same cross section.

We extract the maximum absorption enhancement in a 2 nm-width ring area around the NP, starting from the top of the NP down to the bottom, while it is free-standing in air. In the case of a free-standing sphere in air (fig. 7.b) the enhancement is maximized at the middle of the NP and diminishes away from the middle. That's because at the middle of the NP the E-field is perpendicular to the NP's surface and this satisfy the continuity of the perpendicular component of the displacement vector [3]. Specifically, the perpendicular component of the displacement vector at the air-

particle interface must be continues, $D_1^{\perp} = D_2^{\perp}$, where $D_1^{\perp}$ is the displacement vector component in air and $D_2^{\perp}$ is the displacement vector component in the metallic NP. The dielectric displacement is proportional to the electric field and the dielectric function, $\varepsilon_1 E_1^{\perp} = \varepsilon_2 E_2^{\perp}$, the dielectric function of the metal is much bigger from the air ($\varepsilon_1 << \varepsilon_2$), allowing for large E-fields out of the metal ($E_1^{\perp} >> E_2^{\perp}$).

In the case of the nano-columns the above condition is geometrically satisfied at all of the NP's positions, but we do not observe a maximum enhancement spatial evolution (fig. 7.c) similar to that of the sphere. The enhancement factors are much larger at the edges of the nano-column compared to the middle of the sphere, and we obtain comparable values only at the middle of the nano-column. The enhancement is maximized at the edges of the nano-column because of the contribution of a second enhancement mechanism, the lighting rob effect. The lighting rob effect is a purely geometric phenomenon in which the E-field lines get crowded near to sharp metallic features with accompanying E-field enhancement in those "hot-spots" [3,44]. The cooperation of the two enhancement mechanisms is also clearly observed in the last case of a free standing nano-dome, in which case we obtain the highest enhancement at the edges of the NP (figure 7. b).

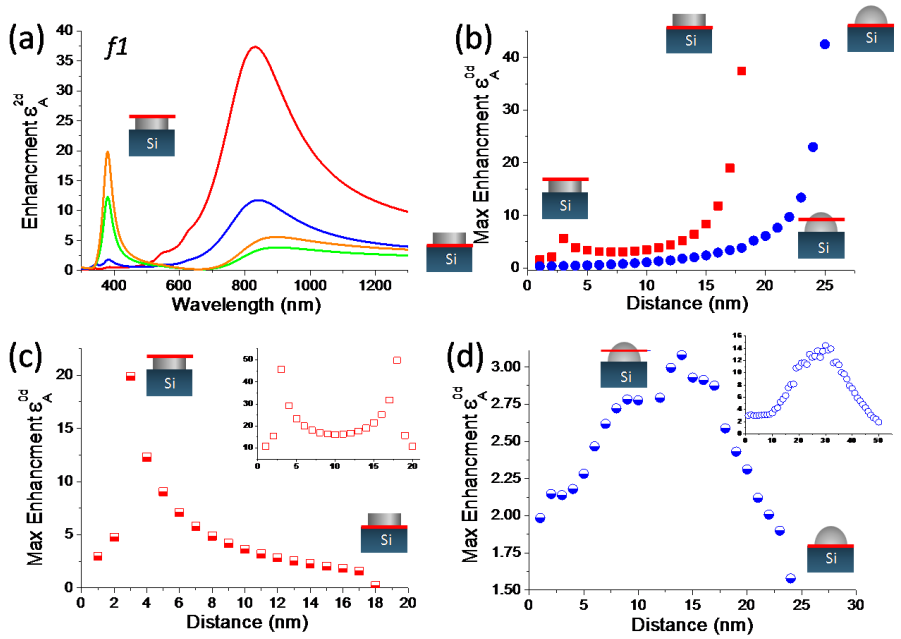

Figure 8. a) The spectral absorption enhancement on different cross planes along a nano-column (as depicted in the insets), showing two plasmon resonances, one at ~380 nm being more intense at the top of the NP (air-LSPR) and one red-shifted at ~830 nm that is more intense at the bottom of the NP (Si-LSPR). We extract separately for each resonance the maximum enhancement from the top of the NP down to the bottom: b) for the Si-LSPR in nano-columns and nano-domes, c) for the air-LSPR at nano-columns (the inset graph depicts the maximum enhancement of the free-standing nano-column in air) and d) for the air-LSPR in nano-dome (the inset graph depicts the maximum enhancement of the free-standing sphere in air).

We perform the same calculations of maximum enhancement for our two NPs on a Si substrate, but in a different way from the free stand NPs. As we mentioned before, in this case we have two plasmon resonances, the one is screened mostly by the air (air-LSPR) and is more intense at the top of the NP and the other one is screened mostly by the substrate (Si-LSPR) and is more intense at the bottom of the NP (fig. 8.a). We thus extract separately the maximum enhancement spatial distribution for each resonance. For the Si-LSPR the maximum enhancement is increased moving from the top down to the bottom, with the trend being the same for both shapes (fig. 8.b). This spatial evolution of Si-LSPR indicates its substrate origin. In contrast, in the case of the air-LSPR in the nano-column (fig. 8.c), the maximum enhancement decreases as we move from the top to the bottom: this spatial evolution is similar to the first "half" graph of the free-standing nano-column in air, shown in the inset. Finally, the spatial evolution of the air-LSPR at the nano-dome (fig. 8.d) is the same with the free-standing sphere in the air showing in the inset, indicating its origin from the environment of air. To resume, the LSPR is modulated across the NP's volume with different resonances at different distances from the substrate. Thus, the fluorescence and Raman enhancement will strongly depend on where on the NP's surface the molecules are adsorbed.

4.3 Tuning the NP LSPR by a dielectric coating

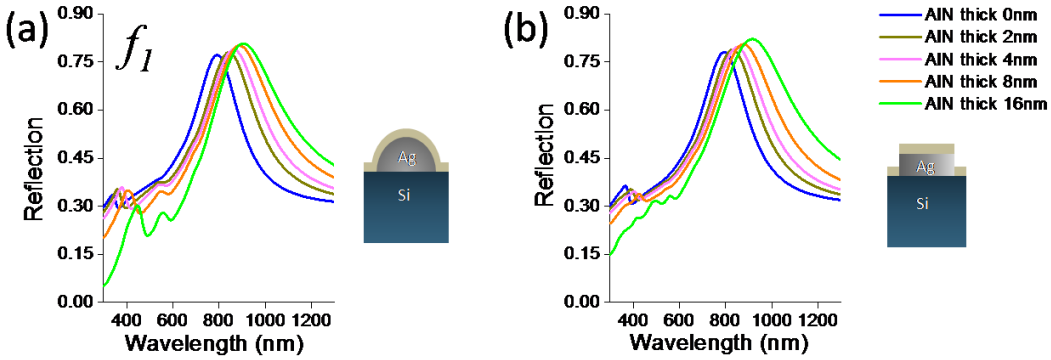

Figure 9. The reflection spectrum of nano-domes (a) and nano-columns (b) for un-coated NPs (blue line) and coated NPs with an AlN cap layer at various thicknesses (2-16 nm). The NPs diameter is d_1=48 nm and the surface coverage is f_1=44%. The inset schematics depict the coating geometry for nano-domes and nano-columns, simulating a realistic experimental coating deposition.

An efficient way to tune the LSPR wavelength at a pre-determined spectral position is by coating the NPs with a dielectric layer, as it is known that the resonance wavelength is sensitive to the dielectric environment. This is very important in terms of SERS applications, because once can design all the aforementioned resonant effects of a plasmonic template to be excited by the experimental laser of the Raman Spectroscopy. In this way we theoretically design and experimentally verify the optical response of our two plasmonic templates (nano-domes, nano-columns), coated

with an AlN dielectric layer at various thicknesses. Thus, in figure 9 we present the simulated reflection spectrum for our two shapes with and without AlN coating. We observe that increasing the thickness of the AlN cap layer the LSPR wavelength is red shifted for both shapes. The way the coating covers the NP is differentiated for the two shapes, as is depicted at the insets of fig.9: for simplicity we assume a purely vertical coating deposition method (e.g. by a sputtering methods). Specifically, in the case of nano-domes, we assume that the AlN is homogeneously deposited around the NP, and in the case of nano-columns we assume the AlN is coated only at the top and at the bottom of the NP. This way, we can hope to have a straightly comparison between theory and experiments.

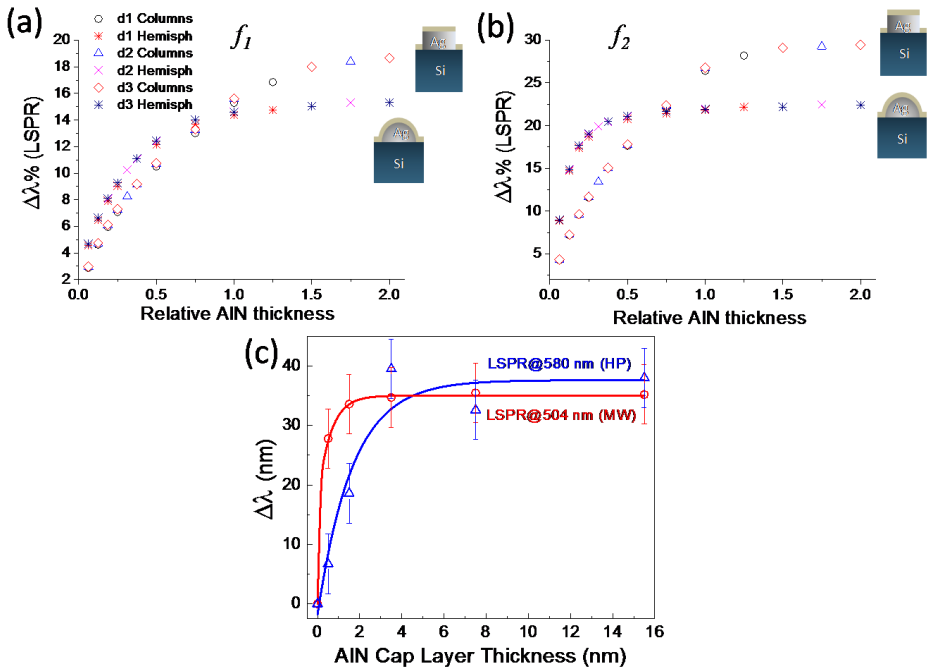

Figure 10. The simulated percentage LSPR red-shift from the un-coated NP LSPR, as a function of AlN relative thickness, for the two studied shapes and three sizes (d_1, d_2, d_3), at the surface coverages: a) f_1 = 44% and b) f_2 = 67%. c) The experimental red-shift (nm) compared to the uncoated NPs as a function of AlN thickness for two plasmonic templates is shown. The initial un-coated plasmonic templates, where produced by two thermal annealing methods of a thin silver film on a Si substrate: a thermal annealing produced by a Hot Plate (HP), and a thermal annealing produced by a Micro Wave (MW) commercial oven. It appears that the two kinds of thermal annealing produce NPs with different shapes, nano-columns with HP annealing and nano-domes with MW annealing, as inferred by comparing theoretical and experimental results.

We simulate NPs arrays of our two characteristic shapes and three sizes (d_1, d_2, d_3), without and with an AlN coating layer at various thicknesses, and extract the shape effects of the LSPR response under the dielectric layer. We obtain for each case the LSPR wavelength and calculate the percentage modulation of the LSPR red-shift compared to the un-coated NP arrays. We plot the percentage change of the LSPR red-shift as a function of the relative AlN thickness for the two NP arrangements at

surface coverage 44% (fig.10.a) and surface coverage 67% (fig.10.b). To have a direct, normalized comparison between different NP sizes, the relative AlN thickness is obtained from normalizing the AlN thickness with the height of the nano-column. In figure 10.a we observe that increasing the AlN thickness, the LSPR modulation for the two shapes is different, this difference being more dramatic for the big surface coverage, shown in figure 10.b. Specifically, for the nano-domes, the LSPR is red-shifting rapidly for small variations of AlN thickness, but then quickly it saturates. In contrast, for nano-columns, the LSPR redshifts slowly for small variations of AlN thickness, but saturates at larger AlN thickness. Clearly, these trends are only shape-depended, they do not depend on the NP size, as they appear identical for the three different NP volumes.

This shape-depended trend appears to be reproduced in the experimental results presented in figure 10.c, in which we plot the experimental spectral red shift (nm) of the LSPR from that of the uncoated NPs, as determined by reflectivity spectra, as a function of AlN thickness for two plasmonic templates. The initial pre-coated plasmonic templates where produced by two different thermal annealing methods of a thin silver film on a Si substrate, the first was a thermal annealing produced by a Hot Plate (HP) and the second was a thermal annealing produced by a Micro Wave (MW) commercial oven. We don't know yet the exact shape of the produced NPs, which is the subject of on-going experimental work. It appears that the two kinds of thermal annealing produce NPs with different shapes, closer to nano-columns with the HP annealing processes and closer to nano-domes with MW annealing process, as can be inferred by comparing the theoretical and experimental results.

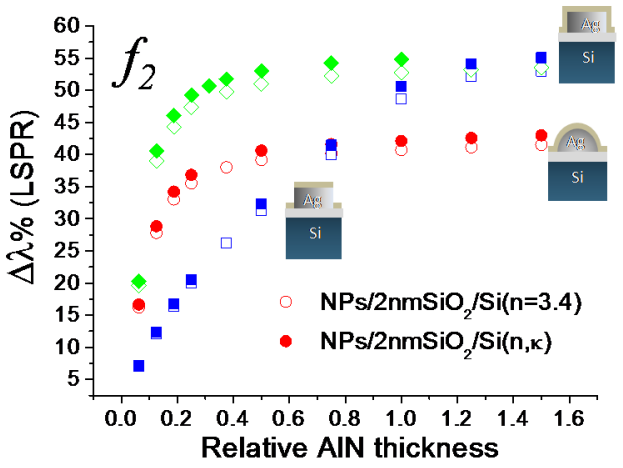

Figure 11. The simulated percentage LSPR red-shift from the un-coated NPs LSPR as a function of AlN relative thickness, for the large NPs (d_1) at the big surface coverage (f_2). The NP arrays are assumed to be on a 2 nm SiO_2 native oxide on top of a non-absorbing Si substrate (open shapes) or an absorbing (realistic dielectric function) Si substrate (solid shapes). The inset schematics depict 3 different forms of coating, the two studied above for the nano-domes (red shapes) and nano-columns (blue shapes), and a third one involving a uniform coating coverage of the nano-columns.

Now, we focus on the effect of the substrate and on the way coating material actually coats the nanoparticle. In doing so, we simulate and calculate the optical response of the NPs arrays on different substrates and different deposition geometries of the AlN coating. Thus, we present in figure 11 the simulated percentage LSPR red-shift from the un-coated NPs as a function of AlN relative thickness, for the large NPs (d_1) at the high surface coverage (f_2). Same results were obtained for the other sizes and surface coverages. The NPs arrays are assumed to be on top of a native 2 nm SiO_2 thin film (obtained in experiments) which is on top of either a non-absorbing Si substrate or an absorbing (realistic dielectric function) Si substrate. Also, except of the aforementioned geometry of coating for the two shapes, for the nano-columns we also consider the same coating as nano-spheres (see the figure insets), i.e. uniform coating thickness everywhere (a rather extreme case experimentally), in order to understand the shape-depended trend. We observe that the absorption in the Si substrate does not affect the shape-depended trend, both substrates yield the same LSPR evolution as a function of AlN relative thickness. Comparing now the different coating geometries we observe that the nano-domes and nano-columns with the AlN layer uniformly around their surface yield the same trend, with the latter, however, saturating to the same values as the nano-column with vertical coating. To summarize, the evolution of the LSPR spectral position as a function of AlN thickness does not depend on the substrate, while the NP shape dependence becomes relevant as long as the deposition method produces uniform coating geometries or not.

4.4 Conclusions

Functional plasmonic templates for SERS applications composed of metallic NPs arrays on a substrate can be developed by either top-down (e.g. nanolithography) or bottom-up (e.g. self-assembly by laser or thermal annealing of a thin metal film) processes, each case resulting into different particle shapes, sizes and arrangements. In this work we explored theoretically how the LSPR traits (electric field enhancement, scattering etc) are modulated depending on the different final configuration. Thus, we examined two "extreme" shapes on a Si substrate: nano-columns as a representative NP shape by top-down methods and spherical nano-domes as a representative NP shape by bottom-up methods. Intermediate shapes can in general be developed by different bottom-up methods. In order to extract only the shape effects, different NP sizes and arrangements where tested under the condition of keeping particle volume and cross section the same for the two shapes.

We produced detailed electric field enchantment maps showing that depending on the shape, the frequency at which maximum field enhancement occurs varies depending on the location on the NP's surface, pointing towards modulated LSPR oscillations across the NP's surface. Specifically, we find and identify two different LSPRs across the NP's surface at different spectral positions, the one being screened

mostly by the surrounding air and being more intense at the top of the NP (air-LSPR), while the other one being screened mostly by the Si substrate and being more intense close to the substrate (Si-LSPR). This results to different maxima of electric field enhancement across the NP at different spectral positions. Thus, the fluorescence and Raman enhancement will depend on were on the NP's surface the analyzed molecules are adsorbed.

Furthermore, to tune the LSPR frequency in relevance to enhanced spectroscopy applications, we examined the effect of thin dielectric coatings (AlN) on the NPs. Assuming that a typically employed sputtering method would produce a strictly vertical deposition geometry, we find that the changes in LSPR spectral position as a function of the AlN thickness is strongly depended on the NP shape. The theoretical results are in good agreement with recent experiments of AlN deposited on Ag NPs. Finally, the evolution of the LSPR spectral position with increasing thickness of AlN does not depended on the exact details of the dielectric function of the substrate, while the relevance of the NP shape actually depends on the deposition geometry of the coating.

4.5 References

[1] S. Eustis, M. A. El-Sayed, Why gold nanoparticles are more precious than pretty gold: Noble metal surface plasmon resonance and its enhancement of the radiative and nonradiative properties of nanocrystals of different shapes. Chem. Soc. Rev. 35, 209-217 (2006).

[2] K.A. Willets, R.P. Van Duyne, Localized Surface Plasmon Resonance Spectroscopy and Sensing, Annu. Rev. Phys. Chem., 58, 267-297, (2007).

[3] S.A. Maier, Plasmonics: fundamentals and applications, Springer, New York, (2007).

[4] C.F. Bohren, D.R. Huffman, Absorption and scattering of light by small particles. Wiley Interscience, New York (1983)

[5] K.S. Lee, M.A.J. El-Sayed, Gold and silver nanoparticles in sensing and imaging: sensitivity of plasmon response to size, shape and metal composition, Phys. Chem. B, 110, 19220-19225, (2006)

[6] M.M. Miller, A.A. Lazarides, Sensitivity of metal nanoparticle surface plasmon resonance to the dielectric environment, J. Phys. Chem. B, 109, 21556-21565, (2005)

[7] O. Kvitek, J. Siegel, V. Hnatowicz, V. Svorcik, Noble metal nanostructures: influence of structure and environment on their optical properties, J. Nanomater. 743684, (2013)

[8] N.J. Halas, Playing with plasmons: tuning the optical resonant properties of metallic nanoshells, MRS Bull, 30, 362-367, (2005)

[9] S. Underwood, P. Mulvaney, Effect of solution refractive index on the color of gold colloids, Langmuir, 10, 3427-3430, (1994)

[10] J.J. Mock, M. Barbic, D.R. Smith, D.A. Schultz, S.J. Schultz, Shape effects in plasmon resonance of individual colloidal silver nanoparticles, Chem. Phys., 116, 6755-6759, (2002)

[11] S. Schultz, D. R. Smith, J. J. Mock, D. A. Schultz, Single-target molecule detection with nonbleaching multicolor optical immunolabels. Proc. Natl Acad. Sci. USA 97, 996-1001 (2000).

[12] J. Yguerabide, E. E. Yguerabide, Light-scattering submicroscopic particles as highly fluorescent analogs and their use as tracer labels in clinical and biological applications. I. Theory. Anal. Biochem. 262, 137-156 (1998).

[13] J. M. Nam, C. S. Thaxton, C. A. Mirkin, Nanoparticle-based bio-bar codes for the ultrasensitive detection of proteins. Science 301, 1884-1886 (2003)

[14] C. R. Yonzon, et al. Towards advanced chemical and biological nanosensors - an overview. Talanta 67, 438-448 (2005).

[15] A. J. Haes, L. Chang, W. L. Klein, R. P. Van Duyne, Detection of a biomarker for Alzheimer's Disease from synthetic and clinical samples using a nanoscale optical biosensor. J. Am. Chem. Soc. 127, 2264-2271 (2005).

[16] A. D. McFarland, R. P. Van Duyne, Single silver nanoparticles as real-time optical sensors with zeptomole sensitivity. Nano Lett. 3, 1057-1062 (2003).

[17] G. Raschke, et al. Biomolecular recognition based on single gold nanoparticle light scattering. Nano Lett. 3, 935-938 (2003).

[18] R. Elghanian, J. J. Storhoff, R. C. Mucic, R. L. Letsinger, C. A. Mirkin, Selective colorimetric detection of polynucleotides based on the distance-dependent optical properties of gold nanoparticles. Science 277, 1078-1081 (1997).

[19] K. M. Mayer, J. H. Hafner, Localized Surface Plasmon Resonance Sensors, Chem. Rev., 111, 3828-3857, (2011)

[20] M. Moskovits, Surface-enhanced spectroscopy, Rev. Mod. Phys, 57, 783-826 (1985).

[21] C. L. Haynes, C. R. Yonzon, X. Zhang, R. P. Van Duyne, Surface-enhanced Raman sensors: Early history and the development of sensors for quantitative biowarfare agent and glucose detection. J. Raman Spectrosc. 36, 471-484 (2005).

[22] Y. Fang, N. H. Seong, D. D. Dlott, Measurement of the Distribution of Site Enhancements in Surface-Enhanced Raman Scattering, Science, 321, 388-392 (2008).

[23] K. Kneipp, Y. Wang, H. Kneipp, L. T. Perelman, I. Itzkan, R. R. Dasari, M. S. Feld, Single Molecule Detection Using Surface-Enhanced Raman Scattering (SERS), 78(9), 1667(4), (1997).

[24] J. F. Li, Y. F. Huang et al. Shell-isolated nanoparticle-enhanced Raman Spectroscopy, Nature, 464, 392-395, (2010).

[25] S. Nie, S. R. Emory, Probing Single Molecules and Single Nanoparticles by Surface-Enhanced Raman Scattering, Science 275, 1102-1106, (1997).

[26] Y. Chen, K. Munechika, D. S. Ginger, Dependence of fluorescence intensity on the spectral overlap between fluorophores and plasmon resonant single silver nanoparticles. Nano Lett. 7, 690-696 (2007).

[27] E. R. Lu, P. Etchegoin, Principles of Surface Enhanced Raman Spectroscopy and related plasmonic effects, Elsevier, (2009).

[28] E. Hutter, J. H. Fendler, Exploration of Localized Surface Plasmon Resonance. Adv. Mater., 16, 1685-1706, (2004).

[29] M. J. Banholzer, J. E. Millstone, L. Qin, C. A. Mirkin, Rationally Designed Nanostructures for Surface-Enhanced Raman Spectroscopy. Chem. Soc. Rev. 37, 885-897,(2008).

[30] X. M. Qian, S. M. Nie, Single-Molecule and Single-Nanoparticle SERS: From Fundamental Mechanisms to Biomedical Applications. Chem. Soc. Rev. 37, 912-920 (2008).

[31] L. Qin, S. Zou, C. Xue, A. Atkinson, G. C. Schatz, C. A. Mirkin, Designing, Fabricating, And Imaging Raman Hot Spots. Proc. Natl. Acad. Sci. U.S.A. 103, 13300-13303, (2006).

[32] J. P. Camden, J. A. Dieringer, Y. Wang, D. J. Masiello, L. D. Marks, G. C. Schatz, R. P. V. Duyne, Probing the Structure of Single-Molecule Surface-Enhanced Raman Scattering Hot Spots. J. Am. Chem. Soc., 130, 12616-12617, (2008).

[33] C. Talley, J. Jackson, C. Oubre, N. Grady, C. Hollars, S. Lane, T. Huser, P. Nordlander, N. Halas, Surface-Enhanced Raman Scattering from Individual Au Nanoparticles and Nanoparticle Dimer Substrates. Nano Lett., 5, 1569-1574, (2005).

[34] M. Rycenga, P. H. C. Camargo, W. Li, C. H. Moran, and Y. Xia, Understanding the SERS Effects of Single Silver Nanoparticles and Their Dimers , One at a Time, J. Phys. Chem. Lett., 1, 696-703, (2010).

[35] J. H. Seo, J. H. Park, S. I. Kim, B. J. Park, Z. Ma, J. Choi, B. K. Ju, Nanopatterning by Laser Interference Lithography: Applications to Optical Devices, Journal of Nanoscience and Nanotechnology, 14, 1521-1532, (2014).

[36] S. J. Henley, J. D. Carey, S. R. P. Silva, Laser-nanostructured Ag films as substrates for surface-enhanced Raman spectroscopy, Applied Physics Letters, 88, 081904, (2006)

[37] S. J. Henley, S. R. P. Silva, Laser direct write of silver nanoparticles from solution onto glass substrates for surface-enhanced Raman spectroscopy, Applied Physics Letters, 91, 023107 (2007)

[38] K. Christou, I. Knorr, J. Ihlemann, H. Wackerbarth, V. Beushausen, Fabrication and Characterization of Homogeneous Surface-Enhanced Raman

Scattering Substrates by Single Pulse UV-Laser Treatment of Gold and Silver Films, Langmuir, 26(23), 18564-18569, (2010)

[39] C.H. Lin, L. Jiang, J. Zhou, H. Xiao, S.J. Chen, H.L Tsai, Laser-treated substrate with nanoparticles for surface-enhanced Raman scattering, 35(7),Opt. Let, (2010)

[40] N. T. Panagiotopoulos, N. Kalfagiannis, K. C. Vasilopoulos, N. Pliatsikas, S. Kassavetis, G. Vourlias, M. A. Karakassides, P. Patsalas, Self-assembled plasmonic templates produced by microwave annealing: applications to surface-enhanced Raman scattering, Nanotechnology, 26 205603 (2015).

[41] E. D. Palik, Handbook of Optical Constants of Solids, Academic, San Diego, (1998).

[42] E. Lidorikis, Modeling of enhanced absorption and Raman scattering caused by plasmonic nanoparticle near fields, Journal of Quantitative Spectroscopy and Radiative Transfer, 113, 2573–2584, (2012).

[43] F. J. Garcıa-Vidal and J. B. Pendry, Collective Theory for Surface Enhanced Raman Scattering, Physical Review Letters, 77 6, 1163-1166 (1996).

[44] J. Grand, M. Lamy de la Chapelle, J. L. Bijeon, P. M. Adam, A. Vial, and P. Royer, Role of localized surface plasmons in surface-enhanced Raman scattering of shape-controlled metallic particles in regular arrays, Phys. Rev. B, 72, 033407, (2005).

Chapter 5 Laser Induced Self-Assembly and Nano-Structuring

Abstract

Nano-structuring of metals is one of the greatest challenges for the future of plasmonic and photonic devices. Such a technological calls for the development of ultra-fast, high-throughput and low cost fabrication techniques. Laser processing, accounts for the aforementioned properties, representing an unrivalled tool towards the anticipated arrival of modules based in metallic nano-structures, with an extra advantage: the ease of scalability. Specifically, laser nano-structuring of ultra-thin metal film or an alternative ceramic/metal film on a substrate results respectively on surface (MNPs on the surface of the substrate) or subsurface (MNPs embedded in a dielectric matrix) plasmonic patterns with many applications. In this work we investigate theoretically and compare to experiments the photo-thermal processes involved in surface and sub-surface plasmonic nano-structuring. To this end, we present a design process and develop functional plasmonic nano-structures with pre-determined morphology. Especially, by tuning the annealing parameters like the laser's fluence and wavelength or/and the structure parameters like thickness of the metallic film and the volume ratio of the ceramic metal composite, one can arrive at nano-structures with pre-designed morphology. For the surface plasmonic nano-structuring we utilize the ability to tune the laser's wavelength to either mach the absorption spectral profile of the metal or to be resonant with the plasma oscillation frequency (LSPR), i.e. we utilizate different optical absorption mechanisms that are size-selective which enables the fabrication of pre-determined patterns of metal nanostructures. Thus, we overcome a great challenge of Laser Induced Self Assembly by combining simultaneously large-scale character with atomic scale precision. On the other hand, for subsurface plasmonic nano-structuring we utilize the temperature gradients that are developed spatially across the metal/dielectric nano-composite structure during the laser treatment. We find that the developed temperature gradients are strongly depended on the nanocrystalline character of the dielectric host which determines its thermal conductivity, the composition of the ceramic/metal and the total thickness of the nano-composite film. The aforementioned materials' parameters combined with the laser annealing parameters can be used to pre-design the final morphology of the sub-surface plasmonic structure. In both cases we can develop templates with desirable optical response which can be used for many technological applications. Finally, the proposed process can serve as a platform that will stimulate further progress towards the engineering of plasmonic devices.

5.1 Introduction

Plasmonic Nanoparticles (PNPs) are metallic nanoparticles with sizes smaller than the wavelength of visible light. Under the irradiation of light, the free electrons in a PNP are driven by the alternating electric field and collectively oscillate at a resonant frequency in a phenomenon known as Localized Surface Plasmon Resonance (LSPR) [1-10]. This strong light/electron coupling forces the confinement of light into small volumes, resulting into extreme local fields, light scattering and absorption [11-13]. The LSPR phenomenon induced in PNPs depends strongly on their composition, size, shape, distribution and on the refractive index of the employed dielectric environment [14-19]. In this regard, efforts are undertaken in order to control these structural parameters depending on the growth conditions [5, 6, 20-23]. Noble metals gold and silver are considered more suitable for PNPs due to their stability when formed into nanoparticles and their strong LSPR absorption bands in the visible region of the spectrum [12, 21].

Plasmonic materials and devices based on PNPs have attracted considerable attention due to the exploitation of LSPR, an enabling optical phenomenon for a number of exciting applications including biochemical sensing [24-27], surface enhanced spectroscopes [11, 28-34], information and communication technologies [35-38], solar energy harvesting [39-45], optical encoding [46-49], surface decoration [50], lighting [51] and many others. A critical parameter in delivering the aforementioned devices is the materials' preparation methods, which should allow for the production of nanostructures with tunable plasmonic properties. So far, nanomaterials and nanodevices manufacturing has traditionally followed two distinct routes: a) the top-down approach, a process that starts from a uniform material and subsequently uses finer and finer tools for creating correspondingly smaller structures, like lithographic processes [52-54] and/or ion beam nanofabrication [55], and b) the bottom-up approach, where smaller components of atomic or molecular dimensions self-assemble together, according to a natural physical principle or an externally applied driving force, to give rise to larger and more organized systems, like atomic layer deposition [56], cold welting [57], flash thermal annealing [47,58,59], pattern transfer [60] and template stripping [61-63]. In practice, the top-down route offers unparallel control and reproducibility down to a few nanometers in feature size but at high cost for a large area processing, while the bottom-up approach naturally applies for macroscopic scale nano-patterning albeit without the fine feature and reproducibility control.

Laser radiation might be viewed as the means to a third intermediate, route for nanotechnology. Light matter interactions offer precise energy delivery and control over the physico-chemical processes in the nanoworld. Amongst the methodologies followed for creating nanoparticle arrangements and/or nano-composite thin films, Laser Annealing (LA) has been proven to be simple and versatile, providing freedom of design, fast processing, compatibility with large scale manufacturing and allowing

for the use of inexpensive flexible substrates [46, 48, 64]. For example, LA of a thin metal film results into nanoparticle arrangements on top of the substrate [31, 34, 64-76], while embedded nanoparticles in a dielectric matrix can be fabricated by the LA of a stack of alternating layers of metal and dielectric [46, 47].

Here, we perform a theoretical investigation to extract the underline physical understanding of the photo-thermal processes involved in surface and sub-surface laser nano-structuring. In doing so, we propose a way to experimentally develop plasmonic nano-structures with pre-determined morphology. Thus, we present the theoretically results associated with the contributed experiments. We illustrate that theory and experiments are in good agreement and thus prove that theory can assist and drive the developing of functional plasmonic nano-structures. Especially, by tuning the annealing parameters like lasers' fluence and wavelength and/or the structure parameters like thickness of the metallic film and the volume ratio of the ceramic metal composite once can arrive at nano-structures with pre-designed morphology.

Specifically, for the sub-surface nano-structuring we first develop an analytical model which calculates the light propagation properties and obtain a detailed spatial absorption distribution in the multilayer and the substrate. Furthermore we compare the analytical absorption distribution with the numerical one extracted from Finite Differences Time Domain (FDTD) calculations and we find excellent agreement. This spatial distribution is then integrated with the experimental laser temporal profile and solved in a 1D heat transport equation, arriving at the temperature transients at each point in the multilayer volume. We perform this analysis for different structures' parameters like metal/ceramic volume ratios, thickness of the multilayer and thermal conductivity of the dielectric ceramic matrix. We find that significant temperature gradients are developed spatially across the nano-composite structure, which are strongly depended on the aforementioned materials' parameters. Furthermore, presenting the experimental results we show that these temperature gradients create different annealing conditions across the nano-composite structure and can be used to design the final morphology of the plasmonic structure.

On the other hand for the surface plasmonic nanostucturing, we first simulate the UV and optical light absorption for different silver nanoparticle sizes and arrangements on top of Si substrate and thus we get the spatial absorption profile. For the UV and optical calculations a full vector 3D FDTD simulator is used in order to capture all possible absorption mechanisms. Thus, we find and identify different absorption mechanisms which are size selective and enable geometric specificity such as: a) interband absorption, resulting from the excitation of the metal's internal d-electrons into the conduction band and b) intraband absorption, resulting from the metal's free electrons resonantly excited at the specific spectral position of the LSPR. Utilizing the absorption spatial profile, we then perform heat diffusion simulations taking into account the exact laser temporal pulse profile and arrive at the transient temperature profile in each nanoparticle. From this we map the maximum temperature

rise as a function of particle size, laser wavelength and laser fluence. In these maps we distinguish spectral regions of higher and lower temperature which can be used to provide a recipe for the modification of the plasmonic templates towards a predefined morphology. In particular, by sequentially tuning the laser wavelength into resonance with different physical processes such as the LSPR of the metal particles or the interband transitions of the metal's d-electrons, we can selectively target the melting and re-solidification of different particle size groups. This idea is implemented in experiments, in which repeated laser treatments can target different NPs size groups with different laser wavelengths, driving the final size distribution towards the predetermined one. We term this process: "Modification of Nanoparticle Arrays by Laser Induced Self Assembly" (MONA-LISA).

5.2 Subsurface nano-structuring

5.2.1 Theoretical Approach

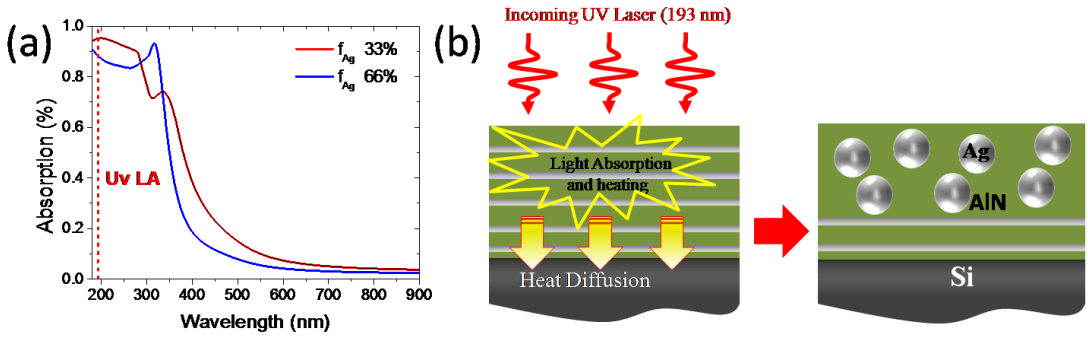

Figure 1. a) Spectral absorption of a stratified metal (Ag) dielectric (AlN) structure illustrated in (b) for two metal volume ratios 33% and 66%. The high UV absorption can be utilized for the further modification of the nano-composite. b) Schematic illustration of the laser treatment of the multilayer structure. Under UV laser radiation, the absorbed energy is converted into heat, which is diffused by thermal conduction into the Si substrate. The result of the laser treatment is to totally transform the multilayer structure into a nano-composite of embedded plasmonic metallic NPs inside a dielectric matrix.

We start our approach by theoretically exploring a stratified multilayer structure of alternative dielectric (AlN) and metal layers (Ag) on a Si substrate (fig 1). The optical response of such multilayer shows high UV absorption (fig 1.a) due to silver's interband transitions at this spectral range. Absorption is higher at lower Ag volume ratio because of the lower reflection losses compared to the higher volume ratio. This UV absorption can be utilized to locally melt the structure and modify the multilayer, transforming it into a plasmonic nano-composite with metallic NPs embedded in a dielectric matrix (fig 1.b). The morphology of the nano-composite and its optical response can be tuned by choosing materials and laser annealing parameters.

In recent experiments, multilayers of alternative dielectric (AlN) and metal (Ag) layers on Si substrate were subjected to a single shot UV (193 nm) laser annealing, leading to the subsurface formation of plasmonic NPs demonstrating LSPR [46]. The morphology of the sub-surface nano-structuring depends on the nanocrystaline character of the dielectric which is strongly related to its thermal conductivity, the metal volume ratio and the total thickness of the multilayer. These parameters can be controlled from the conditions of the experiments. In light of these results, we examine theoretically the opto-thermal processes involved in such experiments. This way we can physically understand the contribution of each one of the above parameters to the final structure. Furthermore, by changing the multilayer components one can arrive at subsurface plasmonic nano-structuring with pre-designed morphology.

Specifically, starting from the UV optical constants of the metal and dielectric we develop an analytical model which provides the absorption spatial distribution in the multilayer. This spatial distribution is then time integrated with the experimental laser's temporal profile and solved in 1D heat transport equation, arriving at the temperature transients at each point in the multilayer's volume. The spatial temperature distribution is a crucial parameter determining the final morphology of the sub-surface nano-structure and we will show that it strongly depends on the thermal conductivity of the dielectric, the metal's volume ratio and the total thickness of the multilayer.

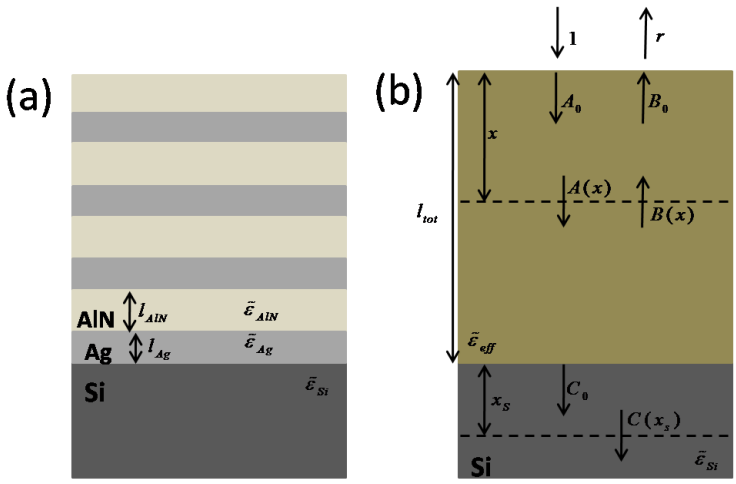

Figure 2. Schematic of the multilayer structure a) the stratified dielectric (AlN) /metal (Ag) multilayer structure and b) the effective composite structure illustrating the analytical model

We assume a AlN/Ag bilayer on Si substrate, where l_{AlN} , $\tilde{\varepsilon}_{AlN}$, l_{Ag} , $\tilde{\varepsilon}_{Ag}$ are the thickness and the complex dielectric function of AlN and Ag respectively, the thickness of the Si is semi-infinite and $\tilde{\varepsilon}_{Si}$ is the dielectric function of Si. The volume ratio of AlN is $f_{AlN} = l_{AlN} / (l_{AlN} + l_{Ag})$ and the volume ratio of Ag is $f_{Ag} = l_{Ag} / (l_{AlN} + l_{Ag})$. The optical constants are obtained from optical ellipsometric measurements for Ag [77] and for AlN [78]. The multilayer structure can be

fabricated by alternating magnetron sputtering for each one of the individual layers with exact control to the thickness of each layer (fig. 2.a). We find the effective medium dielectric function $\tilde{\varepsilon}_{eff} = f_{AlN}\tilde{\varepsilon}_{AlN} + f_{Ag}\tilde{\varepsilon}_{Ag}$ and the effective refractive index $\tilde{n}_{eff} = \sqrt{\tilde{\varepsilon}_{eff}} = n_{eff} + i\kappa_{eff}$ where n_{eff}, κ_{eff} is the real and imaginary part of the complex refractive index respectively. Utilizing the effective medium optical constants we can now model a uniform film which has the same thickness and optical response with the multilayer (fig 2.b). This film is used to develop an analytical model based on transfer matrixes, providing the absorption spatial distribution in the nano-composite and substrate under UV illumination.

Specifically, as it is shown in fig. 2.b, under illumination a portion of light is reflected (r is the reflected wave) and the rest undergoes multiple reflections from the air/film and film/Si interfaces and gets absorbed along the way. The resulting coherent downward and upward waves are denoted by $A(x)$ and $B(x)$ respectively. The transmitted wave is denoted by C, with $C(x_s)$ the wave at a specific distance x_s from the Si-film interface. Practically, $C(x_s)$ diminishes in the first 100 nm due to high absorbance of Si in the UV region.

We first calculate the incident and transmitted waves from the effective film, through transfer matrixes:

$$\begin{pmatrix} C_0 \\ 0 \end{pmatrix} = I_{\tilde{n}_{Si}\tilde{n}_f} P_{\tilde{n}_f l_{tot}} I_{\tilde{n}_f n_a} \begin{pmatrix} 1 \\ r \end{pmatrix} = \begin{pmatrix} M_{11} & M_{12} \\ M_{21} & M_{22} \end{pmatrix} \begin{pmatrix} 1 \\ r \end{pmatrix} \tag{4.1}$$

where $I_{\tilde{n}_f n_a}$ is the interface matrix from air to the film , $P_{\tilde{n}_f l_{tot}}$ is the propagation matrix in the film and $I_{\tilde{n}_{Si}\tilde{n}_f}$ is the interface matrix from film to Si substrate:

$$I_{\tilde{n}_f \tilde{n}_{air}} = \frac{1}{2\tilde{n}_f} \begin{pmatrix} \tilde{n}_f + n_a & \tilde{n}_f - n_a \\ \tilde{n}_f - n_a & \tilde{n}_f + n_a \end{pmatrix}$$

$$P_{\tilde{n}_f l_{tot}} = \begin{pmatrix} e^{ik_f l_{tot}} & 0 \\ 0 & e^{-ik_f l_{tot}} \end{pmatrix} \tag{4.2}$$

$$I_{\tilde{n}_{Si}\tilde{n}_f} = \frac{1}{2\tilde{n}_f} \begin{pmatrix} \tilde{n}_{Si} + \tilde{n}_f & \tilde{n}_{Si} - \tilde{n}_f \\ \tilde{n}_{Si} - \tilde{n}_f & \tilde{n}_{Si} + \tilde{n}_f \end{pmatrix}$$

where $n_a, \tilde{n}_f, \tilde{n}_{Si}$ are the refractive indexes of the air ,the effective index of the film and the refractive index of the Si substrate respectively. From eq. 4.1 and 4.2 we can derive the complex components of the matrix M :

$$M_{11} = \frac{1}{2}\left(1+\frac{n_a}{\tilde{n}_{Si}}\right)\cos(k_f l_{tot}) + \frac{i}{2}\left(\frac{n_a}{\tilde{n}_f}+\frac{\tilde{n}_f}{\tilde{n}_{Si}}\right)\sin(k_f l_{tot})$$

$$M_{21} = \frac{1}{2}\left(1-\frac{n_a}{\tilde{n}_{Si}}\right)\cos(k_f l_{tot}) + \frac{i}{2}\left(\frac{n_a}{\tilde{n}_f}-\frac{\tilde{n}_f}{\tilde{n}_{Si}}\right)\sin(k_f l_{tot}) \tag{4.3}$$

where $k_f = 2\pi\tilde{n}_f / \lambda$ is the wave vector inside the film. The other two components are the respective complex conjugates, i.e. $M_{12} = M_{21}^*$ and $M_{22} = M_{11}^*$. Combining Eqs. 4.1 and 4.3 we get the reflected $r = -M_{21}/M_{22}$ and transmitted $C_0 = \det(M)/M_{22}$ waves.

We focus now on the air-film interface and we associate the waves before the inter-face with the waves after the interface:

$$\begin{pmatrix} A_0 \\ B_0 \end{pmatrix} = I_{\tilde{n}_f n_a}\begin{pmatrix} 1 \\ r \end{pmatrix} = \begin{pmatrix} N_{11} & N_{12} \\ N_{21} & N_{22} \end{pmatrix}\begin{pmatrix} 1 \\ r \end{pmatrix} \tag{4.4}$$

where the components of the matrix N and the reflection r are known. The fields after the air-film interface are:

$$A_0 = \frac{N_{11}M_{22} - N_{12}M_{21}}{M_{22}}$$

$$B_0 = \frac{N_{21}M_{22} - N_{22}M_{21}}{M_{22}} \tag{4.5}$$

These waves are counter propagating in the film, and at a distance x from the interface they are $A(x) = A_0 e^{ik_f x}$ and $B(x) = B_0 e^{-ik_f x}$, both waves decreasing exponentially with distance along the propagation direction (x for the forward wave, $-x$ for the backward wave). Also the wave propagating in the semi-infinite silicon substrate is described as $C(x_s) = C_0 e^{ik_s x_s}$, where x_s is the distance from the film-Si interface and $k_s = 2\pi\tilde{n}_s / \lambda$ is the wave vector in the Si substrate. We find that this wave becomes insignificant after the first 100 nm of Si due to high Si absorption in UV

Now we are able to calculate the Poynting vector flux S at each point in the film and the Si substrate [79]:

$$S(x) = \mathrm{Re}\{\tilde{n}_f\}\left(|A(x)|^2 - |B(x)|^2\right) - 2\,\mathrm{Im}\{\tilde{n}_f\}\,\mathrm{Im}\{A(x)B^*(x)\} \tag{4.6}$$

$$S(x_S) = \mathrm{Re}\{\tilde{n}_f\}|C(x_S)|^2 \tag{4.7}$$

The first term in eq. 4.6 associated to the forward $A(x)$ and backward $B(x)$ waves, as if each of them were propagating independent of each other. The second term, which is absent in the case of non absorbing media, appears here because of the interference between the counter-propagating waves in the absorbing film. Finally, the absorption spatial distribution per nm vertical distance is calculated from the top of the film down to the Si substrate:

$$A(x) = S(x) - S(x-1) \tag{4.8}$$

where x is measured in nm. Furthermore we perform Finite-Difference Time-Domain (FDTD) simulations in which Maxwell's equation are explicitly solved, and obtain numerically the absorption spatial distribution in order to compare it with the analytically one extracted from the above model. We assume two multilayer structures with different volume ratios of silver, one with $f_{Ag} = 33\%$ (20 repetitions of 4nm AlN/2nm Ag bilayers on Si substrate, with a total multilayer thickness $l_{tot} = 120nm$) and one with $f_{Ag} = 66\%$ (20 repetitions of 2nm AlN/4nm Ag bilayers on Si substrate, total multilayer thickness $l_{tot} = 120nm$), described by the thickness and dielectric functions of the individual layers, and obtain a detailed map of the UV (λ=193 nm) absorption spatial distribution. On the other hand the analytical absorption profile is calculated by the analytical model, taking only in account the effective medium dielectric function and the total thickness of the multilayer. Comparing numerical and analytical absorption spatial profiles for the two silver volume ratios we find excellent agreement as it is illustrated in fig 3.a and b. From now on we use the analytical model to obtain the absorption spatial distribution in the multilayer and Si substrate.

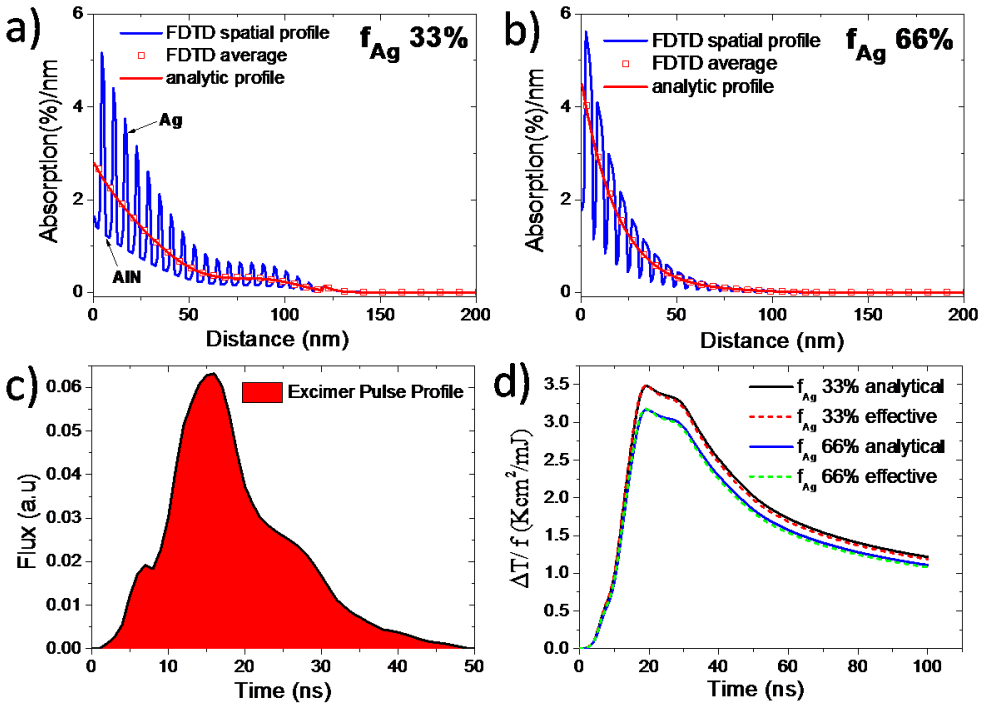

Figure 3. UV (193 nm) absorption spatial distribution in our multilayer structure (20 AlN/Ag bilayers on Si, total thickness 120nm) extracted numerically (FDTD) and analytically, from the top of the multilayer down to the Si substrate, for two volume ratios of Ag a) 33% and b) 66%. c) The temporal pulse profile of the excimer laser. d) Explicit and effective medium-based normalized temperature transients at the top of the multilayer for the two Ag's volume ratios in a w-AlN matrix (280 W/mK).

The obtained absorption spatial distribution $a(z)$ combined with the excimer laser pulse profile $\varphi(t)$ (fig. 3.c) are used as the laser induced heating source $Q(z,t) = a(z) \cdot \varphi(t)$, and solved in the 1D heat transport equation described in section 2.4. By time integrating the heat transport equation we arrive at the transient temperature at each point in the multilayer volume normalized to the total laser fluence *f*, i.e. in degrees per mJ/cm^2 (fig 3.d). We stress here that in this part we only study the linear heat transport regime to get insight into the temperature transients and gradients that can be developed, and do not consider nonlinear effects on the materials properties, nor the thermodynamics of phase changes, e.g. melting and resolidification. Regarding radiation and convection losses from the top surface, a simple estimate suffices to show that they are of no consequence, and will be presented in the next section after we obtain our first estimates on the temperature profiles created during the laser treatment.

In the heat transport calculations we follow the effective medium approach similarly to optics calculation. We first simulate the whole multilayer structure formed of 20 repetitions of AlN/Ag bilayers which is described by the individual layer thickness and material parameter. The materials' paremeters mass density $\rho(z)$, heat capacity $c(z)$, and thermal conductivity $k(z)$ are taken from literature [81], their

values and optical constants are shown in table 1. All of them have a spatial dependence due to the interchange of different materials. We also simulate the effective multilayer structure described by the total thickness of the multilayer and the effective medium materials parameters. The effective thermal conductivity and capacitance are defined as [81]:

$$k_{eff} = \frac{k_{AlN} k_{Ag} (l_{AlN} + l_{Ag})}{k_{Ag} l_{AlN} + k_{AlN} l_{Ag}}$$

$$(c\rho)_{eff} = f_{AlN} (c_{AlN} \rho_{AlN}) + f_{Ag} (c_{Ag} \rho_{Ag}) \quad (4.9)$$

Thus, we obtain the explicit and effective normalized transient temperatures at each point in the multilayer volume for the two Ag's volume ratios. Comparing explicit and effective transient temperatures we find excellent agreement at each point in the multilayer volume and the substrate for both volume ratios. This agreement is depicted in fig 2.d in which we compare the transient temperatures at the top of the multilayer. The effective material description is much more convenient given that it allows us to use a much larger grid size compared to the one required in the explicit model (note that the individual layer thicknesses are ~2nm). Given the large gain in computational speed, from now on we only use the effective parameters to extract the normalized transient temperatures.

So far we have developed a semi-analytical opto-thermal model which provides the normalized transient temperatures at each point in the multilayer structure. Utilizing this model we calculate the peak temperature spatial distribution for each point from the top of the multilayer down to the Si substrate. Peak temperature can be a critical parameter for the final distribution of the embedded NP's in the dielectric matrix after LA process and is strongly related to the Ag's volume ratio, the thermal conductivity of AlN and the total thickness of the multilayer. We continue now by exploring each one of the above parameters.

Table 1. Material values used in the opto-thermal calculations.

Material	n	κ	Mass Density ($grcm^{-3}$)	Heat Capacity (J/KgK)	Thermal Conductivity (W/mK)
AlN	1.57	0.19 [78]	3.26	740	10 - 285
Ag	1.03	1.18 [77]	10.49	235	429
Si	0.88	2.76 [77]	2.33	710	149

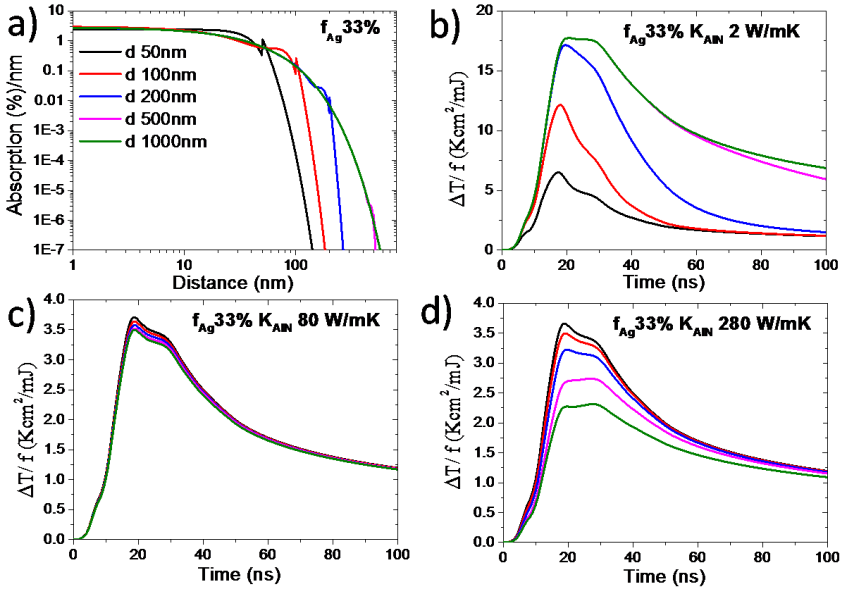

Figure 4. a) UV (193 nm) absorption spatial distribution from the top of the multilayer down to the Si substrate, for five AlN/Ag multilayer thicknesses (50nm, 100nm, 200nm, 500nm, 1000nm) extracted from the explicit simulation model. Normalized transient temperatures on the top of the multilayer, for five thicknesses and three AlN thermal conductivities: b) a low value 2 W/mK (a-AlN) c) a middle value 80 W/mK and d) a high value 280 W/mK (w-AlN).

Utilizing the semi-analytical model for opto-thermal calculations, described above, we present the absorption spatial distribution (fig 4.a) and the normalized transient temperatures (fig 4.b, c and d) of the nano-composite thin film for different thicknesses and dielectric thermal conductivities of AlN (k_{AlN}). The k_{AlN} is sensitive to the deposition method and conditions, and can show a large variations ranging from 2 W/mK for amorphous AlN (a-AlN) [82] to 285 W/mK high crystalline AlN (w-AlN) [83]. To explore its effect, we plot the temperature transients for several different values of k_{AlN}. We observe that for low k_{AlN} values 2 W/mK (Fig 4.b), increasing the thickness of the nano-composite results into an increase of the temperature on the top of the multilayer, because the total thermal insulation is increased proportionally to the thickness. The laser's thermal flux is diffused slowly from the top of the multilayer down to the Si substrate, which has a high thermal conductivity 149 W/mK, and thus results into higher temperatures. This effect stops for increasing k_{AlN}, because the thermal flux diffuses faster into Si and any increment of thickness does not significantly affect the temperature (fig 2.c). Thus, because of higher effective thermal conductivity of multilayer, we get much lower temperatures than those with low k_{AlN} values. On the other hand, for even higher thermal conductivity, e.g. 280 W/mK (fig 1.d), increasing the nano-composite thickness causes the temperature to decrease, because the total effective thermal conductivity is now larger that of Si, which now becomes the thermal bottleneck. Also in effect is the fact that the thermal capacitance of the composite is larger than that of Si, and so increasing its thickness also results into smaller temperatures.

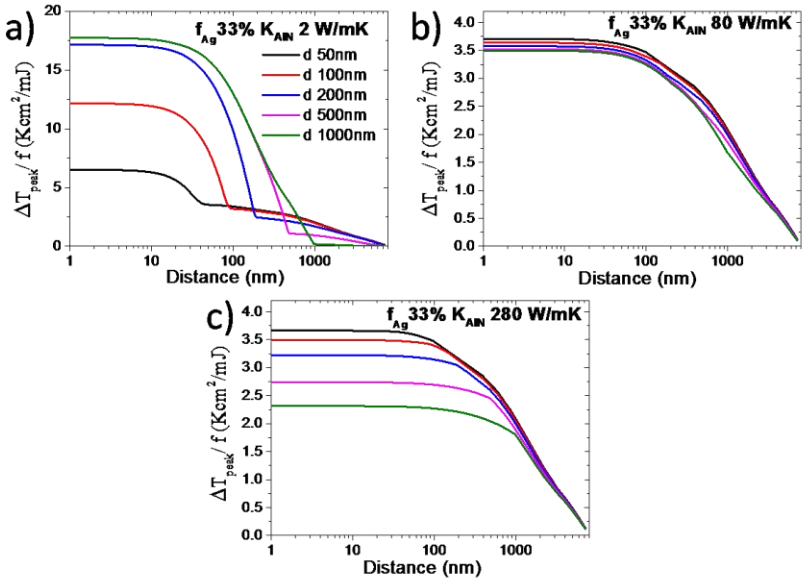

Figure 5. Peak-temperature spatial distribution at each point in the multilayer from the top down to the Si substrate, for three AlN thermal conductivities: a) 2 W/mK b) 80 W/mK and c) 280 W/mK.

Furthermore, we plot the peak temperature at each point in the multilayer volume from the top of the multilayer down to the Si substrate (Fig5 a, b and c) for three k_{AlN} values. We observe the same trend as we explained before for the normalized transient temperatures. Also, at low k_{AlN} values (fig 5.a) we observe that the peak temperature at the first nanometers of the Si substrate is decreased increasing the thickness of the multilayer thus, because the thermal flux spends more time in the multilayer and diffuses slowly in the Si substrate (the equivalent of using a wider pulse with the same total pulse energy).

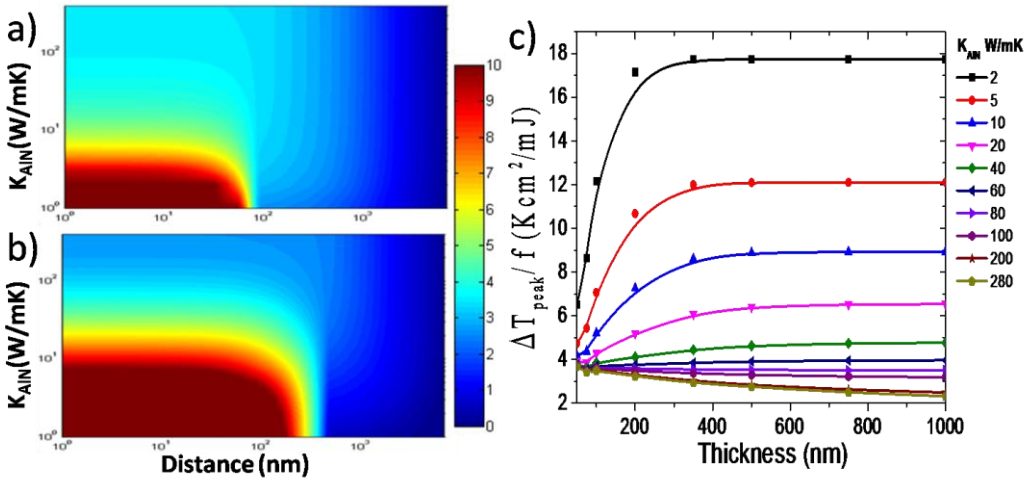

Figure 6. Map of the Peak-Temperature absorption spatial distribution from the top of the multilayer down to the Si substrate (1nm - 8 μm) as a function of k_{AlN} (1-400 W/mK) for two multilayer's thicknesses a) 100 nm b) 500 nm. c) The Peak Temperature on the top of the multilayer as a function of its thickness for various k_{AlN} values. The silver volume ratio is 33%.

At this point we examine the dependence of k_{AlN} on to the peak temperature spatial distribution across the multilayer structure and the Si substrate. Here, we suppose a wide range of k_{AlN} (1-400 W/mK) above the aforementioned limits (2-285 W/mK) in order to expand our calculations to a wider range of dielectric materials. In doing so, we plot the peak temperature spatial distribution as a function of k_{AlN} for two multilayer's thicknesses, 100 nm (fig. 6.a) and 500 nm (fig. 6.b). We observe that for high of k_{AlN} values the temperature gradient is almost constant across the multilayer. For low k_{AlN} values on the other hand, a significant temperature gradient is developed across the multilayer, the same trend is observed for both multilayer thicknesses. Higher temperatures close to the surface and lower temperatures close to the substrate will result into different annealed conditions across the nano-composite thickness. Comparing now the two thicknesses and focused on the Si substrate we observe that the smaller the thickness, the higher the temperatures at the top of the Si substrate, as we have explained before. We perform the same calculations for a nano-composite of 66% of Ag's volume ratio and we observe the same trend, but with lower temperatures due the high thermal conductivity of silver, which results into a higher effective thermal conductivity of the multilayer.

Furthermore, we examine the dependence of the the temperature on the multilayer thickness. In doing so, we plot the peak temperature on the top of the multilayer as a function of thickness for various k_{AlN} values, as plotted in fig 6.c. We observe that for low k_{AlN} values and low increases of the film thickness, the temperature increases rapidly, but by further increasing the thickness the temperature becomes constant. That's because the thermal insulation provided by the resistive film increases with thickness, and after a point the peak temperature at the top saturates to a specific value. This effect is less intense for higher k_{AlN} values, because the effective thermal conductivity is increased. We also observe that for $k_{AlN} = 80W/mK$ the temperature is almost constant for all the thicknesses' values: here the effective film behaves similarly to silicon, and thus increasing its thickness is of no consequence. Above this value the effect is reversed, i.e. the temperature decreases as the film thickness is increasing. That's because for high k_{AlN} values the thermal diffusivity is very high and the thermal capacitance becomes the crucial parameter: increasing the thickness, thermal capacitance is increased and thus results to lower temperatures as we mentioned above.

5.2.2 Combined discussion on theory and experiments

In this section we present relevant recent experiments and apply the above-described theoretical opto-thermal modeling to understand the light-matter interactions and heat diffusion mechanisms taking place in these experiments. Specifically, we present the results of a single ultra-short UV laser annealing (LA) step on a ceramic/metal (in particular AlN/Ag and Y_2O_3/Ag) multilayer film. We demonstrate that this LA step is capable of driving the subsurface modification of the metallic multilayers resulting into localized surface plasmon resonance (LSPR) behavior from NPs that are formed and dispersed in a depth of several nm away from the surface. We present an extensive investigation considering the morphological (thicknesses of the individual layers) and microstructural (crystallinity of ceramic layers) features of the multilayers, their thermal conductivity, as well as the fluence of the laser and the environmental pressure during LA. The experimental results are complemented by detailed photo-thermal calculations to obtain insights on the basic mechanisms of morphology change upon LA.

Specifically, multilayers consisting of alternate thin layers of AlN and Ag were fabricated in an in-house built high vacuum system employing the dual cathode reactive magnetron sputtering. The AlN crystal structure was varied in the two sets of AlN/Ag by applying two different power values to the Al target, 100W and 15W. This variation leads to different categories of sputtered AlN as indicated from XRD measurements [46]: at 100W we obtain high crystalline wurtzite AlN (w-AlN) while at 15W we obtain amorphous AlN (a-AlN). The produced samples were subjected to LA with an excimer ArF source (193 nm, pulse duration of 25 ns). The effect of a single-pulse LA step onto the structural and optical properties was investigated as a function of fluence (400-700 mJ/cm^2) in an ambient atmosphere or under high pressure. Figure 7 illustrates cross sectional TEM images showing the morphology of samples before and after LA at 600 mJ/cm^2.

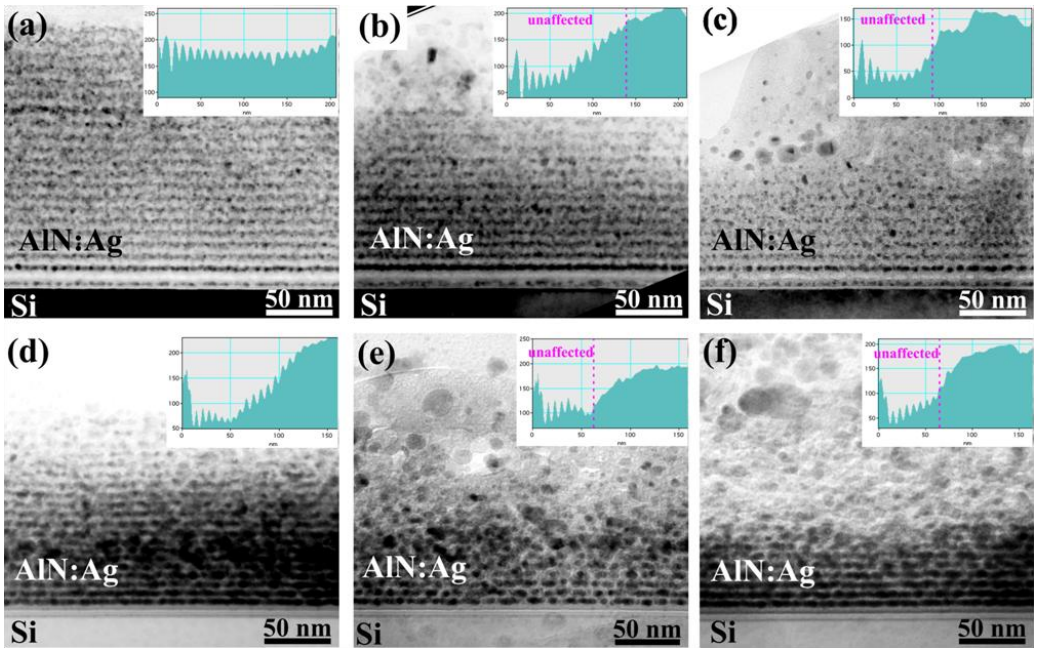

Figure 7. TEM cross sectional images of: a) the as deposited multilayer structure of w-AlN/Ag, b) the (a) after ambient LA, c) the (a) after high pressure LA, and (d) the as deposited multilayer structure of a-AlN/Ag, e) the (d) after ambient LA, f) the (d) after high pressure LA. LA fluence for all relevant samples in this figure was set at 600 mJ/cm^2 [46].

TEM observations from the as-deposited samples (fig. 7.a and b) verified their multilayer character. In both samples Ag was arranged in 21 layers. After LA treatment the upper part of the multilayer has highly effected. The multilayer structure is destroyed and the enlarged NPs are rather homogenously distributed inside the AlN matrix, retaining a high density in the case of a-AlN, while on the contrary, in the case of w-AlN the laser treated part of the sample is mostly depleted of Ag indicating a higher diffusivity of Ag in w-AlN compared to a-AlN.

Considering LA with a single pulse of 600 mJ/ cm^2 at ambient pressure, the w-AlN/Ag presents a destruction of periodicity affecting only the top six Ag layers, while two more layers are partially destroyed. The sample thickness that retains a stratified arrangement is indicated by a dashed line in the inset of fig 7.b, which depicts the contrast intensity profile along the film thickness. In the case of a-AlN/Ag, this structural re-arrangement is more extensive as shown in fig. 7.e, and it affects the top ten Ag layers, while again two additional layers are partially affected. XRD profile analysis of the Ag (111) peak of the laser-treated films confirmed the existence of a bimodal Ag size distribution corresponding to Ag grains located in the higher treated part and the lower untreated part of the film, confirming the TEM results in larger scale.

Similar results were obtained for LA experiments performed under high pressure for the case of w-AlN (fig. 7.c). Typically in LA, a high pressure environment is employed in order to suppress or even eliminate any ablation of the sample. Evidently, a high applied pressure leads to a significant extension of the periodicity destruction depth in the case of a-AlN (fig. 7.f). The variation in the NP

size distribution and of the total depth of LA process in the films can be attributed to the different thermal conductivities, k_{AlN} , of AlN, which depending on its microstructure may span more than an order of magnitude between crystalline and poorly textured AlN [82, 83]. This majorly affects the thermal energy dissipation in the surrounding medium and thus the behavior of Ag upon LA.

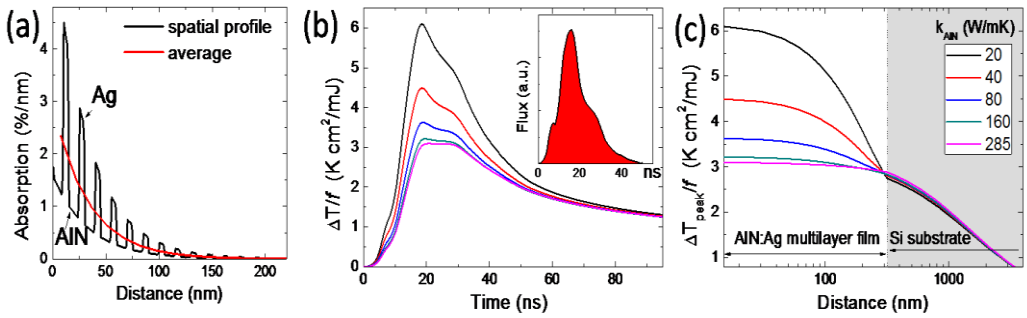

Figure 8. (a) UV laser (193 nm) absorption profile in our model structure (21 repetitions of 5 nmAg/10 nm AlN bilayers on Si). (b) Normalized temperature transient at the top of the multilayer for various values of k_{AlN} . The inset shows the pulse profile of the excimer laser, (c) the normalized peak temperature spatial distribution for the corresponding cases of (b). Large gradients across the film are obtained for low values of k_{AlN} [46].

The above considerations make AlN's thermal conductivity a crucial parameter in the LA process. k_{AlN} is sensitive to the deposition method and conditions, and can show large variations ranging from about 10 W/mK for amorphous AlN [82] to 285W/mK for single crystal [83]. To explore its effect, we plot the temperature transient (at the top of the multilayer) for several different values of the AlN thermal conductivity in figure 8.b. All other parameters are taken at their crystalline value (see table 1). A significant difference depending on k_{AlN} is found for the peak temperature rise when the laser pulse is on, but it quickly diminishes afterwards. The most important effect of k_{AlN} is shown in the spatial distribution of the peak temperature rise plotted in figure 8.c. In particular, for high values of k_{AlN} the temperature profile is almost constant across the multilayer, even though most of the laser fluence is absorbed within the first 100 nm, as shown in figure 8.a, where we plot the spatial absorption profile within the multilayer. A combinatory look on figures 7 and 8.a suggests that layers below the 8th layer of Ag do not efficiently absorb the UV laser light. This provides a recipe for future practical applications in order to avoid complex structures of 21 repetitions; it seems that 3-4 bilayers would be enough for an effective LA reconstruction featuring a plasmonic response. By the same token, however, we should also note that for fewer bilayers, the cooling through the substrate would be more effective and higher LA fluence could eventually be required. In any case, thinner films would in general result into relatively smaller temperature gradients and thus into more uniform reconstructions even for low k_{AlN} values.

Going back to our thick, 21-bilayer film, we note that for low values of k_{AlN}, a significant temperature gradient is developed across the multilayer (fig. 8.c). Higher temperatures close to the surface and lower close to the substrate will result into differently annealed structures, explaining our experimental results. We also simulated a multilayer consisting of 10nm Ag/5nm AlN (not shown here). As expected, due to the higher percentage of Ag the overall thermal conductivity of the multilayer film is much higher, and the temperature gradients developed are much smaller, even for low values of k_{AlN}. In this case, a more uniform annealing profile in the film is expected.

We stress here that up to now we have only studied the linear heat transport regime to get insight into the temperature transients and gradients that can be developed, and have not considered the thermodynamics of phase changes, e.g. melting and re-solidification. Regarding radiation and convection losses from the top surface, a simple estimate suffices to show that they are of no consequence. For example, in the extreme case of figure 8(b) and for a laser fluence of 1000 mJ/cm^2, a peak temperature of about 6000 K is achieved. If we further assume the extreme cases of unit thermal emissivity, surface-to-air heat transfer coefficient 200 W/m^{2}K (appropriate for forced air cooling [84]) and that this heat exchange with the environment occurs for 30 ns (the approximate pulse duration), we get a total energy loss of about 0.1 mJ/cm^2, which is 4 orders of magnitude smaller than the input fluence, and thus will not have any effect on the temperature transients and profiles.

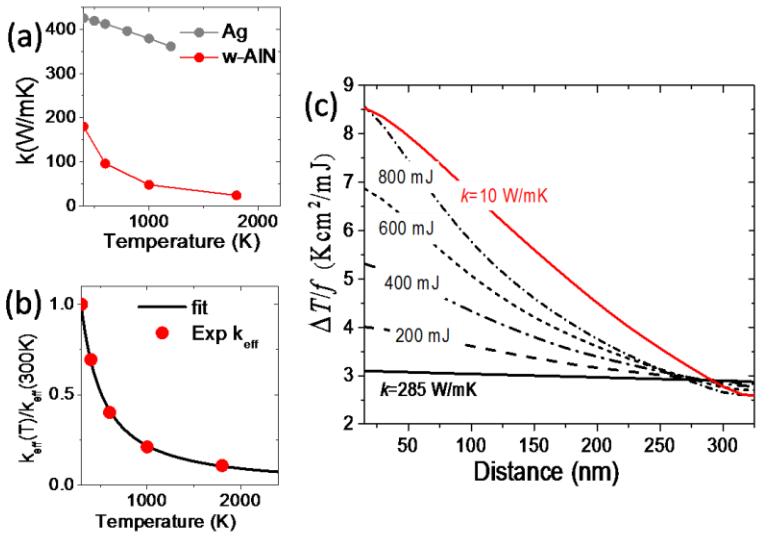

Figure 9. a) The experimental temperature dependent thermal conductivities of Ag [80] and w-AlN [83] assumed in this work. b) The effective non-linear thermal conductivity obtained from (a) for 33% volume ratio of Ag (red points) on which we perform a fit (black line) to obtain the exact non-linear thermal conductivity at each temperature. c) Peak transient temperature distribution as a function of distance from the film's top surface, at different incident laser fluence assuming the nonlinear thermal conductivity for the multilayer structure (w-AlN and Ag from (b)). Broken lines are for nonlinear w-AlN and Ag for different laser fluence. Solid lines are for the linear case (zero fluence limit) for w-AlN (k = 285 W/mK) and for an ultra-low conductance a-AlN (k=10W/m K), both for a linear Ag thermal conductivity of 429 W/m K [46].

One critical oversimplifying assumption up to now has to do with neglecting the fact that the thermal parameters of materials are actually temperature dependent. The most striking nonlinearity is found in the thermal conductivity of w-AlN, whose relative change with temperature is shown in figure 9.a. Other parameters such as thermal capacity and mass density also have a thermal dependence, but of a smaller magnitude. Since the highest temperatures are going to be reached inside the film, and to keep our discussion simple, we ignore here nonlinearities associated with the Si substrate. Utilizing the experimental temperature dependent thermal conductivities of Ag [80] and w-AlN [83] (fig. 9.a) we calculate the non-linear effective thermal conductivity according to equation 4.9 for specific Ag volume ratio ($f_{Ag} = 33\%$), depicted by the red points of fig. 9.b. In order to extract the exact effective thermal conductivity at each temperature we fit (black line fig. 9.b) the experimental temperature depended effective thermal conductivity with:

$$k_{eff}(T) = k_{eff}(300K) \times aT^{b} \tag{4.10}$$

where $k_{eff}(300K) = 321W/mK$ and a , b are fitting parameters with a = 1233 and $b = -1.25$. Having parametrized the non-linear thermal conductivity we are able to calculate the transient temperatures at each point in the multilayer structure from the heat transfer equation which now becomes:

$$(c\rho)_{eff}(z)\frac{\partial T(z,t)}{\partial t} = \frac{\partial}{\partial z}\left[k_{eff}(T(z,t))\frac{\partial T(z,t)}{\partial z} \right] + Q(z,t) \tag{4.11}$$

In figure 9.c we plot the peak transient temperature distribution as a function of distance from the film surface for different laser fluence. For comparison we plot the linear response of w-AlN (solid black line) and of a linear a-AlN with k=10W/mK (solid red line). The nonlinear multilayer lines span the space between the two linear curves as the incident fluence increases. Thus the nonlinearity in thermal conductivity increases the temperature gradients developed in the film. Interestingly, the gradients are generally sharper in the nonlinear w-AlN case (e.g. compare the 800 mJ case with the linear a-AlN k=10W/mK case, where the peak surface temperatures are the same), meaning that a composite with a matrix of high thermal conductivity (e.g. w-AlN) will get restructured only close to the film's top surface, while a composite with a matrix of low thermal conductivity (e.g. a-AlN) will get restructured within a wider length inside film. This perfectly explains the behavior observed in our experiments, as seen in the TEM images of figures 7(b), (e) and (c), (f).

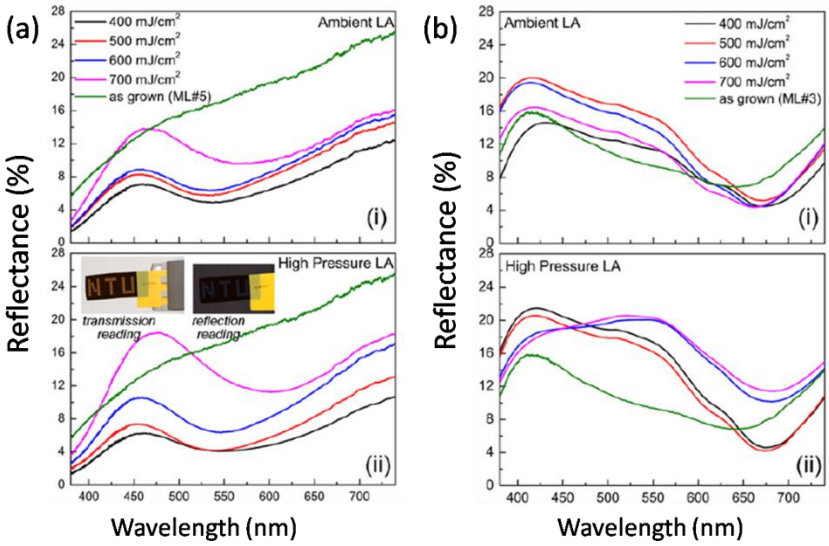

Figure 10. (a) ORS of LA processed a-AlN/Ag multilayer under ambient environment (i) and under high pressure (ii), (b) ORS of LA processed w-AlN/Ag multilayer under ambient environment (i) and under high pressure (ii). The corresponding spectra from the as-grown samples are also shown for comparison. Inset digital photos in (a), in white light reflection and transmission mode, depict sample a-AlN grown on PET subjected to LA at 700 mJ/ cm^2 [46].

As expected, the size and distribution of Ag NPs within the amorphous or nanocrystalline AlN matrix determines their LSPR. In figures 10.a and b we present the experimental optical reflectance spectroscopy (ORS) data from a-AlN and w-AlN, respectively. In addition, the insets of figure 10.a (ii) demonstrate an example of a multilayer sample deposited on PET subjected to LA at 700 mJ/cm^2 under high pressure. These digital photos, in white light reflection and transmission mode, clearly present the plasmonic response (i.e. different reflection and thus different color) of the treated areas of the film. The optical response of these samples is in agreement with the above mentioned experimental results and the outcomes of the photo-thermal modeling. Indeed, in the case of a-AlN the low k_{AlN} values, allows for high temperatures to be developed inside the film's volume, and thus to NP enlargement with a broad plasmonic response and a monotonic increase in reflection intensity. At the same time the red-shift of the LSPR spectral position with respect to the fluence can be attributed either to the formation of bigger Ag NPs and/or to the formation of a more dense environment, possibly by changing the refractive index of the host [46]. On the contrary, for the case of w-AlN (figure 10.b) the narrow reconstruction length, in relation to its nanocrystalline character, leads to a non-monotonic behavior of the LSPR characteristics with respect to the fluence. Clearly, higher reflectance values are observed at high pressure LA, probably as a result of the suppression of Ag outdiffusion.

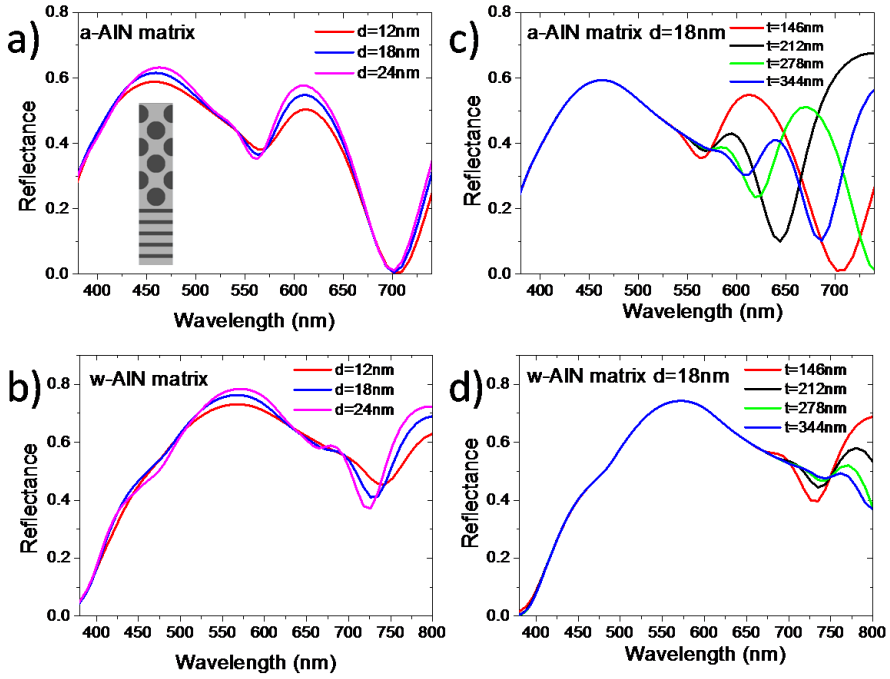

Figure 11. Calculated optical response of Ag NPs inside an a) a-AlN and b) w-AlN matrix for three particle sizes. The Ag NPs are arranged in an fcc lattice (Ag volume filling ratio of 33%) extending 140nm from the surface, leaving five bilayers of 5nm Ag/10nm w-AlN (i.e. 75nm) unstructured before the Si substrate. A projection of the simulated structure for NPs of diameter d=24 nm is shown in the inset. c) Same configuration as (a) increasing only the thickness (t) of the structured Ag NPs arrangement from 146 nm up to 344 nm for the same NPs' size d=18nm. d) Same configuration as (b) increasing only the thickness (t) of the structured Ag NPs arrangement from 146 nm up to 344 nm for the same NPs' size d=18 nm.

To better understand the optical characterization results, we calculated the optical reflectance from a distribution of Ag NPs inside an a-AlN matrix and a w-AlN matrix and compare it with the corresponding experimental ORS of LA processed samples. For simplicity we assume the Ag NPs to be arranged in an fcc lattice, for a reconstructed thickness of 140 nm, leaving five bilayers of 5nm Ag/10nm w-AlN (i.e. 75nm) unstructured before the Si substrate (see inset in fig. 11.a). We consider three different particle sizes at fixed volume filling ratio of 33%. In fig 11.a we observe two peaks, the first one is around 450-475 nm, it corresponds to NPs' LSPR, is red-shifted increasing the NPs' size and becomes more intense. The calculated optical response is in good agreement with experimental ORS of the corresponding annealed structure of a-AlN (fig. 10.a), in which we observe that increasing the fluence of LA, the LSPR is red-shifted and becomes more intense at the same wavelength range 450-475 nm. The second peak at 600-625 nm corresponds to film's multiple reflections, is verified in fig. 11.c in which we observe that increasing the thickness of the structured NPs arrangement with respect to the NPs' size and volume filing ratio, multiple reflections are differentiated but the LSPR is not, because it depends only from the NPs' size and distribution. The absence of multiple reflections at experimental results could be attributed to the high absorbance of the a-AlN matrix which is underestimated in our simulations.

The same trend is observed in the case of the w-AlN matrix (fig. 11. b), in which the NPs' LSPR is slightly red-shifted and becomes less intense as NPs' size increased, at the spectral range of 550-575nm. This is in good agreement with the corresponding experimental results and in particular for the case of laser annealing the w-AlN structure under high pressure with 600 and 700 mJ (fig 10.b.ii), for NPs' diameter of 18nm and 24nm respectively. The rest of the resonances in fig.11.b above 700nm, correspond to the film's multiple reflections, as verified in fig. 11.d in which we observe that increasing the thickness of the structured NPs arrangement with respect to the NPs' size and volume filing ratio, multiple reflections are differentiated but the LSPR is not as we explained above. Multiple reflections are also observed in experimental ORS of w-AlN, which correspond to the dips above 650nm fig.10.b (ii), and are clear here because of the lower absorption of high crystalline w-AlN compared with the low crystalline a-AlN. Furthermore, we verify that there is a small red-shift of the LSPR peak as the Ag NP size increases. This is expected: the LSPR of NP arrays red-shifts for increasing NP size and blue-shifts for increasing relative (i.e. distance/radius) NP separation [85]. For a fixed NP volume filling ratio (i.e. assuming no metal is diffused out of the film), however, the relative separation remains fixed, and so we only expect to observe a red-shift with NP size increase.

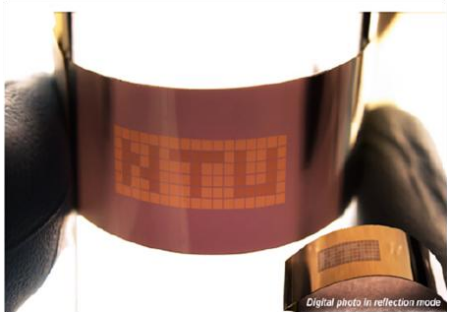

Figure 12. Digital photo of a flexible plasmonic demonstrator capable of optical reading. Photo captured under white light illumination in transmission and reflection (inset) mode. The spots reading 'NTU' were fabricated by LA of the sample with 25 pulses at 15 mJ/cm^2 whereas the surrounding matrix spots were annealed with 1 pulse of 45 mJ/cm^2.[46]

Finally, we present a demonstration of "plasmonic optical encoding and reading" on an Y_2O_3/Ag thin film on a PET substrate. The Y_2O_3 matrix was chosen because of its low thermal conductivity [86] which works as an efficient barrier protecting the underlying PET film from high temperatures. The digital photo of figure 12 represents the sample's appearance in transmission mode under white light illumination (its appearance in reflection mode is also presented in the inset of figure 12). Specifically, 'NTU' (Nottingham Trent University, who was the academic partner performing the laser annealing experiments) spots were fabricated by delivering 25 pulses of 15 mJ/cm^2 while the surrounding matrix was fabricated by delivering a single pulse of 45 mJ/cm^2. The minimum feature size of this type of 'plasmonic writing' is only limited by the LA wavelength and instrumentation, and

could thus easily reach the sum-micron regime. Thus, we have demonstrated the cold character of LA by creating plasmonic templates on flexible polymeric substrates. From the point of view of applications on optical encoding of information, these examples signify the simplicity, flexibility and versatility of the proposed engineering approach. An additional feature of the produced encapsulated plasmonic NP patterns is their capability of providing two views of the same image with complementary colors in reflection and transmission.

5.3 Surface nano-structuring

5.3.1 Theoretical Aproach

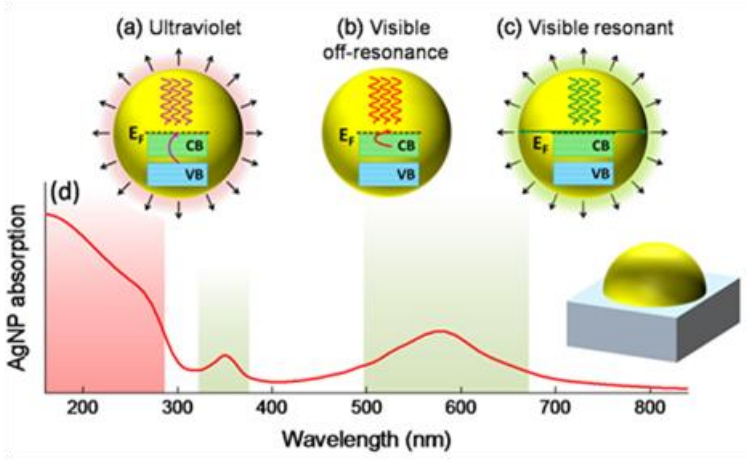

Figure 13. (a-c) Schematic representation of the main physical mechanisms of absorption we exploit in the current work and their corresponding thermal effect on metallic nanostructures. d) Calculated absorption spectrum of a 40 nm diameter Ag nanoparticle (Ag NP) on top of a Si substrate, as shown in the inset schematic. Interband absorption (mode a) dominates the red shaded region, while intraband absorpiton (LSPR driven, mode c) is dominating the green shaded regions (at ~350 nm the quadrupole 428 and ~580 nm the dipole LSPR contributions respectively).

Plasmonic templates can be fabricated by LA annealing of a thin metal film on a substrate, resulting into nanoparticle arrangements with many plasmonic applications (mentioned in Introduction). At the very heart of these applications lie the light-matter interactions, in the form of coherent surface plasmon oscillations excited by the incident light at specific frequencies, with high selectivity on the metal nanostructure's size and shape. But selective plasmon excitation translates into selective light absorption, and thus into selective heating of the nanostructure. It is natural thus to allow this core property of the target application to become itself one of the drivers in a multi-pulse laser induced self-assembly process, i.e. a repeated heating, melting and resolidification process, driving the NP formation and self-assembly. Furthermore, besides heating, selective cooling is also an integral part of restructuring. But as the cooling rate depends on the geometric features of the nanostructure, a second driver for the self assembly process is introduced.

The available light absorption mechanisms in the case of nano-structured noble metals such as Ag, Au and Cu, can be intuitively summarized in the following modes:

a) interband absorption, probing the metal's internal d-electrons (fig.13.a). This is typically enabled at UV frequencies and in general is not size-dependent,

b) off-resonance intraband (free electron) absorption (fig.13.b), which however is too weak to cause substantial temperature rise,

c) resonant intraband absorption (fig.13.c), probing the conduction electrons with laser wavelengths close to the spectral position of LSPR. This mechanism is strongly size and shape-selective.

As an example, the overall absorption profile of an Ag nanoparticle (hemispherical shape) with diameter of 40 nm on top of a Si substrate is plotted in fig. 13.d, showing the spectral domains of the two absorption mechanisms. Utilization of modes (a) and (c), combined with the size selectivity of cooling (~nanostructure surface/volume ratio) provides an exceptional tool for controlling the self-assembly of nanoparticles. Computer simulations can help us explore the potential of these tools, thus we examine NPs of different sizes and arrangements at the whole UV and optical spectrum. The computational procedure is presented above.

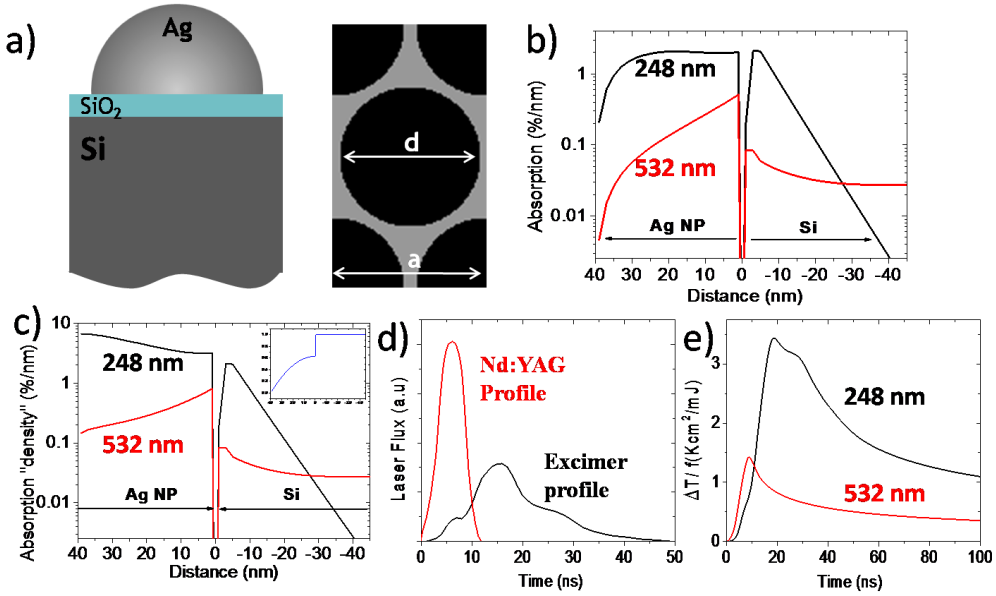

Figure 14. a) Schematic of the simulation system front view and top view respectively, involving a hexagonal lattice of Ag hemispherical NPs at a period (a) to diameter (d) ratio 1.2. b) Absorption percentage per nm vertical distance from the top of the NP (diameter 80nm) down to the Si substrate, for the two main LA wavelengths. c) Absorption "density" (%/nm) which is produced from the absorption spatial distribution (b) normalized by the absorbing cross sectional area of the NP (inset graph). d) The laser pulse temporal profiles assumed in the theoretical study correspond to that of an excimer laser (for the 150 - 280nm range) or that of a Nd:YAG (for the 300 - 900 nm range). Both profiles were experimentally determined. e) Normalized transient temperature rise (in degrees per mJ laser fluence) at the NP center for the 80 nm Ag dome, for the LA wavelengths.

As a starting point, we assume that after some laser treatment of a thin silver film on a Si substrate, Ag NPs with specific diameters has been formed on the top of the Si substrate. Our target is then to consider what the effect of a new incoming laser pulse would be. We assume a hexagonal lattice of Ag-hemispheres on a Si substrate for different separation aspect ratios (periodicity (a) / diameter (d)). A schematic of the simulation system is depicted in fig 14.a. We assume three extreme cases, when NPs are slightly overlapping with each other (separation aspect ratio 0.9), when the NPs just attach each other (separation aspect ratio 1), and when the NPs are well isolated (separation aspect ratio 1.2). A cross section of the final case is illustrated in fig.14.a in order to present the photo-thermal procedure. The NP's diameter range from 10nm-120nm, which span the experimentally relevant sizes as obtained from AFM and SEM images.

For the optical calculations, a full-vector 3D FDTD simulator is used in order to capture all possible absorption mechanisms. The absorption spatial distribution is calculated for a wide range of frequencies, in the UV (150nm-280nm) and visible spectrum (300nm - 900nm). The fraction of light absorbed in the sample, expressed as the percentage of the incident radiation absorbed per nm of vertical distance, is calculated (Fig 14.b) for the two primary wavelengths used in experimental study (λ=248 nm from the excimer laser and λ=532 nm from the Nd:YAG laser) for Ag hemispheres of 80 nm diameter. Very efficient UV absorption is obtained for both Ag and Si due to strong direct interband transitions in both materials, while much weaker absorption if found in the visible. For demonstration reasons, this absorption spatial distribution can be normalized by the corresponding cross-sectional absorbing area of the NP (inset graph of fig. 14.c), to get the phenomenological absorption "density" (fig. 14.c).

The absorption spatial distribution is time-integrated with the appropriate laser's temporal profile for each wavelength, depicted in fig. 14.d (excimer for the 150-180nm range and Nd:YAG for the 300-900 nm range), in a numerical solution of the numerically 1D heat transport equation presented in section 2.4. Thus, we get the temperature transient profile at every point in the structure in degrees/mJ laser fluence. In figure 14.e we present the temperature transients for the two primary wavelengths used in experimental study. This way we get the mapping of the maximum temperature rise as a function of particle size, laser wavelength and laser fluence. As a higher temperature for a particular size group means the melting of this group and the survival of the others, these maps can provide a recipe that allows the design of pre-determined plasmonic arrangements.

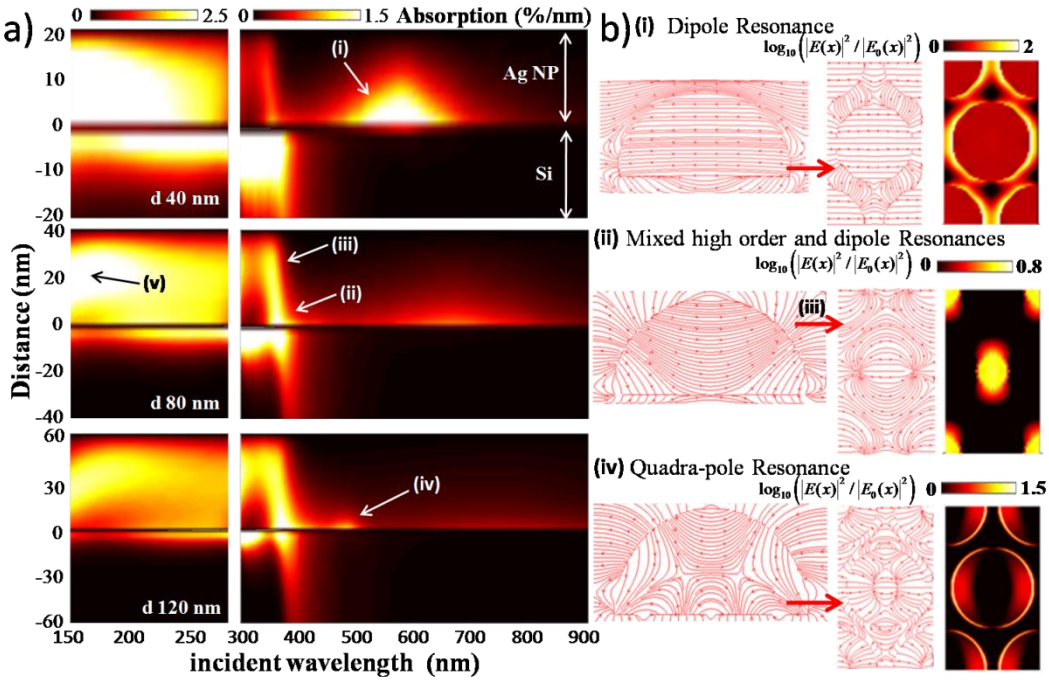

Figure 15. a) Color map of the absorption profile (in percent per nm vertical distance) from the top of the NP down to the Si substrate for three NP diameters (40 nm, 80 nm, 120 nm), at separation aspect ratio a/d = 1.2, plotted for UV (150 nm – 280 nm) and UV-NIR (300 nm – 900 nm) wavelengths. The inset arrows show the main absorption mechanisms, the first four (i, ii, iii, iv) are related to Ag intraband (mode c in fig.13) transitions and the fifth (v) are related to Ag interband transition (mode a in fig.13). b) Electric field spatial distribution plotted at vertical (at the middle of NP) and horizontal (at specified positions on NP's volume shown by the red arrows) cross sectional planes, at resonance wavelengths, in order to identify the intraband resonances. The color maps are the horizontal cross sections of electric field's enhancement. Both of them are shown for the corresponding size depicted by the arrows in (a). The resonances are: (i) dipole LSPR located at the bottom of the NP (573 nm), (ii, iii) mixed high order (365 nm) and dipole (345 nm) resonances located throughout the NP's volume, (iv) quadrupole resonance (484 nm) located at the bottom of the NP, but clearly seen only for big NPs'.

First, we explore the different absorption mechanisms which are size selective and enable geometric specificity. In fig. 15.a we present the absorption spatial distribution as a function of wavelength from the top of the NP down to the Si substrate for three NP's diameters. At the UV zone (150 nm-280 nm) the absorption is taking place through the interband's transitions of metals d-electrons. We observe that by increasing the NP's size, most of the absorption is taking place in the NP's volume and less occurs in the Si substrate. On the other hand, in the optical zone (300 nm-900 nm) most of the absorption is taking place through the intraband transitions of metal's free electrons, and we observe different resonances.

To identify these resonances we plot (fig.15.b) a vertical cross section of the E field distribution taken in the middle of the NP, a horizontal cross section of the E field distribution taken at specific points on the NP volume, as well as vertical cross sections of the logarithmic E field enhancement $\log_{10}\left(|E(x)|^2/|E_0(x)|^2\right)$. In fig 15.b.i we observe a dipole resonance which is located at the bottom of the NP and related to

the NP free electron oscillations near the substrate. We also notice in the absorption profiles the well known red shift as the NP's diameter is increased and the reduction in absorption. The other resonances between 345nm - 400nm (15.b.ii, iii) are located within all of the NP's volume and involve higher order LSPR modes screened mostly by the substrate (ii) or a dipole LSPR in the upper part of the NP screened mostly by the surrounding air (iii). Specifically, for big NPs we observe a quatrupole resonance which is located to the bottom of the NP and related to NP's free electron oscillations near to the substrate (15.b.iv).

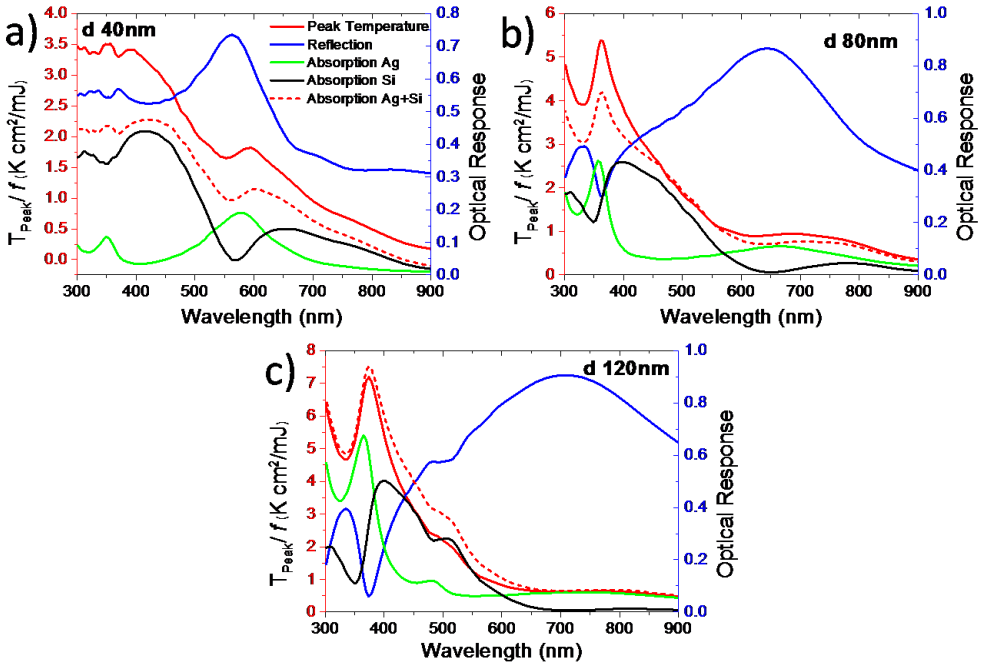

Figure 16. The peak temperature at the middle of the NP as a function of wavelength, plotted in the red axes, and the reflection, absorption taking place in Ag NPs, absorption taking place in 1 μm of Si substrate and the sum of the two absorptions, plotted in blue axes. The separation aspect ratio of the hemispheres is 1.2 for NP arrangements of a) 40 nm b) 80 nm and c) 120 nm diameter.

There is a very interesting interplay with the intraband resonances (shown in fig. 16), where at the exact resonance wavelength we have lower temperature due to enhanced reflection, while at slightly longer wavelengths the temperature reaches a peak. The peak temperature is observed when the sum of the absorption in Ag and Si is increased. The absorption in Ag NPs at resonance wavelengths is red-shifted compared to the reflection, with the red-shift increasing for large NPs. On the other hand the absorption in Si substrate is enhanced away from Si interband transitions (which are below 400 nm) due the electric's field enhancement at the vicinity of the Ag NPs, at the resonance wavelength. The contribution of the two different materials' absorptions results into the wavelength dependence of the peak temperature. This feature provides an interesting mechanism for size control, whereby the NPs whose LSPR falls exactly at the same wavelength of the LA, will have enhanced reflection and less absorption, resulting that into lower temperatures rises.

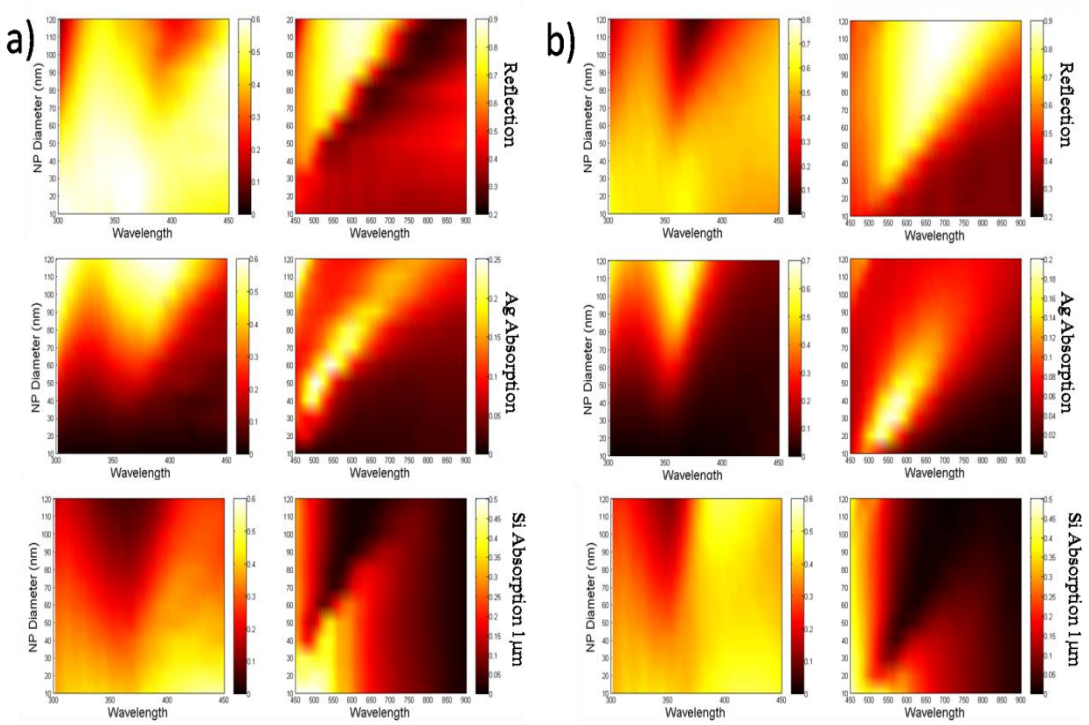

Figure 17. The size dependent optical response as a function of wavelength, in the near UV zone (300 nm – 450 nm) and visible zone (450 nm – 900 nm): a) an average of NPs slightly overlaping each other (a/d=0.9) and of NPs attaching each other (a/d=1), b) NPs fairly isolated (a/d=1.2).

Understanding the maximum temperature rise as a function of particle size and wavelength is thus of crucial importance. Toward this goal, we plot the optical response (fig.17) as a function of NPs' diameter (10 -120nm) and wavelength for two NPs' arrangements. The first one is when the NPs are slightly overlapping or just touching each other (fig.17.a) and the second one when the NPs are fairly isolated (fig.17.b). In the first spectral range (300 - 450 nm) we observe high reflectance especially for small NPs of the first case (fig.17.a) where the metallic NPs pose an almost uniform metallic surface. Increasing the size we observe the aforementioned resonances which involve a higher order LSPR modes screened mostly by the substrate (fig.16.ii) or a dipole LSPR in the upper part of the NP screened mostly by the surrounding air (fig.16.iii), which is depicted in the NPs absorption. Also at this spectral range Si is characterized by high absorption which is depicted in both cases (17.a and b). Also notice that the absorption in Si decreases at the spectral ranges of maximum reflection, as was mentioned before. In the second spectral range (450nm-900nm) we observe that the reflection increases and red-shifts as the NPs' size increases, due to the dipole LSPR mode (fig. 16.i). This resonance enhances also the absorption in Si away from its absorptive spectral region as was mentioned above. The contribution of both absorption will result into a temperature spectral dependence on the NPs size.

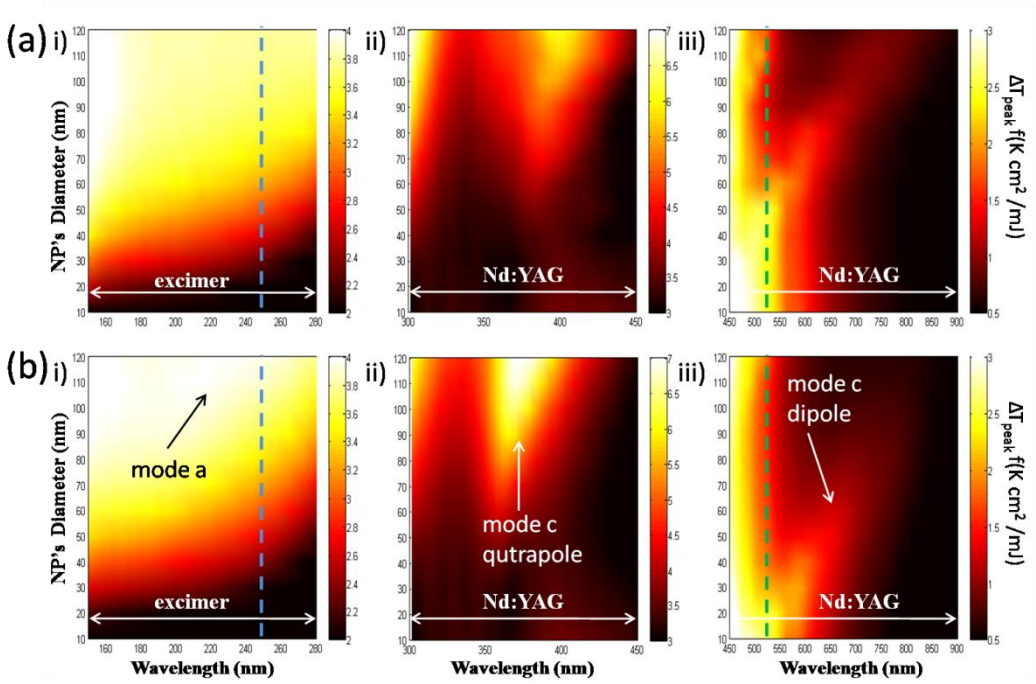

Figure 18. Normalized peak temperature as a function of irradiation wavelength and NP's size, for two arrangements: a) an average of NPs slightly overlaping each other (a/d=0.9) and of NPs attaching each other (a/d=1), b) NPs fairly isolated (a/d=1.2). These are ploted in the three wavelength zones: i) UV zone (150 nm-280 nm) utilizing the excimer temporal profile, ii) near UV zone (300 nm - 450 nm) utilizing the Nd:YAG temporal profile and iii) visible zone (450 nm – 900 nm) utilizing the Nd:YAG temporal profile. Indicated with the two dashed lines are the two primary laser wavelengths used in this study, at 248 nm excimer laser and 532 nm Nd:YAG laser used at UV and visible zone respectively. The different heating regimes are attributed to the different absorption modes and different cooling geometries, and can be utilized to tailor-design the LA process.

Taking into account the absorption spatial profile from the top of the NP down to the Si substrate, for each NP between 10 nm-120 nm and for both arrangements, we arrive at the map of the maximum temperature rise as a function of NP's size, wavelength and laser's fluence, utilizing in each spectrum the appropriate lasers temporal profile (figure 18). In these maps we can distinguish areas of higher and lower temperature. Thus, by sequentially tuning the LA wavelength to match with different absorption mechanisms and applying the proper lasers power, we can selectively target the melting and resolidification of different particle size groups. Specifically, in the UV zone utilizing the interband transitions (mode a) we can remove the big NPs and arrive at nanostructures with small size distributions. In near-UV, utilizing the intraband transitions, especially the higher order resonances (mode a), we can also remove the big NPs. Finally, small NP's can be removed in the visible zone utilizing dipole resonance (mode c). Combining the different absorption mechanisms we can target at specific NPs' size groups and arrive at nanostructures with predesigned morphology. This is the main concept behind our approach: repeated laser treatments, targeting different nanoparticle size groups with different laser wavelengths, driving the size distribution to the final predetermined one. We call this process "Modification of Nanoparticle Arrays by Laser Induced Self Assembly" (MONA-LISA).

5.3.2 Combined discussion on theory and experiments

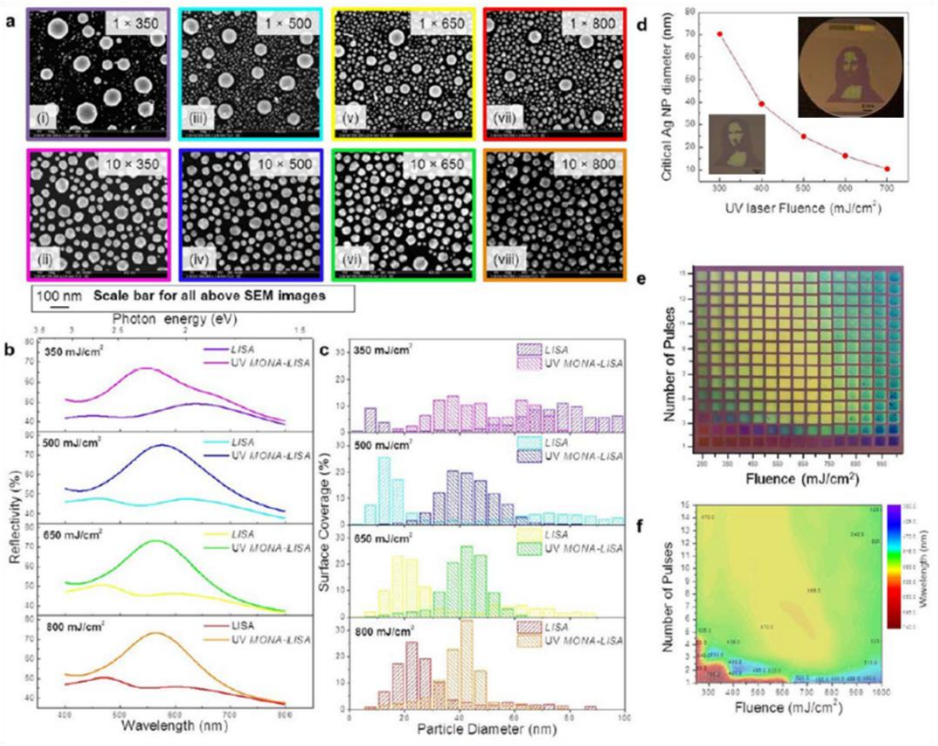

Figure 19. a) SEM images of samples processed with LISA (1 pulse, 248 nm LA) and UV MONA-LISA (10 pulses, 248 nm) under various applied fluences, b, The effect of LISA and UV MONA-LISA on the optical reflectivity spectra of a 10 nm Ag thin film under various applied fluences. c) Surface coverage of the nanoparticles in relation to the particle diameter for all the cases of (a). d) Critical nanoparticle diameter (the diameter value under which every particle remains practically cold during the UV LA process, hence these particles cannot be further manipulated upon irradiation) as a function of applied laser fluence. Inset depicts two portraits of Da Vinci's Mona Lisa: Upper inset is a macroscopic, large-scale pattern engraved on a full 2" Si wafer coated with 10 nm Ag (purple areas correspond to a process of one pulse at 500 mJ/cm^2 whereas the green areas to three pulses of the same fluence). Lower inset is a microscopic pattern engraved on the same wafer in a single pixel processing using series of photolithographic masks. e) A digital photo of a grid of LISA / UV MONA-LISA spots of varying fluence (x-axis) and number of pulses (y-axis) produced on a 10 nm Ag thin film. f) Contour plot of the dominant LSPR maximum acquired from optical reflectivity spectra from each spot of (e) (in the case of bimodal responses the maximum reflectivity response has been reported) [64].

We now present the recent experimental demonstration of MONA-LISA. The first step is a single shot UV LA to initialize nanoparticle formation from a semi-continuous metal thin film, by Laser Induced Self-Assembly (LISA). This results into the restructuring of the silver thin film into nanoparticle arrangements in macroscopic scales (several mm^2). The LISA process with a UV laser (248 nm) is strongly fluence-dependent as demonstrated in the SEM images of fig. 19.a. The Ag NPs size distributions are generally bimodal, consisting of one set of coarse and one set of fine NPs. Increasing the laser fluence from 350 mJ/cm^2 - 800 mJ/cm^2 results into a decreasing difference between the two NP sets, as shown by the quantified SEM images (fig. 18.c, purple, cyan, yellow and red lines).

The modification of NP assemblies by multiple laser pulses (MONA-LISA process) involves the utilization of the selective optical absorption and the heat dissipation, as presented in the theoretical approach above. In order to demonstrate this, we subject the initial assemblies of NPs to a series of UV and/or VIS LA steps.

Firstly, we consider the case of UV MONA-LISA, i.e. processing by multiple UV (248 nm) laser pulses, and we correlate the effect of interband absorption with the size-selective heat dissipation. Fig. 19.b shows the optical reflectivity spectra of a 10 nm Ag film recorded after UV MONA-LISA using 10 successive UV laser pulses at various fluences (magenta, blue, green and orange lines for 350, 500, 650, 800 mJ/cm^2, respectively). Comparing these spectra with those from the previous LISA processing, reveals that the consecutive pulses transform the two reflectivity peaks into one, indicating a gradual transformation of the bimodal distributions into unimodal ones. This is also confirmed by the corresponding SEM images and the size distribution histograms in Figs. 19.a and 19.c (magenta, blue, green and orange bars), respectively. The reshaping of the particles is predominantly due to the disappearance of the larger particles.

The physics behind that observation is based on the faster heat dissipation from the finer nanoparticles due to their higher effective surface (surface to volume ratio). As a result, the finer nanoparticles remain cold during UV MONA-LISA. This was quantified correctly by our photothermal calculations, which determined the equi-temperature contour lines vs nanoparticle diameter, from which the critical size under which every particle remains practically cold during the UV MONA-LISA process of Ag on Si can be inferred. Assuming for simplicity the bulk Ag melting temperature of 960 ^{0}C, the calculated values of the critical diameter vs. the fluence of the 248 nm laser are presented in fig. 19.d. Note that the critical diameter is strongly dependent on the thermal conductivity of the substrate, as a less thermally conductive substrate would hinder heat dissipation. The UV MONA-LISA process is thus based on the larger particles having the ability to raise their temperature above their melting point, and consequently melting and re-solidifying forming smaller particles with a stochastic size distribution, while the smaller ones remain below the melting threshold and therefore remain practically unaffected. Evidently, successive pulses suppress the population of the coarse particles, gradually transforming them to stable fine particles via stochastic size redistribution.

The wide range of size distributions achieved by LISA and UV MONA-LISA results in a vast colour palette of plasmonic responses as those presented in figures 2.e and 2.f (real colour appearance of the Ag nanoparticle assemblies and quantitative spectral reflectivity response, respectively). Combining the LISA and MONA-LISA process with projection masks, enables the production multicolour images of high spatial resolution and colour contrast as the one presented in the inset of fig. 19.d, depicting the two portraits of Da-Vinci's "Mona Lisa".

The implementation of MONA-LISA employing exclusively UV pulses has the inherent limitation of the UV absorption being rather insensitive to nanoparticle size, and as a result the size selectivity of the process is based exclusively on the size selectivity of the heat dissipation. This has the severe consequence that only the coarse particles are affected after successive laser pulses. In order to probe and manipulate the finer particles we must exploit their selective optical absorption via LSPR using a visible laser wavelength that would result in stronger optical absorption and hence higher temperature rise, as predicted by the computational results presented in the previous section in fig. 18.

The optimum condition of narrowing the bandwidth of the LSPR at 532 nm was achieved by applying 500 pulses at 125 mJ/cm^2 which shows that the VIS MONA-LISA is slower compared to the UV MONA-LISA that reached at steady state at 10 pulses. This is well expected considering the computational results of fig. 18, where a lower temperature rise is evident at visible wavelengths compare to UV processing.

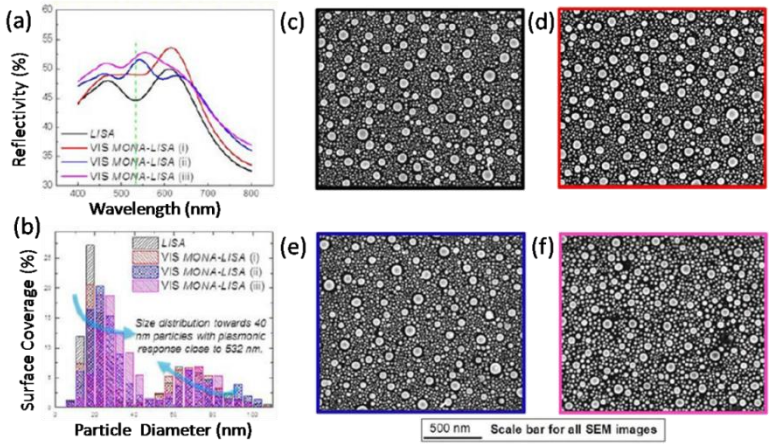

Figure 20. a) Optical reflectivity spectra of LISA (2 pulse, 248 nm at 350 mJ/cm^2 - black line), used as a template for the subsequent Visible MONA-LISA (500 pulses (red line), 2000 pulses (blue line) and 4000 pulses (magenda line), 532 nm at 125 mJ/cm^2). The green dashed line sets the 532 nm mark. b) Surface coverage of the nanoparticles in relation to the particle diameter for each laser treatment of (a). c) SEM image of LISA processed sample. d) SEM image of the Visible MONA-LISA (i) sample (500 pulses). e) SEM image of the Visible MONA-LISA (ii) sample (2000 pulses) and f) SEM image of the Visible MONA-LISA (iii) sample (4000 pulses) [64].

Exploring the VIS-MONALISA we start from a UV LISA process (248 nm, 2 pulses at 350 mJ/cm^2) which demonstrates a double reflectance peak, due to its bimodal nanostructuring, notably with no particular response close to 532 nm, as shown in fig. 20.a (black line). Applying, VIS MONA-LISA to this area, with 500 pulses (i), 2000 pulses (ii) and 4000 pulses (iii) results in gradually changing the bimodal distribution to one with a peak very close to the laser processing wavelength (532 nm). The corresponding SEM images are shown in fig.20.c,d,e,f. Analysis of these SEM images result in the histograms of fig.20.b. It is noteworthy that the VIS MONA-LISA probes particularly the finer Ag nanoparticles (<20 nm) confirming the computational analysis presented in figure 18.b. As seen in the SEM images, our

theoretical assumption of NPs in a fairly isolated arrangement at separation aspect ratio (a/d=1.2) is in close agreement with the experimental case.

5.4 Conclusions

5.4.1 Sub-surface nano-structuring

Functional plasmonic templates consisting of embedded NPs in a dielectric matrix can be fabricated by LA of a stratified metal/dielectric nano-composite. We performed an extensive theoretical investigation to highlight the underline physics of laser induced sub-surface plasmonic nano-structuring. First, we developed an accurate semi-analytical model to estimate the photo-thermal processes involved during the LA of a stratified Ag/AlN multilayer film. Using this model, we calculated the transient temperature distribution at each point in the multilayer structure. We found that the temperature spatial distribution strongly depends on the structure parameters like the metal volume ratio, the total thickness of the multilayer film and the thermal conductivity of the dielectric. By properly designing these parameters, combined with tuning the LA conditions (wavelength and fluence) once can arrive at plasmonic templates with predetermined morphology and optical response.

The latter was depicted in the experiments in which multilayers of alternative AlN/Ag layers were subjected UV LA (193 nm), leading to a subsurface formation of plasmonic NPs inside AlN matrix with a localized surface plasmon resonance responce. The effect of LA on the structural modification and the resulting optical properties of the films, was investigated as a function of laser fluence under ambient atmosphere or under a high pressure. We found that a parameter that majorly affects the annealing process and determines the resulting reconstruction is the thermal conductivity of the dielectric medium, which provides an interesting route for tailoring the optical response of such structures.

The aforementioned photo-thermal modeling was performed to investigate the laser-matter interactions and heat diffusion in the metal/ceramic multilayers upon LA. The theoretical results covered an extensive range of values in order to present a generic study for different dielectrics. They revealed the paramount role of the thermal conductivity of the dielectric as well as of the relative content of the metal/dielectric components within the multilayer. In particular, low values (a-AlN and Y_2O_3) lead to a significant temperature gradient across the multilayer structure resulting into broadband size distributions for the Ag particles. On the contrary, high k values (such as in the case of w-AlN) lead to a narrower size distribution of Ag particles within a shallower depth from the film surface. The developed temperature gradient is strongly affected by nonlinearities in material properties, and is also affected by the individual layer thickness and in particular the thickness ratio between Ag and the dielectric in one bilayer: due to the high thermal conductivity of Ag, the higher the Ag content is, the smaller the temperature gradients are within the film, even for low values of the dielectric thermal conductivity.

Furthermore, the optical response of the produced plasmonic nano-composites can be tuned by the fluence of LA as it is depicted from experimental ORS and confirmed from FDTD calculations. Specifically, increasing the fluence of the LA bigger NPs are produced with higher reflectance values and red-shifted LSPRs.

Finally, we demonstrated the cold character of LA by creating plasmonic templates on flexible polymeric substrates. From the point of view of applications on optical encoding of information, these examples signify the simplicity, flexibility and versatility of the proposed engineering approach. An additional feature of the produced encapsulated plasmonic NP patterns is their capability of providing two views of the same image with complementary colors in reflection and transmission.

5.4.2 Surface nano-structuring

Functional plasmonic templates consisting of metallic NPs on a substrate can be fabricated by LA of a thin metal film on the substrate. We performed an extensive theoretical investigation to highlight the photo-thermal processes involved in laser induced surface plasmonic nano-structuring. Specifically, we explored templates consisting of hemi-spherical Ag NPs on Si substrate, for different NPs arrangements and sizes, for both UV and optical irradiation. We found and identified different absorption mechanisms which are size selective and enable geometric specificity such as: a) interband absorption taking place at the UV zone, probing the metal's internal d-electrons and b) intraband absorption taking place at the near-UV, and visible zone, probing the metal's free electrons at the specific spectral position of LSPR.

Then, we performed heat diffusion simulations combining the absorption spatial profile found from the optical calculations with the appropriate experimental laser temporal profile, and resulted into a mapping of the maximum temperature rise as a function of particle size, laser wavelength and laser fluence. In these maps we distinguish spectral regions of higher and lower temperature, which can be used to provide a recipe that allows the design for the modification of NP configuration towards a pre-designed one. In particular, by sequentially tuning the laser wavelength into resonance with different physical absorptions, we can selectively target the melting and re-solidification of different particle size groups. This idea was implemented in experiments, in which repeated laser treatments targeted different NPs size groups with different laser wavelengths, and drove the final size distribution. We termed this process: "Modification of Nanoparticle Arrays by Laser Induced Self Assembly" (MONA-LISA). Specifically, in the experiments, successive pulses of UV LA reduced the volume fraction of larger nanoparticles (>50 nm), while VIS LA further refined the size distributions by reducing the volume fraction of the smaller nanoparticles (<20 nm). This combined UV and VIS LA treatment provides unprecedented control on the size distributions and plasmonic behaviour of nanoparticle arrays of noble metals.

5.5 References

[1] S.A. Maier, Plasmonics: fundamentals and applications, Springer, New York, (2007)

[2] U. Kreibig, M. Vollmer, Optical Properties of Metal Clusters, Springer, Berlin, (1995)

[3] K.A. Willets, R.P. Van Duyne, Localized Surface Plasmon Resonance Spectroscopy and Sensing, Annu. Rev. Phys. Chem., 58, 267-297, (2007)

[4] G.V. Hartland, Optical Studies of Dynamics in Noble Metal Nanostructures, Chem. Rev., 111, 3858-3887, (2011)

[5] M.R. Jones, K.D. Osberg, R.J. Macfarlane, M.R. Langille, C.A. Mirkin, Templated techniques for the synthesis and assembly of plasmonic nanostructures. Chem. Rev. 111, 3736-3827, (2011)

[6] X. Lu, M. Rycenga, S.E. Skrabalak, B.J Wiley, Y. Xia, Chemical synthesis of novel plasmonic nanoparticles, Annu. Rev. Phys. Chem., 60, 167-192, (2009)

[7] N.J. Halas, Plasmonics: an emerging field fostered by Nano Letters, Nano Let. 10, 3816-3822, (2010)

[8] M.L. Brongersma, V.M. Shalaev, The case for plasmonics, Science, 328, 440-441, (2010)

[9] J.A. Fan, C Wu, K. Bao, J. Bao, R. Bardhan, N.J. Halas, V.N. Manoharan P. Nordlander, G. Shvets, F. Capasso, Self-assembled plasmonic nanoparticle clusters, Science, 328, 1135-1138, (2010)

[10] E. Ozbay, Plasmonics: merging photonics and electronics at nanoscale dimensions, Science, 311, 189-193, (2006)

[11] E. Lidorikis, Modeling of enhanced absorption and Raman scattering caused by plasmonic nanoparticle near fields, Journal of Quantitative Spectroscopy and Radiative Transfer, 113, 2573–2584, (2012)

[12] C.F. Bohren, D.R. Huffman, Absorption and scattering of light by small particles. Wiley Interscience, New York (1983)

[13] A.J. Haes, C.L. Haynes, A.D. McFarland, G.C. Schatz, R.P. Van Duyne, S.L. Zou, Plasmonic materials for surface-enhanced sensing and spectroscopy, MRS Bull, 30, 368-375, (2005)

[14] K.S. Lee, M.A.J. El-Sayed, Gold and silver nanoparticles in sensing and imaging: sensitivity of plasmon response to size, shape and metal composition, Phys. Chem. B, 110, 19220-19225, (2006)

[15] M.M. Miller, A.A. Lazarides, Sensitivity of metal nanoparticle surface plasmon resonance to the dielectric environment, J. Phys. Chem. B, 109, 21556-21565, (2005)

[16] O. Kvitek, J. Siegel, V. Hnatowicz, V. Svorcik, Noble metal nanostructures: influence of structure and environment on their optical properties, J. Nanomater. 743684, (2013)

[17] N.J. Halas, Playing with plasmons: tuning the optical resonant properties of metallic nanoshells, MRS Bull, 30, 362-367, (2005)

[18] S. Underwood, P. Mulvaney, Effect of solution refractive index on the color of gold colloids, Langmuir, 10, 3427-3430, (1994)

[19] J.J. Mock, M. Barbic, D.R. Smith, D.A. Schultz, S.J. Schultz, Shape effects in plasmon resonance of individual colloidal silver nanoparticles, Chem. Phys., 116, 6755-6759, (2002)

[20] G. Walters, I. P. Parkin, The incorporation of noble metal nanoparticles into host matrix thin films: synthesis, characterisation and applications, J. Mater. Chem., 19, 574-590, (2009)
[21] M. Rycenga, C. M. Cobley, J. Zeng, W. Li, Christine H. Moran, Q. Zhang, D. Qin, Y. Xia, Controlling the Synthesis and Assembly of Silver Nanostructures for Plasmonic Applications, Chem. Rev., 111, 3669-3712, (2011)
[22] L. Armelao, D. Barreca, G. Bottaro, A. Gasparotto, S. Gross, C. Maragnob, E. Tondello, Recent trends on nanocomposites based on Cu, Ag and Au clusters: A closer look, Coordination Chemistry Reviews, 250, 1294-1314, (2006)
[23] M. B. Cortie, A. M. McDonagh, Synthesis and Optical Properties of Hybrid and Alloy Plasmonic Nanoparticles, Chem. Rev., 111, 3713-3735, (2011)
[24] J.N. Anker, W.P. Hall, O. Lyandres, N.C. Shah, J. Zhao, R.P. Van Duyne, Biosensing with plasmonic nanosensors, Nat. Mater.,7, 442-453, (2008)
[25] K. M. Mayer, J. H. Hafner, Localized Surface Plasmon Resonance Sensors, Chem. Rev., 111, 3828-3857, (2011)
[26] Y.Jin, Engineering Plasmonic Gold Nanostructures and Metamaterials for Biosensing and Nanomedicine, Adv. Mater., 24, 5153-5165, (2012)
[27] E. Usukura, S. Shinohara, K. Okamoto, J. Lim, K. Char, K. Tamada, Highly confined enhanced surface fluorescence imaging with two-dimensional silver nanoparticle sheets, Appl Phys Lett,104, 121906 (2014)
[28] Moskovits M., Surface-enhanced spectroscopy, Rev. Mod. Phys, 57, 783-826 (1985)
[29] K. Kneipp, Y. Wang, H. Kneipp, L. T. Perelman, I. Itzkan, R. R. Dasari, M. S. Feld, Single Molecule Detection Using Surface-Enhanced Raman Scattering (SERS), 78(9), 1667(4), 1997
[30] Y. Fang, N.H. Seong, D.D. Dlott, Measurement of the Distribution of Site Enhancements in Surface-Enhanced Raman Scattering, Science, 321, 388-392 (2008)
[31] S. J. Henley, J. D. Carey, S. R. P. Silva, Laser-nanostructured Ag films as substrates for surface-enhanced Raman spectroscopy, Applied Physics Letters, 88, 081904, (2006)
[32] S. J. Henley, S. R. P. Silva, Laser direct write of silver nanoparticles from solution onto glass substrates for surface-enhanced Raman spectroscopy, Applied Physics Letters, 91, 023107 (2007)
[33] K. Christou, I. Knorr, J. Ihlemann, H. Wackerbarth, V. Beushausen, Fabrication and Characterization of Homogeneous Surface-Enhanced Raman Scattering Substrates by Single Pulse UV-Laser Treatment of Gold and Silver Films, Langmuir, 26(23), 18564-18569, (2010)
[34] C.H. Lin, L. Jiang, J. Zhou, H. Xiao, S.J. Chen, H.L Tsai, Laser-treated substrate with nanoparticles for surface-enhanced Raman scattering, 35(7),Opt. Let, (2010)
[35] D. Wan, H. L. Chen, S. C. Tseng, L. A. Wang,Y. P. Chen, One-Shot Deep-UV Pulsed-Laser-Induced Photomodification of Hollow Metal Nanoparticles for High-Density Data Storage on Flexible Substrates, ACS Nano, 4, 165-173, (2010)

[36] P. Zijlstra, J. W. M. Chon, M. Gu, Five-dimensional optical recording mediated by surface plasmons in gold nanorods, Nature, 459, 410-413, (2009)
[37] C. Ryan, C. W. Christenson, B. Valle, A. Saini, J. Lott, J. Johnson, D. Schiraldi, C. Weder, E. Baer, K. D. Singer, J. Shan, Roll-to-Roll Fabrication of Multilayer Films for High Capacity Optical Data Storage, Adv. Mater., 24, 5222-5226, (2012)
[38] W. T. Chen, P. C. Wu, C. J. Chen, C. J. Weng, H. C. Lee, T. J. Yen, C. H. Kuan, M. Mansuripur, D. P. Tsai, Manipulation of multidimensional plasmonic spectra for information storage, Appl Phys Lett, 98, 171106, (2011)
[39] N. Lagos, M. M. Sigalas, E. Lidorikis, Theory of plasmonic near-field enhanced absorption in solar cells, Applied Physics Letters, 99, 063304, (2011)
[40] N. Kalfagiannis, P. G. Karagiannidis, C. Pitsalidis, N. T. Panagiotopoulos, C. Gravalidis, S. Kassavetis, P. Patsalas, S. Logothetidis, Plasmonic silver nanoparticles for improved organic solar cells, Solar Energy Materials and Solar Cells, 104, 165-174, (2012)
[41] H. A. Atwater, A. Polman, Plasmonics for improved photovoltaic devices Nat. Mater.,9, 205-213, (2010)
[42] M. J. Beliatis, S. J. Henley, S. Han, K. Gandhi, A. A. D. T. Adikaari, E. Stratakis, E. Kymakis and S. R. P. Silva, Organic solar cells with plasmonic layers formed by laser nanofabrication, Physical Chemistry Chemical Physics, 15, 8237-8244, (2013)
[43] H. Zoubos, L. E. Koutsokeras, D. F. Anagnostopoulos, E. Lidorikis, S. A. Kalogirou, A. R. Wildes, P. C. Kelires and P. Patsalas, Broadband optical absorption of amorphous carbon/Ag nanocomposite films and its potential for solar harvesting applications, Solar Energy Materials and Solar Cells, 117, 350-356, (2013)
[44] S. S. Kim, S. I. Na, J. Jo, D. Y. Kim, Y. C. Nah, Plasmon enhanced performance of organic solar cells using electrodeposited Ag nanoparticles, Appl Phys Lett, 93, 073307(3), (2008)
[45] J. R. Cole, N. J. Halas, Optimized plasmonic nanoparticle distributions for solar spectrum harvesting, Appl. Phys. Lett., 89, 153120(3), (2006)
[46] A. Siozios, N. Kalfagiannis, D.V. Bellas, C. Bazioti, G.P. Dimitrakopulos, G. Vourlias, W.M. Cranton, E. Lidorikis, D.C. Koutsogeorgis, P. Patsalas, Sub-surface laser nanostructuring in stratified metal/dielectric media: a versatile platform towards flexible, durable and large-scale plasmonic writing, Nanotechnology, (2015) 26 155301 (10pp).
[47] C. Bazioti, G. P. Dimitrakopulos, T. Kehagias, P. Komninou, A. Siozios, E. Lidorikis, D. C. Koutsogeorgis, P. Patsalas, Influence of laser annealing on the structural properties of sputtered AlN:Ag plasmonic nanocomposites, Journal of Materials Science, 49, 3996-4006, (2014)
[48] A. Siozios, D. C. Koutsogeorgis, E. Lidorikis, G. P. Dimitrakopulos, T. Kehagias, H. Zoubos, P. Komninou, W. M. Cranton, C. Kosmidis, P. Patsalas, Optical Encoding by Plasmon-Based Patterning: Hard and Inorganic Materials Become Photosensitive, Nano Letters, 12, 259-263, (2012)
[49] A. Siozios, H. Zoubos, N. Pliatsikas, D. C. Koutsogeorgis, G. Vourlias, E. Pavlidou, W. Cranton, P. Patsalas, Growth and annealing strategies to control the microstructure of AlN:Ag nanocomposite films for plasmonic applications, Surface and Coatings Technology, 255, 28-36, (2014)

[50] M. Torrell, P. Machado, L. Cunha, N. M. Figueiredo, J. C. Oliveira, C. Louro, F. Vaz, Development of new decorative coatings based on gold nanoparticles dispersed in an amorphous TiO2 dielectric matrix, Surface & Coatings Technology, 204, 1569-1575, (2010)

[51] J. Henson, J. C. Heckel, E. Dimakis, J. Abell, A. Bhattacharyya, G. Chumanov, T. D. Moustakas and R. Paiella, Plasmon enhanced light emission from InGaN quantum wells via coupling to chemically synthesized silver nanoparticles Appl. Phys. Lett., 95, 151109 (3), (2009)

[52] J. H. Seo, J. H. Park, S. I. Kim, B. J. Park, Z. Ma, J. Choi, B. K. Ju, Nanopatterning by Laser Interference Lithography: Applications to Optical Devices, Journal of Nanoscience and Nanotechnology, 14, 1521-1532, (2014)

[53] U. Guler, J. C. Ndukaife, G. V. Naik, A. G. A. Nnanna, A. V. Kildishev, V. M. Shalaev, A. Boltasseva, Local Heating with Lithographically Fabricated Plasmonic Titanium Nitride Nanoparticles, Nano Lett., 13, 6078-6083, (2013)

[54] G. Bracher, K. Schraml, M. Ossiander, S. Frédérick, J. J. Finley, M. Kaniber, Optical study of lithographically defined, subwavelength plasmonic wires and their coupling to embedded quantum emitters, Nanotechnology, 25, 075203 (6pp), (2014)

[55] J. Toudert, D. Babonneau, S. Camelio, T. Girardeau, F. Yubero, J. P.Espinós and A. R. Gonzalez-Elipe, Using ion beams to tune the nanostructure and optical response of co-deposited Ag:BN thin films, Journal of Physics D: Applied Physics, 40, 4614-4620, (2007)

[56] V. A. Sivakov, K. Höflich, M. Becker, A. Berger, T. Stelzner, K. E. Elers, V. Pore, M. Ritala and S. H. Christiansen, Silver Coated Platinum Core–Shell Nanostructures on Etched Si Nanowires: Atomic Layer Deposition (ALD) Processing and Application in SERS, Chem. Phys. Chem., 11, 1995-2000, (2010)

[57] Y. Lu, J. Y. Huang, C. Wang, S. Sun and J. Lou, Cold welding of ultrathin gold nanowires, Nature Nanotechnology, 5, 218-224, (2010)

[58] Y. K. Mishra, S. Mohapatra, D. Kabiraj, B. Mohanta, N. P. Lalla, J.C. Pivin, D. K. Avasthi, Scripta Materialia, Synthesis and characterization of Ag nanoparticles in silica matrix by atom beam sputtering, 56, 629-632, (2007)

[59] I. Tanahashi, Y. Manabe, T. Tohda, S. Sasaki, A. Nakamura, Optical nonlinearities of Au/SiO2 composite thin films prepared by a sputtering method, Journal of Applied Physics, 79, 1244-1249, (1996)

[60] D. Lin, H. Tao, J. Trevino, J. P. Mondia, D. L. Kaplan, F. G. Omenetto, L. Dal Negro, Direct Transfer of Subwavelength Plasmonic Nanostructures on Bioactive Silk Films, Adv. Mater., 24, 6088-6093, (2012)

[61] P. Nielsen, P. Morgen, A. C. Simonsen, O. Albrektsen, Hemispherical Shell Nanostructures from Metal-Stripped Embossed Alumina on Aluminum Templates, Journal of Physical Chemistry C, 115, 5552-5560, (2011)

[62] J. H. Park, P. Nagpal, K. M. McPeak, N. C. Lindquist, S. H. Oh, D. J. Norris, Fabrication of Smooth Patterned Structures of Refractory Metals, Semiconductors, and Oxides via Template Stripping, ACS Applied Materials and Interfaces, 5, 9701-9708, (2013)

[63] P. Farzinpour, A. Sundar, K. D. Gilroy, Z. E. Eskin, R. A. Hughes, S. Neretina, Dynamic templating: a large area processing route for the assembly of periodic arrays of sub-micrometer and nanoscale structures, Nanoscale, 5, 1929-1938, (2013)

[64] N. Kalfagiannis, A. Siozios, D. V. Bellas, D. Toliopoulos, L. Bowen, N. Pliatsikas, W. M Cranton, C. Kosmidis, D. C. Koutsogeorgis, E. Lidorikis, P. Patsalas, Selective MOdification of Nanoparticle Arrays by Laser-Induced Self Assembly (MONA-LISA): putting control into bottom-up plasmonic nanostructuring, (Submitted)

[65] S. J. Henley, J. D. Carey, S. R. P. Silva, Pulsed-laser-induced nanoscale island formation in thin metal-on-oxide films, Phys. Rev. B, 72, 195408 (10), (2005)

[66] M. J Beliatis, S. J. Henley, S. R. P. Silva, Engineering the plasmon resonance of large area bimetallic nanoparticle films by laser nanostructuring for chemical sensors, Opt. Lett. 36, 8, 1362-1364, (2011)

[67] K. Christou, I. Knorr, J. Ihlemann, H. Wackerbarth, V. Beushausen, Fabrication and Characterization of Homogeneous Surface-Enhanced Raman Scattering Substrates by Single Pulse UV-Laser Treatment of Gold and Silver Films, Langmuir, 26(23), 18564-18569, (2010)

[68] C. Favazza, R. Kalyanaraman, R. Sureshkumar, Robust nanopatterning by laser-induced dewetting of metal nanofilms, Nanotechnology, 17, 4229-4234, (2006)

[69] H. Krishna, N. Shirato, C. Favazza, R. Kalyanaraman, Pulsed laser induced self-organization by dewetting of metallic films, J. Mater. Res., 26, 2, 154-169, (2011)

[70] C.E. Rodrígueza, R.J. Peláeza, C.N. Afonsoa, S. Riedelb, P. Leidererb, D. Jimenez-Reyc, A. Climent- Fontc, Plasmonic response and transformation mechanism upon single laser exposure of metal discontinuous films, Applied Surface Science, 302, 32-36, (2014)

[71] F. Ruffino, A. Pugliara, E. Carria, C. Bongiorno, C. Spinella, M. G. Grimaldi, Formation of nanoparticles from laser irradiated Au thin film on SiO2/Si: Elucidating the Rayleigh-instability role, Materials Letters, 84, 27-30, (2012)

[72] F. Ruffino, E. Carria, S. Kimiagar, I. Crupi, F. Simone, M. G. Grimaldi, Formation and Evolution of Nanoscale Metal Structures on ITO Surface by Nanosecond Laser Irradiations of Thin Au and Ag Films, Science of Advanced Materials, Vol. 4, 708-718, (2012)

[73] F. Ruffino, A. Pugliara, E. Carria, L. Romano, C. Bongiorno, G. Fisicaro, A. La Magna, C. Spinella, M. G. Grimaldi, Towards a laser fluence dependent nanostructuring of thin Au films on Si by nanosecond laser irradiation, Applied Surface Science, 258, 9128-9137, (2012)

[74] S. J. Henley, C. H. P. Poa, A. A. D. T. Adikaari, C. E. Giusca, J. D. Carey, S. R. P. Silva, Excimer laser nanostructuring of nickel thin films for the catalytic growth of carbon nanotubes, Applied Physics Letters, 84, 4035, (2004)

[75] S. J. Henley, J. D. Carey, S. R. P. Silva, Metal nanoparticle production by pulsed laser nanostructuring of thin metal films, Applied Surface Science, 253, 8080-8085, (2007)

[76] J. Trice, D. Thomas, C. Favazza, R. Sureshkumar, R. Kalyanaraman, Pulsed-laser-induced dewetting in nanoscopic metal films: Theory and experiments, Phys. Rev. B, 75, 235439, (2007)

[77] E. D. Palik, Handbook of Optical Constants of Solids, Academic, San Diego, (1998).

[78] In-lab ellipsometric measurements

[79] O. Deparis, Poynting vector in transfer-matrix formalism for the calculation of light absorption profile in stratified isotropic optical media, Optic letters, Vol. 36, No. 20 (2011).
[80] David R. Lide 2005 CRC Handbook of Chemistry and Physics, 85th Edition (CRC Press).
[81] S. R. Choi, D. Kim, S. H. Choa, S. H. Lee and J. K. Kim, Thermal Conductivity of AlN and SiC Thin Films, International Journal of Thermophysics, Vol. 27, No. 3, May 2006.
[82] C. Duquenne, M. P. Besland, P. Y. Tessier, E. Gautron, Y Scudeller and D. Averty, Thermal conductivity of aluminium nitride thin films prepared by reactive magnetron sputtering, J. Phys. D: Appl. Phys. 45 015301-8 (2012).
[83] G. A. Slack, R. A. Tanzilli, R. O. Pohl and J. W. Vandersande, The intrinsic thermal conductivity of AIN J. Phys. Chem. Solids 48 641-7 (1987)
[84] W. C. E. W. James, G. L. Rorrer and R. E. Wilson 2008 Fundamentals of Momentum, Heat and Mass Transfer (New York: Wiley).
[85] P. K. Jain, W. Huang, and M. A. El-Sayed, On the universal scaling behavior of the distance decay of plasmon coupling in metal nanoparticle pairs: a plasmon ruler equation, Nano Lett. 7, 2080-2088 (2007).
[86] P. H. Klein and W. J. Croft Thermal conductivity, diffusivity, and expansion of Y2O3, Y3Al5O12, and LaF3 in the range 77–300 K (1967) J. Appl. Phys. 38 1603-7.

Chapter 6 General Conclusions

In this thesis we designed and evaluated the optical performance of various NC metal-dielectric absorbers, as candidates for solar selective coatings in high temperature applications of parabolic trough collectors. Improving the optical properties of solar selective coatings and increasing the operating temperature above the current limits of 400 ^{0}C, one can improve the power cycle efficiency and get reductions in the cost of solar electricity. To do so, we explored different dielectric NCs consisting of various transparent matrixes (SiO_2, AlN, SiC) and metallic inclusions (Cu, Ni) a characteristic noble metal and transition metal respectively. We evaluated their performance in terms of total energy efficiency as a function of metal volume ratio, shape of inclusions, surface roughness and thickness of the NC, in a wide range of temperatures (400 ^{0}C - 1000 ^{0}C) and concentration ratios (80-500 suns), and devised the rules for obtaining NC coatings with high efficiency. Comparing the two metals we found similar efficiencies. Also, we found that for one of the best candidate for solar selective coating (low index matrix with low volume filling of Cu NPs), increasing the operating temperature from the recent limits of 400 ^{0}C and 80 suns concentration to 870 ^{0}C and 500 suns concentration we get an increese in efficiency from 0.405 to 0.52 respectively, which means ~30% better performance. Furthermore, we extensively investigate the spectral selectivity of a TCO material to be used as a selective coating on the inner glass envelop surface. Such materials are characterized by high transmittance in the solar spectrum and high reflectance in the IR spectrum. By free-designing such a coating, we achieve an extra gain between 5-11% for low index NCs and 9.5-21% for the high index NCs, depending on the concentration ratio.

Furthermore, we explored how the LSPR traits (electric-field enhancement, scattering) are modulated depending on the NP shape, which varies depending on the final NP configuration achieved in a top-down or bottom-up methods, and in relevance to SERS applications. For simplicity, we examined two “extreme” shapes: nano-columns as a representative NP shape of top-down methods and spherical nano-domes, as a representative NP shape of bottom-up methods. We produced detailed electric field enchantment maps showing that depending on their shape, the frequency at which maximum field enhancement occurs, varies depending on the location on the NP surface, pointing towards modulated LSPR oscillations across the NP’s volume. This results into different maximum electric field enhancement across the NP occurring at different spectral positions. Thus, the fluorescence and Raman enhancement will depend on were on the NP’s surface the molecules are adsorbed. Also, to tune the NP LSPR, we examined the effect of thin dielectric coatings (AlN) on the MNPs. The response is again found to be dependent on the NP’s shape, and results compared well to recent experiments.

Finally, we introduced a modeling and design process for the development of functional plasmonic templates with pre-determined properties, relevant to the aforementioned applications and many others. We extensively explored the photo-thermal processes involved in laser-induced: a) sub-surface and b) surface nano-structuring. In the first case, laser annealing of a stratified metal-dielectric multilayer structure, resulted into nano-composites consisting of embedded MNPs inside a dielectric matrix. In the second case, laser annealing of a thin metal film on a substrate, resulted on MNPs on a substrate. By tuning the annealing parameters like laser fluence and wavelength and/or the structure parameters like the thickness of the metallic film and the volume ratio of the ceramic metal composite, one can arrive at nano-structures with pre-designed morphology.

In the case of subsurface plasmonic nano-structuring, we developed an accurate semi-analytical model to estimate the photo-thermal processes involved during the LA of a stratified Ag/AlN multilayer film. Using this model, we calculated the temperature spatial distribution across the multilayer structure. We found that strong temperature gradients are developed across the multilayer structure, which depend on structure parameters like the metal volume ratio, the total thickness of the multilayer film and the thermal conductivity of the dielectric. By properly designing these parameters, combined with the LA conditions (wavelength and fluence) one can arrive at plasmonic nano-composites with predetermined morphology and optical response.

In the case of surface plasmonic nano-structuring, we extensively explored templates consisting of spherical nano-domes of Ag NPs on Si substrate, for different NPs arrangements and sizes, and irradiation between the UV and optical spectrum. We identified and utilized different absorption mechanisms, which are size selective, and thus enable geometric specificity, such as: a) interband absorption taking place in the UV zone, probing the metal's internal d-electrons and b) intraband absorption taking place in the visible zone, probing the metal's free electrons at the specific spectral position of LSPR. Then, we performed heat diffusion simulations, and mapped the maximum temperature rise as a function of particle size, laser wavelength and laser fluence. In these maps we distinguish spectral regions of higher and lower temperature, which can be used to provide a recipe that allows the pre-designed modification of NP configuration. In particular, by sequentially tuning the laser wavelength into resonance with different physical absorption mechanisms, we can selectively target the melting and re-solidification of different particle size groups. This idea was implemented in experiments, in which repeated laser treatments with different laser wavelengths targeted different NPs size groups, driving the final size distribution towards the predetermined one. We termed this process: "Modification of Nanoparticle Arrays by Laser Induced Self Assembly" (MONA-LISA).

Papers

1. A. Siozios, N. Kalfagiannis, **D.V. Bellas**, C. Bazioti, G.P. Dimitrakopulos, G. Vourlias, W.M. Cranton, E. Lidorikis, D.C. Koutsogeorgis, P. Patsalas, Sub-surface laser nanostructuring in stratified metal/dielectric media: a versatile platform towards flexible, durable and large-scale plasmonic writing, Nanotechnology,Volume: 26, Issue: 15, Article Number: 155301, (2015).
2. N. Kalfagiannis, A. Siozios, **D. V. Bellas**, D. Toliopoulos, L. Bowen, N. Pliatsikas, W. M Cranton, C. Kosmidis, D. C. Koutsogeorgis, E. Lidorikis, P. Patsalas, Selective MOdification of Nanoparticle Arrays by Laser-Induced Self Assembly (MONA-LISA): putting control into bottom-up plasmonic nanostructuring, (Submitted 2015).
3. **Dimitris V. Bellas** and Elefterios Lidorikis, Design of high-temperature solar-selective coatings for application in solar collectors, (Under Preparation).
4. **D. V. Bellas**, A. Siozios, N. T. Panagiotopoulos, P. Patsalas, E. Lidorikis, Shape effects of Ag plasmonic nanoparticles on a substrate in relation to enhanced spectroscopy applications, (Under Preparation).
5. **D.V. Bellas**, D.Toliopoulos, A. Siozios, N. Kalfagiannis, D.C.Koutsogeorgis, P. Patsalas , E. Lidorikis, Simulating the opto-thermal processes involved in laser induced self-assembly of surface and sub-surface plasmonic nano-structuring, (Under Preaparation)

Conferences

1. Design of nanocomposite metalodielectric absorbers for application to solar collectors. **Dimitris V. Bellas** and Elefterios Lidorikis. 8th International Conference on Nanoscience & Nanotechnologies (NN11),12-15 July 2011, Thessaloniki, Greece (poster presentation).
2. Design of nanocomposite metalodielectric absorbers for application to solar collectors. **Dimitris V. Bellas** and Elefterios Lidorikis. E-MRS Spring Meeting, Strasbourg France, May 14-18 2012 (oral presentation).
3. Exploring the shape effects of Ag plasmonic nanoparticles on a substrate, relevant to enhanced spectroscopy applications. **D. V. Bellas**, A. Siozios, N. T. Panagiotopoulos, P. Patsalas, E. Lidorikis. 10th International Conference on Nanoscience & Nanotechnologies (NN13) 9-12 July 2013, Thessaloniki, Greece, (oral presentation).
4. Simulating the opto-thermal processes involved in laser induced self-assembly of surface and sub-surface plasmonic nano-structuring. **D. V. Bellas**, D .Toliopoulos, A. Siozios, N. Kalfagiannis, L. Bowen, N. Pliatsikas, G. Vourlias, K. Vazioti, G. P Dimitrakopoulos, D. C. Koutsogeorgis, P. Patsalas , E. Lidorikis, 11th International Conference on Nanoscience & Nanotechnologies (NN14) 8-11 July 2014, Thessaloniki, Greece, (oral presentation).

Acknowledgments

With great pleasure, I would like to deeply thank my supervisor Associate Professor Elefterios Lidorikis for his guidance, support and encouragement during the entire length of my PhD research, as well as for being a continuous source of new ideas that led to the research of this thesis. I am very lucky that he gave me the opportunity to work in a very exciting research area and for providing the necessary help in several occasions.

I would also like to express my gratitude to the member of the PhD advisor committee Associate Professor Panagiotis Patsalas for an excellent collaboration in all this time, for his physical insight and guidance, and for providing the experiments presented in this work. I'm also grateful to the Associate Professor Demosthenes Koutsogeorgis, Dr Nikolaos Kalfagiannis, Dr Nikolaos Panagiotopoulos and Dr Anastasios Siozios who carried out the experiments, and for many illuminating discussions on the combination of theory and experiments. Moreover, I would like to thank Professor Apostolos Avgeropoulos who was the third member of the PhD advisor committee and he replaced from the Associate Professor Nikolaos Zafeiropoulos (because now he is on sabbatical at KAUST University), for his support in the entire undergraduate and graduate years. Associate Professor Nikolaos Zafeiropoulos and the members of the examination committee Professor Vasileios Kalpakidis, Associate Professor Dimitrios Papageorgiou, Associate Professor Christina Lekka and Assistant Professor Leonidas Gergidis are acknowledged for reading the thesis and for their valuable suggestions.

I would like to thank the technical staff of the laboratory Mr Kostas Dimakopoulos and Mr Kostas Prouskas for their assistance in solving software and hardware problems that I had encountered during the PhD, their assistance was very important.

I would like to thank my friends and colleagues at the laboratory for their support and excellent collaboration. The older PhD students George Bokas, Martha Gialampouki and Julio Gutierrez Moreno for their help and support from the beggining of the PhD in several occasions. And the new members, Dr Nojoon Myoung, Dr Sofia Evangelou, Ioannis Vaggelidis, Alva Dagli, Alexis Kotanidis, Koulla Ioannou and Spyros Doukas for their friendship and excellect collaboration, providing me any help whenever I needed.

Also, I would like to express a big "thank you" to those friends that have stood by me all these years and have helped me in their own special way. My friend Dr Dimitris Moschovas who stood by me all these years as a very good friend, encourage and support me in many ways and many times. My friends, Dr Alexandra Lagogianni, Dr Theodore Makris, Dr George Zapsas, Dr George Gikas and Nikolaos Plakoutsis who have supported me in their own special way all these years.

My deepest gratitude goes to my family, my parents Vasilis and Eleni, and my sister Chrysanthi that supports me in every step I take in life and every decision I make, without their support and love I would never be here now. This thesis is dedicated to them.

Finally, I would like to thank the research project “Heracleitus II” that financially supported me during the period of this thesis and gave me the opportunity to be fully committed in research.

This research has been co-financed by the European Union (European Social Fund – ESF) and Greek national funds through the Operational Program "Education and Lifelong Learning" of the National Strategic Reference Framework (NSRF) - Research Funding Program: Heracleitus II. Investing in knowledge society through the European Social Fund.

Η παρούσα έρευνα έχει συγχρηματοδοτηθεί από την Ευρωπαϊκή Ένωση (Ευρωπαϊκό Κοινωνικό Ταμείο - ΕΚΤ) και από εθνικούς πόρους μέσω του Επιχειρησιακού Προγράμματος «Εκπαίδευση και Δια Βίου Μάθηση» του Εθνικού Στρατηγικού Πλαισίου Αναφοράς (ΕΣΠΑ) – Ερευνητικό Χρηματοδοτούμενο Έργο: Ηράκλειτος ΙΙ. Επένδυση στην κοινωνία της γνώσης μέσω του Ευρωπαϊκού Κοινωνικού Ταμείου.